LASER-POLARIZED ^{129}Xe MAGNETIC RESONANCE SPECTROSCOPY AND IMAGING; THE DEVELOPMENT OF A METHOD FOR *IN VIVO* PERFUSION MEASUREMENT

Matthew S. Rosen

A dissertation submitted in partial fulfillment
of the requirements of the degree of
Doctor of Philosophy
(Physics)
in The University of Michigan
2001

Doctoral Committee:

Professor Timothy E. Chupp, Chair
Assistant Professor Alberto G. Rojo
Professor Rudolf P. Thun
Associate Research Scientist Kevin P. Coulter
Assistant Research Scientist Scott D. Swanson

"A human person must put propriety and music first."

Hsi-yu Chi, *The Journey to the West*

For my mother, Deborah M. Rosen

TABLE OF CONTENTS

LIST OF FIGURES

LIST OF TABLES

Chapter 1

Introduction

Overcoming the Powers of Evil in NMR

This thesis describes the application of spin-exchange optical-pumping techniques to *in vivo* magnetic resonance studies, thus extending the utility of laser-polarized noble gases from applications in high density nuclear targets [1, 2], neutron polarizers [3], and in benchtop tests of fundamental symmetries [4-9]. *In vivo* magnetic resonance with laser-polarized ^{129}Xe is still in its infancy, and the work presented in this thesis includes many of the first experiments in this field. The intent of this thesis is to establish an experimental and theoretical foundation for the quantitative non-invasive *in vivo* measurement of perfusion with laser-polarized ^{129}Xe magnetic resonance.

In the past two decades, nuclear magnetic resonance (NMR) techniques have led to the development of magnetic resonance imaging (MRI) (for review see [10]). MRI has become a powerful, non-invasive diagnostic and research technique in medicine, and it is the imaging modality of choice for many regions of the body. Magnetic resonance images are tomographic representations of the spatial variation in the density and magnetic properties of nuclear moments (typically ^{1}H). In conventional magnetic resonance, the spin polarization used in imaging is determined by the Boltzmann equilibrium. Large, static magnetic fields are used to induce a Boltzmann polarization of water protons (^{1}H). The NMR signal per unit volume is proportional to the nuclear magnetization $\rho\mu P$, where ρ is the density, μ is the nuclear magnetic moment, and P is the nuclear polarization. The nuclear magnetic moments are small (of order 10^{-23} erg/G), and the induced Boltzmann nuclear spin polarization is tiny ($7\ 10^{-6}$ at 2 T). Despite this, the high proton density in

tissue-bound water compensates and makes high-resolution ^{1}H MRI possible. However, several MRI techniques, such as those used in functional studies of the brain, suffer from low signal-to-noise resulting from the small ^{1}H polarization.

Optical-pumping/spin-exchange ("laser polarization") techniques produce long-lived, non-equilibrium nuclear polarization in noble gas isotopes (*e.g.*, ^{3}He and ^{129}Xe) of order 0.1 to 1 by spin-exchange with optically pumped Rb vapor (for a review see [11]). This large nuclear polarization is an elegant way to overcome what Ernst calls the "the powers of evil in NMR," *i.e.*, the inherently low sensitivity of NMR [12]. With typical ^{129}Xe polarizations five order of magnitude larger than Boltzmann equilibrium, the use of polarized noble gases as the imaged species presents many new MRI and NMR possibilities.

In 1994 the first MRI experiment using laser-polarized ^{129}Xe in a biological system was performed [13]. A few milliliters of ^{129}Xe gas were laser-polarized in Princeton, NJ and driven 100 miles to Stony Brook, NY where it was imaged in the airspaces of the excised lungs of a mouse. Motivated by this initial demonstration, we have subsequently shown that *in vivo* magnetic resonance tracer techniques with laser-polarized ^{129}Xe provide a powerful enhancement to currently existing MRI methods.

The study of the manner in which inert gases are taken up by the tissues of the body has a long history [14-17]. Xenon, in particular, is highly soluble in blood [18] and freely diffusible across biological membranes *in vivo* [17]. Xenon is chemically inert, and is carried to distant organs where it accumulates in tissue. These properties spawned nuclear medicine techniques which analyze *in vivo* xenon uptake and washout curves to study cerebral blood flow [19], kidney perfusion [20], and heart perfusion [21]. These techniques use both radioactive ^{133}Xe, in x-ray emission computed tomography (SPECT) [19], and stable xenon, as an x-ray attenuation agent in transmission computed tomography (CT) [22, 23].

Laser-polarized ^{129}Xe magnetic resonance overcomes some limitations of conventional magnetic resonance, and it raises the possibility of imaging tissue to which polarized ^{129}Xe is carried as a magnetic tracer by flowing blood (see table 1.1). The long relaxation times in blood [24] and tissue [25, 26] allow *in vivo* NMR study. The large range of chemical shifts of ^{129}Xe *in vivo* allow background-free tissue-specific measurement of dissolved phase ^{129}Xe NMR signal. The goal of this thesis is the extension of xenon nuclear medicine

	^{1}H	^{129}Xe
Localization	Intrinsic (tissue, water, fat)	Airspaces (lung, sinus) Soluble in blood/tissue
Density	6 10^{22}/cc (liquid)	3 10^{19}/cc (gas)
Polarization	7 10^{-6} at 2 T and 300 K (equilibrium)	0.1 to 1 (non-equilibrium)
Relaxation time	of order 1 second *in vivo*	Hours/days (frozen) Seconds (*in vivo*)
Larmor frequency	42 MHz/T	12 MHz/T

Table 1.1: Comparison of *in vivo* ^{1}H and laser polarized ^{129}Xe magnetic resonance.

techniques with the use of laser-polarized ^{129}Xe magnetic resonance, and the development of a new framework by which non-invasive quantitative measurement of tissue perfusion and physiological function may be made.

The most interesting motivation for the quantitative study of tissue perfusion comes from the relationship between cerebral circulation and brain function. For over one hundred years, it has been known that a close relationship exists between neural activity and blood flow. Roy and Sherrington suggested in 1890 that cerebral blood flow (CBF) is controlled locally and does not passively follow changes in systemic blood pressure [27], and it is now established that local cerebral circulation corresponds with local variation in functional activity. This coupling between functional activity and perfusion within small regions of the brain forms the basis of the study of regional brain activation, and has in turn greatly enriched the understanding of the functional organization of the central nervous system. Cerebral metabolic rates of oxygen and glucose use are now known to be locally adjusted to meet the metabolic needs through local regulation of CBF. Although the brain is topologically complex, specific brain regions perform specific functions, making an anatomical map of brain function possible. Sensory stimulation, motor activity and information processing in the brain all correlate with changes in regional cerebral blood flow (rCBF). Measurement of changes in blood flow are suitable as functional brain mapping studies. The ultimate goal of a totally noninvasive method that enables the mapping of CBF with high temporal and spatial resolution has not yet been attained, and knowledge of brain function would be greatly extended by a quantitative, high-resolution, and non-

invasive method of measuring rCBF in an animal model.

Given the high levels of ^{129}Xe nuclear polarization currently achievable with laser-polarization [28, 29] and the desirable chemical and biological properties of Xe for measuring tissue perfusion, we have applied magnetic resonance and spin-exchange optical pumping techniques to the goal of a quantitative technique for the measurement of perfusion with laser-polarized ^{129}Xe magnetic resonance. This thesis describes experiments in which laser polarized ^{129}Xe is delivered to living rats by inhalation and transported to tissue via blood flow where it is detected using MR spectroscopy and imaging techniques. The time-dependent spatial distribution of ^{129}Xe signal intensity reflects local blood volume, blood flow rates, and the efficiency of perfusion and diffusive transport in tissues, and we propose a new method of using laser-polarized ^{129}Xe magnetic resonance to quantitatively measure tissue perfusion.

This thesis describes the developments in our laboratory over the past 6 years. The *in vivo* ^{129}Xe magnetic resonance research program immediately presented a daunting shift from our past experience in spin-exchange optical pumping; could we even consider putting a valve on a carefully prepared optical-pumping cell containing high-pressure xenon and hot alkali metal vapor, increasing the laser-polarized ^{129}Xe production volumes more than ten-fold, delivering it to a breathing animal, and imaging the ^{129}Xe magnetic moment density in organs which are reached by blood flow? Emphasized herein are those experimental strides and *in vivo* results essential to establish the feasibility of a ^{129}Xe magnetic resonance tracer method for perfusion measurement.

Chapter 2 introduces the fundamentals of Rb depopulation optical pumping and Rb-^{129}Xe spin-exchange. This description includes a review of the mechanisms that contribute to depolarization of both Rb and ^{129}Xe. Estimates of these rates in the optical pumping cell used in this experiment are given. The numerical optical-pumping/spin-exchange calculations used to evaluate polarizer design parameters and polarizer cycle optimization are described.

Chapter 3 describes the design, construction, performance, and optimization of the laser-polarized ^{129}Xe production and delivery system that is used in all the *in vitro* and *in vivo* MR imaging experiments in this thesis. The advent of this system marked the beginning of our ability to produce liter-volumes of polarized ^{129}Xe, and represented an order of

magnitude increase over previously reported production volumes of polarized ^{129}Xe. The additional hardware necessary to interface to the imaging system is also described.

Chapter 4 describes the experimental measurements of the distribution and dynamics of laser-polarized ^{129}Xe magnetization obtained from rodents *in vivo*. The results presented in this chapter include many of the first experiments in this field, including the first *in vivo* ^{129}Xe NMR spectrum from the head, the first tissue images of ^{129}Xe, and the first *in vivo* ^{129}Xe chemical-shift resolved images (in one- and two-dimensions). These results establish the experimental feasibility of laser-polarized ^{129}Xe as an *in vivo* magnetic resonance tracer. The dynamics of polarized ^{129}Xe uptake *in vivo* are presented. The assignments of the multiple ^{129}Xe resonances observed *in vivo* are given, based on analysis of spectroscopic, uptake, and imaging results of this chapter.

Chapter 5 presents a full description of the ^{129}Xe magnetic tracer theory. The theoretical framework for the ^{129}Xe magnetic resonance tracer method is developed and a model of the *in vivo* transport of laser polarized ^{129}Xe to tissue under realistic experimental NMR conditions is presented. It will be shown that careful control of the NMR parameters will allow the rate of blood flow to perfused tissue and the ^{129}Xe tissue relaxation rate to be extracted independently from NMR measurement of the steady-state ^{129}Xe tissue signal. The estimated signal-to-noise ratio for this technique in rat grey-matter is calculated based on the experimental results of Chapter 4. The model is then used to extract perfusion rate and tissue T_1 from simulated measurements of the steady-state ^{129}Xe tissue NMR signal. The limitations and caveats of this method are discussed.

Chapter 6 summarizes the prospects for the future of a laser-polarized ^{129}Xe magnetic tracer method. In particular, increases in ^{129}Xe polarization are essential for the continued success of this field, and the likely technical improvements attainable in the near-term time scales are outlined. A brief overview of the NMR and MRI techniques used in this thesis is provided as an Appendix.

Chapter 2

Rb optical pumping and Rb-^{129}Xe spin-exchange

Spin-exchange optical pumping is a two step process for polarizing ^{129}Xe. In this technique large ^{129}Xe nuclear polarizations are obtained by the transfer of photon angular momentum first to alkali-metal electrons and subsequently to ^{129}Xe nuclei. These optical-pumping and spin-exchange techniques are the heart of ^{129}Xe polarizer used in the experiments in this thesis. This chapter reviews the essential Rb optical pumping (OP) and ^{129}Xe spin-exchange (SE) physics, including polarization relaxation mechanisms.

2.1 Optical Pumping in Rb

Optical pumping of alkali metals, first described by Kastler [30], is the efficient transfer of photon angular momentum to the internal degrees of freedom of an alkali metal vapor by resonant scattering. Optical pumping in alkali metals has been treated in detail by Happer [31], and pumping in dense Rb vapors has been specifically studied by Wagshul and Chupp [32] and Appelt et al. [33]. The work described in this dissertation uses a method known as depopulation pumping to polarize the electron ground state of Rb atoms. In this technique, a static magnetic field (B_0) is applied along the long axis of a cylindrical glass cell containing Rb vapor which splits the degenerate Zeeman levels and provides the axis of quantization. Light resonant with the Rb D1 transition (794.7 nm) drives electron transitions between the $5^2S_{1/2}$ ground state and the $5^2P_{1/2}$ excited state (figure 2.1) If the incident light is right circularly polarized ($\sigma+$), angular momentum conservation prevents the

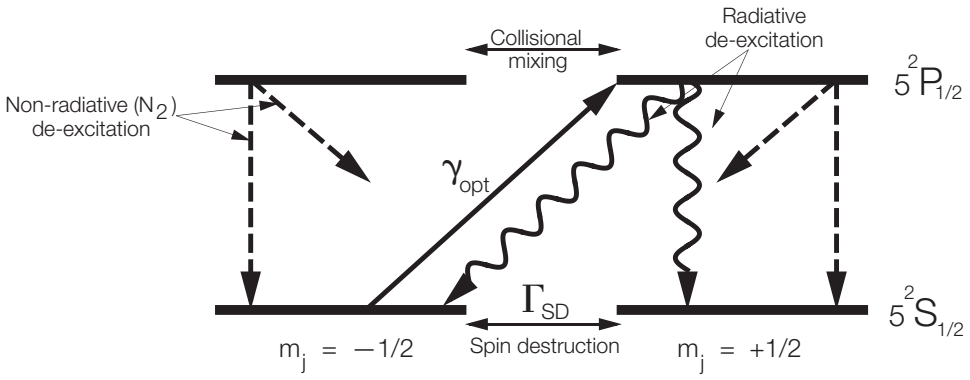

Figure 2.1: Depopulation optical pumping in Rb with circularly polarized light. Both radiative and collisional (non-radiative) transitions are shown. This schematic neglects Rb nuclear spin.

$5^2S_{1/2}$ $m = +1/2$ magnetic sublevel from being excited. The absorption of a $\sigma+$ photon only drives transitions from the $m = -1/2$ ground state to the $m = +1/2$ excited state. Once in the $m = +1/2$ sublevel of the $^2P_{1/2}$ excited state, the atom can, via spontaneous emission, decay to either $^2S_{1/2}$ ground state sublevel with the relative decay probabilities given by the Clebsh-Gordon coefficients (1/3 to the $m = +1/2$ ground state and 2/3 to the $m = -1/2$ ground state). An electron decaying to the spin-down groundstate is repumped to the spin-up excited state. Once in the spin-up ground state, no further optical excitation can occur. In the absence of any relaxation processes all spins will accumulate in the spin-up ground state.

The $^2P_{1/2}$ excited state can decay radiatively by emitting randomly-polarized resonant photons. In our experiments, the Rb number density (typically 10^{12}–10^{13} cm^{-3}) is sufficient so that the Rb vapor is optically thick and most of these decay photons are reabsorbed. When these photons are reabsorbed, the $m = +1/2$ ground-state can be pumped to the $m = -1/2$ ground-state, reducing the ground-state spin polarization. This process is known as radiation trapping. To prevent radiation trapping, nitrogen is added to collisionally de-excite the excited Rb atoms before they can reradiate a photon. Sufficient quenching gas ensures that an excited atom has little chance of reradiating a photon which might multiple scatter before escaping from the pumping cell and thereby depolarize the Rb vapor. A collision with a N_2 molecule transfers energy from the Rb excited state to

vibrational and rotation degrees of freedom in the diatomic molecule. The cross section for N_2 quenching of Rb ($^2P_{1/2}$ –$^2S_{1/2}$) is measured [34] as 58 Å^2. The natural excited state Rb lifetime of about 28 ns [35] is shortened to about 1 ns in the presence of 100–150 Torr of N_2. Therefore only about 5% of the atoms decay radiatively under our optical pumping conditions. The presence of quenching gas essentially eliminates radiation trapping as a source of relaxation of Rb polarization.

The presence of N_2 and Xe gas in the optical pumping cell also collisionally mixes the Rb $^2P_{1/2}$ sublevels. This mixing rapidly equalizes the magnetic sublevel population of the $^2P_{1/2}$ excited state. Rapid collisional N_2 quenching of these equally populated excited-state sublevels repopulates the ground-state sublevels equally since collisional decay to either ground state sublevel is equally probable. Thus an atom excited from the $-1/2$ ground-state has equal probability of collisionally relaxing to the $+1/2$ or $-1/2$ ground-state, and needs on average two absorbed photons are needed to pump a spin-down ground-state electron into the spin-up ground-state.

The Rb level diagram of figure 2.1 neglects the Rb nuclear spin. The two naturally occurring isotopes, ^{85}Rb (72% abundant) and ^{87}Rb (28% abundant) have nuclear spin I = 5/2 and 3/2, respectively. The hyperfine coupling of the Rb nuclear spin to the Rb electron spin splits the ground and excited states of each isotope into two hyperfine levels, $F = I + 1/2$ and $F = I - 1/2$. Excitation from one of the $2F + 1$ ground-state sublevels to one of the excited-state sublevels by σ+ light still requires a $\Delta m_F = +1$ transition. As in the simplified case, there is one ground-state sublevel that can not be pumped by σ+ light and polarization will accumulate in this state. Initially, however, it does take many more pumping cycles to transfer population to this state. The Rb nuclear sublevels act as a reservoir of angular momentum, and the optical pumping process is slowed. This so-called slowing factor [32, 33, 36] can be neglected in our discussions as the rapidly-reached steady-state Rb polarization remains unchanged. Optical pumping/spin-exchange production of polarized ^{129}Xe in the work reported here typically occurs at high gas density (1–3 amagat[1]). This high gas density broadens the hyperfine structure of the D1 absorption line to the extent that it is no longer resolvable. In our experiments, the absorption linewidth is typically 40 GHz (14 GHz/amagat for N_2 and 18 GHz/amagat for ^{129}Xe), compared to the

1.The density of an ideal gas at STP is 1 amagat = 2.69 10^{19} cm^{-3}

largest Rb hyperfine splitting of 6835 MHz. Under these conditions both hyperfine states are equally likely to absorb the light, and the simple model of figure 2.1 is sufficient.

The ultimate polarization that an optically pumped alkali-vapor can attain depends on the ground-state electron polarization relaxation rate. Relaxation of the Rb ground-state sublevels is known as spin-destruction, to which many processes contribute. Neglecting effects of alkali-metal nuclear-spin, the optical pumping rate equations for the ground-state sublevel populations are

$$\frac{d}{dt}\rho_{\mathrm{Rb}}(\pm 1/2) \;=\; \pm\left[\gamma_{opt} + \frac{\Gamma_{SD}}{2}\right]\rho_{\mathrm{Rb}}(-1/2) \mp \frac{\Gamma_{SD}}{2}\rho_{\mathrm{Rb}}(+1/2), \tag{2.1}$$

where Γ_{SD} is the total Rb ground-state spin-destruction rate, and γ_{opt} is the scattering rate per Rb atom. The scattering rate is defined by

$$\gamma_{opt} \;=\; \int \Phi(\nu)\sigma(\nu)d\upsilon, \tag{2.2}$$

where $\Phi(\nu)$ is the incident laser photon flux per unit frequency, and $\sigma(\nu)$ is the pressure-broadened Rb D1 absorption cross section. Here it is assumed that the rate of collisional de-excitation of Rb $5^2P_{1/2}$ atoms is much greater than γ_{opt}. Rewriting equation 2.1 in terms of the Rb polarization, $P_{\mathrm{Rb}} = \rho_{\mathrm{Rb}}(+1/2) - \rho_{\mathrm{Rb}}(-1/2)$,

$$\frac{dP_{\mathrm{Rb}}}{dt} \;=\; \gamma_{opt}(1 - P_{\mathrm{Rb}}) - \Gamma_{SD}P_{\mathrm{Rb}}. \tag{2.3}$$

Assuming an initially unpolarized Rb vapor, the solution to equation 2.3 is

$$P_{\mathrm{Rb}}(t) \;=\; \frac{\gamma_{opt}}{\gamma_{opt} + \Gamma_{SD}}(1 - e^{-(\Gamma_{SD} + \gamma_{opt})t}). \tag{2.4}$$

High Rb polarization is obtained through minimization of depolarizing processes. When the optical pumping rate is high compared to the total electron spin-destruction rate (Γ_{SD}) between ground state sublevels, the m = –1/2 ground state sublevel will be depopulated and significant ground state Rb polarization results. The steady state Rb polarization from equation 2.4 is simply

$$P_{\mathrm{Rb}} = \frac{\gamma_{opt}}{\gamma_{opt} + \Gamma_{SD}}. \tag{2.5}$$

Relaxation of the polarized Rb ground state can be caused by many mechanisms. In our optical pumping cells, the source of these spin-destroying processes include spin-exchange and spin-rotation collisions with Rb and other atoms and molecules, collisions with the container walls, and radiation trapping. The contribution of each relaxation process to Γ_{SD} is discussed below.

Collisions in the optical pumping cells can occur between Rb, ^{129}Xe, and N_2. The angular momentum vectors in the collision process are shown schematically in figure 2.2

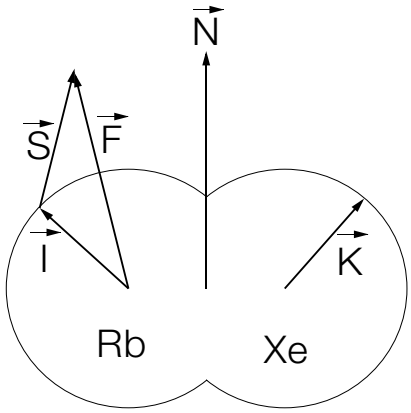

Figure 2.2: Rb-Xe molecule and the various angular momenta.

for a typical binary collision. Relaxation mechanisms are characterized by their respective velocity-averaged cross section, $<\sigma v>$. For binary collisional processes in general, the rate of depolarization per Rb atom can be described by the product of a rate constant and the number density of the species X colliding with Rb, *i.e.*,

$$\Gamma_i = \langle \sigma_i v \rangle [X] \equiv \kappa_i [X] \tag{2.6}$$

where Γ_i is the collisional relaxation rate per Rb atom for process i, $<\sigma_i v>$ is the velocity-averaged cross section, $[X]$ is the number density of species X, and κ_i is the relaxation rate constant for a given process. The relative velocity, v, depends on the atomic species involved in the collision. To evaluate and compare relaxation rates, the typical running

conditions of the polarizing cell for our ^{129}Xe polarizer are now used. The densities of the constituents of the optical pumping cell in this experiment during normal operating conditions are: [Xe] = 4.2 10^{19} cm^{-3} (2.2 amagat), [N_2] = 4.2 10^{18} cm^{-3} (0.2 amagat), and [Rb] ~ 8 10^{12} cm^{-3} at T = 105 °C.

2.1.1 Spin rotation collisions

The spin-rotation interaction occurs during collisions between Rb and the other atoms in the optical pumping cell. This interaction couples the spin of the Rb electron $\boldsymbol{S}$ to the rotational angular momentum $\boldsymbol{N}$ of the colliding binary pair. The spin-rotation interaction is responsible for most of the spin relaxation of alkali-atoms mixed with noble gases [37]. The spin-rotation interaction is written

$$H_{SR} = \gamma(R)\boldsymbol{N}\cdot\boldsymbol{S}, \tag{2.7}$$

where the spin-rotation coupling constant γ is a function of the internuclear separation R of the colliding pair and of the species of atom colliding with Rb. The spin-rotation interaction arises from precession of the electron spin about motionally produced magnetic fields during the collision. Spin-rotation rate constants have been measured to be $\kappa_{SR,\mathrm{N2}}$ = 9.38 10^{-18} cm^{3}s^{-1} [32] and $\kappa_{SR,\mathrm{Xe}}$ = 5.2 10^{-15} cm^{3}s^{-1} [38] for Rb-N_2, and Rb-^{129}Xe, respectively. In the OPSE cell used in this experiment, the calculated spin-rotation contributions to the Rb relaxation are $\Gamma_{SR,\mathrm{N2}}$ = 40 Hz, and $\Gamma_{SR,\mathrm{Xe}}$ = 2.2 10^5 Hz.

2.1.2 Spin exchange collisions

Binary collisions between Rb atoms can result in a spin-exchange interaction written schematically as

$$\mathrm{Rb}(\uparrow) + \mathrm{Rb}(\downarrow) \rightarrow \mathrm{Rb}(\downarrow) + \mathrm{Rb}(\uparrow), \tag{2.8}$$

where arrows indicate the electron spin state. This interaction between pairs of Rb atoms with electron spins $\boldsymbol{S}_i$ and $\boldsymbol{S}_j$ is dominated by the total spin-conserving exchange interaction [33]

$$H_{SE,\,Rb} \;=\; J\boldsymbol{S_i}\cdot\boldsymbol{S_j} \tag{2.9}$$

where the coupling constant of the interaction $J = J(R)$ arises both from the electromagnetics and from the requirement of proper symmetrization of the wave functions of the colliding atoms. The Rb–Rb spin-exchange rate constant has been measured to be $\kappa_{SE,\mathrm{Rb}} = 8.8\ 10^{-10}\ \mathrm{cm^3 s^{-1}}$ [39]. This corresponds to a calculated Rb-Rb spin-exchange rate in this experiment of $\Gamma_{SE,\mathrm{Rb}} = 7$ kHz. However, total spin $\boldsymbol{S} = \boldsymbol{S_i} + \boldsymbol{S_j}$ is conserved in this interaction, so Rb-Rb spin-exchange does not contribute to Rb depolarization.

Collisions between a Rb atom and a non-alkali atom also results in a spin-exchange interaction, although this has a different physical origin than Rb-Rb spin-exchange. As above, the spin-exchange interaction is written schematically as

$$\mathrm{Rb}(\uparrow) + \mathrm{B}(\downarrow) \rightarrow \mathrm{Rb}(\downarrow) + \mathrm{B}(\uparrow), \tag{2.10}$$

where B is any of the non-alkali constituents of the optical-pumping cell: ^{129}Xe or N_2. The origin of the nuclear-electron spin-exchange interaction is the magnetic dipole-dipole interaction

$$H_{SE} \;=\; \alpha\boldsymbol{K}\cdot\boldsymbol{S} \tag{2.11}$$

where α is a function of the internuclear separation of the Rb-Xe or Rb-N_2 pair. Spin-exchange from the Rb electron to Xe nucleus is the mechanism that produces polarized ^{129}Xe in these experiments and is discussed in more detail in section 2.2. The Rb-Xe spin-exchange rate constant has been measured as $\kappa_{SE,\mathrm{Xe}} = 3.70\ 10^{-16}\ \mathrm{cm^3 s^{-1}}$ [40], and the Rb-N_2 spin-exchange constant is suggested to be $\kappa_{SE,\mathrm{N2}} = 8\ 10^{-19}\ \mathrm{cm^3 s^{-1}}$ [41]. The calculated relaxation rates (per Rb atom) are $\Gamma_{SE,\mathrm{Xe}} = 2\ 10^4$ Hz, and $\Gamma_{SE,\mathrm{N2}} = 3$ Hz.

2.1.3 Rb-Rb spin relaxation

Relaxation due to collisions between polarized Rb atoms can be significant at high alkali-metal vapor pressures. These spin-destroying collisions between polarized Rb atoms are written schematically as

$$\mathrm{Rb}(\uparrow) + \mathrm{Rb}(\uparrow) \rightarrow \mathrm{Rb}(\downarrow) + \mathrm{Rb}(\uparrow). \tag{2.12}$$

Many interactions contribute to Rb-Rb spin relaxation including nuclear quadrupole relaxation in Rb singlet dimers [42] and the spin-axis interaction in triplet dimers [43], and several mechanisms remain under investigation [43, 44], In particular, the spin-non-conserving anisotropic spin-axis interaction that couples the electron spins to the orbital angular momentum of the short-lived Rb-Rb molecule was first postulated to be

$$H_{SS} = \frac{2}{3}\lambda[3S_\zeta S_\zeta - S(S+1)], \tag{2.13}$$

where S_ζ is the electron spin component along the internuclear axis [45]. Recent observation of the existence of resonances in the magnetic decoupling curves of Rb relaxation are consistent with the existence of a spin-axis interaction in spin-polarized alkali vapors [43].

An additional source of Rb-Rb relaxation comes from the spin-rotation interaction of the type described in section 2.1.1 [45]. Calculations [46] suggest that the rate constant for Rb–Rb spin-rotation is of similar magnitude to that of Rb-N_2 spin-rotation. The five orders of magnitude difference in the number density between N_2 and Rb in our ^{129}Xe polarizer cells makes the resulting contribution to Rb relaxation due to Rb-Rb spin rotation negligible *i.e.*, $\Gamma_{SR,\mathrm{Rb}} < 10^{-5}$ Hz.

The total Rb-Rb collision induced relaxation rate constant ("Rb spin-destruction") was measured by Wagshul *et al.* to be $\kappa_{\text{Rb-Rb}} = 8.11\ 10^{-13}$ cm^{3}s^{-1} [32, 47]. Using this measured value results in a calculated total Rb-Rb relaxation rate for this the cells used in our experiments $\Gamma_{\text{Rb-Rb}} = 6$ Hz.

2.1.4 Collisions with the cell walls

Collisions between Rb and the walls of the optical pumping cell can result in Rb relaxation due to both paramagnetic impurities in the glass and chemisorption at the wall. If the residence time of an adsorbed Rb atom on the wall is sufficiently long, these impurities will completely depolarize the Rb. This problem is mitigated to some extent by the use of wall coatings, details of which (with particular emphasis on ^{129}Xe relaxation) are discussed in Chapter 3. In fact, evidence suggests that uncoated glass walls can be thought of as com-

pletely depolarizing [48-50]. Relaxation of Rb polarization on the cell walls has historically been a serious problem at low pressures (below 10^{-3} Torr) where the Rb mean free path is large compared to the dimensions of a typical cell, since diffusion of Rb to the walls determines the wall relaxation rate. In these cases depolarization at the cell walls seriously limits the attainable alkali-vapor polarization. In the multi-atmospheric pressures of the optical pumping cells used in our polarizer, the Rb diffusion constant in xenon is quite small: D_{Rb} = 0.06 $\mathrm{cm}^2\mathrm{s}^{-1}$ at 2.2 atm and 105 °C [35]. As a result, relaxation due to wall collisions is only significant within a small distance of the wall, i.e. of order $\sqrt{D_{Rb}/\gamma_{opt}}$, where γ_{opt} is the Rb optical pumping rate. With typical Rb optical pumping rates $\gamma_{opt} \geq 10^4\ \mathrm{s}^{-1}$, the layer of Rb polarization destroyed due to wall collisions is only appreciable within $2\ 10^{-3}$ cm of the wall. The change in Rb polarization due to this process is described by the diffusion equation

$$\left.\frac{\partial P_{\mathrm{Rb}}}{\partial t}\right|_{wall} = D\nabla^2 P_{\mathrm{Rb}}. \tag{2.14}$$

An order of magnitude estimate for the rate of depolarization is given by considering only the lowest-order diffusion mode [35] which is $\Gamma_{diff} \sim D/l^2 \sim 4\ 10^{-2}$ Hz, where l is a characteristic dimension of the cell. The exact solution of equation 2.14 in a cylindrical cell of length l and radius a is given by Minguzzi *et al.* [51] The rate constants for the $(m, n)^{\mathrm{th}}$ diffusion mode are

$$\Gamma_{diff}^{mn} = D\left(\frac{n^2\pi^2}{l^2} + \frac{\mu_m^2}{a^2}\right) \tag{2.15}$$

where μ_m is the m-th zero of the zeroth-order Bessel function. Again considering only the lowest-order diffusion mode (higher diffusion modes effect only those Rb atoms closest to the cell walls), with $a \ll l$ in our cell and $\mu_1 = 2.405$, an order of magnitude estimate is given by $\Gamma_{diff} \sim 0.2$ Hz.

Table 2.1 summarizes the Rb relaxation processes, origin, and estimated relaxation rates in the polarizing cell as described in Chapter 3. Rates are given only for processes that contribute to Γ_{SD}. Of these, Rb–^{129}Xe spin-rotation clearly dominates Rb ground-state spin relaxation in our system.

Mechanism		Rate (Hz)	κ (cm^3s^{-1})
Spin Rotation	Rb-N_2	40	$9.38\ 10^{-18}$ [32]
	Rb-^{129}Xe	$2.2\ 10^5$	$5.2\ 10^{-15}$ [38]
Spin Exchange	Rb-Rb	N. A.	$8.8\ 10^{-10}$ [39]
	Rb-N_2	3	$8\ 10^{-19}$ [41]
	Rb-^{129}Xe	$2\ 10^4$	$3.7\ 10^{-16}$ [40]
Rb-Rb spin relaxation		6	$8.11\ 10^{-13}$ [47]
Diffusion to walls		0.2	
Radiation trapping		N. A.	

Table 2.1: Mechanisms that contribute to Rb depolarization and the calculated rates (per Rb atom) for the cell used in the ^{129}Xe polarizer. Rate constants and their references are given for binary processes.

2.2 Spin Exchange Polarization of ^{129}Xe

The exchange of angular momentum from the Rb electron to ^{129}Xe nucleus during collisions is the mechanism that produces polarized ^{129}Xe in these experiments, and was introduced in section 2.1.2. Spin exchange can occur during either of the two collisional interactions that occur in mixtures of Rb, N_2 and Xe: during the formation of loosely bound Rb-^{129}Xe van der Waals molecules or during Rb-^{129}Xe binary collisions (figure 2.3). At the total gas pressures used in the polarizer cells (*i.e.*, several amagats), the collisionally limited lifetimes of van der Waals molecules are extremely short, and the spin-exchange rate due to binary collisions greatly exceeds the spin-exchange rate due to the formation of van der Waals molecules [40]. Thus at the operating pressures of the OPSE cell used in this thesis, Rb-Xe spin-exchange can be treated as if it were entirely due to binary collisions; there is no spin-exchange due to Van der Waals molecule formation.

The dipolar Rb-Xe spin-exchange coupling (equation 2.11) is dominated by the Fermi-contact interaction

$$\alpha(R) = \frac{16\pi}{3}\frac{\mu_B\mu_K}{K}|\psi(R)|^2, \tag{2.16}$$

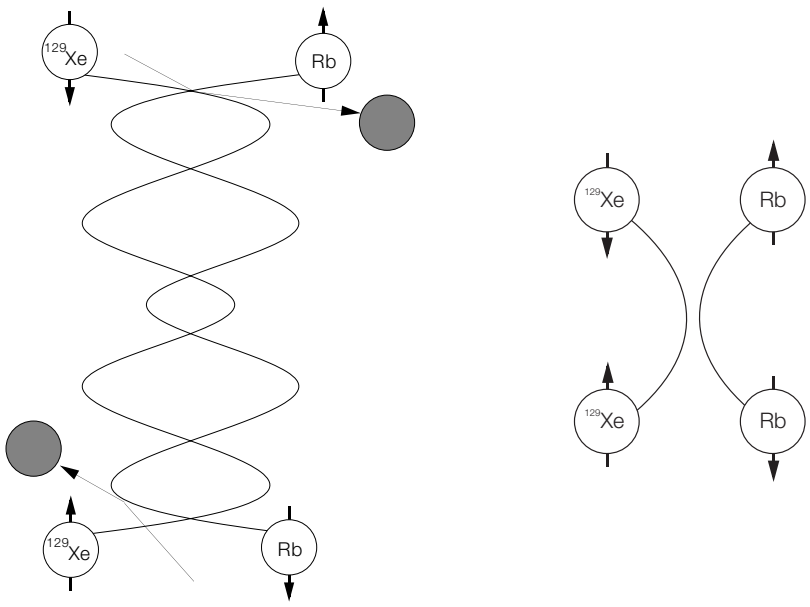

Figure 2.3: Two types of spin-exchange collisions: (A) RbXe van der Waals molecule formation in a three body process. (B) RbXe binary collision.

where μ_B is the Bohr magneton, μ_K is the magnetic moment of the ^{129}Xe nucleus, and $\psi(R)$ is the wave function of the Rb valence electron evaluated at the position of the noble-gas nucleus. For spin-exchange to noble-gases, Herman [52] has shown that there is an enhancement of $\psi(R)$,

$$\psi(R) = \eta\phi(R) \tag{2.17}$$

where $\phi(R)$ is the Rb valence-electron wave function in the absence of the noble gas, and for Rb-^{129}Xe spin-exchange, the enhancement factor η has been calculated to be $\eta = 50$ [11]. The enhancement comes from the fact that the Rb valence electron can be exchanged with one of the ^{129}Xe electrons of the same spin state, thus effectively increasing the probability of finding the Rb valence electron at the ^{129}Xe nucleus [53].

Analogous to the Rb optical pumping equations (equation 2.1), the polarization of ^{129}Xe is characterized by spin-exchange rate and a relaxation rate. We write the rate equation for the ^{129}Xe ground-state spin-up nuclear sublevel $\rho_{Xe}(+1/2)$ as

$$\frac{d\rho_{\mathrm{Xe}}}{dt}(+1/2) \;=\; \left[\gamma_{SE}\rho_{\mathrm{Rb}}(+1/2) + \frac{\Gamma}{2}\right]\rho_{\mathrm{Xe}}(-1/2) - \left[\gamma_{SE}\rho_{\mathrm{Rb}}(-1/2) + \frac{\Gamma}{2}\right]\rho_{\mathrm{Xe}}(+1/2)\,, \tag{2.18}$$

where Γ is the total ^{129}Xe ground-state polarization-relaxation rate and γ_{SE} is the Rb-^{129}Xe spin-exchange rate (per ^{129}Xe atom). The ^{129}Xe spin sublevel populations $\rho_{\mathrm{Xe}}(\pm 1/2)$ are normalized such that $\rho_{\mathrm{Xe}}(+1/2) + \rho_{\mathrm{Xe}}(-1/2) = 1$ and $P_{\mathrm{Xe}} = \rho_{\mathrm{Xe}}(+1/2) - \rho_{\mathrm{Xe}}(-1/2)$. Rewriting equation 2.18,

$$\frac{dP_{\mathrm{Xe}}}{dt} \;=\; \gamma_{SE}(P_{\mathrm{Rb}} - P_{\mathrm{Xe}}) - \Gamma P_{\mathrm{Xe}}\,. \tag{2.19}$$

In a vapor with a steady-state Rb polarization P_{Rb}, the time-dependence of the ^{129}Xe polarization given an initial ^{129}Xe polarization $P_{\mathrm{Xe}}(t = 0) = 0$ is

$$P_{\mathrm{Xe}}(t) \;=\; \frac{\gamma_{SE}}{\gamma_{SE} + \Gamma} P_{\mathrm{Rb}}\left(1 - e^{-(\gamma_{SE} + \Gamma)t}\right). \tag{2.20}$$

The simplifying assumption of a constant P_{Rb} is reasonable since characteristic Rb pumping times are on the order of 10^{-3} s or less, while pumping times for ^{129}Xe are on the order of ten minutes. From equation 2.20, the steady-state ^{129}Xe polarization is $P_{Xe}^{\infty} = \gamma_{SE}P_{\mathrm{Rb}}/(\gamma_{SE} + \Gamma)$, with a polarization or "spinup" time of $T_{spinup} = (\gamma_{SE} + \Gamma)^{-1}$. Rewriting the steady-state ^{129}Xe polarization as

$$P_{Xe}^{\infty} \;=\; \left(\frac{\gamma_{opt}}{\gamma_{opt} + \Gamma_{SD}}\right)\left(\frac{\gamma_{SE}}{\gamma_{SE} + \Gamma}\right), \tag{2.21}$$

it is clear that high levels of ^{129}Xe polarization are only achieved when the rate of Rb optical-pumping rate exceeds the rate of Rb spin-destruction $\gamma_{opt} \gg \Gamma_{SD}$ and when Rb-Xe spin-exchange exceeds ^{129}Xe spin-relaxation, $\gamma_{SE} \gg \Gamma$. The first condition, $\gamma_{opt} \gg \Gamma_{SD}$, is problematic because Γ_{SD} is quite large ($\sim 10^5$ Hz) under the normal operating conditions in the pumping cell. The use of high-power laser diode arrays (LDAs) addresses this issue by providing a high intensity laser source, i.e., a large optical pumping rate. With their broad spectral width (typically 750–1500 GHz FWHM), LDAs are far from being the ideal

light sources for OPSE production of polarized ^{129}Xe, however their low cost per watt compared to Ti:Sapphire lasers and their ease of use has facilitated the increased polarization of ^{129}Xe. The limitations and benefits of these light sources are discussed in more detail in chapter 3.

The second condition for production of high ^{129}Xe polarization, $\gamma_{SE} \gg \Gamma$, is satisfied by careful preparation of the optical pumping cells and by the minimization of external environmental contributions to Γ. Two specific interactions that contribute to Γ in the pumping cell are relaxation due to magnetic-field inhomogeneties and relaxation due to collisions with the walls.

2.2.1 Relaxation due to magnetic-field inhomogeneties

The contribution to ^{129}Xe relaxation in the polarizing cell due to magnetic-field inhomogeneties can be estimated [54, 55] from

$$\Gamma_{\nabla B} = D_{\mathrm{Xe}} \frac{\left|\nabla B_x\right|^2 + \left|\nabla B_y\right|^2}{B_0^2}, \tag{2.22}$$

where D_{Xe} is the Xe self-diffusion constant, B_0 is the mean magnetic field (assumed to lie along the z axis), and $\left|\nabla B_x\right|$ and $\left|\nabla B_y\right|$ are the spatial gradients of the transverse components of the magnetic-field. For the ^{129}Xe polarizer installed adjacent to the 2 T MRI magnet, the measured transverse magnetic gradients at the optical pumping cell are $\left|\nabla B_x\right| \sim \left|\nabla B_y\right| = 1.2\ 10^{-3}$ T cm^{-1}. With a mean holding field of $B_0 = 4.5\ 10^{-2}$ T, and $D_{\mathrm{Xe}} = 0.04$ cm^{2}s^{-1} (at 2.2 amagat and 100 °C) [56], the calculated limit for $\Gamma_{\nabla B}$ is $5.7\ 10^{-5}$ s^{-1}, a time constant of roughly 5 hours. Thus the requirement that $\Gamma_{\nabla B} \ll \gamma_{SE}$ is easily satisfied, over the practical range of γ_{SE}, by the measured magnetic inhomogeneity $\left|\nabla B_\perp\right| / B_0 < 0.05$ cm^{-1}

2.2.2 Wall relaxation

As discussed in section 2.1.4, the glass walls of the optical pumping cell often contain paramagnetic impurities which cause depolarization. ^{129}Xe polarization is much more significantly affected by relaxation at the walls than is Rb, since the ^{129}Xe repolarization rate (i.e. the Rb-Xe spin-exchange rate) is many orders of magnitude smaller than the Rb repump-

ing rate. Zeng et al. found that silicone-based wall coatings significantly reduced ^{129}Xe surface relaxation [57]. The loss of ^{129}Xe polarization to the walls can be described by a relaxation time T_w. Wall coatings are thought to reduce both the sticking time and also increase the distance between the colliding xenon and the wall impurities. We have measured relaxation rates for uncoated Pyrex cells to be typically $2\ 10^{-2}$ s^{-1}, and in silane-coated cells this relaxation decreases to values measured from $1.5\ 10^{-3}$ to $3\ 10^{-3}$ s^{-1}, about the same order as the Rb-Xe spin-exchange rate. Wall relaxation is the dominant contributor to the total ^{129}Xe relaxation rate in these cells, and silane wall coatings are discussed in detail in section 3.1.2.

2.3 Simulation Framework

Computer simulations based on numerical methods developed by Chupp and Wagshul [32] are used in this thesis to numerically model optical pumping and spin-exchange. These simulations model the propagation of optical pumping light through the cylindrical OPSE cell and compute the average Rb polarization in the cell. The laser photon flux per unit frequency $\Phi(r, z, \nu)$ is position dependent; unpolarized Rb absorbs and scatters resonant light, burning a hole in the intensity profile as it propagates through the cell. The propagation of pumping light through the cell is given by

$$\frac{d\Phi(r, z, \nu)}{dz} = -[\mathrm{Rb}]\sigma(\upsilon)[1 - P_{\mathrm{Rb}}(r, z)]\Phi(r, z, \nu). \tag{2.23}$$

where the laser light is incident along the z-axis of the cylindrical OPSE cell with length l and radius a, and the laser is assumed to be cylindrically symmetric. The spatial dependence of the optical pumping rate (photon scattering rate) comes from the spatial dependence of the laser flux $\Phi(r, z, \nu)$:

$$\gamma_{opt}(r, z) = \int d\nu \Phi(r, z, \nu)\sigma(\nu). \tag{2.24}$$

The steady-state Rb polarization $P_{\mathrm{Rb}}(r, z)$ satisfies the diffusion equation [32]

$$D_{\mathrm{Rb}}\nabla^2 P_{\mathrm{Rb}}(r,z) - \frac{\Gamma_{SD}}{S(r,z)}P_{\mathrm{Rb}}(r,z) + \frac{\gamma_{opt}(r,z)}{S(r,z)}(1 - P_{\mathrm{Rb}}(r,z)) \;=\; 0 \qquad (2.25)$$

where D_{Rb} is the Rb diffusion constant and S is the slowing factor which depends on Rb polarization and therefore on position. Equations 2.23 and 2.25 can be solved by relaxation methods in two dimensions [32] for a given laser power and profile, Rb number density, wall relaxation rate, and pressure broadening.

A simplified computational model[1] is used in simulations of the pumping cell in this thesis, where diffusion in the radial direction and diffusion between slabs is neglected, and uniform Rb density and wall relaxation rates are assumed. Diffusional losses due to the completely depolarizing front and rear walls of the cell are included and computed for each slab. The spatial dependence of the steady-state Rb polarization in this model is given by

$$P_{\mathrm{Rb}}(z) \;=\; \frac{\gamma_{opt}(z)}{\gamma_{opt}(z) + \Gamma_{SD} + D_{\mathrm{Rb}}/z^2}, \qquad (2.26)$$

where D_{Rb}/z^2 is used as a rough estimate of the wall induced relaxation rate.

The computational procedure is as follows. The incident light profile at the front of the cell, $\Phi(0,\nu)$, is computed for a given laser spectrum and power. The cell is modeled by slabs of length $\delta_z \ll \sqrt{D_{\mathrm{Rb}}/\gamma_{opt}(z=0)}$. Starting from the front window, the Rb polarization in each slab is computed using equation 2.26, with boundary conditions at the walls assumed to be $P(r,0) = P(r,l) = P(a,z) = 0$. The light profile for the next slab is then computed from equation 2.23 using this value of P_{Rb}. In this way, the Rb polarization in each slab is computed for the entire cell length. The average Rb polarization for the entire cell is found, and equation 2.20 is used to compute the average ^{129}Xe polarization.

There are several prominent uncertainties that make comparison between these simulations and experimental results difficult. The Rb number density in the optical pumping cell is not precisely known because of uncertainty in the cell temperature due to local heating by the laser light, the Rb chemistry at the cell walls, and the frequent filling and emptying of the cell. Additionally, uncertainties in modeling the trajectory of the divergent laser beams through a long cell make accurate determination of $\Phi(z,\nu)$ difficult. Nevertheless, these simulations agree reasonably well in systems with simple geometries [32, 47, 58]. For

1. The computer code for these simulations was written by Drs. Kevin Coulter and Robert Welsh.

example, simulations for the ^{129}Xe polarizer used in this experiment will be shown to agree with our measured values of ^{129}Xe polarization to better than a factor of two. These simulations provide a framework within which crucial cell design parameters can be explored, and specific results are shown in chapter 3.

Chapter 3

^{129}Xe polarization and delivery system

This chapter describes the design and construction of the patented [59] laser-polarized ^{129}Xe production and delivery system (figure 3.1 and figure 3.2) used in all the *in vitro* and *in vivo* ^{129}Xe MR imaging experiments described in this thesis. The advent of this system marked the beginning of our ability to produce liter-volumes of polarized ^{129}Xe and represents an order of magnitude increase over previously reported production volumes. The entire apparatus including lasers and optics, rapidly actuated valves, heating and cooling systems, and transport tubing lies in the high magnetic field environment of a 2 T MRI magnet. With approximately 3–7% polarization, 148 cc-atm of xenon is produced and stored as xenon ice every 5 minutes, and large quantities of polarized ^{129}Xe are obtained by cycling the accumulation process. The polarized ^{129}Xe is subsequently delivered in a controlled fashion to a sample or subject. Experiments with this device have established the feasibility of laser-polarized ^{129}Xe as an *in vivo* magnetic tracer for MRI. This reliable, effective, and relatively simple production method for large volumes of ^{129}Xe can be applied to other areas of research involving the use of laser-polarized noble gases.

3.1 Optical Pumping/Spin Exchange

This section describes the design, construction, and performance of the optical pumping/spin-exchange (OPSE) stage of the apparatus. The OPSE cells (figure 3.3) are typically 17 cm long, 25 mm outer diameter Pyrex cylinders (nominally 66 cc volume) with end windows blown flat during construction. The use of welded optically-flat windows was

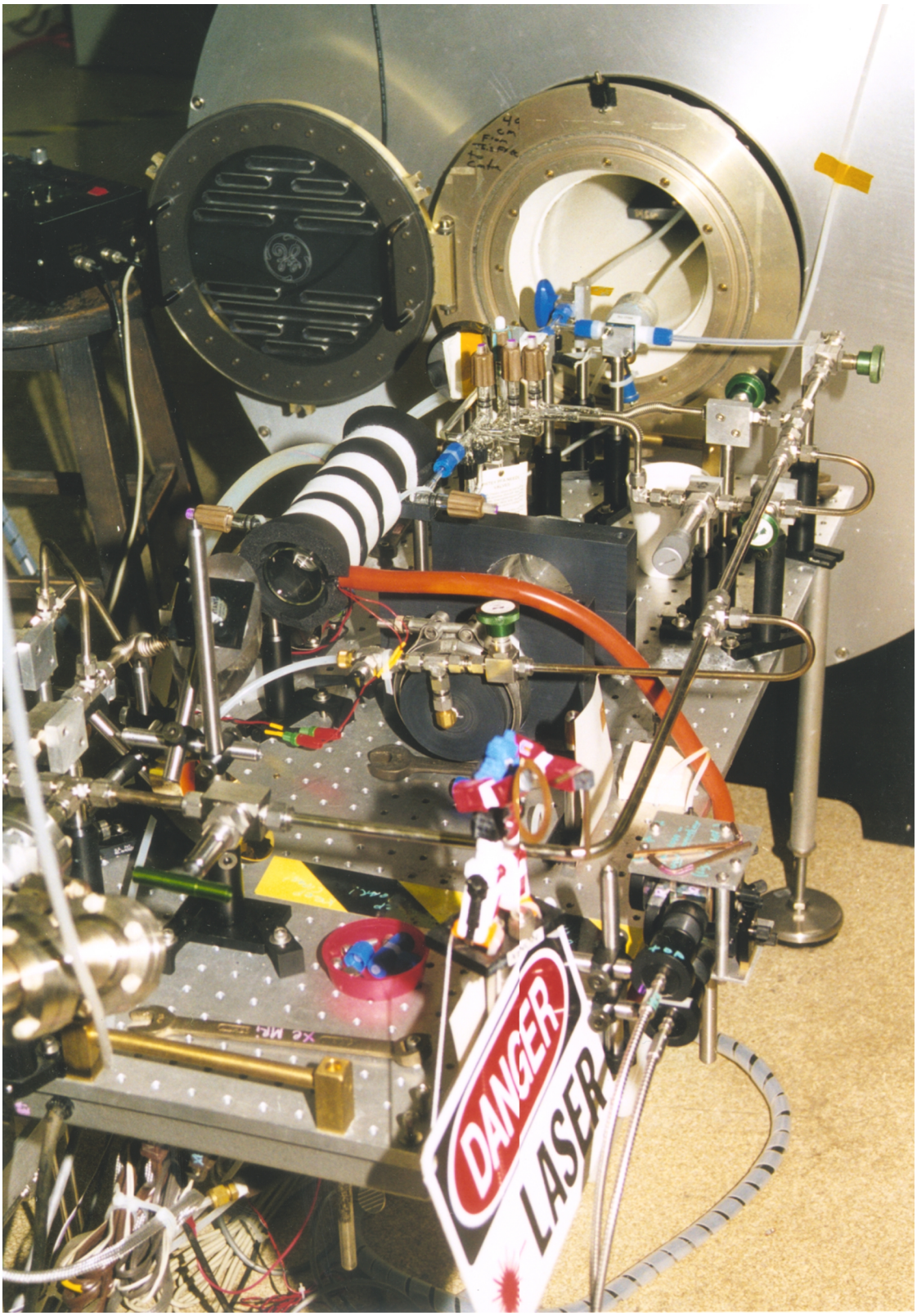

Figure 3.1: The ^{129}Xe polarizer installed adjacent to the 2 Tesla magnet.

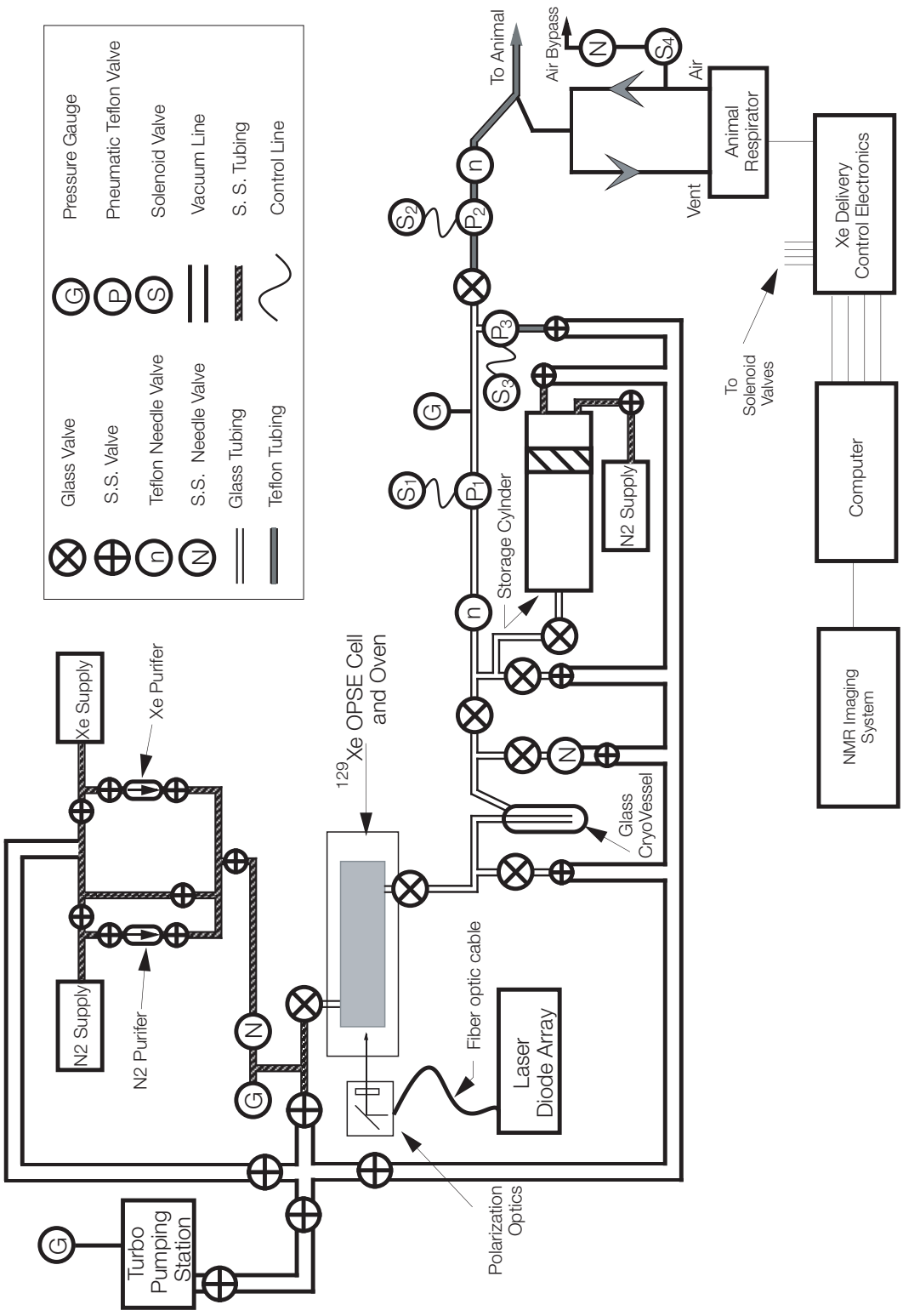

Figure 3.2: Schematic of the ^{129}Xe polarizer and delivery system.

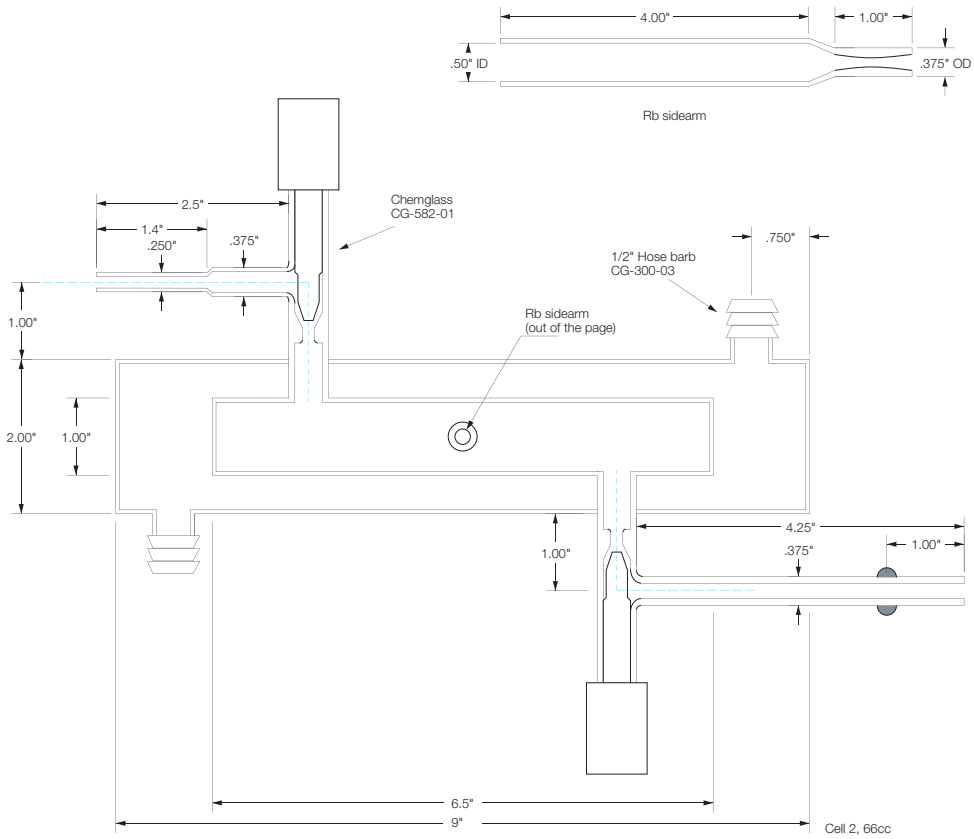

Figure 3.3: The OPSE cell and sidearm assembly

avoided for many years for fear of the windows bursting at the high operating pressures in the cell. However, excellent results have recently been obtained with a cell ("cell 5") with optical flats. A Pyrex sidearm for Rb loading is attached to the center of the cell, perpendicular to the plane of the valves. A Pyrex outer jacket serves as an oven through which hot air is blown to heat the inner pumping cell. Two Pyrex high-vacuum valves with glass valve stems (Chemglass, Inc., Vineland, NJ) are mounted transverse to the long axis near each end of the cell. The cell interfaces to the cell filling stage at one end and to the polarized ^{129}Xe delivery system at the other. Teflon valve stems with Teflon TFE encapsulated O-rings (Chemglass CG-560-01) were tried, but the Rb rapidly reacted with the Teflon stems at cell operating temperatures of 100–120 °C.

3.1.1 Cell manufacture

The production of OPSE cells is a multiple step process lasting several days. The first steps

in OPSE cell production are the chemical cleaning and coating of the cell interior to minimize depolarizing ^{129}Xe-wall interactions. The details of this cleaning and coating procedure are described in the following section (section 3.1.2). After cleaning and coating, the cell is attached to a turbomolecular pumping manifold using a 3/8" Cajon compression fitting. A Rb ampoule is broken open and slid into the glass sidearm which is then sealed with a Pyrex-working oxy-propane flame. The cell is baked out at 150 °C under vacuum. The outgassing of the cell during this process is evident from the increase in pressure over the first hour of heating. During bakeout the Rb ampoule is kept at room temperature to prevent migration of Rb vapor into the outgassing cell and also from contaminating the vacuum system. Cell bake-out is performed with both of the cell glass valves open to prevent the O-rings from developing compression-set and losing their resilience. A stainless steel Cajon compression fitting (with Viton O-rings) is used to cap the open end of the cell during this time. The cell is baked until the pressure equilibrates—typically at 10^{-7} Torr after 24–36 hours of baking. After bakeout, and the cell has returned to room-temperature, Rb is chased with a cool flame from the sidearm into the pumping cell. After sufficient Rb metal condenses out in the cell, the sidearm is then pulled off with a working-flame. The flame must never contact any coated surface in order to avoid burning the coating. For this reason, care is taken during the coating process to keep coating solution out of the sidearm and pulloff. After removing the sidearm the cell is pumped down to its final pressure, typically less than 2 10^{-8} Torr. The optical pumping cell is then backfilled with one amagat of purified N_2 and mated to the optical pumping/delivery system.

The magnetic properties of the Viton O-rings used on the glass valve stems have been found to vary greatly; many were found to be substantially magnetic at 2 T. A domestic mil-spec Viton compound (Lutz Sales Co, Inc., Hanover Park, IL) was found to be non-magnetic, and all the O-rings used in the cell and the system are made of this compound in size 007 (OR-007-2502-560) and size 009 (OR-009-2502-560). An extremely low vapor pressure (typically 10^{-12} Torr at 23 °C) perfluronated grease, Christo-lube MGC 109 (LTI, Jackson, OH), is used to lubricate all O-rings. This perfluornated grease is used instead of hydrocarbon-based greases (such as Apiezon M) because of its alkali resistance and stability at high temperature.

3.1.2 Octadecyltrichlorosilane coatings

Relaxation of ^{129}Xe magnetization at the walls of the OPSE cell limits the maximum attainable ^{129}Xe polarization. In an effort to reduce these depolarizing wall-interactions, wall coatings are applied to the cell walls. These coatings typically consist of a class of organosilane compounds which form oriented monolayers at solid-fluid interfaces by direct adsorption. The actual mechanism by which the silane coating acts to decrease wall spin relaxation is not well understood, but it is likely that the hydrocarbon chain on the silane, which forms an interlocking polymer with neighboring silane molecules, acts to both lower the binding potential by presenting a surface of hydrogen atoms and to separate the ^{129}Xe from paramagnetic impurities in the glass. In order for a coating to be suitable for OPSE cells, it must be highly resistant to alkali vapor attack at the relatively high operating temperatures of the OPSE cell (150–200 °C).

Although silane compounds are widely used as wall coatings to prevent spin-relaxation, methods for preparing and coating the glass surface vary considerably [5, 49, 50]. Evaporatively applied coatings such as Surfasil (tetramethylchlorosilane) and dimethyldichlorosilane [57] are widely used, but are difficult to apply to complex cell geometries and are not well suited to high temperature environments. The use of n-Octadecyltrichlorosilane (OTS, CH_3-$(CH_2)_{17}$-$SiCl_3$) as a wall coating for ^{129}Xe cells was first described by Oteiza [5]. Although good cells could be produced, the coating method was frequently unreliable and the important parameters not well understood.

A refined coating procedure was developed for the OPSE cells used in the ^{129}Xe polarizer in this dissertation, based largely on the detailed study of OTS chemisorption and polymerization by Sagiv [60-62]. The key steps of the OTS coating chemistry (shown schematically in figure 3.4) are: 1) hydrolysis at the glass/coating-solution interface, 2) adsorption, and 3) polymerization. OTS itself is easily hydrolyzed under the influence of atmospheric humidity and may form undefined polymerized material in contact with water [60, 63]. To avoid this, the coating solution is always freshly prepared and used immediately after mixing, and during this step the coating solution is kept away from water. For the same reason, the cell itself must be dry since OTS is highly reactive with water, but the glass surface must also be sufficiently hydrated before coating. OTS does not adsorb to a dehydrated glass surface, and a dehydrated surface can result from simply rins-

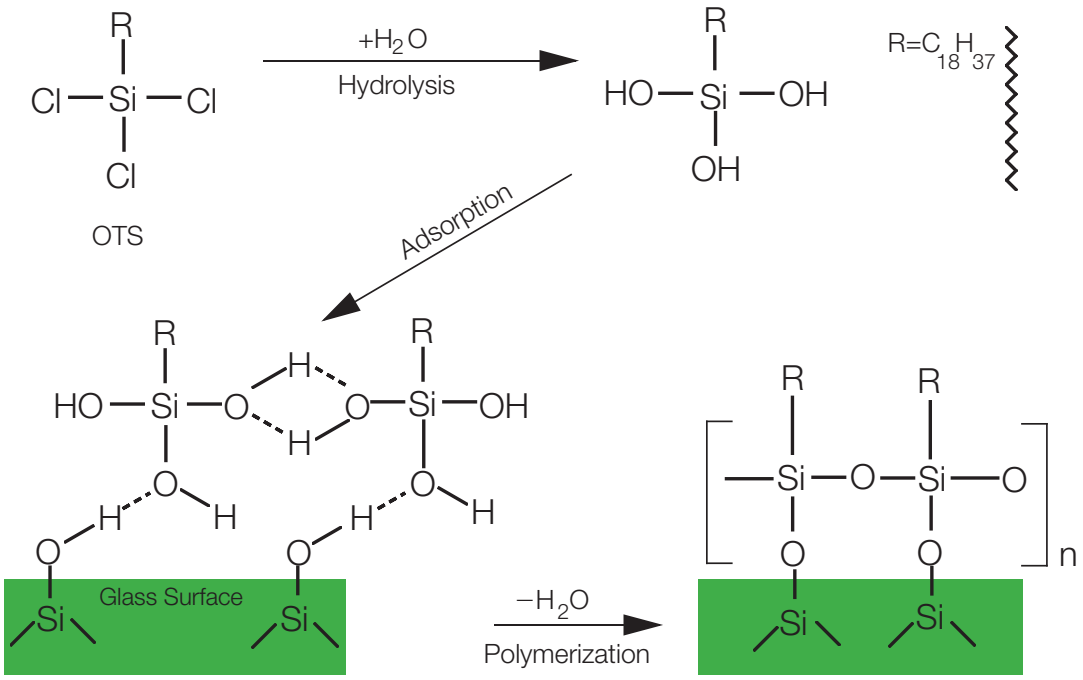

Figure 3.4: Chemisorption of n-octadecyltrichlorosilane (OTS) on glass

ing the cell in methanol. In order to re-hydrate the glass, it is essential that water is the final cell rinse before coating. Trial and error, with particular attention to the three stages of OTS chemisorption, resulted in the coating procedure of table 3.1

Proper polymerization of OTS at the glass surface requires clean glass. High purity HPLC or spectrophotometric grade solvents are used in the cleaning and coating procedure. In order to remove a broad range of surface contaminants from the glass, the cell is cleaned with a long soak in an acid solution (known as "Piranha" in the semiconductor industry) followed by a sequence of polar and non-polar solvent rinses. Piranha solution is a hot and caustic solution and extreme care must be taken during its use. All of the solutions used in the cleaning procedure are poured into the cell through the glass Rb sidearm. Clean Teflon valve stems with teflon-encapsulated O-rings are inserted into the glass valve bodies to keep the solutions from leaking out of the cell. These stems are highly resistant to all of the chemicals used in the cleaning and coating process. Glass tubing is attached to the inlet and outlet of the cell with teflon PFA elbows so the cell can vent to atmosphere during cleaning and coating, thus preventing trapped air from impeding the flow of liquids

Cleaning	Coating
1. Wash in hot soapy Alcanox in deionized (DI) H_2O for 2 minutes. 2. Rinse (3×) with DI H_2O. 3. 1–3 hours in *Piranha solution*. 4. Rinse (3×) with DI H_2O. 5. Rinse (3×) with Methanol. 6. Rinse (3×) with DI H_2O. 7. Dry under rough vacuum, at room temperature. *Piranha solution*: (30% H_2O_2 + 97% H_2SO_4 3:7 v/v)	1. Prior to coating, allow cell to rehydrate in air for ~ 1 hour. 2. 5 minutes in *Coating solution*. Do not allow solution to enter pull-off. 3. Rinse (3×) with $CHCl_3$. 4. Bake under rough vacuum, at 200 °C for >16 hours. DO NOT preheat oven. *Coating solution*: 2mM (0.788 cc/Liter) solution of OTS in 80% n-hexane + 12% CCl_4 + 8% $CHCl_3$ (v/v). Mix thoroughly with magnetic stirrer.

Table 3.1: OPSE cell cleaning and coating procedures

into the cell.

After cleaning, cells are dried under rough vacuum. Previously, cells were dried by flowing dry N_2 through them, however droplets of water often recondensed in a dry-appearing cell after the flow of N_2 was stopped. The OTS coating solution is poured into the cell through one of the valve bodies while the other remains plugged. Extreme care is taken to keep the coating solution below the level of the sidearm pull-off. After the coating solution is poured out, the cell is baked. OTS polymerization is accelerated at high temperature, and baking the newly coated cell at high temperature in a vacuum-oven is important as it allows the hexane to outgas from the silane-matrix [60]. After baking the cells, OTS polymerization is verified by filling the cell with about 10 mL of DI water and observing the curvature of the meniscus; coated glass dramatically beads water and no meniscus will form. The water is then drained, and the cell is baked again under vacuum until dry. This reliable and effective coating procedure is used for all the ^{129}Xe polarizer cells in this dissertation, as well as for the dual species ^{3}He–^{129}Xe maser cells made in our group [8] and for other glass components of the ^{129}Xe polarizer. Cells coated with this procedure have measured ^{129}Xe relaxation times from 300 to 1000 s.

3.1.3 Optical pumping setup

This section describes the specifics of optical pumping in the ^{129}Xe polarizer. Hot air (typically 80–120 °C) flows through the OPSE cell oven and maintains a Rb vapor density

in the cell of typically 10^{12}–10^{13} cm^{-3}, estimated from the vapor pressure curve measured by Killian [64],

$$[\mathrm{Rb}] = \frac{10^{10.55 - 4132/T}}{1.38\times10^{-16}T}, \tag{3.1}$$

where T is the cell temperature in Kelvin and [Rb] has units of cm^{-3}. The calculated Rb-^{129}Xe spin-exchange rate, $\gamma_{SE} = \kappa_{SE}[\mathrm{Rb}]$, varies from 5 10^{-4} s^{-1} at 80 °C to 7 10^{-3} s^{-1} at 120 °C. Temperature of the cell oven is regulated by an Omron E5EK temperature controller which can monitor the cell temperature at two locations: the hot air inlet and the hot air outlet. The thermal mass of the cell is sufficiently large that the use of the outlet RTD to control the heating from room temperature to operating temperature causes the inlet air temperature to drastically overshoot set-point temperature (by as much as 50–100 °C). In order to avoid overheating the OTS coating (which has been shown to fail in the presence of Rb vapor at temperatures above 190 °C [5]), initial cell heating is controlled using the front RTD. The cell temperature is affected by power deposited into the cell by the pumping lasers, and this is observed as an increase in outlet temperature when the lasers are turned on. Since the temperature measured by the outlet RTD more accurately reflects this laser heating effect, the temperature controller is switched to the outlet RTD once the cell has reached operating temperature to regulate cell temperature. At an operating temperature of 105 °C, the temperature differential between the inlet and outlet RTDs is typically 10–12 °C (inlet higher than outlet). With 20–40 W of laser light illuminating the cell, the temperature differential between inlet and outlet RTDs drops to less than 1 °C.

The magnetic holding field for optical pumping is provided by the 2 T magnet fringe field. In our setup, the magnetic field at the cell is approximately 450 Gauss, oriented predominately along the long axis of the OPSE cell. A Helmholtz coil pair would also produce a suitable magnetic field and allow the polarization stage to be set up in a magnetic field-free environment. The ^{129}Xe relaxation rate due to wall collisions (Γ_{wall}) in OTS-coated cells is strongly dependent on magnetic field [65], and fields above 20 Gauss result in a calculated $\Gamma_{wall} \ll \gamma_{SE}$ over the typical range of operating temperatures.

The contribution to ^{129}Xe relaxation in the pump cell from magnetic-field inhomogeneities was estimated in section 2.2.1 to be $\Gamma_{\nabla B}$ is 5.7 10^{-5} s^{-1}, a time constant of roughly

5 hours. This satisfies the requirement that environmental relaxation not dominate spin-exchange: $\Gamma_{\nabla B} \ll \gamma_{SE}$. This is satisfied over the practical experimental range of γ_{SE} by the requirement $\left|\nabla B_{\perp}\right| / B_0 < 0.05\ \mathrm{cm}^{-1}$.

For each experiment, the OPSE cell is filled with 1700 Torr of highly purified natural xenon (26.4% ^{129}Xe) and 150 Torr of N_2. Choice of optimum Rb vapor density depends on the available laser spectral density as well the cell relaxation rates; the optimization of the OPSE parameters is discussed below.

3.1.4 OPSE cell design

This section describes the practical design considerations of the polarizer cell geometry. Prior to this work, there was no technique for production of laser-polarized ^{129}Xe in the large quantities needed for *in vivo* MRI. Cell geometries in Rb-^{129}Xe spin-exchange systems were usually small sealed spheres containing a few cc-atm of ^{129}Xe, with their size primarily determined by the geometric constraints of the experiment [4, 5, 8, 66]. The goal of the polarization system in this experiment is to produce batches of polarized ^{129}Xe that are accumulated and subsequently delivered. For a fixed amount of ^{129}Xe to be polarized in each batch, the optimal OPSE cell length lies somewhere between two extremes: short cells (at high xenon pressure) and long cells (at low xenon pressure). Easy-to-make short cells require a high xenon pressure and consequently suffer from a large Rb-^{129}Xe spin-rotation rate which limits the ultimate ^{129}Xe polarization. In principle, longer cells with lower xenon pressures always provide higher ^{129}Xe polarization since Rb-^{129}Xe spin-rotation, which dominates Rb spin-destruction, scales with [Xe]. However, it is difficult to evenly illuminate long cells using a divergent light source, and the total cell length is also limited by practical space considerations.

In order to determine the optimum cell size, the maximum ^{129}Xe polarization as a function of OPSE cell length was calculated, based on the model of section 2.3. The diameter of the cells is limited by the practical problem of maximizing the incident flux of four laser beams. A cell window with 1.94–2.22 cm diameter works well for four beams. A simulation with radius $r = 0.97$ cm and wall relaxation time $T_{wall} = 300$ s (i.e., a typical "good" cell) is shown in figure 3.5. The total amount of ^{129}Xe is constant for each curve, so the ^{129}Xe pressure varies inversely with the cell length. Depending on available lab resources,

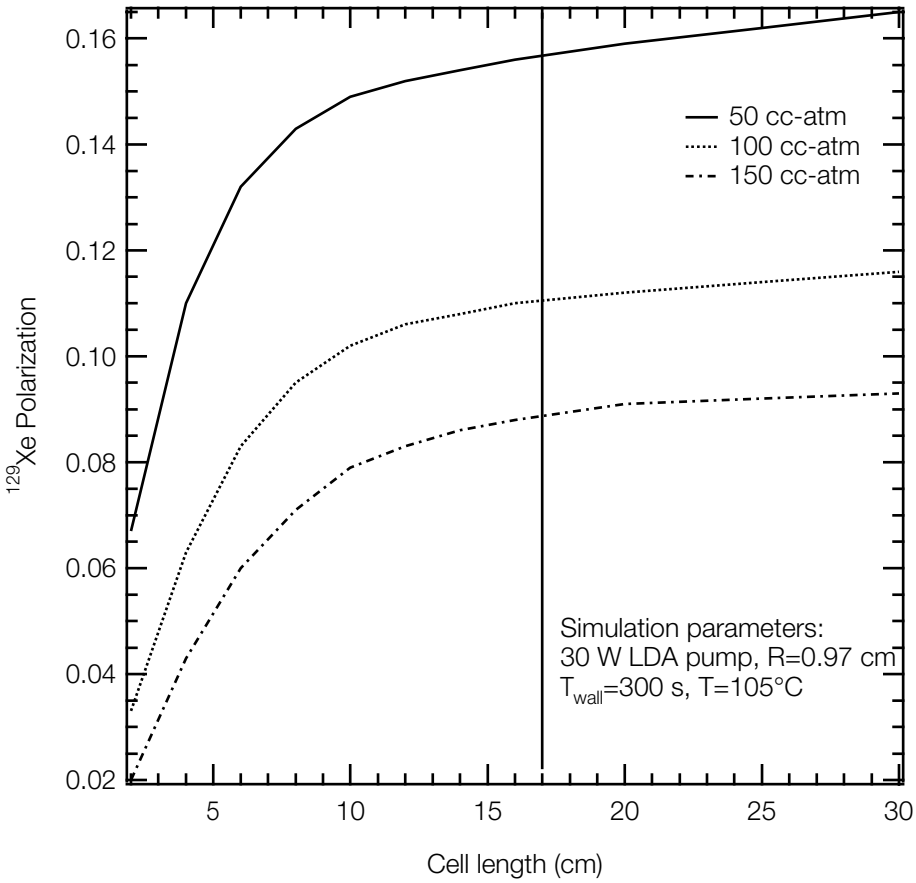

Figure 3.5: Calculation of the ^{129}Xe polarization as a function of OPSE cell length, for three ^{129}Xe production amounts. ^{129}Xe number is constant along each curve. The solid line at 17 cm indicates the length of the cells used in the polarizer.

the polarizer runs with 15–45 W of LDA light, and so 30 W of light with the spectral profile of an Optopower LDA was used in the calculation. In all the cases, the N_2 pressure is fixed at 150 Torr, and the Rb density is assumed constant throughout the cell as by Killian's formula (equation 3.1). Note that the polarization starts to saturate above about 10 cm for the family of curves shown here. A cell length of 17 cm (the solid line in figure 3.5) was chosen for all of the cells used in the polarizer as a compromise between the length at which the polarization saturates, and the practical consideration of increasing the cell length.

3.1.5 OPSE operation and performance

This section describes the operation and performance of the ^{129}Xe polarization stage and compares the measured ^{129}Xe polarization to the simulation calculations as a function of several operating parameters. The OPSE cell is connected to two distinct regions of the polarizer system (see figure 3.2): 1) the unpolarized gas handling side (known as the filling manifold) constructed largely of stainless steel and 2) the polarized gas transport side described in section 3.3. The cell is evacuated and filled through the inlet valve on the cell, with the filling procedure as follows: Nitrogen gas is metered into the manifold through a needle valve, and the manifold and cell are filled to a pressure P'. The gas pressure is read with a capacitive manometer gauge (MKS Baratron, model 122A) mounted in the room temperature manifold. The cell inlet valve is then closed and the manifold pumped out. The manifold and OPSE cell are then isolated from the pump, and the cell inlet valve opened. Nitrogen gas rushes out of the cell, rapidly equalizing the pressure on both sides of the inlet valve, achieving a final N_2 pressure P which is 150 Torr for all of the experiments presented here. The ratio P' / P is measured for each cell, and is typically 2.5. Natural abundance xenon is then metered into the system, and the manifold and cell are filled to the final pressure which is typically 1850 Torr. The inlet valve is then closed, and the manifold is evacuated.

For each cell the ^{129}Xe wall relaxation rate is estimated from the measurement of the ^{129}Xe spin-up rate; the ^{129}Xe spin-up rate is $\Gamma_{spinup} = \kappa_{SE}[\mathrm{Rb}] + \Gamma_{wall}$, with $\kappa_{SE} = 3.70\ 10^{-16}\ \mathrm{cm^3 s^{-1}}$ and [Rb] given by Killian's formula (equation 3.1). Since the Rb-^{129}Xe spin-exchange constant is known to no better than a factor of two, the ^{129}Xe spin-up measurements are performed at lower than typical operating [Rb] where the contribution of Rb-^{129}Xe spin-exchange to the ^{129}Xe spin-up rate is reduced; $\Gamma_{SE} = 5.3\ 10^{-4}\ \mathrm{s^{-1}}$ at 80 °C and $2.9\ 10^{-3}\ \mathrm{s^{-1}}$ at 105 °C. A spin-up of one cell ("Cell 5") at 80 °C is shown in figure 3.6. For each time point, the cell was filled and the lasers were unblocked. After optical pumping, the gas was expanded into to the ^{129}Xe "Big Rig" NMR probe (see section 3.1.6) in the center of the 2 T magnet, and a FID was acquired. The measured spin-up rate for this cell was $\Gamma_{spinup} = 2.73\ 10^{-3}\ \mathrm{s^{-1}}$ at 80 °C, with contribution from $\Gamma_{wall} = 1/(450\ \mathrm{s})$. This is consistent with ^{129}Xe wall rates measured in OTS-coated cells used in other experiments in our group [8]. The wall relaxation rate measured in this way is used to parameterize a

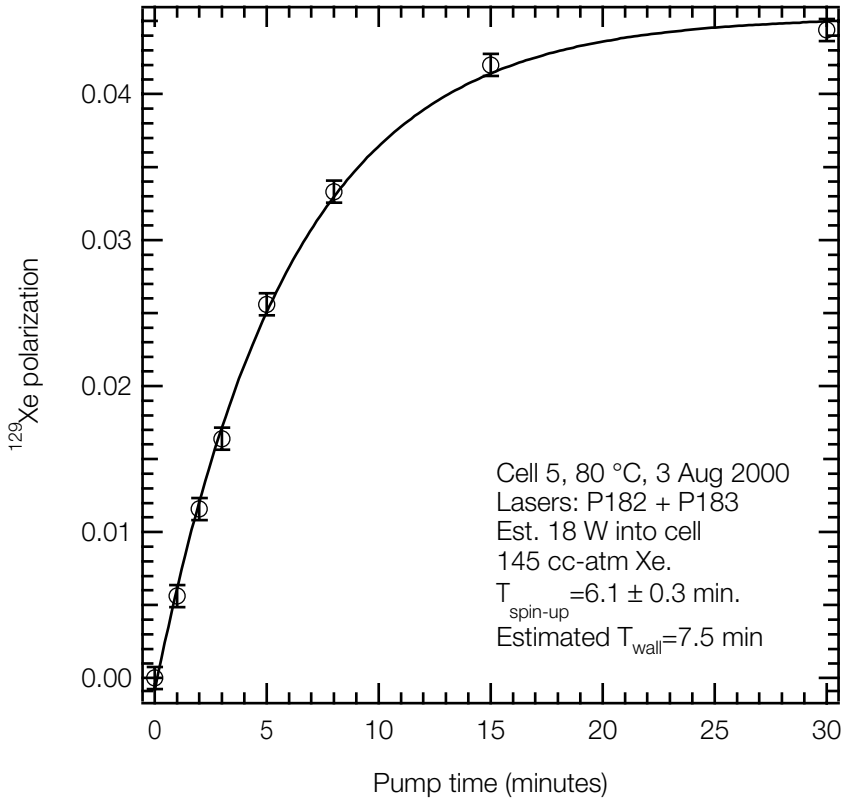

Figure 3.6: Spin-up of Cell 5 at 80 °C with two Optopower lasers (P182 and P183). The NMR signals were calibrated by comparison to thermally polarized ^{129}Xe NMR signal

given cell in optical-pumping calculations.

The large amounts of polarized ^{129}Xe needed for *in vivo* experiments are obtained by operating the polarizing stage in batch mode—i.e., the cell is filled, optically pumped for a cycle time τ, the polarized ^{129}Xe gas stored, and the process is repeated. The choice of optimal cycle time is discussed in detail section 3.8, and for typical polarizer operation the cycle time τ = 5 minutes. Therefore, the practical figure of merit for determination of cell operating temperature is the ^{129}Xe polarization after 5 minutes of optical pumping. The optimal operating temperature for the OPSE cell was determined by measurement of the ^{129}Xe polarization (after 5 minutes of optical pumping) as a function of cell temperature, and a typical temperature dependence is shown in figure 3.7. At each temperature, the cell was allowed to thermally equilibrate for 20 minutes, after which time the cell was filled and the lasers were unblocked. After 5 minutes of optical pumping, the gas was expanded into the ^{129}Xe "Big Rig" NMR probe in the center of the 2 T magnet, and a FID was acquired.

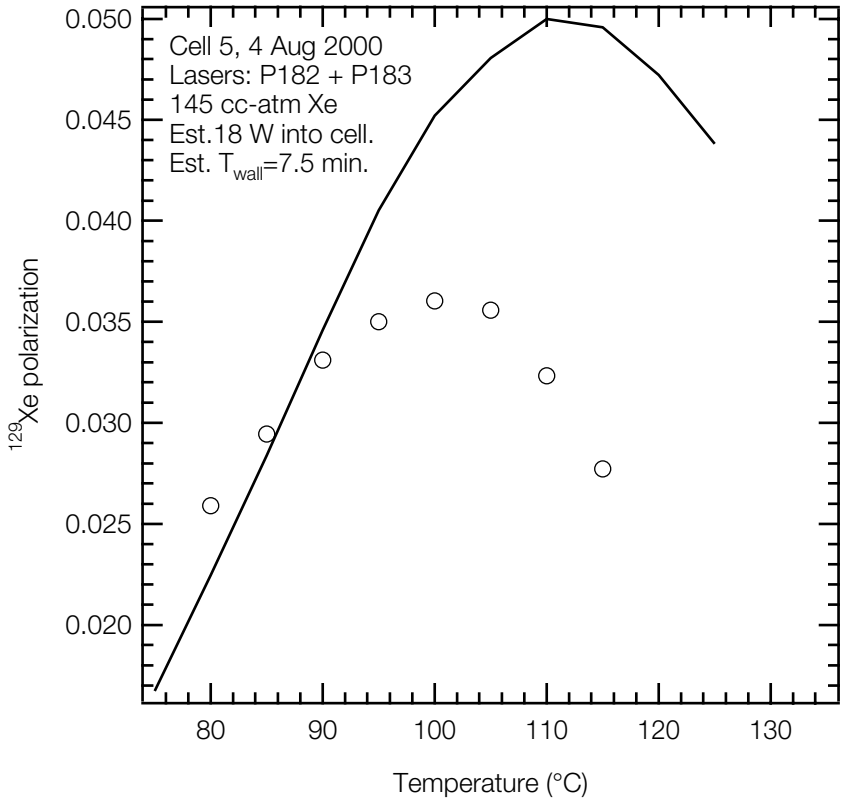

Figure 3.7: Typical temperature dependence of ^{129}Xe polarization with two Optopower LDAs after 5 minutes of optical pumping. Solid line is the simulation result for the ^{129}Xe polarization after 5 minutes pumping using an 18 W LDA profile light source and T_{wall} = 7.5 minutes. The drop in ^{129}Xe polarization at higher temperatures (i.e., at higher Rb densities) is due to decreased optical pumping efficiency as the Rb vapor becomes optically thick. The NMR signals were calibrated by comparison to thermally polarized ^{129}Xe NMR signal.

The solid line plotted in figure 3.7 is the simulation result for the ^{129}Xe polarization after 5 minutes pumping with an 18 W LDA profile light source and T_{wall} = 7.5 minutes, for a cell with the same geometry and pressures as "Cell 5". It should be noted that any temperature dependence of the ^{129}Xe wall relaxation rate is neglected in OPSE calculations. The value of Γ_{wall} obtained from the spin-up measurement at 80 °C is used in the simulation over the range of temperatures 75–130 °C.

The Rb-^{129}Xe spin-exchange rate is proportional to [Rb], and if we ignore the temperature dependence of the Rb polarization, the ^{129}Xe polarization increases with [Rb]. As

the cell is heated, increasing the Rb density, the optical thickness of the Rb vapor also increases. This decreases the volume of the cell which is illuminated with resonant pumping light, decreasing the average Rb polarization [47] and consequently decreasing the average ^{129}Xe polarization. The effect of ^{129}Xe wall relaxation on the temperature dependence of the ^{129}Xe polarization is easily understood from calculations shown in figure 3.8.

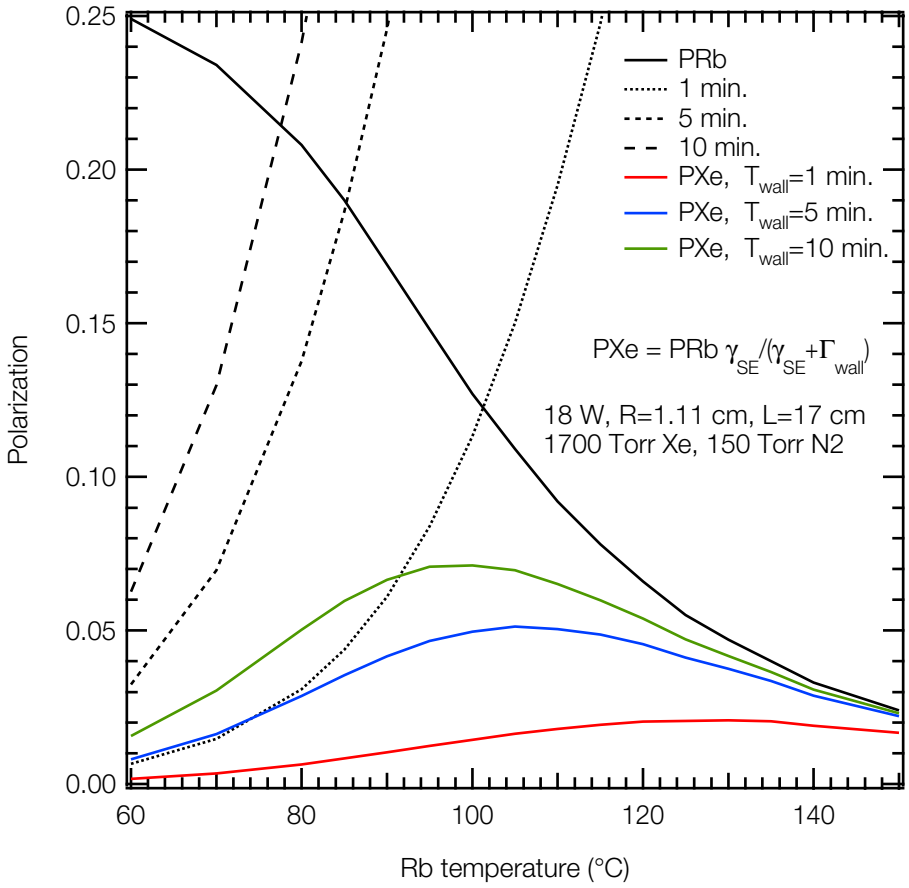

Figure 3.8: Calculation of steady-state Rb and ^{129}Xe polarizations as a function of temperature and T_{wall}. The dashed lines are the factor $\gamma_{SE}/(\gamma_{SE} + \Gamma_{wall})$ evaluated for the listed T_{wall}. Since Rb spin-relaxation is dominated by Rb-Xe spin-rotation and not by Rb-^{129}Xe spin-exchange, P_{Rb} is independent of P_{Xe} and is the same for all the cases shown.

Cells with short T_{wall} have a flatter temperature dependence and achieve maximum ^{129}Xe polarization at higher temperatures.

Measurement of the ^{129}Xe polarization as a function of xenon pressure in the OPSE

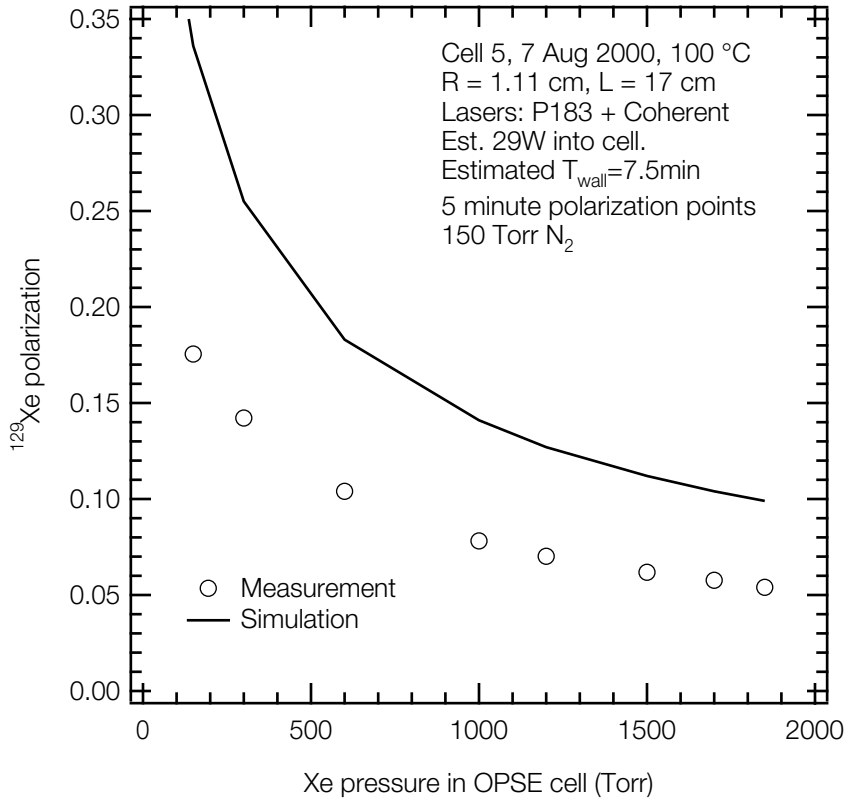

Figure 3.9: ^{129}Xe polarization vs. xenon pressure, polarized for 5 minutes with one Opto-power and one Coherent LDA. Solid line is simulation result for the ^{129}Xe polarization after 5 minutes pumping using a 29 W LDA profile light source and T_{wall} = 7.5 minutes. The NMR signals were calibrated by comparison to the thermally polarized ^{129}Xe NMR signal.

cell is shown in figure 3.9. As above, the solid line plotted in figure 3.9 is the simulation result for the ^{129}Xe polarization after 5 minutes of optical pumping. An 18 W LDA profile pumping source and a ^{129}Xe wall relaxation time of T_{wall} = 7.5 minutes were used for a cell with the same geometry as "Cell 5". The strong dependence of the ^{129}Xe polarization on xenon pressure is a consequence of Rb spin-relaxation being dominated by Rb-Xe spin-rotation. Very high ^{129}Xe polarizations (*i.e.*, 35%) are achieved at low xenon pressures (*i.e.*, 150 Torr ^{129}Xe). Operation of the polarizer stage at this low xenon pressure is not practical given the production requirement of several-hundred cc-atm per *in vivo* experiment; 150 Torr Xe in the typical OPSE cell corresponds to 13 cc-atm of xenon polarized each cycle. With a cycle time τ of 5 minutes, the resultant production rate of 156 cc-atm/

hour is not sufficiently rapid given the practical time limit for polarized ^{129}Xe accumulation, currently limited by the T_1 of frozen ^{129}Xe at 77 K (see section 3.4) to approximately one hour.

Calculations of the ^{129}Xe polarization, using the best estimates of T_{wall}, incident laser power, and spectral density, are consistently higher than the measured ^{129}Xe polarization. However, over a wide range of xenon pressures and cell temperatures, these simulations agree with measured ^{129}Xe polarization to better than a factor of two. Uncertainty in modeling the trajectory of the divergent laser beams through the OPSE cell is likely the dominant source in the discrepancy between calculation and experiment. It should be noted that we have not made measurements of the loss of ^{129}Xe polarization during transport from the OPSE cell to the probe where the NMR signal is acquired. Although calculations of transport losses due to magnetic field gradients are estimated to be negligible (see section 3.3), and although NMR measurements are made as quickly as possible after the gas is introduced to the probe, the ^{129}Xe polarization data should be considered a lower limit on the ^{129}Xe polarization in the pump cell.

Calculations of the temperature dependence of ^{129}Xe polarization (as in figure 3.7 and figure 3.8) reflect the T_{wall} dependent shape of experimental observations quite accurately, for cells with T_{wall} from 50–450 s. However, the calculations consistently indicate a temperature offset 10–12 °C higher from what is experimentally observed. This is likely due to the fact that the RTD temperature readings are lower than the actual Rb temperature in the cell as a result of laser heating. This is a well known problem in OPSE experiments that use high power laser diode arrays [67, 68].

3.1.6 Polarization calibration

Calibrated measurement of the laser-polarized ^{129}Xe polarization is made by comparison of the laser-polarized ^{129}Xe NMR signal with a thermally-polarized ^{129}Xe NMR signal. Since the thermal ^{129}Xe polarization is 4–5 orders of magnitude smaller than the laser-polarized signal, many thermal NMR spectra must be averaged in order to obtain a reasonable SNR. In order for the thermal ^{129}Xe longitudinal magnetization to return to its equilibrium value after each NMR pulse, a pulse repetition time (TR) of a several T_1s must be used. We measure T_1 relaxation times of ^{129}Xe gas in Pyrex vessels at 2 T to be of order 3

hours, so a thermal experiment consisting of several thousand tips is clearly impractical. It has been shown that the presence of one atmosphere of paramagnetic O_2 reduces the ^{129}Xe T_1 to 0.3 s^{-1} amagat^{-1} [69]. We exploit this short T_1 of ^{129}Xe mixed with O_2 to acquire several thousand thermal signals in an overnight run in the calibration apparatus known as "Big Rig".

The Big Rig assembly (figure 3.10) sits in the center of the 2 T magnet at room temper-

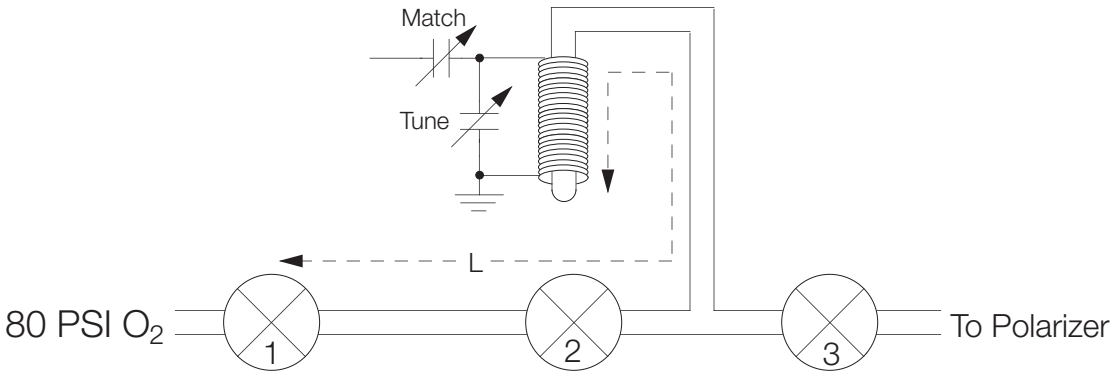

Figure 3.10: "Big Rig" assembly used to measure the laser-polarized ^{129}Xe polarization.

ature and mates to the polarizer with PFA tubing. All of the valves on Big Rig are PFA plug valves (PFA-4354, Whitey, Ohio). After evacuating Big Rig, the volume between valve 2 and valve 3 (V_{23}) is filled with roughly 1 amagat of polarized ^{129}Xe and valve 3 is closed. A single 60° tip is sufficient to obtain a signal from the laser-polarized gas with a typical SNR of several hundred with the Big Rig solenoid NMR coil (Q ~ 200). Oxygen is then introduced into the Big Rig through valve 1, filling the volume between valves 1 and 2 (V_{12}) with 80 PSIG of O_2. Valve 1 is closed and valve 2 is opened, allowing the gases to mix. The final density of O_2 in V_{23} is 1.3 amagat. The gases are allowed to mix for several characteristic interdiffusion times,

$$\tau \cong \frac{L^2[\mathrm{Xe}]}{4\pi^2 D}, \tag{3.2}$$

where $D = 0.06$ cm^2 s^{-1} [70] is the diffusion constant of O_2 in xenon at 1 amagat, [Xe] is the xenon density in the volume $V_{12} + V_{23}$ (in units of amagats), and L is the characteristic

length of the Big Rig. From equation 3.2, the interdiffusion time is roughly $\tau \sim 3$ minutes for $L = 20$ cm. After waiting 30–60 minutes for the gases to mix, 3000–5000 thermal ^{129}Xe NMR spectra are acquired with pulse TR of 10 s. The ^{129}Xe T_1 in the presence of 1.3 amagat O_2 in the Big Rig has been measured to be 2.3 s, so a pulse period of 10 s allows 99% of the ^{129}Xe magnetization to recover between pulses. These spectra are summed to obtain the thermal signal (figure 3.11). The bandwidth, receiver gain, pulse width and pulse

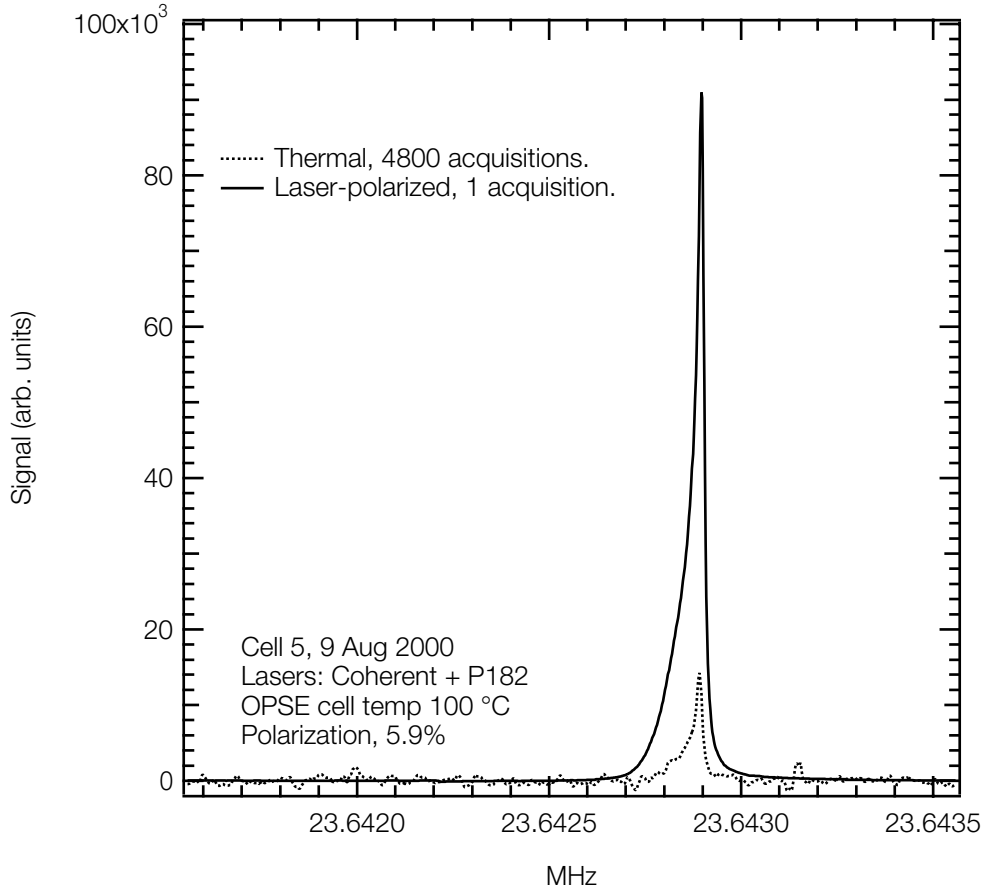

Figure 3.11: Typical ^{129}Xe laser-polarized and thermal NMR signal acquired from the Big Rig at 2 T. The cell was pumped for 30 minutes for this measurement. The thermal signal is the sum of 4800 acquisitions. The ^{129}Xe polarization in this case (from equation 3.3) is 5.9%. The small frequency shift of the laser-polarized resonance with respect to the thermal resonance is due to transverse magnetic gradients induced by the large laser-polarized ^{129}Xe sample magnetization [5].

power are all kept fixed for the laser-polarized and thermal ^{129}Xe measurements, and the probe Q and tuning do not change over the measurement period. The absolute polarization of the laser-polarized (LP) ^{129}Xe is given by

$$P_{LP} = \frac{S_{LP}N_{thermal}}{S_{thermal}N_{LP}}\frac{V_{23}}{V_{12}+V_{23}}P_{thermal}, \tag{3.3}$$

where S_{LP} is the integrated laser-polarized NMR signal, $S_{thermal}$ is the integrated thermal NMR signal, $N_{thermal}$ and N_{LP} are the number of acquisitions used to acquire the thermal and LP signal, and the ^{129}Xe thermal polarization $P_{thermal} = \tanh(\mu B/k_B T)$ is 1.9 10^{-6} at 300 K and 2 T. The ratio of volumes in Big Rig is measured to be $V_{23}/(V_{12}+V_{23}) = 0.87$. The day-to-day repeatability of the thermal signal acquired from Big Rig is better than 5%.

3.2 Laser System and Optics

The availability of low-cost, high-power, relatively inexpensive laser diode arrays (LDAs) has been central in the ability to situate the ^{129}Xe polarizer adjacent to the 2T MRI magnet. Previous to the development of this technology, optical pumping typically used Ti:sapphire lasers pumped by large frame Ar^{++} lasers. Ar^{++} lasers require 60 kW of electrical power, well-regulated high-flow cooling water, and substantial laboratory real estate. It would have been nearly impossible to install a Ar^{++}/Ti-sapphire system in the 2 T laboratory given these requirements. Additionally, these systems require constant alignment and maintenance. Two fiber-coupled laser diode arrays (OptoPower, OPC-A016-FCPS) have been the workhorses of these experiments, with each providing up to 15 watts of CW laser light. These self-contained wall-plug units have a broad spectral profile with a typical FWHM of 15–20 Å (figure 3.12). In addition to the Optopowers, a Coherent FAP 30W fiber-coupled laser diode array system was occasionally available and was used in the polarizer in place of one of the Optopowers. A computer-controlled scanning monochrometer was used to acquire spectral profiles for each laser, and the operating temperature and current were adjusted to center the laser spectral profile about the Rb D1 resonance at 794.7 nm.

The output from each 1.5 mm fiber bundle is an unpolarized beam with circularly

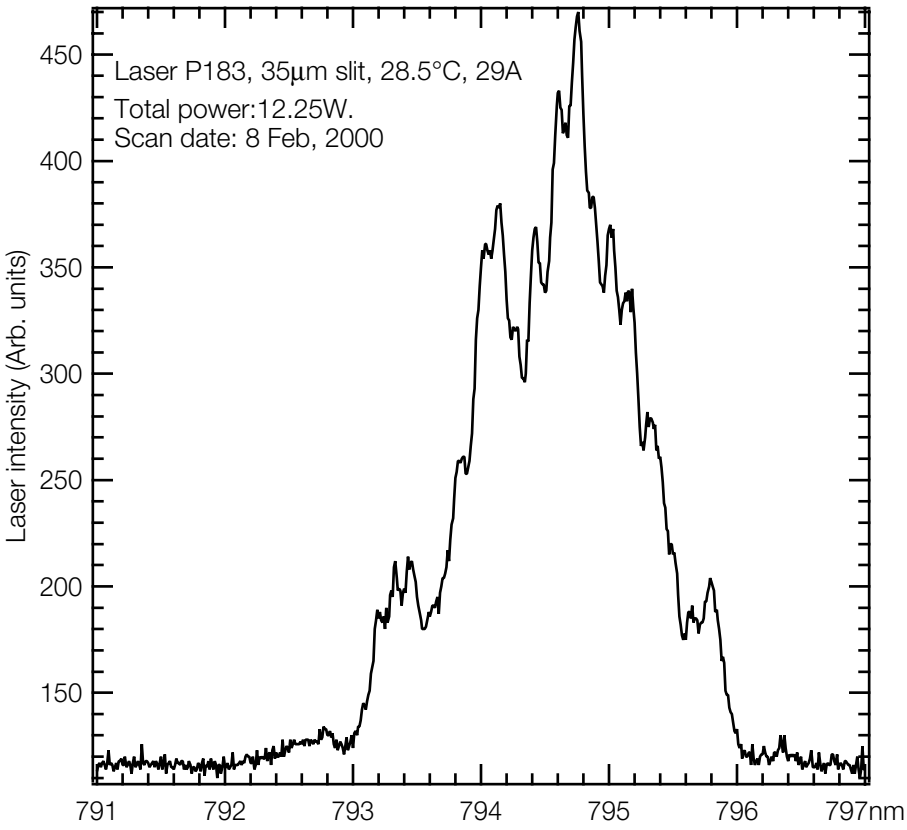

Figure 3.12: Spectral profile of laser P183. This spectrum is typical of Optopower LDAs.

symmetric 12° beam divergence. The LDA light is collimated and circularly polarized with the optics assembly shown in figure 3.13 [68]. The light from each fiber is incident on an AR coated convex lens to reduce its divergence. The beam then passes through a linearly polarizing beam-splitter cube, which splits the light into two linearly polarized beams. The two output beams from the beamsplitter have orthogonal linear polarizations. In order to produce the same helicity of circularly polarized light from each beam, the $\lambda/4$ plates have their axes mounted perpendicular to each other. Each LDA has a separate set of optics, so two lasers produce 4 beams of right circularly polarized light which is incident on the OPSE cell. Spot size at the oven window for each beam is roughly 10–12 mm. Circular polarization of each beam is measured to be greater than 90%, and is typically 95%. The maximum power with the lasers lines centered on Rb D1 line was 13.8 W for each of the Optopower LDAs and 30 W for the Coherent LDA. Because of the difficulty in properly collimating and directing the beam, and due to the reflections from the uncoated oven

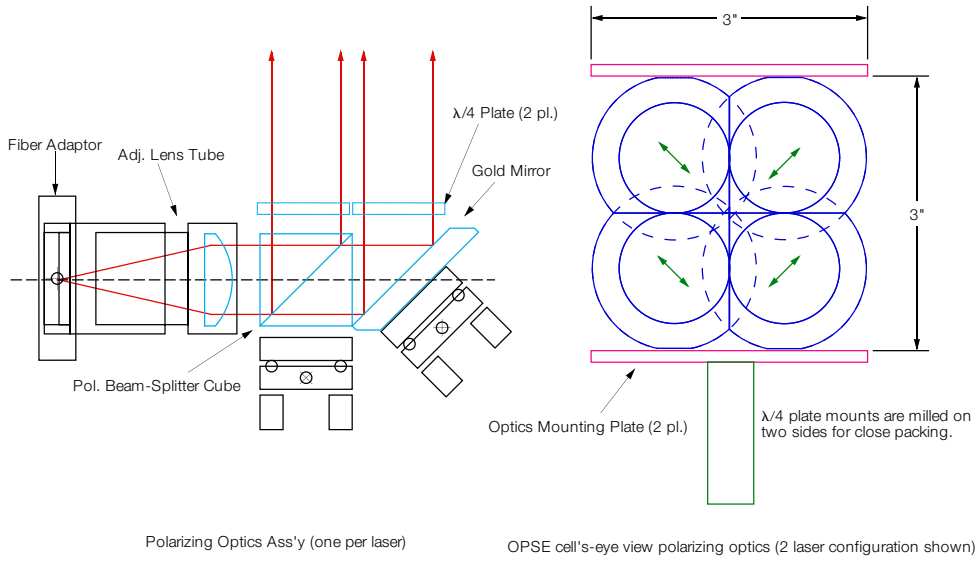

Figure 3.13: Beam shaping and polarizing optics. Arrows indicate the λ/4 plate axis.

and cell windows, only approximately 66% of the laser power is expected to pass through the windows into the cell. The total power penetrating the cell is estimated as 18.2 W for both Optopowers (P182 + P183) together, and 28.9 W for one Optopower (P183) and one Coherent together. Furthermore, only a fraction of the laser power reaching the cell actually contributes to optical pumping due to the broad spectral profile of the diode lasers. Simulations estimate typically 0.5 W absorbed. The benefit of narrowing the laser spectral profile to ^{129}Xe polarization is discussed in Chapter 6 [71-74].

3.3 ^{129}Xe Transport Manifold

Once polarized, ^{129}Xe is transported from the optical pumping cell through the transport manifold for accumulation, storage, and delivery to the subject or sample. All the materials in the transport system were chosen to be both compatible with the transport of polarized ^{129}Xe and be suitable for use in the high magnetic-field environment near the MRI magnet. In order to keep the system leak-tight against contaminants that would depolarize ^{129}Xe (such as paramagnetic O_2), ultra-high vacuum (UHV) techniques are used throughout the system, however, many of the components typically used in UHV systems, such as stainless steel valves and tubing, rapidly depolarize ^{129}Xe. Glass isolation valves are located between regions where polarized ^{129}Xe is transported in the manifold and each UHV valve.

These glass valves are kept closed while polarized gas is transported through the system, and are operated in conjunction with the UHV valves when pumping out the manifold. The manifold is constructed out of OTS-coated Pyrex, and individual substructures, such as the OPSE cell, mate to the glass manifold with unions made from a Teflon perfluoroalkoxy copolymer resin known as PFA (Swagelok, Hudson OH).

Flexible PFA tubing is used as a very convenient way to connect the PFA plug valve at the polarized ^{129}Xe outlet of the apparatus to the various probes and experimental platforms. The ^{129}Xe T_1 in a 31 cm long, 1.6 mm diameter piece of PFA was measured by fill-

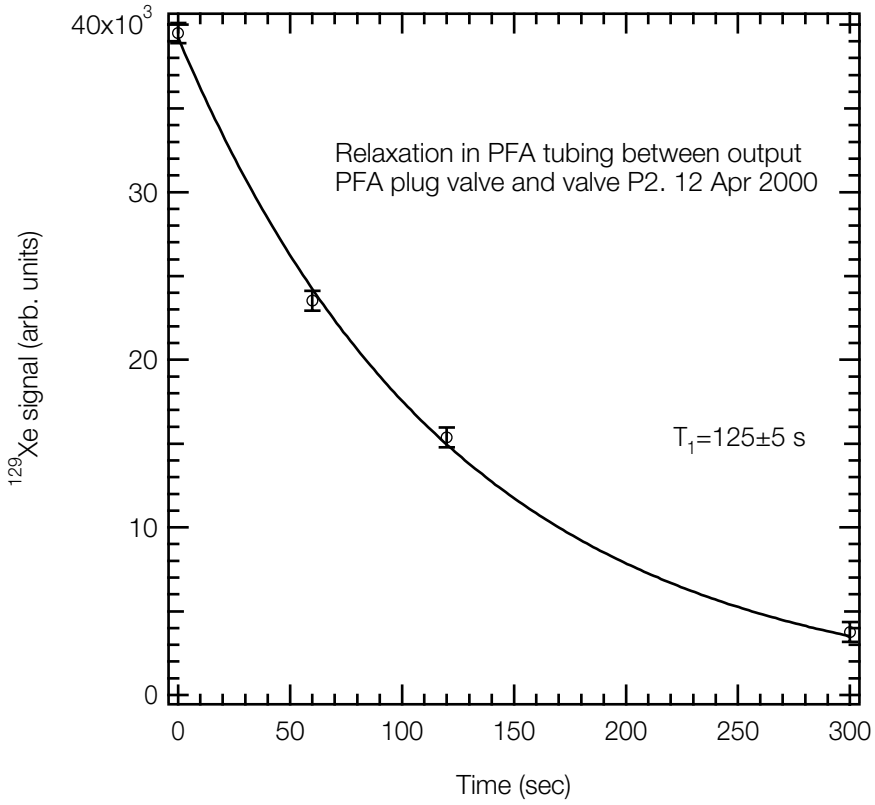

Figure 3.14: ^{129}Xe relaxation in the PFA tubing between polarizer output valve and pneumatic valve P_2.

ing its volume with polarized ^{129}Xe, waiting a time T, and then delivering the gas to Big Rig where an FID was acquired. The PFA tubing relaxation time calculated from the fit of a single exponential to this data (figure 3.14) is 125 ± 5 s. The longest amount of time that

polarized ^{129}Xe spends in this 2.5 cc volume of tubing occurs when an animal is being ventilated. The usual *in vivo* delivery rate is 1.33 cc/s, so polarized ^{129}Xe spends less than 2 seconds in this region and ^{129}Xe relaxation in PFA is not expected to contribute substantially to polarization loss. There is, however, a region of the polarizer with an extremely short T_1, measured to be 23 ± 2 s. This short T_1 region is the volume between the pneumatic valve P_1 and the polarizer output valve, and incudes the Honeywell pressure gauge and the internal volume of the valve P_1. The Honeywell pressure sensor (internal volume of less than 0.1 cc) was removed but the relaxation rate in the "bad" region remained the same. Although this needs to be more carefully studied, the most likely source for this relaxation is the body of valve P_2, which is machined from Teflon polytetrafluoroethylene (PTFE).

This 8 cc "bad" region was discovered because it causes significant depolarization if ^{129}Xe is allowed to sit in this region between runs. During a typical *in vivo* run, we expect less than a 10% loss of ^{129}Xe polarization due to this region—not a significant problem in normal operation. However, if the *in vivo* delivery of polarized ^{129}Xe needs to be paused for more than a few seconds, the volume up to the gas storage "syringe" should first be evacuated to pump out the depolarized ^{129}Xe.

3.3.1 Estimate of ^{129}Xe transport losses

Polarized ^{129}Xe flowing through the delivery system moves through a non-uniform magnetic field. In order to transport ^{129}Xe magnetization to the subject or sample without loss of polarization, the local magnetic field must change slowly enough that the nuclear spins are able to follow it adiabatically. The polarizer apparatus is situated so that it is convenient to describe an inhomogeneous magnetic field as a combination of a large static field along the direction of the 2 T solenoid, $B_0\mathbf{z}$, and a smaller perpendicular component *i.e.*,

$$\boldsymbol{B} = B_0\hat{z} + B_x\hat{x} + B_y\hat{y}. \tag{3.4}$$

The angle between the total field and $\boldsymbol{z}$ is given by θ, where

$$tan\theta \;=\; \frac{B_{\perp}}{B_0}, \tag{3.5}$$

where $B_{\perp}$ is defined as

$$B_{\perp} \equiv \sqrt{B_x^2 + B_y^2}. \tag{3.6}$$

Adiabatic transport occurs when the nuclear spins, initially aligned along **z**, are able to follow the changing direction of the magnetic field. This adiabatic condition is written

$$\frac{d\theta}{dt} \ll \gamma B \tag{3.7}$$

For polarized gas moving with an arbitrary velocity with respect to the field, we can write

$$\frac{d\theta}{dt} \;=\; v_x\frac{d\theta}{dx} + v_y\frac{d\theta}{dy} + v_z\frac{d\theta}{dz}. \tag{3.8}$$

Solving equation 3.5 for θ in the small angle approximation, equation 3.8 becomes

$$\frac{d\theta}{dt} \;=\; v_x\frac{d}{dx}\left(\frac{B_{\perp}}{B_0}\right) + v_y\frac{d}{dy}\left(\frac{B_{\perp}}{B_0}\right) + v_z\frac{d}{dz}\left(\frac{B_{\perp}}{B_0}\right). \tag{3.9}$$

Neglecting terms of order θ^2, equation 3.9 can be written

$$\frac{d\theta}{dt} \approx \frac{\boldsymbol{v}\cdot\nabla B_T}{B_0}. \tag{3.10}$$

The most stringent requirement on $d\theta/dt$ is found when the gas is moving along the direction of ∇B_T. In this case, the adiabatic condition combining equation 3.7 and equation 3.10 is

$$|\boldsymbol{v}| \ll \frac{\gamma B_0^2}{|\nabla B_T|}. \tag{3.11}$$

The mean magnetic field at the optical pumping cell in our experiments is B ~ 500 gauss with $|\nabla B_T|$ ~ 12 gauss/cm. In this case, the adiabatic condition is satisfied for gas velocities

$v \ll 10^9$ cm s^{-1}. Given the absence of large transverse magnetic field gradients in the vicinity of the 2 T magnetic (typically less than 15 gauss cm^{-1}) and typical molecular speeds of order 10^4 cm s^{-1} [75], the adiabatic condition of equation 3.11 is generally irrelevant in laboratory practice and ^{129}Xe atoms will always adiabatically follow the local direction of the magnetic field.

3.4 Polarized ^{129}Xe Accumulation

A batch mode production method is used to accumulate large volumes of polarized ^{129}Xe. This exploits the long lifetimes of ^{129}Xe in the OTS-coated OPSE cell at 450 Gauss (typically 300–600 seconds) and the extremely long lifetimes achievable in the frozen state [76]. The relaxation rate of frozen ^{129}Xe is magnetic field dependent up to about 500 Gauss, and in many experiments [77] a permanent magnet is used to reduce relaxation in the frozen ^{129}Xe by storing the sample at high magnetic field [29]. In this experiment, the magnetic field (provided by the fringe field of the 2 T magnet) at the ice storage cell is 500 Gauss. The ^{129}Xe ice relaxation time (T_1^{ice}) at LN_2 temperature in this field was measured (figure 3.15) to be 1 hour. Significantly longer relaxation times are obtainable at lower temperatures [78]. The polarized gas mixture is pumped from the OPSE cell through the evacuated ice storage cell. The ice storage cell is a 5 cc OTS coated Pyrex trap immersed in LN_2. Xenon freezes and remains in the storage cell while the N_2 gas is pumped away. Cryotrapping [79, 80] occurs in mixtures of condensable and non-condensable gases and can prevent complete xenon accumulation. The geometry of the freezing cell and the turbulent flow of gas through it minimizes cryotrapping. Additionally, the pumping of the hot gas mixture from the OPSE cell through room-temperature tubing into the cryogenic trap cools the gas and rapidly reduces the Rb vapor pressure. This prevents significant Rb vapor from being delivered to the subject or sample. It should be noted that after four years of running, no evidence has been observed to indicate that Rb accumulates in the cryogenic trap. The polarization/accumulation cycle is repeated several times over 20–30 min to accumulate additional polarized xenon as ice.

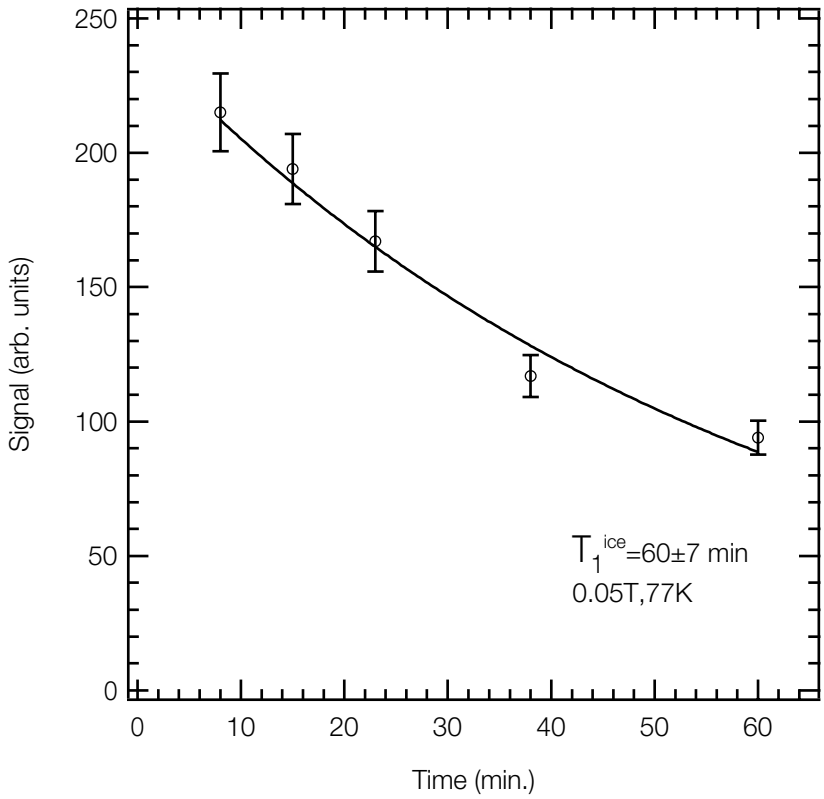

Figure 3.15: ^{129}Xe ice relaxation time at 77 K and 500 Gauss. Gas was polarized for 10 minutes and then released into the 77 K vessel. After a time *T*, the vessel was connected to the "Big Rig" solenoid and warmed with warm water. The xenon ice was observed to be completely melted in roughly 30–40 seconds. A single FID was acquired one minute after thawing began. A fit of a single exponential yields an ice T_1 of 60±7 minutes. Error bars at each point indicate the standard deviation of two measurements.

3.5 Polarized ^{129}Xe Gas Storage

Once a sufficient volume of polarized ^{129}Xe has been accumulated as ice, the ice is thawed for subsequent delivery to the subject or sample. The polarized gas storage system receives the polarized ^{129}Xe after it has been thawed, and is used to provide a constant pressure polarized ^{129}Xe source for our experiments. The gas storage assembly resembles a large syringe, consisting of a gas storage cell and a piston. The gas storage cell is a precision bore, 7.6 cm diameter, 25 cm long Pyrex cylinder internally coated with OTS. The Teflon piston, with a teflon-encapsulated viton O-ring (International Seal, Henderson, NV), fits inside

this cylinder and seals gas-tight. One end of the cylinder is welded to a piece of 6 mm Pyrex tube, and a thick bead is pushed out at the open end. The beaded end of the cylinder is sealed to a Nylatron cap with a Teflon-lined beaded-pipe clamp.

The cylinder is evacuated and pressurized through the 6 mm Pyrex tube via the ^{129}Xe transport manifold. The space behind the piston is pressurized or evacuated via a connection in the plastic cap. The piston is initially located at the back of the cylinder. The 1 Liter cylinder volume is subsequently evacuated via the gas transport manifold. The xenon cryotrap is rapidly thawed, and the polarized gas freely expands into the storage cylinder. The valve between the cryovessel and the syringe is closed and a N_2 source provides back pressure to the piston producing a constant pressure polarized ^{129}Xe source for the delivery system. The magnitude of the ^{129}Xe NMR spectrum vs. time acquired from a volume probe around a 0.7 cc glass vial is shown in figure 3.16, where 1.2 cc (±5%) of ^{129}Xe was

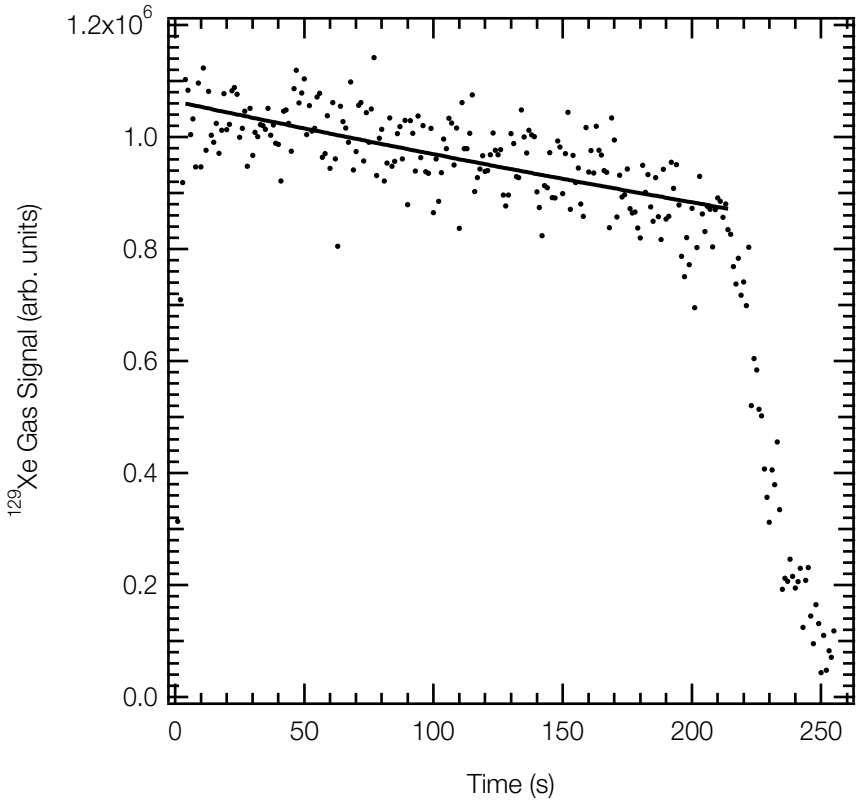

Figure 3.16: Determination of "syringe" T_1. A fit of a single exponential yields a syringe T_1 of 1076±71 s.

delivered every second for 220 s. The signal decreases rapidly after delivery from the storage syringe was stopped due to repeated 25° tips of the same gas. The ^{129}Xe gas polarization lifetime (T_1) in the "syringe" is roughly 18 minutes with no observed dependence on the position of the piston in the cylinder (*i.e.*, the surface-to-volume ratio).

3.6 Polarized ^{129}Xe Delivery

After accumulation, the syringe contains polarized ^{129}Xe gas. This is to be delivered in a controlled manner and with a minimal loss of polarization to the subject or sample located in the center of the NMR imaging system. The polarized gas delivery system transports polarized ^{129}Xe continuously at a fixed rate or in metered volumes to a sample, and in single breath doses to an animal subject. The repeated delivery of small volumes of polarized gas to an animal subject allows for averaging of signals over repeated inhalations and is essential for systematic studies *in vivo*. Polarized ^{129}Xe is transported from the gas storage system to the sample or animal without coming in contact with oxygen. This is critical to ensure low loss of ^{129}Xe polarization. For *in vivo* work, O_2 is precisely mixed with polarized xenon at the animal interface via the air bypass needle valve. The control of remotely activated valves allows complete automation of the delivery cycle and the operational procedure described below.

3.6.1 Operation

The volume between the pneumatically actuated Teflon valves P_1 and P_2 (M222CPFS-T, Teqcom Industries, Santa Ana CA) serves as a ballast volume. The pneumatic valves (P_i) are controlled via solenoidal valves (S_i), which are outside the high magnetic field environment of the NMR magnet. These solenoidal valves are driven by the control electronics. A non-magnetic pressure transducer (136PC100G2, Honeywell Microswitch, Freeport IL) mounts into the glass transport manifold via an O-ring seal and senses the ballast volume pressure, P_{mon}. The control electronics package circuitry monitors the ballast volume pressure. The control electronics fill the ballast volume with polarized ^{129}Xe to a set pressure by actuating P_1. The polarized ^{129}Xe in the ballast volume is then delivered directly to the sample or subject by actuation of P_2. A Teflon-stem needle valve (Chemglass, Vineland

NJ) provides a variable gas conductance between the xenon syringe and the gas delivery system. This valve is adjusted to match the rate of gas flow to the switching speed of the pneumatic valves. P_1 is mated to the glass transport manifold, and P_2 is an integral part of the experimental platform containing the NMR probe and the sample or subject, located near the center of the magnet. P_2 mates to a Teflon PFA (Swagelok, Hudson OH) plug valve on the delivery system via PFA tubing. This flexible tubing is minimally depolarizing over the typical resonance time of gas in the tubing (T_1 of about 125 sec), and the ease of connection to the system allows for rapid removal and installation of the experimental platform in the magnet.

3.6.2 *In vivo* xenon delivery cycle timing

The delivery stage of the polarizer is controlled by a package of analog and digital circuitry (figure 3.17, figure 3.18, and figure 3.19), which is responsible for control of the volume of delivered gas, and the delivery cycle decision making. In a typical *in vivo* experiment, a 200–500 g rat is anesthetized, and a non-metallic endotrachial tube is placed in the airway. The animal is placed on the experimental platform, which contains the NMR probe and valve P_2. The connection to the delivery system is made, and the ballast volume is evacuated. The animal is normally ventilated on a commercial small animal ventilator (Harvard Apparatus model 683) until the "xenon-enable" switch is engaged, at which time the xenon breathing cycle commences. The xenon delivery control logic is clocked by the commercial ventilator. An operational timing diagram is shown in figure 3.20. The xenon breathing cycle begins by waiting until the end of the exhalation cycle, at which point S_4 is opened, venting the ventilator through to air a vernier needle valve. This vernier valve allows for precision regulation of the fraction of breathing gas (typically O_2 or 95% O_2/5% CO_2) to be mixed with polarized xenon at the animal (figure 3.21). At the start of the inhalation cycle P_1 opens. The pressure P_{mon} of the xenon in the ballast volume is continuously compared to the set-point pressure, P_{set}. P_{set} uniquely determines the tidal volume of polarized ^{129}Xe delivered to the animal each breath. When $P_{set} = P_{mon}$, P_1 is closed and P_2 is opened, allowing the gas to flow to the animal. The animal exhalation cycle takes place as usual, through the ventilator exhaust. The animal can be switched back to breathing air by disengaging "xenon-enable", causing the xenon delivery system to finish its cur-

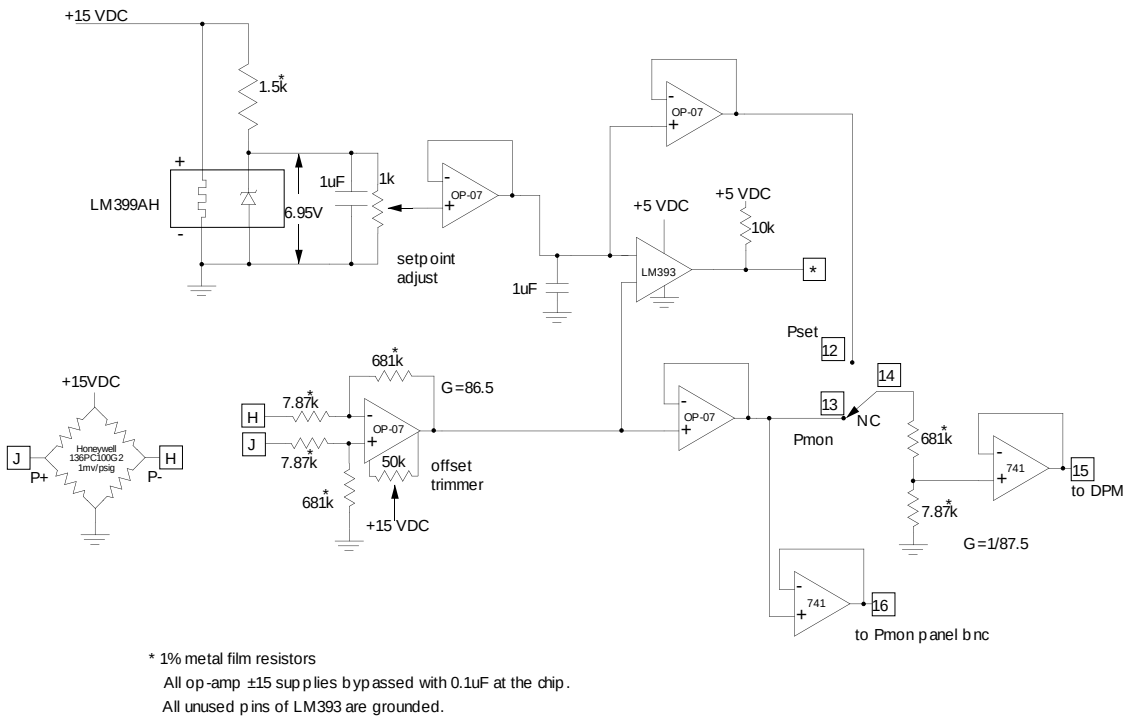

Figure 3.17: Delivery electronics: Analog subsystem.

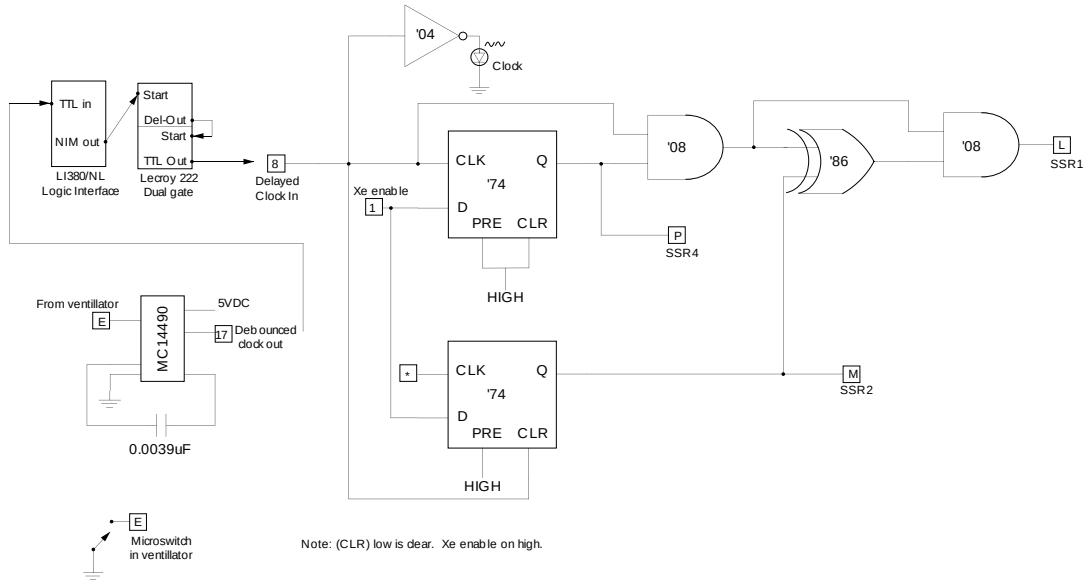

Figure 3.18: Delivery electronics: Digital subsystem.

rent xenon breathing cycle, and closing S_4 at the beginning of the next inhalation cycle. If the xenon pressure in the ballast volume P_{mon} does not reach P_{set} within the inhalation

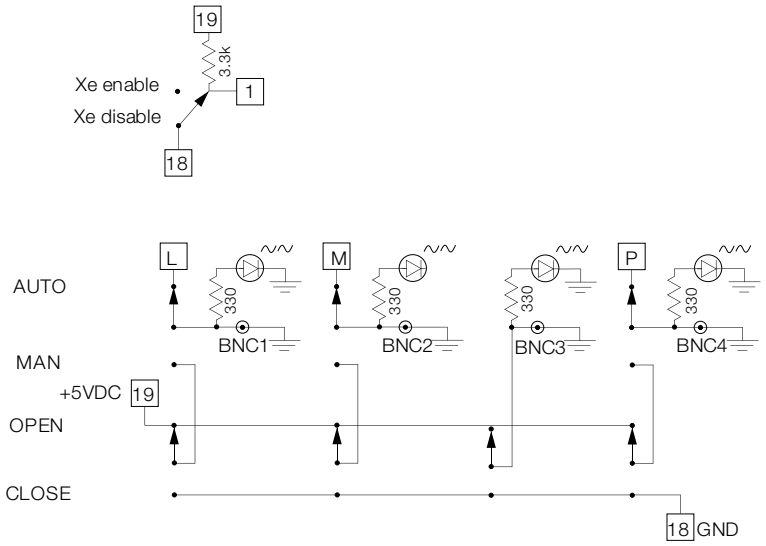

Figure 3.19: Delivery electronics: Front panel.

cycle, the polarized ^{129}Xe is not delivered, and the animal exhaust cycle is respected. The xenon delivery system then commences a pressure building sequence, until $P_{set} = P_{mon}$. If the xenon pressure in the ballast volume P_{mon} does not reach P_{set} within a selectable number of cycles, the pressure building sequence will time-out and return the animal to normal ventilation. If the xenon pressure in the ballast volume accidently exceeds the tidal set point P_{set}, no xenon will be delivered, and the animal is returned to normal ventilation. The ballast volume can be pumped out when xenon breathing is disabled through P_3. Flow of xenon from the animal back to the commercial ventilator is prevented by a one-way glass valve in the respirator line, at the animal subject.

3.6.3 Performance and calibration

The amount of xenon delivered to the subject or sample is determined by the ballast volume V_b (*i.e.*, the volume between valves P_1 and P_2) and the delivery pressure setpoint P_{set}. Once the delivery pressure setpoint is reached, valve P_2 opens and gas is delivered until the ballast volume reaches atmospheric pressure. The amount of xenon delivered N_{Xe} is simply

$$N_{Xe} \equiv \frac{P_{set} V_{ballast}}{T}, \tag{3.12}$$

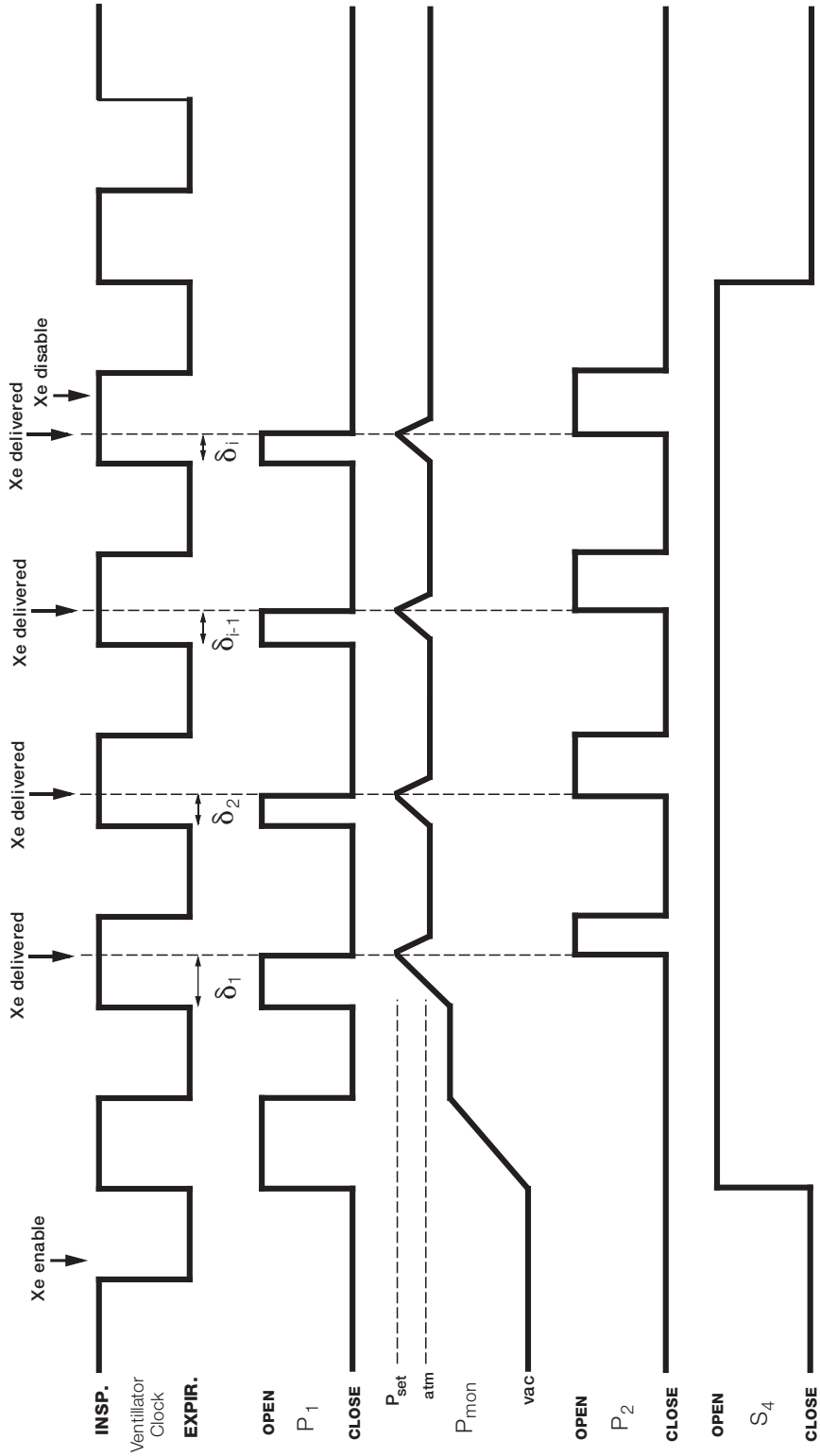

Figure 3.20: Timing diagram for xenon delivery summarizing the key operational elements described in the text. The time interval δ_i is controlled by the electronics package.

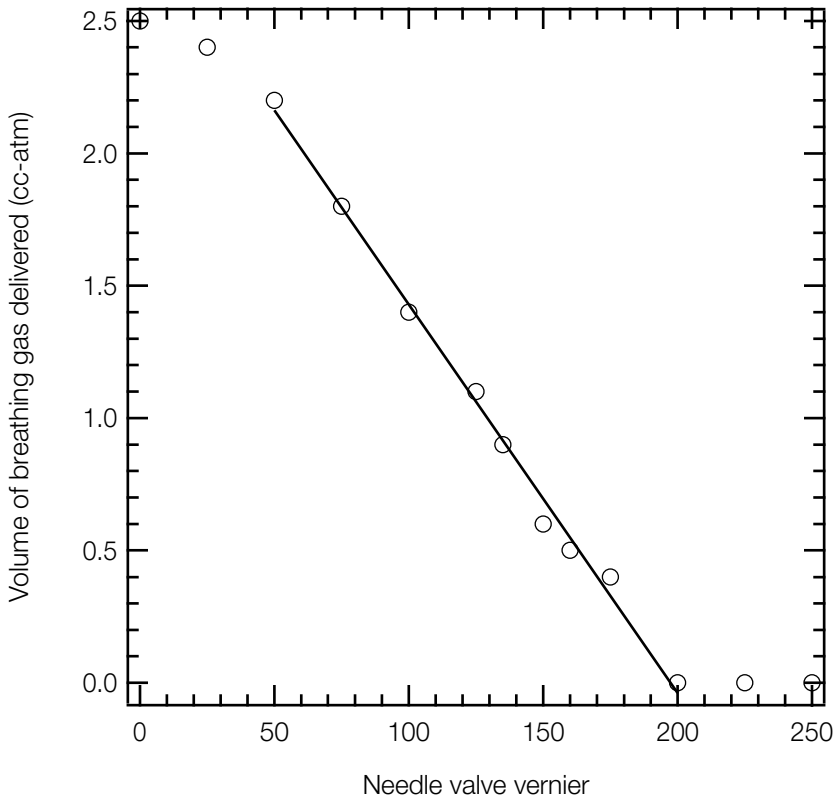

Figure 3.21: Volume of breathing gas delivered as a function of bypass needle valve setting, with ventilator set to deliver 2.5 cc per breath.

where P_{set} is the pressure setpoint above equilibrium pressure with the sample (atmospheric pressure for a rat), V_b = 10.9 cc, and T is the laboratory temperature. The ballast pressure gauge is calibrated to read in units of PSIG, to which an offset is added by the control electronics to keep the comparator away from 0 volts near the typical 1 atm gauge operating pressures. In terms of the control panel settings then the amount of xenon delivered at 23 °C is

$$N_{Xe} = 0.74 P_{set} - 1.18\,, \tag{3.13}$$

where N_{Xe} here has units of cc atm, and P_{set} has units conveniently called "PSIGO" (*i.e.*, **PSI G**auge with **O**ffset) on the control electronics box. The performance of the xenon delivery stage is shown in figure 3.22. Small adjustments to the Teflon-stem needle valve appreciably affect the gas conductance and can significantly affect the operation of the

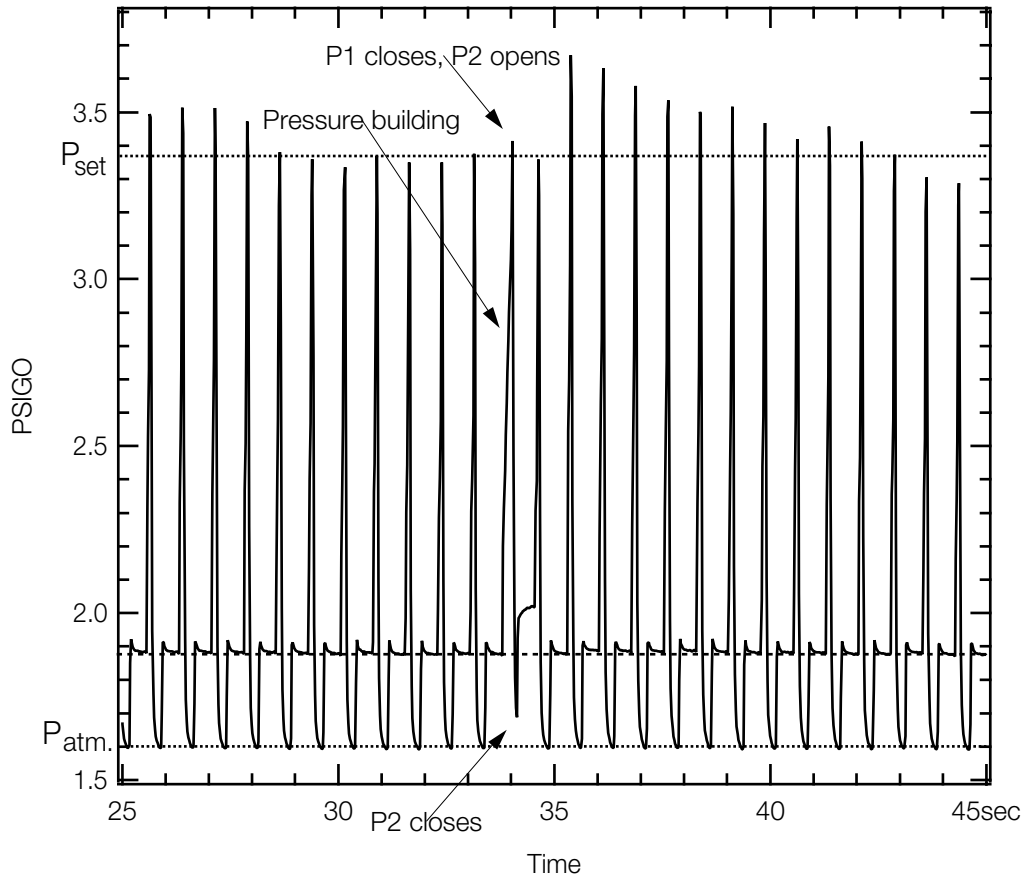

Figure 3.22: Xenon delivery performance: ballast pressure P_{mon} measured during an *in vivo* run. The variance of δ by the control electronics is easily seen at $t = 34$ s. In this run, however, the ballast volume did not completely exhaust before P_2 closed at the beginning of the exhaust cycle, preventing complete xenon delivery to the subject. Delivered gas volume for this run was 1.37 ± 0.07 cc-atm.

delivery stage. For this reason, the volume of gas delivered is always measured using a calibrated glass syringe at the experimental platform; any adjustment of the needle valve requires that the delivery volume be remeasured.

3.7 Experimental Platform

This section describes the experimental platform, and the overall delivery system's *in vivo* performance. The experimental platform (figure 3.23) is the modular interface between the polarizer and the subject or sample. This Nylatron platform contains the NMR probe,

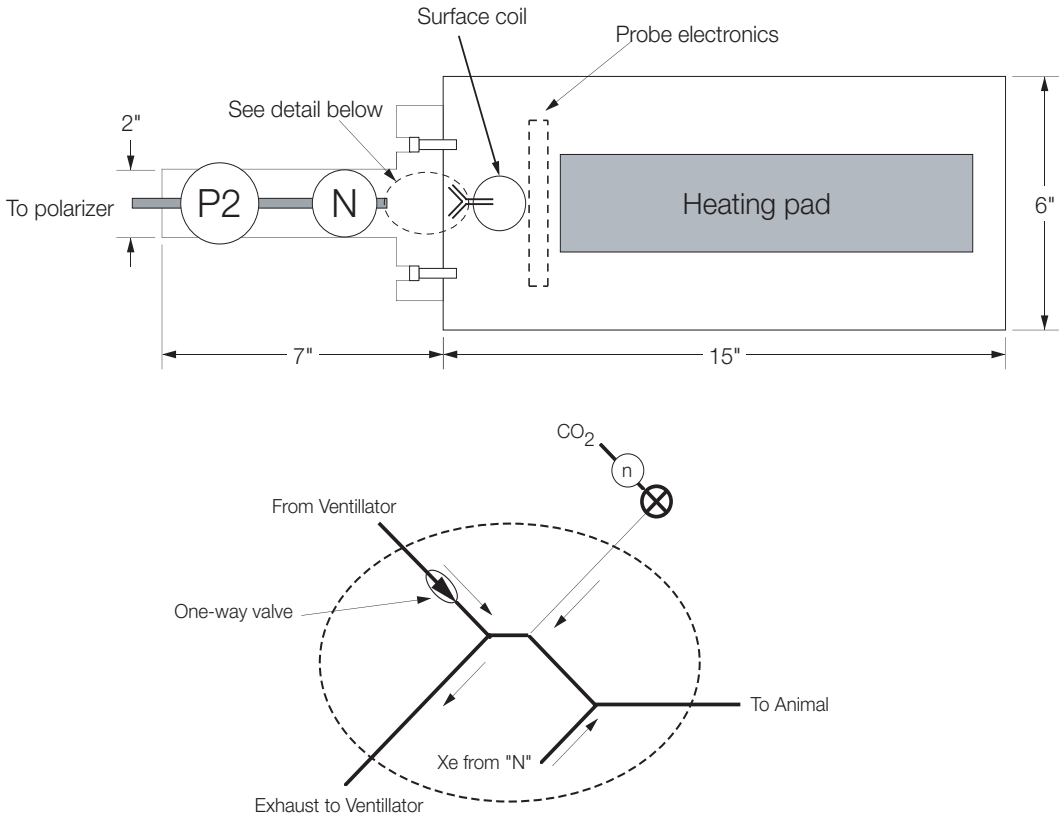

Figure 3.23: Experimental platform and detail.

pneumatic valve P_2, animal pulse-oxymetry probe, and the hot water blanket used for maintaining animal temperature. All individual components are attached to the platform with non-magnetic nylon screws. The platform also contains a Teflon PFA needle valve through which polarized ^{129}Xe flows before reaching the animal. The variable conductance of this valve is adjusted to smooth the xenon pressure profile and provides a more physiologically appropriate pressure profile (figure 3.24). A miniature glass one-way valve on the platform prevents backflow of xenon into the breathing gas supply line. CO_2 can be introduced either into the breathing mixture or titrated directly to the animal via small-bore Tygon tubing, which minimizes dead space.

3.7.1 RF probes

The RF coils used for pulsing and detecting the ^{1}H and ^{129}Xe frequencies (23 MHz and 85 MHz at 2 T, respectively) are part of the experimental platform. These tuned antennas

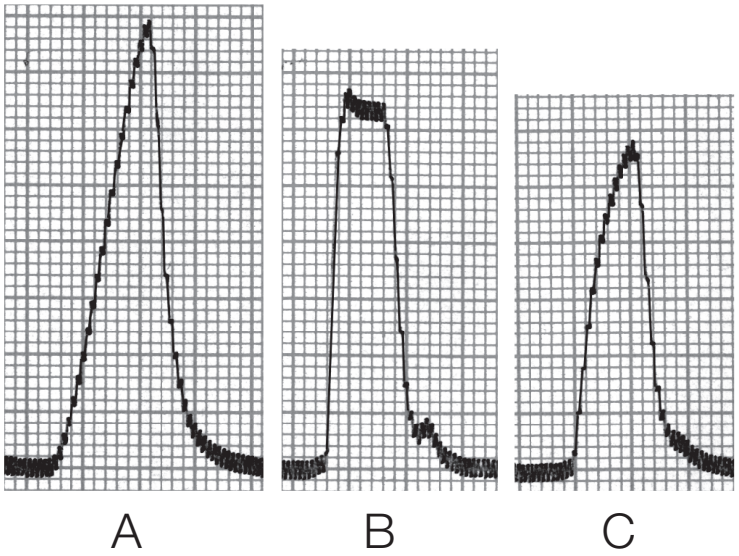

Figure 3.24: Delivery pressure vs. time profiles measured at animal with an in-line pressure transducer. (A) Mechanical ventilator. (B) Xenon delivery. (C) Xenon delivery with PFA needle valve in place. Horizontal scale is 40 ms per small division, vertical scale is 1 10^{-2} PSIG per small division.

have a high Q factor (typically greater than 100 unloaded). At the Larmor frequencies in this experiment, the attainable probe Q is limited by dielectric losses due the presence of the sample in the probe. We use two different coil geometries for our *in vivo* rat experiments depending on the region to be studied. Whole body experiments require sensitivity over a large volume of the subject, while experiments in more localized areas of interest (such as the head) can be effectively studied using smaller probes. The goals for all of the RF coils are RF homogeneity over the sample region and a design for which the subject or sample can be loaded easily into the coil.

The first "volume" probes we used were built on cylindrical acrylic forms. These had excellent RF homogeneity, but the task of squeezing an animal into the tight-fitting probe from the end while trying to maintain an airway connection proved extremely difficult. The volume coil geometry that proved to be useful for the whole-body experiments with rats is a split cylinder built on a glass form. This is a "clam shell" design; the bottom half of the probe is bolted to the experimental platform and the top half can be removed so that

the animal subject can be inserted. The electrical connections between the two halves are soldered once the animal is in place. The resonator circuit is a slotted resonator built in

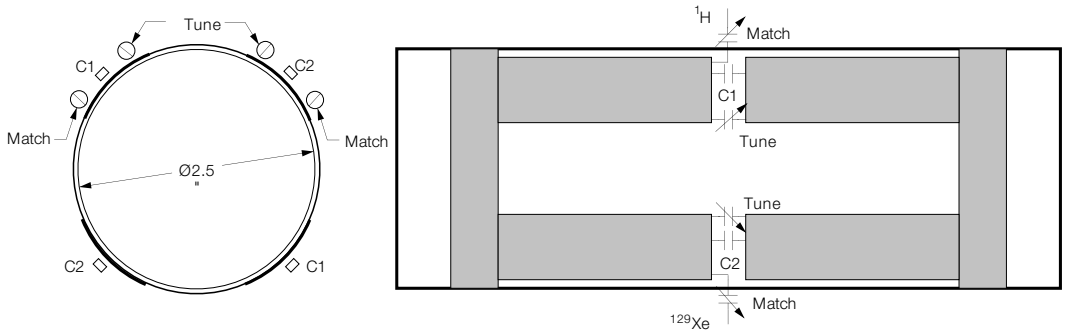

Figure 3.25: Dual tuned volume probe.

our lab (figure 3.25), based on the design by Alderman and Grant [81]. The volume coil has the advantage of high RF homogeneity, but because of it large size, it suffers from low filling factor (and consequently low SNR) if it is used to study regions where only a fraction of the total volume contributes to the detected signal. The sensitivity can be improved for small areas of interest with the use of surface coils, which have the advantage of a high filling factor and can be geometrically matched to the region of interest. A three-turn doubly-tuned ^{1}H-^{129}Xe "surface" coil with a 3.5 cm diameter was constructed (figure 3.26) and used for all of the *in vivo* head studies in this thesis. This single-coil double-resonance probe uses a variable length transmission line as one of the tuning elements, and is based on the design of Cross, et al. [82]. The sample coil is positioned between two cables of length $\lambda/4$ (where λ is the higher frequency wavelength in the cable). One of these is shorted at the far end, and one remains open. Detailed analysis of this probe construction is given by Cross, et al. [82].

Conventional NMR RF coil geometries, such as solenoidal and saddle-shaped coils, have a large size relative to the volume-of-interest under investigation. Surface coils, however, can be relatively small and placed adjacent to a larger object. Thus, the surface coil receiver can obtain a higher SNR than conventional coils and also has the advantage that its geometry can be designed to suit the object under study. Surface coils and volume coils

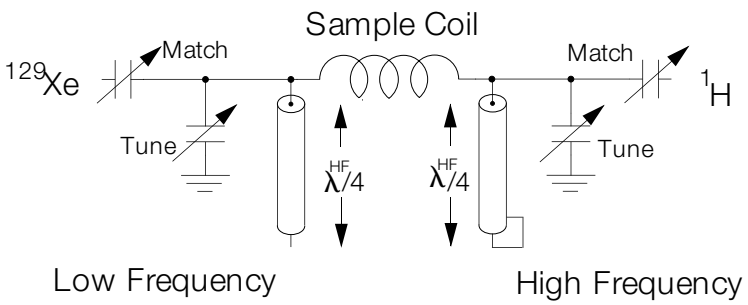

Figure 3.26: Doubly tuned single coil surface probe.

differ greatly in the RF field they generate. Volume coils generate, in principle, a homogeneous RF field over the region in which the sample is placed. Surface coils on the other hand produce a highly inhomogeneous RF field, where B_1 decreases with increasing distance from the coil. The inhomogeneity of the B_1 RF has major experimental implications since the coil is used not only as a signal receiver but also for RF pulse transmission. The tip angle generated by a conventional RF pulse is given by

$$\alpha(\boldsymbol{r}) = \gamma \int_0^T B_1(\boldsymbol{r}, t)dt \tag{3.14}$$

where $\alpha(\mathbf{r})$ is the tip angle at position $\boldsymbol{r}$, $\gamma B_1(\mathbf{r})$ is the RF field strength at position $\boldsymbol{r}$, and T is the RF pulse duration. The ^{129}Xe tip angle for several pulse durations and RF amplitudes is measured for each NMR probe with a glass vessel filled with polarized ^{129}Xe. The ^{129}Xe magnetization is repeatedly tipped by an unknown angle α, and the FID is detected from each pulse. The tip angle α is determined by fitting the NMR signal as a function of pulse number n to

$$S(n, \alpha) = M_0 sin\alpha (cos\alpha)^{n-1}. \tag{3.15}$$

The T_1 of ^{129}Xe in this vessel is approximately three hours, making it trivial to make measurements on a time scale fast with respect to T_1; typically 16–64 pulses with a total acquisition time of less then 1 minute. For the homogeneous volume probes, α determined in this way is an average of the relatively uniform tip angle throughout the probe. For the surface coil, a magnetic gradient is applied in the direction normal to the coil to encode the

spatial dependence of the tip angle and to determine the mean tip angle in the region containing the sample.

RF pulses based on adiabatic spin rotation [83-86] have also been developed and are part of a class of pulses known as BIR ($\mathbf{B}_1$ **I**nsensitive **R**otation). These adiabatic pulses generate a uniform tip angle from a surface coil despite spatial variations in B_1 (even over two orders of magnitude), provided that the B_1 field is above a threshold value. With BIR pulses, the high sensitivity of surface coil receivers is be combined with uniform sample excitation. These adiabatic pulses have the additional advantage that they eliminate the calibration of RF power between experiments. BIR pulses were investigated late into the studies in this thesis and likely applications are to be discussed in Chapter 5.

3.7.2 *In vivo* performance

The overall performance of the delivery system is illustrated in figure 3.27. The magnitude of the ^{129}Xe NMR signal from the lungs of a live rat ventilated for over 1 minute with 60% xenon and 40% O_2. The Xe/O_2 mixture was delivered in 2.2 cc breaths at 80 breaths per minute. The rat was located on the experimental platform at the center of the magnet. A surface coil tuned to the ^{129}Xe gas resonance was placed on the thorax of the animal. The ^{129}Xe signal saturates and can be maintained for extended times with continued inhalation of polarized ^{129}Xe. This constant input magnetization is essential for ^{129}Xe magnetic tracer studies, and we have performed *in vivo* studies with 1:1 Xe/O_2 mixture for run times exceeding 4 minutes with similar results.

3.8 Optimization and Operation

Optimization of the OPSE parameters for many types of experiments that use polarized gases is straight-forward: either the noble gas polarization or the magnetization (*i.e.*, the product of polarization and volume) is maximized, depending on the details of the experiment. Laser-polarized nuclear targets [1, 2, 67, 68], neutron spin filters [3, 41], magnetometers [4, 5], and masers [6-8, 66] are all closed systems with the experiment performed in their sealed OPSE cells. These cells are typically pumped up and run at their steady-state polarization for the duration of the experiment.

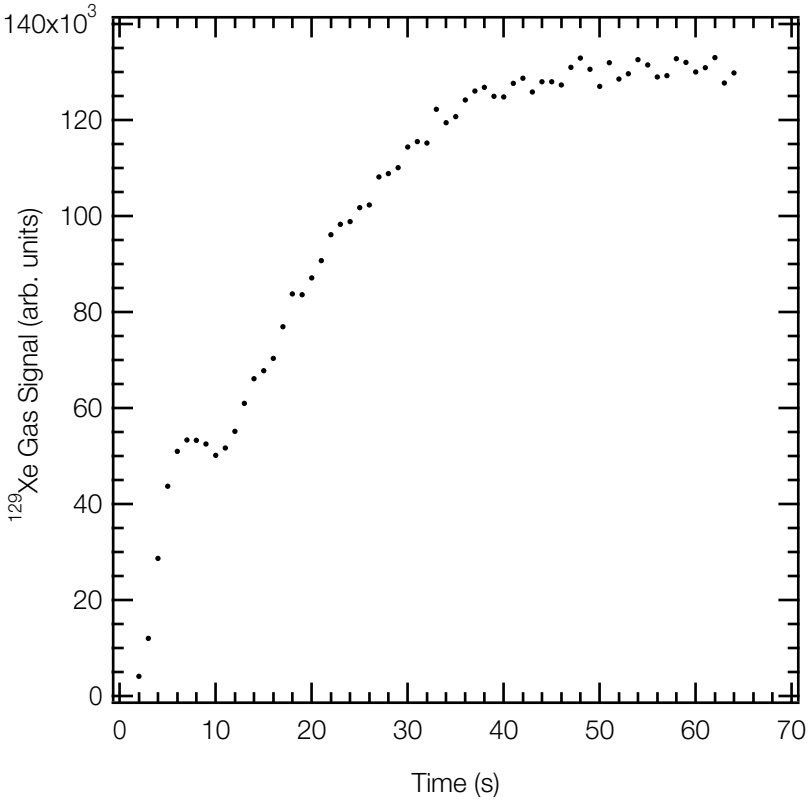

Figure 3.27: Magnitude of ^{129}Xe gas spectrum vs. time acquired from a surface coil placed on the rat thorax. Spectra were acquired every 500 ms. NMR acquisition was triggered by delivery valve P_2. The ^{129}Xe polarization was approximately 4% in this experiment.

A somewhat different approach is required when there is an animal connected to the output of the polarizer. The final ^{129}Xe polarization in spin-exchange optical-pumping is a compromise between the production volume and the polarization rate. A small amount of gas polarized at low rate of production to a very high polarization (*e.g.*, 50 cc atm at 50% polarization in 1 day) has very little practical use in steady-state *in vivo* tissue imaging experiments, where typical tissue saturation times are on the order of 30 seconds and 100 cc atm are used per minute of rodent ventilation time. Additionally, NMR spectroscopy and imaging sequences take time. In particular, the optimal NMR pulse repetition time (TR) for a given pulse sequence depends on the tissue perfusion rate, so for many types of *in vivo* experiments the total experimental duration, and consequently the amount of polarized xenon needed, is fixed by the choice of NMR sequence and basic physiology. The highest obtainable polarization of this fixed amount of xenon provides the maximum

SNR.

An additional constraint on *in vivo* polarizer operation is the need to perform as many experiments as feasible in an imaging day (which is limited by the achievable duration of rodent anesthesia—8 or 9 hours). Additionally, cell filling and gas handling valves are manually operated, so polarizer cycle times need to be physically realizable. We have found that four polarizer cycles, roughly 550 cc of gas and corresponding to more than 4 minutes of ventilation, is a good amount per "run". Each in vivo run may consist of several ^{129}Xe spectroscopy or imaging experiments. Cycling the polarizer every 5 minutes and accumulating xenon for four cycles also allows enough time to acquire ^{1}H images between ^{129}Xe experiments. Our operational approach is to maximize the polarization of this volume of gas in the minimum time possible. This is the principle that guides polarizer optimization for this experiment, and is now described in the context of polarizer operation.

After a polarizing time Δt, the ^{129}Xe polarization in the OPSE cell is (from equation 2.20)

$$P_{\mathrm{Xe}}(\Delta t) \;=\; P_{\mathrm{Xe}}^{\infty}\left(1 - e^{\frac{-\Delta t}{T_{spinup}}}\right). \tag{3.16}$$

After N accumulation cycles (i.e., a total time of $N\Delta t$), the polarization of the ^{129}Xe ice is

$$P_{final}(N \cdot \Delta t) \;=\; \frac{1}{N}\sum_{m\,=\,1}^{N} P_{\mathrm{Xe}}(\Delta t)e^{\frac{-\Delta t(m\,-\,1)}{T_1^{ice}}}. \tag{3.17}$$

The final polarization of the ^{129}Xe for a desired volume is maximized by appropriate choice of P_{Xe}^{∞}, T_{spinup}, and Δt. P_{Xe}^{∞} is computed using the numerical integration method described in section 2.3 over a range of Xe pressure and cell temperature (T) for a given cell geometry and laser spectral profile. The optimal values for the parameters T and Δt are then found by maximizing P_{final}, the maximum attainable ^{129}Xe polarization. In our experiments, the polarizer cell is filled with 1700 Torr of Xe, resulting in 148 cc-atm of Xe polarized per cycle. If a small volume of polarized Xe is desired, the total number (N) of polarization cycles needed is small, and the loss of ^{129}Xe polarization due to T_1^{ice} is negligible since the total accumulation time $\mathrm{N}\Delta t \ll T_1^{ice}$. In this case, $\mathrm{P}_{\mathrm{final}}$ is optimized with a longer pumping time, Δt.

Large volumes of ^{129}Xe require many OPSE production cycles, which results in a longer total accumulation time, $N\Delta t$. As a result, individual batches of polarized ^{129}Xe may spend a significant fraction of T_1^{ice} in the frozen state. In order to prevent large polarization losses due to T_1^{ice}, the cycle time Δt must decrease. A sufficient increase in γ_{SE} is achieved with a corresponding increase in OPSE cell temperature.

Calculations of P_{final} as a function of Δt, for several values of N, are shown in figure 3.28. As in section 3.1.5, calculations of P_{final} agree with experiment to better than a factor

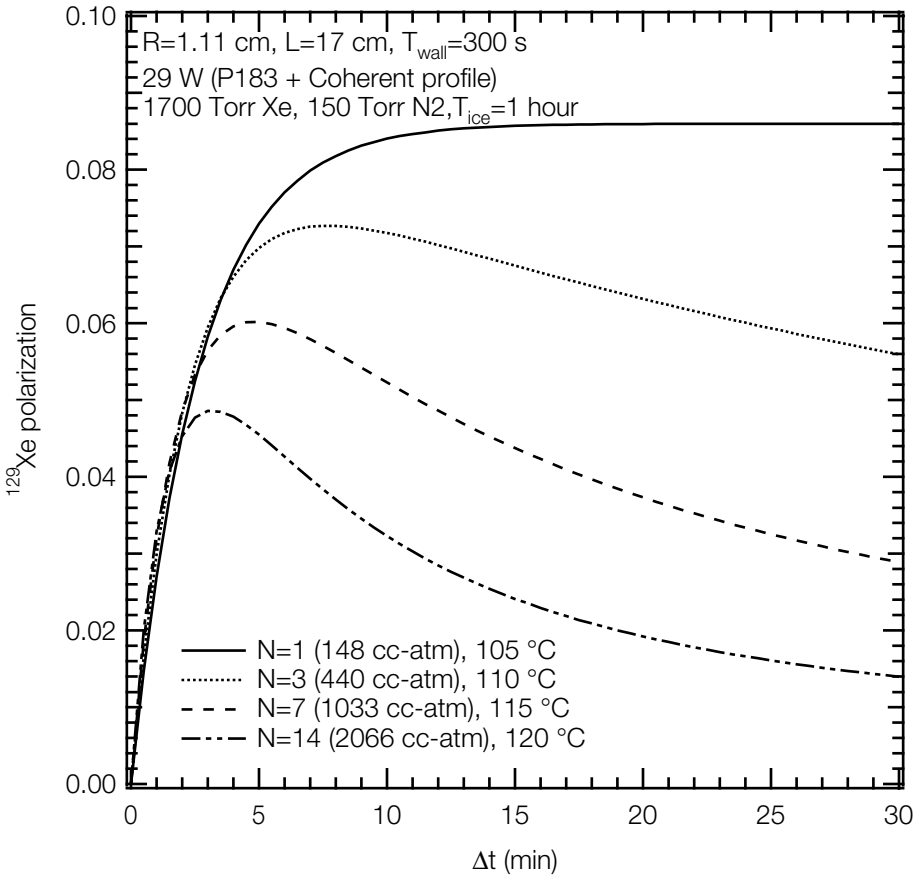

Figure 3.28: Calculation of P_{final}, the polarization of frozen ^{129}Xe after N accumulation cycles, as a function of polarizer cycle time, Δt. The total accumulation time is $N\Delta t$, and 148 cc-atm of xenon is polarized each cycle. Note that the Δt for which P_{final} is maximal decreases with increasing N. The cell temperature, T, indicated for each curve has been chosen to maximize P_{final}. This optimum T for each curve also increases with N.

of 2, and are typically a of factor 1.4 greater than the calibrated ^{129}Xe polarization measurements.

From figure 3.28, the rate at which polarized ^{129}Xe is produced depends on the desired final polarization. The final polarization and production rate for the most common polarizer operational configurations is now given. All of these measurements were made with Cell 5, using one Optopower LDA (P183) and one Coherent LDA providing an estimated 29 W into the cell. A single ($N = 1$) batch, polarized (at 100 °C) for $\Delta t = 5$ minutes results in 148 cc-atm of xenon at 5.3% polarization. As above, this polarization measured with the "Big Rig," and is a lower limit of the ^{129}Xe polarization in the OPSE cell.

A 1:1 Xe/O_2 mixture for *in vivo* ventilation of rats requires roughly 100 cc of polarized Xe per minute of ventilation time, and our NMR spectroscopy and imaging experiments typically last 2–4 minutes. Thus for most all of the *in vivo* experiments, the system is operated for $N = 3$ cycles, with cycle time $\Delta t = 5$ min. This results in 440 cc-atm of Xe polarized to a measured final polarization of 4.5%. In practice, the system cycle time is longer than the 5 minute batch polarization time, since the manual operation of the valves associated with the OPSE cell adds typically about 50 seconds per batch. Modifications could be made so that OPSE cell valves are fully automated thus minimizing this delay. Nevertheless, in its current configuration, 440 cc-atm of Xe are produced in approximately 17.5 minutes to roughly 4.5 % polarization. Although impractical for rodent experiments, $N = 7$ was tried as an measure of overall system production. With a cycle time $\Delta t = 5$ minutes and the cell at 115 °C, 1033 cc-atm of xenon was polarized to 3.8% in roughly 45 minutes.

Chapter 4

Distribution and dynamics of laser-polarized ^{129}Xe magnetization *in vivo*

This chapter presents NMR and MRI studies of laser-polarized ^{129}Xe in living rats. When we began this research many of the critical NMR parameters were entirely unknown, such as the *in vivo* ^{129}Xe relaxation times in blood and tissue. These studies demonstrate that inhaled laser-polarized ^{129}Xe magnetization delivered by inhalation survives transport from the lungs to the more distant organs where ^{129}Xe NMR signals can be observed. The results of this work include the observation, assignment, and dynamic measurement of ^{129}Xe resonances in the brain and body, the first chemical-shift-resolved images of ^{129}Xe in blood, tissue, and gas in the thorax, and the first images of ^{129}Xe in the brain [25, 28, 87, 88].

This chapter compiles our *in vivo* results, emphasizing those essential to evaluate the feasibility of a laser-polarized ^{129}Xe magnetic resonance tracer method for the measurement of tissue perfusion *in vivo*. We hypothesize the biological origin of several *in vivo* ^{129}Xe resonances and support these assignments based on analysis of *in vivo* ^{129}Xe resonance spectroscopy, dynamic uptake, and spatial localization.

4.1 General Experimental Details

This section describes the general experimental details common to all of the *in vivo* ^{129}Xe magnetic resonance experiments described in this thesis, including animal handling and positioning. These experiments were performed on a Omega CSI spectrometer manufac-

tured by General Electric (Fremont, CA) interfaced to a 2.0 T Oxford magnet (17 cm diameter horizontal bore) equipped with self-shielded gradients. All of the *in vivo* experiments in this work are performed with 200–600 gram Sprague-Dawley rats, a purebred strain of *Rattus norvegicus*. All animal procedures were performed under a protocol approved by the University Committee on the Use and Care of Animals (UCUCA), and approximately 25 animals were used during the course of this research. Rats are anesthetized initially with an intraperitoneal injection (0.75 cc/kg body weight) of a ketamine/ xylazine mixture (57 mg/mL ketamine, 8.5 mg/mL xylazine). A 2 inch, 14 or 16 gauge endotracheal tube is placed by trachiostomy and anchored with suture. The endotracheal tube is a two inch Teflon Angiocath I.V. catheter (Becton Dickinson Vascular Access, Sandy, Utah). Rats are ventilated with a small animal ventilator (Harvard Apparatus, South Natick, MA) at 80 breaths per minute with 2.5 cc per breath of either pure O_2 or a mixture of 95% O_2/5% CO_2. Anesthesia is maintained with Halothane (0.5–1.5%) using a calibrated vaporizer (Fluotec, NY). Pulse rate and O_2 saturation is continuously monitored with a pulse oximeter (Nonin, Plymouth MN) via a photo transducer pair wrapped around the tail. Halothane levels are adjusted to keep the cardiac rate typically 200 BPM, although this rate depends on the size of the animal and is adjusted accordingly. Body temperature is maintained by a 37 °C warm water blanket beneath the animal. The rat is placed supine on the experimental platform (see figure 3.23) and, depending on the region of interest, either inside the doubly-tuned ^{1}H-^{129}Xe volume probe or with the top of the head resting in the center of the doubly-tuned surface coil. The platform assembly is placed into the magnet for NMR study, and mated to the output of the polarizer. ^{129}Xe is polarized, stored, and delivered to the animal as described in section 3.6, for between 32 seconds and 4 minutes. The xenon fraction is typically 35–60% of the delivered breathing mixture (although 100% xenon was used in our earliest brain work [25]). NMR pulsing and signal acquisition is cardiac gated for thoracic studies, *i.e.,* at the same point in the rodent cardiac cycle.) After xenon delivery and study, the animal is switched back to normal ventilation, and proton imaging performed. The spectrometer is switched between ^{129}Xe NMR/MRI and ^{1}H imaging many times throughout the study, typically every 20–25 minutes. Following study, the animal is euthanized either through hypercapnia or with an overdose of pentobarbitol. A typical *in vivo* study lasts 8 hours.

4.2 *In Vivo* ^{129}Xe Spectroscopy

NMR spectroscopy of noble gases has a long history, with the first NMR signals from ^{129}Xe and ^{131}Xe detected in 1951 [89]. Of the nine stable xenon isotopes only ^{129}Xe and ^{131}Xe have non-zero nuclear spin. Of these ^{129}Xe is the most widely studied by NMR spectroscopy. ^{129}Xe is a spin 1/2 nucleus with gyromagnetic ratio $\gamma = -7.3995\ 10^7$ rad $T^{-1}s^{-1}$ and a relatively high natural abundance of 26.44 %. The lack of a quadrupole moment in ^{129}Xe contributes to extremely long longitudinal spin relaxations times (T_1), facilitating *in vivo* use. Xenon is highly soluble in blood with an Ostwald coefficient[1] ~ 0.17 [90], and more so in lipids [18, 90-93], and once in the body accumulates in highly-perfused lipid-rich tissue. The large, polarizable xenon electron cloud makes ^{129}Xe sensitive to its local environment, and results in the very large chemical shift range (several hundred ppm) observed in ^{129}Xe spectroscopy [94, 95]. These chemical shifts strongly depend on the structure of the medium and as a result ^{129}Xe NMR has been used to study polymers, porous media, microporous membranes, liquid crystals, zeolites, and surfaces [96-109].

Spectroscopic studies were the first experiments we performed in order to determine the feasibility of *in vivo* ^{129}Xe NMR and to evaluate the range of chemical shifts *in vivo*. Once a laser-polarized ^{129}Xe gas mixture is inhaled, it fills the airspaces of the lungs and is carried to tissue where it accumulates. A major challenge is the efficient delivery of ^{129}Xe magnetization to blood from the lungs, and to tissue by the circulation. The ^{129}Xe longitudinal relaxation time (T_1) of ^{129}Xe in blood determines the loss of polarization during transit from the lungs to the tissue of interest. Therefore, the signal from ^{129}Xe in tissue depends critically on ^{129}Xe T_1 in blood. The T_1 of ^{129}Xe in blood and other tissues was unknown at the beginning of our research and *in vivo* measurement presented many experimental challenges—in fact, *in vitro* measurement of the ^{129}Xe blood T_1 and its dependence on blood oxygenation level still remain uncertain [24, 110-113]. We instead took the approach of direct investigating of the *in vivo* transport of ^{129}Xe magnetization with NMR spectroscopy. These studies demonstrated that the ^{129}Xe blood T_1 was sufficiently long for *in vivo* ^{129}Xe NMR studies, and paved the way for the our more detailed

1.The Ostwald solubility coefficient is the ratio of the volume of gas at 1 atm that can be dissolved in a unit volume of liquid to the total volume of gas.

time- and spatially-resolved studies.

4.2.1 Whole body spectroscopy

The potential for magnetic resonance studies with dissolved-phase ^{129}Xe was explored through *in vivo* ^{129}Xe spectroscopy experiments using the NMR "volume" probe described in detail in section 3.7.1. This large cylindrical antenna (14.5 cm long and 6.0 cm diameter) encompasses the entire rat body. The detected ^{129}Xe signal in these experiments comes from the distribution of ^{129}Xe magnetization excited throughout the entire sensitive volume of the RF coil, *i.e.*, the entire rat body. Spectroscopy was performed using a broadband 10 μs RF pulse with an estimated 13° tip angle (averaged over the probe volume). The spectrometer spectral width was set to 10 kHz in order to span both the gas and tissue-dissolved ^{129}Xe spectral regions. After each RF pulse, free-induction decay (FID) signals (1024 data points) were collected in 350 ms. The RF pulse repetition time (TR) was determined by the cardiac signal measured with the pulse oximeter, and for these experiments the cardiac rate was 280 BPM, thus resulting in a 428 ms TR. Each FID in the final dataset is the sum of two phase-cycled[1] acquisitions, and the effective TR is 856 ms.

The time-domain data was processed by multiplication with a 20 Hz exponential filter, a process commonly known as "line-broadening." Line broadening efficiently reduces the noise amplitude in the frequency domain, provided the time constant of the filter is matched to the effective FID decay time (*i.e.*, T_2^*) [12]. The time-domain data was then Fourier transformed and phased.

Three datasets were acquired from a single animal during 40 seconds of Xe/O_2 (1:1) inhalation, with roughly 5% ^{129}Xe polarization. Each dataset was processed as described above, and then summed over time. The three summed spectra were averaged together. The *in vivo* NMR spectrum of laser-polarized ^{129}Xe in the rat body obtained from this procedure is shown in figure 4.1.

The spectrum of figure 4.1 reveals an important feature of *in vivo* ^{129}Xe spectroscopy; the chemical shift of xenon is very dependent on its biological environment. Relative to

1.The phase of the NMR signal depends on the RF pulse phase, and change of the RF phase by 180° results in signal inversion. The subtraction of two phase-cycled signals results in the coherent superposition of successive FIDs while reducing the background noise and elimination of DC offsets.

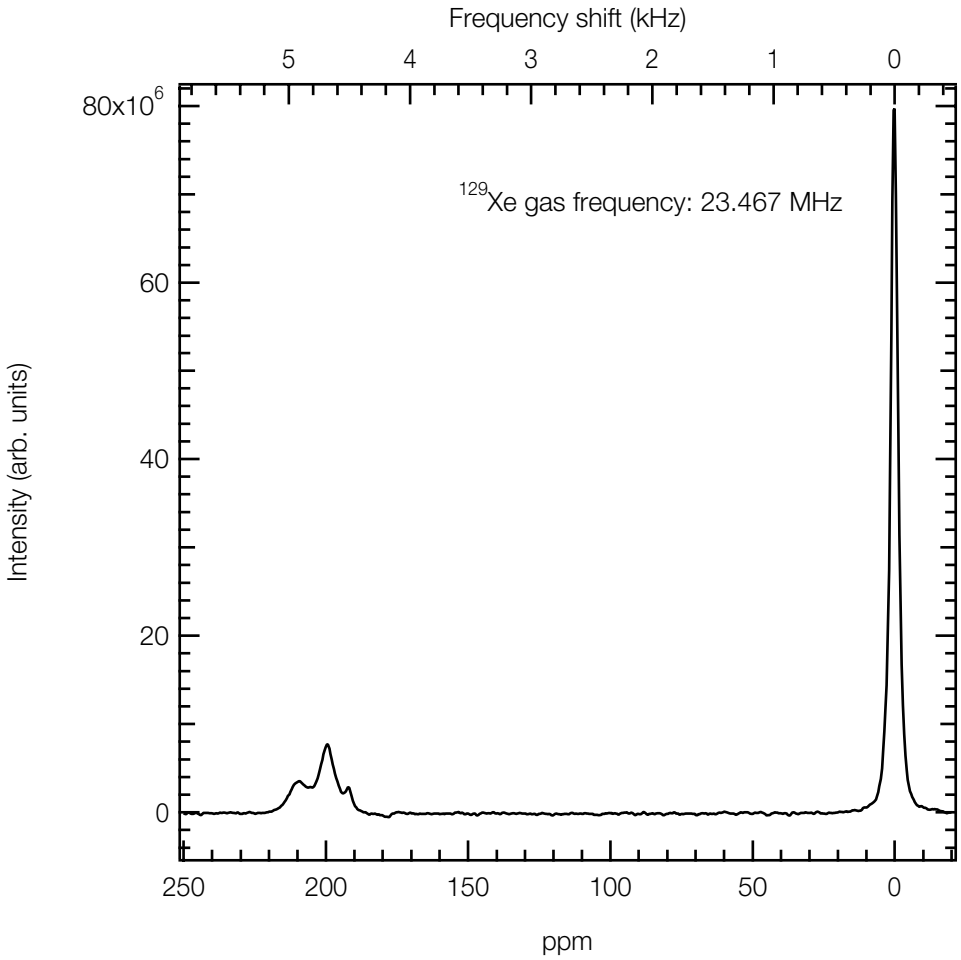

Figure 4.1: *In vivo* NMR spectrum of ^{129}Xe in the rat body acquired at 2 T. The spectrum shows chemical shift peaks indicative of ^{129}Xe dissolved in blood, tissue and fat at 209, 198, and 191 ppm, respectively. The gas resonance is set to 0 ppm. The tip angle used to acquire this spectrum was 13°, sufficiently small to allow ^{129}Xe magnetization to accumulate in tissue and fat compartments reached by blood flow. The RF pulse width was 10 μs, and TR = 428 ms. The ^{129}Xe polarization was roughly 5%. Resonance assignments are discussed in the text.

the ^{129}Xe gas resonance set to 0 ppm, three other ^{129}Xe resonances are observed 190–210 ppm away. These lie in the range of the typical "solvent" chemical shifts for solution phase ^{129}Xe in biological fluids (*c.f.*, 196, 198, and 200.6 for ^{129}Xe in water, olive oil, and egg lecithin, respectively [94, 114]), and we will refer to them as dissolved-phase ^{129}Xe resonances.

In order to understand the origin of the dissolved-phase ^{129}Xe resonances, a second *in*

vivo was spectrum was acquired with the RF pulse duration increased to 200 μs and the pulse frequency moved to center it about the solution-phase frequency. Under these conditions, this narrow-band excitation RF pulse has little power at the gas resonance frequency, which minimizes the destruction of longitudinal gas phase ^{129}Xe magnetization due to repeated RF pulsing. Polarized ^{129}Xe gas in the lungs is the source for ^{129}Xe magnetization in the body, and in general the destruction of longitudinal gas magnetization by NMR pulsing should be minimized if study of solution-phase signals is the primary interest. The tip angle for this experiment was measured to be roughly 30° for the dissolved-phase resonances and estimated to be approximately 1° for the ^{129}Xe gas. A dataset of 64 spectra were acquired from a single experiment acquired during about 25 seconds of Xe/O_2 (1:1) delivery, and the individual spectra were processed as above. The time-averaged spectrum is shown in figure 4.2.

A least-squares fit of the sum of four independent Lorentzians (with a common baseline) to the spectrum of figure 4.2 was performed. The chemical shifts and widths (FWHM), obtained from the fit are given in table 4.1. Support for the biological assignments of the *in vivo* ^{129}Xe resonances will be given throughout this chapter, it will be shown that the ^{129}Xe NMR resonances of figure 4.1 and figure 4.2 are consistent with ^{129}Xe gas (0 ppm), and ^{129}Xe dissolved in blood (209 ppm), tissue (198 ppm), and fat (191 ppm). For clarity, these ^{129}Xe resonances will be referred to by their assignment. The effective T_2^* for each resonance was determined by the FWHM (Γ) of the individual Lorentzian fit,

$$T_2^* = \frac{1}{\pi\Gamma}, \tag{4.1}$$

and is approximately 2 ms for ^{129}Xe dissolved in blood and in tissue, 7 ms for ^{129}Xe dissolved in fat, and 5 ms for ^{129}Xe gas in the lungs.

The differences in the relative intensities of the dissolved-phase ^{129}Xe resonances in figure 4.1 and figure 4.2 are a consequence of the tip angle used to acquire them. The ^{129}Xe magnetization in blood arises from very rapid exchange with alveolar gas and in general, increased sampling of the blood resonance will result in an increased signal. This is quite different from the behavior of ^{129}Xe magnetization in compartments which are reached by

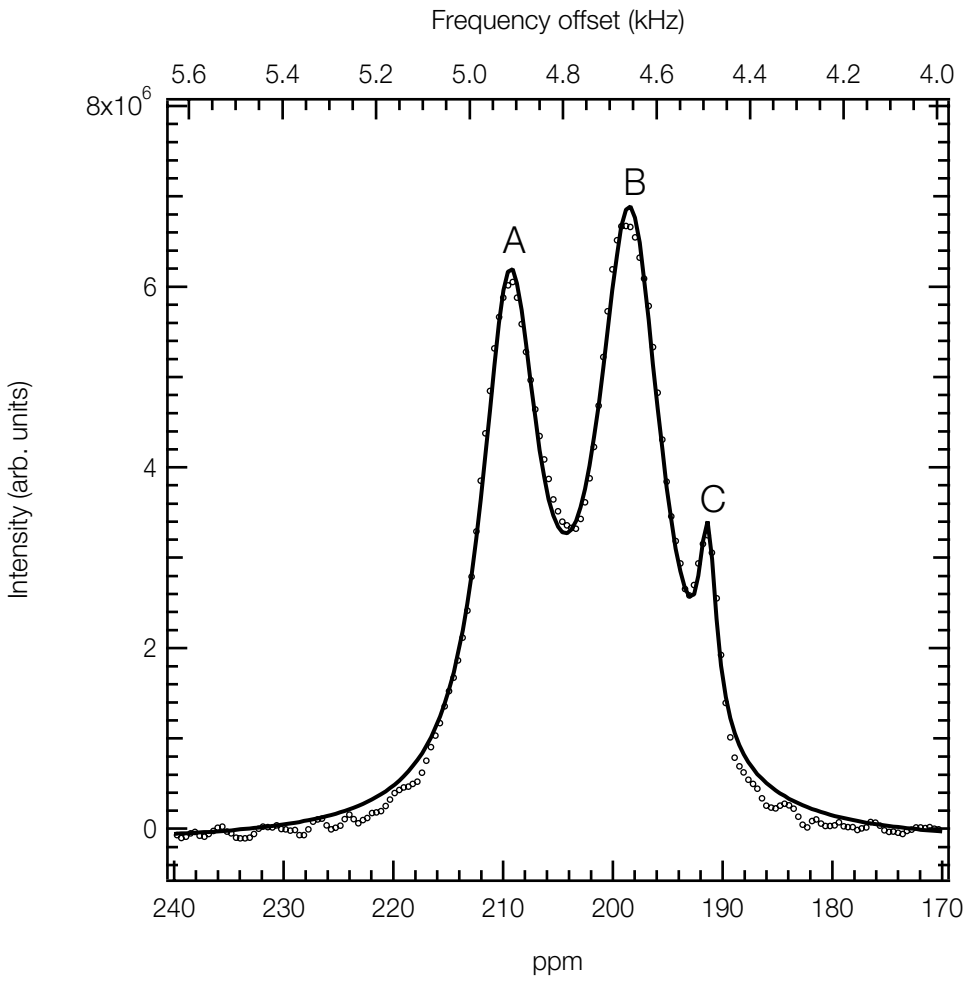

Figure 4.2: *In vivo* NMR spectrum of ^{129}Xe in the rat body at 2 T acquired from a single experiment of about 25 seconds delivery. For clarity, the gas resonance at 0 ppm (peak "D") is not shown. The solid curve is the result of a least-squares fit to the sum of four independent Lorentzians with a common baseline. The tip angle used to acquire this spectrum was nominally 30° for the dissolved-phase resonances and estimated to be 1° for gas. The RF pulse width was 200 μs, and TR = 428 ms.

blood flow, such as tissue and fat in the body, and is an important property of dissolved-phase ^{129}Xe magnetization *in vivo*: the relative intensities of ^{129}Xe magnetization in blood and in perfused tissue depend on the rate of perfusion to, and destruction in, these biological compartments. The choice of NMR tip angle and sampling rate has critical consequences for the dissolved-phase sensitivity of *in vivo* ^{129}Xe NMR. The 30° tip angle used to acquire the spectrum of figure 4.2 samples longitudinal ^{129}Xe-blood magnetization at a

	A	B	C	D
Chemical shift (ppm)	209.3±0.02	198.35±0.02	191.24±0.03	0
Width (ppm)	6.33±0.08	7.28±0.09	1.9±0.1	2.59±0.03
Width (Hz)	150±1.9	173±2.3	45±2.75	61±1
T_2^* (ms)	2.1±0.03	1.8±0.02	7.1±0.4	5.2±0.1
Assignment	Blood	Tissue	Fat	Gas

Table 4.1: NMR parameters extracted from the fit to the body spectrum of figure 4.2. Assignments are discussed in the text.

higher rate than the 13° tip angle used in the experiment of figure 4.1. As a result, ^{129}Xe-blood magnetization leaving the pulmonary vein and pumped through the body by the left heart is reduced, as compared to the 13° spectrum of figure 4.1. Consequently, we would expect a resonance arising from ^{129}Xe in tissue to be relatively smaller in the 30° experiment, and the blood resonance to be correspondingly larger. This analysis is consistent with the assignment of the ^{129}Xe resonances given in table 4.1.

We conclude this section with a comment about magnetic resonance of laser-polarized ^{129}Xe *in vivo*. In general, every excitation pulse destroys some of the laser-polarized ^{129}Xe longitudinal magnetization, which cannot be restored by allowing relaxation back to thermal equilibrium as in conventional NMR. Laser-polarized ^{129}Xe magnetization is only replenished by the delivery of additional polarized gas to the sample or *in vivo* region. This "non-renewable" polarization means that acquisition pulses must generally have small tip angles to avoid destroying all the *in vivo* polarization in a single shot, and consideration is required when designing pulse sequences. The non-renewable nature of laser-polarized ^{129}Xe polarization does provide a unique feature: ^{129}Xe magnetization *in vivo* can be locally "turned off" at will by RF pulse destruction, and a potential application of this is discussed in Chapter 5.

4.3 Dynamic Uptake of ^{129}Xe Magnetization

This section describes the NMR measurement of the time-dependence of the various chemical shift components of ^{129}Xe observed *in vivo*. Study of the *in vivo* dynamics of ^{129}Xe magnetization is a further guide to the biological compartments from which the

chemical-shifts originate, and is essential for the development of new imaging methods that measure tissue perfusion with laser-polarized ^{129}Xe.

In vivo uptake ^{129}Xe magnetization begins with delivery of polarized ^{129}Xe gas by inhalation, and is followed by transport and buildup of the ^{129}Xe in the blood stream and perfused tissues. Lung capillary blood rapidly equilibrates with alveolar gases and as a result, arterial blood is expected to attain maximum ^{129}Xe signal intensity rapidly. The ^{129}Xe signal from perfused tissue is initially zero, so the time-dependent distribution patterns and buildup rates of ^{129}Xe intensity directly reflect the local relaxation and perfusion rates, local xenon solubility, and the efficiency of magnetization exchange between different compartments (*i.e.*, between gas/blood, blood/tissue, and tissue/fat). Similar dynamics between resonances imply fast exchange in contiguous compartments. Conversely, since differential buildup of ^{129}Xe in intracellular compartments on the scale of seconds is unlikely, ^{129}Xe resonances with different time evolution are likely due to ^{129}Xe residing in different anatomical compartments, and possibly separate organs.

4.3.1 Time evolution of whole body spectra

A series of 64 cardiac-gated spectra were acquired with two phase-cycled averages each (*i.e.,* 128 pulses total). The NMR parameters are as in the time-averaged spectrum of figure 4.2. Delivery of the Xe/O_2 (1:1) mixture began at approximately t = 5 s, and continued to t = 30 s during the acquisition. For each of the 64 spectra, the amplitude of each of the resonances was determined by a least-squares fit to a sum of 4 independent Lorentzians with a common baseline, with the frequency and width of each Lorentzian fixed to the values obtained given in table 4.1. The uptake and washout of the amplitudes of the observed ^{129}Xe resonances in the rat body are shown in figure 4.3 and figure 4.4.

Analysis of the combined dynamics of ^{129}Xe gas/blood magnetization in figure 4.3 indicates that ^{129}Xe blood magnetization is proportional to ^{129}Xe gas magnetization (which is dominated by gas in the lung). Xenon is known to rapidly penetrate the alveolar epithelium [115], so the two compartments rapidly equilibrate. The dynamics of end-tidal gas thus mirror those of arterial blood, suggesting exchange between the gas and blood components in the lung that is fast on the experimental time scale of the signal acquisition period of 428 ms. On the basis of its rapid buildup (*i.e.*, with no discernible time lag with

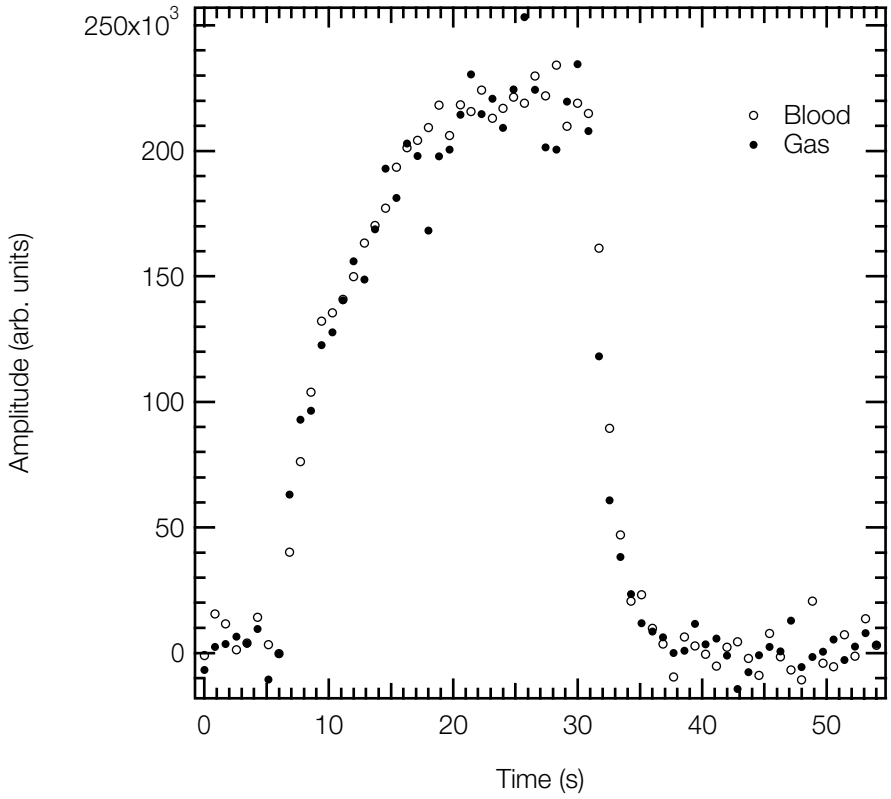

Figure 4.3: Dynamics of ^{129}Xe magnetization *in vivo*: the uptake and washout of ^{129}Xe gas and ^{129}Xe dissolved in blood (209 ppm). The gas resonance amplitude is normalized to the maximum intensity of the blood resonance for comparison. Delivery of the Xe:O_2 (1:1) mixture started at approximately t = 5 s and continued to t = 30 s. Note at 30 s the introduction of additional O_2 leads to a shorter wash-out time constant. The tip angle was 30°, TR was 428 ms, and each spectrum was obtained with two phase-cycled averages.

respect to the gas signal), the most likely location of the 209 ppm ^{129}Xe-blood peak is in the freshly-perfused lung capillary blood and the adjacent pulmonary veins and left heart.

Whereas the blood signal reaches steady-state within about 13 seconds of gas delivery, steady-state is not achieved for either the ^{129}Xe-tissue (198 ppm) or the ^{129}Xe-fat (191 ppm) signal (figure 4.4).

Resonances showing very dissimilar time evolution are likely due to ^{129}Xe residing in distinct anatomical structures, as chemical exchange and diffusion make differential buildup in intracellular compartments on the time scale of seconds very unlikely. Highly-perfused, lipid-rich organs such as the brain, the kidneys, and the heart have a high capac-

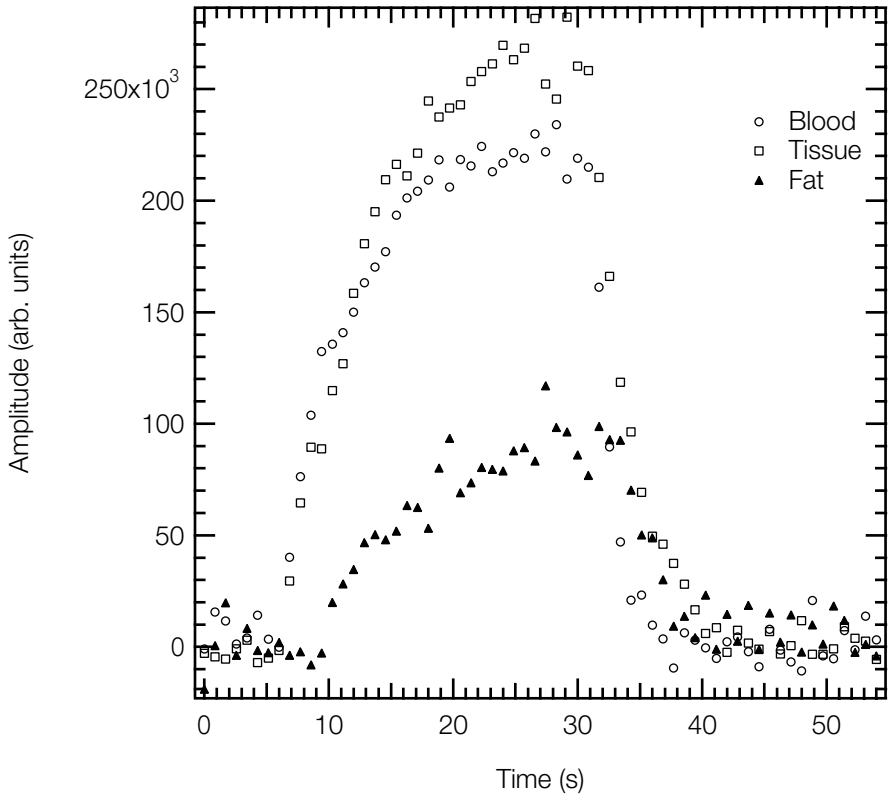

Figure 4.4: Dynamics of ^{129}Xe magnetization *in vivo*: the uptake and washout of ^{129}Xe dissolved in blood (209 ppm), tissue (198 ppm), and fat (191 ppm). Delivery of the Xe:O_2 (1:1) mixture started at approximately t = 5 s and continued to t = 30 s. NMR parameters are the same as in figure 4.3.

ity for dissolved xenon both because of their blood-tissue partition coefficients (table 4.2) and their large organ mass relative to the mass of blood perfusing them (*i.e.*, vascularization that is a small fraction of the total organ mass). Therefore, we conclude that the slow buildup observed is due to this greater distal-organ capacity for xenon and a long intrinsic ^{129}Xe-tissue T_1. The uptake and washout rates of ^{129}Xe in fat are slower than the uptake and washout of ^{129}Xe in tissue, consistent with a both a lower perfusion rate and higher xenon solubility in fat compared to typical tissue.

The uptake and washout rates observed in NMR experiments with laser-polarized ^{129}Xe are affected by the details of the NMR sampling, and are not entirely intrinsic properties of the biological system being studied. This is discussed in more detail in Chapter 5. Nevertheless, important qualitative conclusions can nevertheless be drawn from ^{129}Xe

dynamics *in vivo*.

In order to study the buildup of ^{129}Xe magnetization in compartments where destruction by NMR sampling would not allow significant dissolved-phase magnetization to accumulate, three spectra obtained with 13° tip angle were studied during an experiment of 17 seconds of xenon delivery uptake. The spectra in figure 4.5 spectra were acquired four sec-

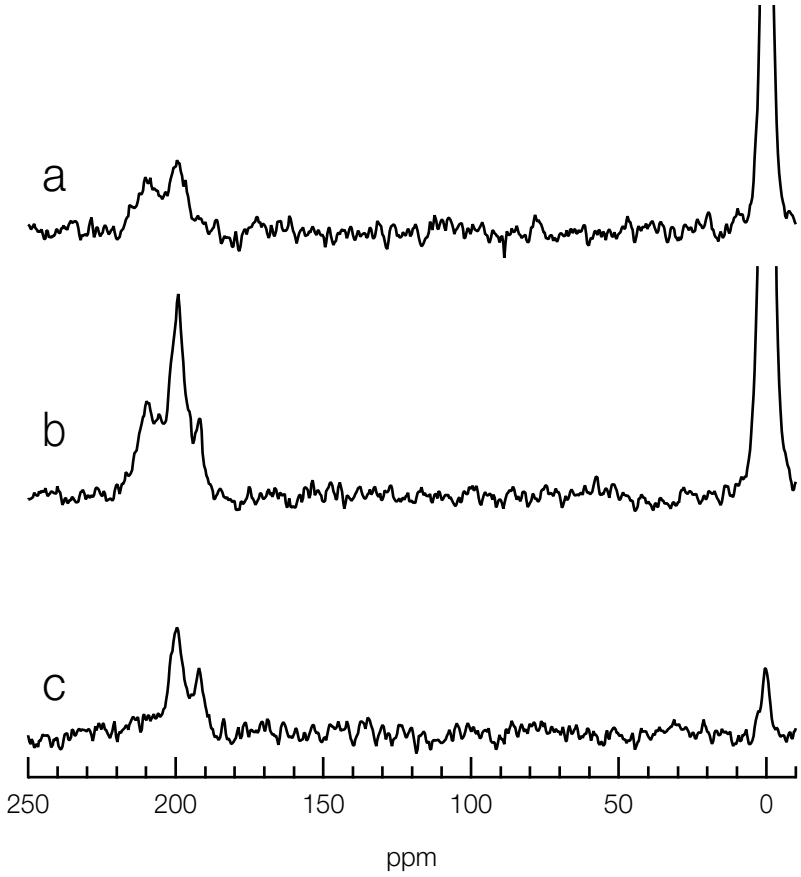

Figure 4.5: Individual ^{129}Xe spectra obtained from the rat body (**a**) 4 seconds after the start of xenon delivery, (**b**) 3 seconds after the end of Xe delivery, and (**c**) 7 seconds after the end of xenon delivery. The tip angle was 13°, and NMR parameters the same as in figure 4.1. All spectra are plotted with the same vertical scale, and were obtained with two phase-cycled averages each.

onds after the start of xenon delivery (figure 4.5**a**), and three seconds (figure 4.5**b**) and seven seconds (figure 4.5**c**) after the end of xenon delivery. These spectra help to clarify the

assignment of the blood and tissue resonances.

Near the beginning of xenon delivery (figure 4.5**a**), ^{129}Xe resonances in gas, tissue, and blood are all present. Xenon rapidly penetrates the alveolar epithelium [115], and the lung perfusion rate is extremely high (43 mL g^{-1} min^{-1} [116]), and as a result a steady-state is rapidly reached between the blood resonance and gas resonance. Consequently, one would not expect to see a large ^{129}Xe-gas resonance without a corresponding ^{129}Xe-blood resonance. The tissue resonance at 199 ppm appears soon after the start of xenon delivery (figure 4.5**a**), and as a result is likely is due to ^{129}Xe in the highly-perfused lung epithelium. The same argument can be applied to the "early" blood resonance of figure 4.5**a**, which must be from ^{129}Xe in the lung capillary bed. We expect that very little ^{129}Xe magnetization would have reached the more slowly perfused fatty tissues, and this is consistent with the conspicuous absence of a ^{129}Xe-fat resonance (191 ppm) in the spectrum of figure 4.5**a**.

The spectra acquired after delivery of the xenon breathing mixture reveal information about the long-lived ^{129}Xe tissue and fat resonances. Shortly after xenon delivery was stopped, all three dissolved-phase resonances are present in figure 4.5**b**, with the tissue resonance at 198 ppm greater than both the blood (209 ppm) and fat (191 ppm) resonances. At seven seconds after the end of xenon delivery (figure 4.5**c**), the coupled blood and gas resonances are small, and the tissue and fat resonances remain. The tissue resonance in this spectrum is likely due the more distal tissues in the body reached by blood flow. The resonance at 191 ppm, assigned to ^{129}Xe in fat, which did not appear at the onset of xenon delivery in figure 4.5**a** and remains after the blood resonance has nearly disappeared in figure 4.5**c**, is consistent with known diffusive properties of xenon into fat (i.e., low flow rat and high solubility), and is consistent with a long ^{129}Xe-fat T_1.

4.4 Spatial Localization and Imaging

This section presents localization studies of ^{129}Xe magnetization *in vivo*. One- and two-dimensional images of the spatial distribution of ^{129}Xe chemical shifts were made with a magnetic resonance method known as chemical shift imaging (CSI). Unlike the tissue distribution of the radioactive isotope ^{133}Xe [117], ^{129}Xe magnetization decays with a longitudinal relaxation rate that depends on its local environment. As a result, the *in vivo* tissue

distribution of ^{129}Xe magnetization may differ significantly from the *in vivo* concentration of xenon in tissue. ^{129}Xe magnetization will accumulate in those organs with a high rate of perfusion and large xenon solubility coefficient (see table 4.2) provided these organs have a relatively short blood transit time from the heart and a long ^{129}Xe T_1. *In vivo* ^{129}Xe longitudinal relaxation times in tissues are largely unknown, and only recently have *ex vivo* studies in rat tissue homogenates been reported [26]. These measurements (made using thermally polarized ^{129}Xe) have acquisition times of nearly 24 hours and were performed at 10 °C. As a result, these *ex vivo* T_1 measurements are not easily applicable to the evaluation the feasibility of *in vivo* ^{129}Xe tissue imaging. The direct measurement of the *in vivo* ^{129}Xe magnetization distribution is essential in order to determine which organs are suitable for study with laser-polarized ^{129}Xe.

4.4.1 One-dimensional CSI

One-dimensional chemical-shift images (CSI) were collected along the anterior-posterior axis of the animal in two separate experiments: one with a 13° and the other with a 30° tip angle. The field-of-view (FOV) for each experiment was 180 mm with 64 phase-encoding steps. The duration of the phase-encode gradient was 500 μs. All other parameters are the same as in figure 4.2. No slice selection gradient was used in these experiments (*i.e.*, spatial information is resolved only along the anterior-posterior direction, and each spectrum is a projection along both the ventral-dorsal and right-left directions). The 1D CSI acquisition sequence began 5 seconds after the Xe/O_2 (1:1) mixture delivery was started and lasted one minute.

Processing of the 1D CSI experiments consisted of several steps. Each of the 64 individual FIDs was multiplied by a 20 Hz exponential apodization filter as described in section 4.2.1. The data were then multiplied by a trapezoidal function in *k*-space. This apodization filter is effectively a low-pass filter in *k*-space, with the pass cutoff frequency set to maximize SNR while minimizing the loss of high-frequency information. The k_z dimension was zero-filled from 64 to 128 data points. Zero-filling is a technique used to increase digital resolution. Digital resolution can be expressed as the spectral width in hertz divided by the number of samples. It is possible to add data points to the end of the FID where the signal has effectively decayed to noise. Generally, data points consisting of

Tissue type	f_i (mL g^{-1} min^{-1})	λ_i
Gray matter	0.85 [115]	0.79[a]
White matter	0.43 [115]	1.32[a]
Muscle	0.06 [116]	0.58 [117]
Adipose fat	0.04 [116]	9.8 [117]
Kidney	4.0 [116]	0.66 [117]
Liver	0.20 [116]	0.72 [117]
Heart	4.9 [116]	0.69 [117]

Table 4.2: Rat tissue perfusion rates (f_i) and xenon blood:tissue partition coefficients (λ_i).

a. From reference [90], *in vitro* data from dogs; at 37°C and 50% hematocrit obtained from tissue/gas and blood/gas partition coefficients.

zeros are added to double the number of samples in the FID, hence the name zero-filling. After zero-filling, the data was Fourier transformed in both dimensions. The localized ^{129}Xe spectra obtained in each experiment are shown as a greyscale image in figure 4.6.

A set of spin-echo ^{1}H images with a 2 mm slice thickness and a 4 mm separation between slices was acquired without repositioning the animal. These cardiac-gated ^{1}H spin-echo images (TR = 428 ms, TE = 18 ms, FOV = 180 mm $\times$ 180 mm) was acquired for anatomical registration of the localized ^{129}Xe spectra. Three representative slices of the ^{1}H data set containing (**1**) brain, (**2**) kidney, and (**3**) heart are shown in figure 4.6 (**1–3**).

The spatial distribution of the ^{129}Xe resonances in blood, tissue, and fat varies markedly between the two ^{129}Xe CSI experiments, and these results are consistent with the hypotheses of table 4.1. Since NMR pulsing with the 30° tip angle samples and destroys ^{129}Xe magnetization in thoracic blood at a higher rate than NMR pulsing with a 13 ° tip, ^{129}Xe NMR signal is not observed in distant tissue. The 13° tip angle allows sufficient ^{129}Xe magnetization to accumulate in thoracic blood so that detectable ^{129}Xe magnetization accumulates in regions identified by the ^{1}H slices to contain the brain and kidney.

In order to more carefully examine the spatial distribution of figure 4.6, the 13° data **A**, **B**, and **C** were spatially summed over the indicated regions, and the spectra corresponding to these regions are shown in figure 4.7 **a–c**. It is interesting that the resonance at 191 ppm assigned to ^{129}Xe-fat is present only near the region containing the heart (figure 4.7 **b**). This further localization suggests assignment to ^{129}Xe dissolved in epicardial fat. The

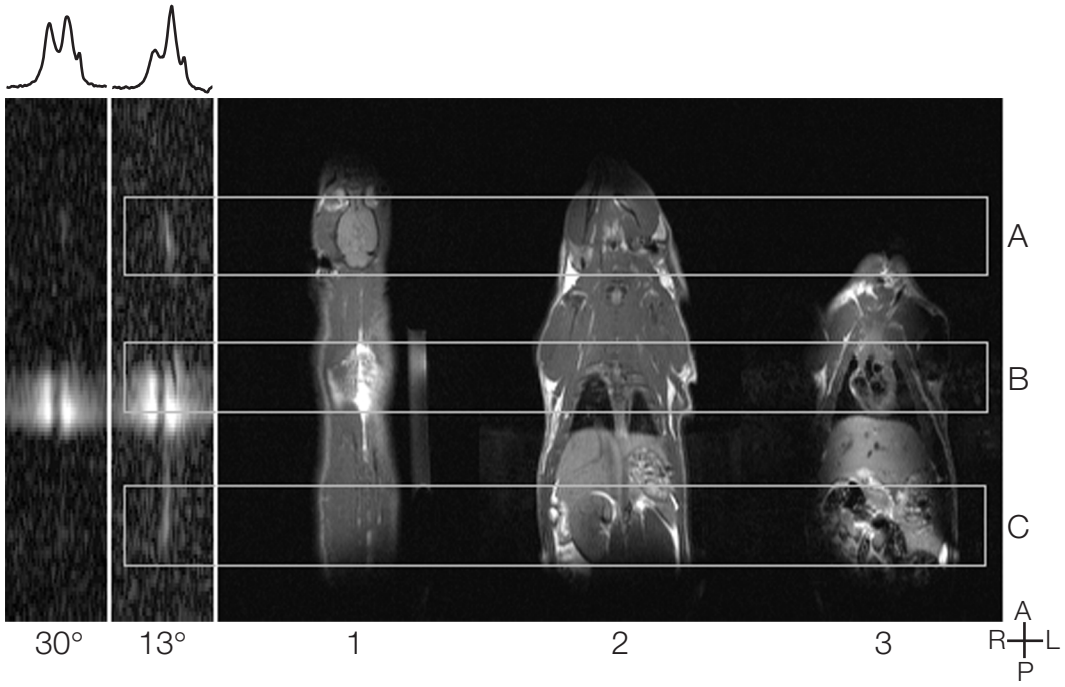

Figure 4.6: One-dimensional CSI of ^{129}Xe dissolved in blood, tissue, and fat in the rat body and ^{1}H spin-echo images for anatomical registration. Two experiments of spatially-resolved spectral information are presented as grayscale images, with the vertical direction the anterior-posterior axis. The field of view in the vertical axis is 180 mm. The horizontal axis in each of the two CSI experiments is the ^{129}Xe chemical-shift (from 235–175 ppm). The spectra integrated along the spatial axis are shown above the CSI datasets for spectral reference. Three representative (3 mm thick) slices from the ^{1}H dataset are shown, numbered **1**, **2**, and **3**. The regions **A**, **B**, and **C** are used to construct the localized spectra of figure 4.7. As discussed in the text, most striking is the fat resonance at 191 ppm, present only in the region containing the heart, and thus assigned to ^{129}Xe dissolved in epicardial fat.

absence of a blood resonance in region encompassing the brain (figure 4.7**a**) is not surprising, given the relatively small volume of blood in the brain (a few percent, by volume). The absence of a blood resonance in the region containing the kidney (figure 4.7**c**) is unexpected given the large volume of blood in the kidney.

These one-dimensional CSI experiments indicate that tissue-phase ^{129}Xe magnetiza-

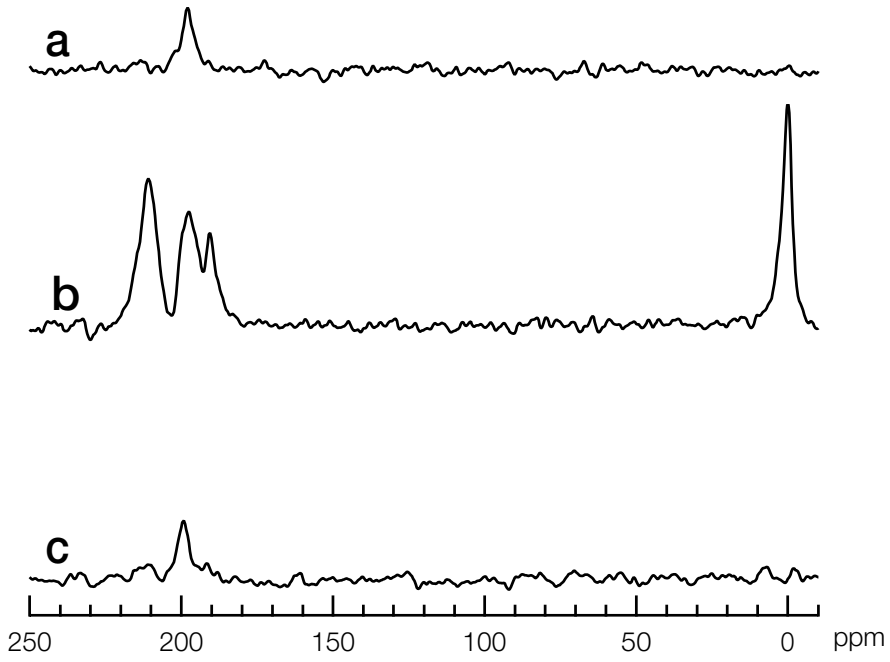

Figure 4.7: Localized spectra of ^{129}Xe in the rat body. Spectra of ^{129}Xe from regions encompassing (**a**) brain, (**b**) heart, and (**c**) kidney. The vertical scale is the same for all the spectra. Each spectrum was obtained by summing the 1D CSI data over the region indicated in figure 4.6. The tip angle in this study was 13°.

tion *in vivo* is primarily located in regions that include the brain, kidney, and thorax of rats. Absence of signal in the liver may be due to short tissue T_1 and/or the low perfusion rate (0.19 mL g min^{-1}). It is important to keep in mind that the ^{129}Xe spectra obtained from the regions **A**, **B**, and **C** are not spatially resolved in any other than the anterior-posterior direction, and these regions contain other tissue, muscle, and bone, adipose fat, skin which could contribute to the regional ^{129}Xe signal. However perfusion rates in these compartments are quite low—skin: 0.15 mL g^{-1} min^{-1}, bone: 0.16 mL g^{-1} min^{-1}, muscle: 0.06 mL g^{-1} min^{-1}, and fat: 0.04 mL g^{-1} min^{-1} [116].

4.4.2 Two-dimensional CSI

This section presents axial and coronal images of thoracic ^{129}Xe magnetization *in vivo*. In the previous section, we used 1D CSI experiments to detect ^{129}Xe magnetization in the brain, kidney, and thorax of Sprague-Dawley rats after the inhalation of laser-polarized ^{129}Xe gas. In order to study of the distribution of ^{129}Xe magnetization in the thorax, a series of 2D CSI experiments was performed. In this section, we exploit the result found in our 1D CSI studies: NMR pulsing at 30° constrains dissolved-phase ^{129}Xe magnetization predominately to the thorax. We also describe several potential clinical applications for *in vivo* ^{129}Xe chemical-shift imaging.

Two-dimensional chemical-shift images were collected in two separate experiments: one in the coronal plane and the other in the axial plane. Each of these experiments was performed during delivery of the Xe/O_2 (1:1) breathing mixture for approximately four minutes. A 30° tip angle and 428 ms TR was used in acquisition, and the NMR parameters are the same as in figure 4.2. No slice selection was used in these experiments, so that each spatially-resolved spectrum is a projection along either the anterior-posterior direction (for the axial image), or the ventral-dorsal (for the coronal image). Each dataset was acquired with 16 $\times$ 16 phase-encode values and two phase-cycled averages per phase-encode. The duration of the phase-encode gradient was 500 μs. The axial images were created from a single dataset with a 4-minute acquisition, and the coronal images were created from the sum of two 4-minute acquisitions. The FOV was 60 mm $\times$ 60 mm in the axial images, and 100 mm $\times$ 100 mm in the coronal images.

The processing of the 2D CSI experiments is as follows. Each of the 256 individual FIDs in the 2D CSI dataset was multiplied with a 20 Hz exponential line-broadening function. The data were then multiplied with a trapezoidal function in both k_x and k_z (for the coronal dataset) or in k_x and k_y (for the axial dataset), and zero-filled from 16 $\times$ 16 to 32 $\times$ 32. After zero-filling, the data were Fourier transformed in both dimensions. For each of the 1024 spectra, a least squares fit to the model of a sum of 3 independent Lorentzians (blood, tissue, and gas) with a common baseline was obtained, and the amplitudes for each spectral component used to create chemical-shift resolved images of the ^{129}Xe magnetization. Cardiac-gated ^{1}H images were collected for spatial registration of the ^{129}Xe signal.

Axial and coronal images of ^{129}Xe gas and ^{129}Xe dissolved in blood and tissue are pre-

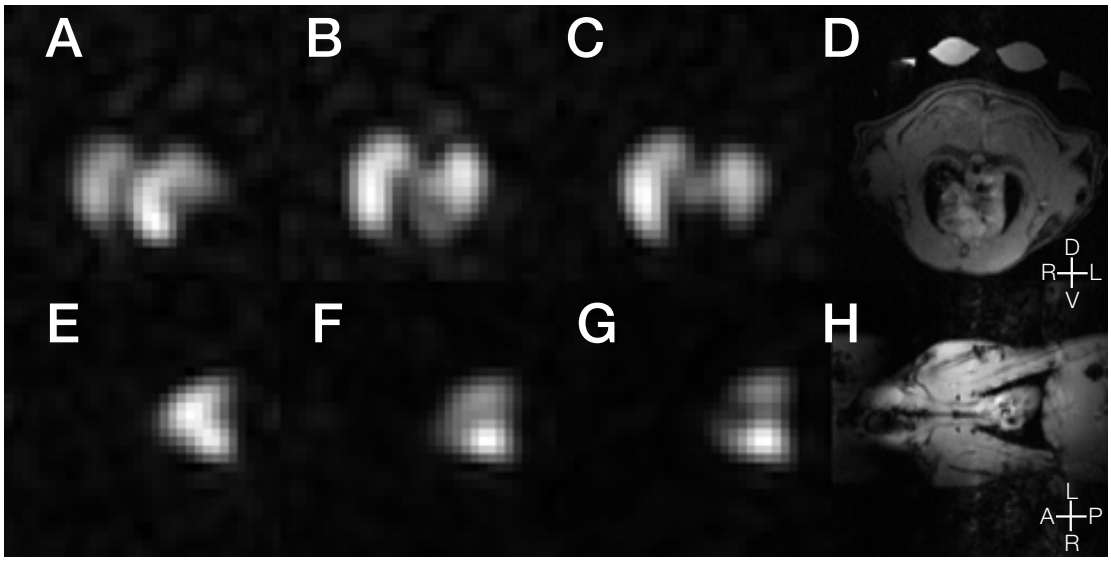

Figure 4.8: ^{129}Xe axial (**A–C**) and coronal (**E–G**) 2D CSI. Images of ^{129}Xe in blood (**A** and **E**), tissue (**B** and **F**), and gas (**C** and **G**) are shown. Cardiac-gated ^{1}H images (**D** and **H**) are shown for anatomical registration (water from the warming blanket is seen on the dorsal side of the axial ^{1}H image). The FOV was 60 $\times$ 60 mm in the axial images and 100 $\times$ 100 mm in the coronal images. The tip angle was 30° for all the ^{129}Xe images.

sented in greyscale alongside the ^{1}H images (figure 4.8), and in false-color ^{129}Xe overlaid on the ^{1}H images (figure 4.9) for anatomical registration.

The images of ^{129}Xe dissolved in blood in figure 4.8 (**A** and **E**) and figure 4.9 (**A** and **D**) are consistent with ^{129}Xe magnetization present in the lung capillary bed, the pulmonary vein, and the left ventricle of the heart, and these images of ^{129}Xe in pulmonary blood represent the first use of laser-polarized ^{129}Xe to image transport of xenon gas across the lung epithelium and into the blood. The distribution of ^{129}Xe-blood magnetization in this region is best understood in terms of rodent circulation and ^{129}Xe gas/blood exchange at the lung.

The largest volume of blood in the thorax is pulmonary blood, which is roughly 7% of the total blood volume in the rat [118]. Venous blood returning to the heart is largely depolarized because the circulation time through the body is long (approximately 20 s) compared to the ^{129}Xe-blood T_1 (approximately 6 s). This blood is pumped from the right heart via the pulmonary artery to the lung epithelium, and saturated with polarized ^{129}Xe.

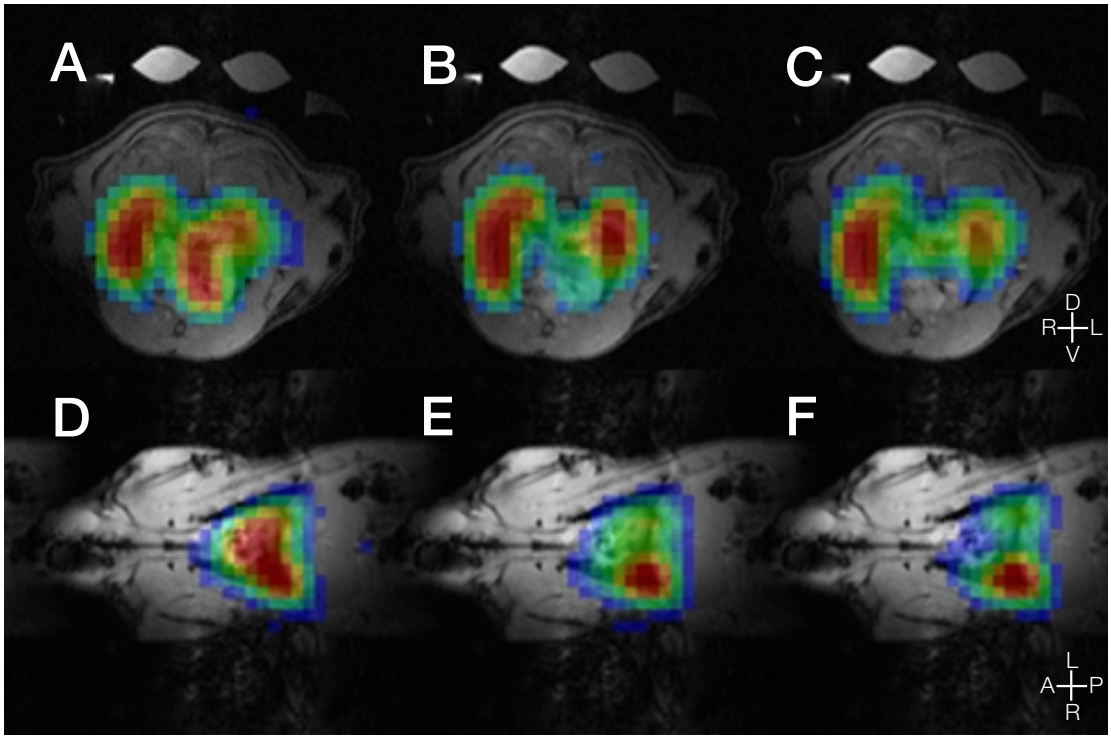

Figure 4.9: False-color overlay of the axial (**A**–**C**) and coronal (**D**–**F**) ^{129}Xe 2D CSI images onto the ^{1}H images. Images of ^{129}Xe-blood (**A** and **D**) indicate ^{129}Xe magnetization in lung vasculature and in the heart ventricle. Images of ^{129}Xe-tissue (**B** and **E**) show ^{129}Xe magnetization in the lung parenchyma and in the myocardium. A lung function-weighted image obtained from the difference of the gas images (**C** and **F**) and the blood images (**A** and **D**) may be used to assess pulmonary health in a single MRI study. Images of ^{129}Xe in myocardial tissue may be used to create a map of myocardial perfusion and heath.

This freshly-perfused blood returns to the left heart via the pulmonary vein, where it is then pumped to the body's main arteries. Thus, we expect that only the venous side of the pulmonary blood to contribute to the thoracic ^{129}Xe-blood signal. The large ^{129}Xe-blood signal observed throughout the lungs indicates efficient transport of magnetization from gas in the lungs in this pulmonary blood. Likewise, the signal from ^{129}Xe-blood in the heart is likewise assumed to arise from the largest volume of freshly-perfused blood in the heart *i.e.*, the left ventricular blood volume, 0.1 mL/100 g BW [118].

The images of ^{129}Xe dissolved in tissue in the thorax shown in figure 4.8 (**B** and **F**) and figure 4.9 (**B** and **E**) are consistent with ^{129}Xe dissolved in lung epithelium. This is corrob-

orated by our time-resolved spectroscopy studies that show ^{129}Xe passing through a tissue phase in the lungs before reaching the pulmonary blood (figure 4.5**a**). ^{129}Xe magnetization in tissue is also observed in the region of the heart, and suggests ^{129}Xe is present in myocardial tissue.

Clinical applications exist for ^{129}Xe-tissue images obtained from the thorax. Restricted blood flow and unperfused regions would be revealed by the absence of a ^{129}Xe-tissue signal in that region, and the presence of detectable ^{129}Xe magnetization in the myocardium may be used to measure cardiac perfusion, in a manner in similar to the use of ^{133}Xe nuclear medicine [21]. Since chronic cardiac dysfunction is often associated with alterations of coronary microcirculation [119, 120], a quantitative and noninvasive measurement of regional myocardial perfusion might provide the specificity necessary to assess of cardiac dysfunction.

The images of ^{129}Xe gas in figure 4.8 (**C** and **G**) and figure 4.9 (**C** and **F**) show ^{129}Xe present in the air spaces of the lung and trachea. Although images constructed from ^{129}Xe CSI data currently have lower spatial resolution than the high-resolution magnetic resonance images of laser-polarized ^{3}He gas [121, 122], spatial resolution is often secondary to the need to assess pulmonary perfusion and ventilation in pulmonary medicine. The efficiency of gas/blood exchange in alveoli is determined both by local ventilation and by regional perfusion, and an image that could indicate gas-exchange can be considered to be maps of lung function. This type of imaging would be sensitive to regions of lung with abnormal ventilation but normal perfusion (as is the case in airway diseases such as chronic obstructive pulmonary diseases), as well as regions of lung with normal ventilation but poor perfusion, such as in the case of pulmonary embolism. CSI with laser-polarized ^{129}Xe has the potential to be used to assess lung function through comparison of the distribution of lung gas with the distribution of ^{129}Xe dissolved in blood and tissue, and to replace standard ventilation-perfusion techniques [123] with a single MRI study.

We now examine several individual ^{129}Xe spectra from the coronal 2D CSI dataset. These spectra from the CSI dataset corresponding to their indicated regions on the 16 $\times$ 16 grid overlaid on the coronal ^{1}H image of figure 4.10. Each of the five spectra (**a**–**e**) corresponds to the ^{129}Xe magnetization in the indicated 2D pixel of the proton image, projected in the ventral-dorsal direction over the thickness of the animal. These five spectra

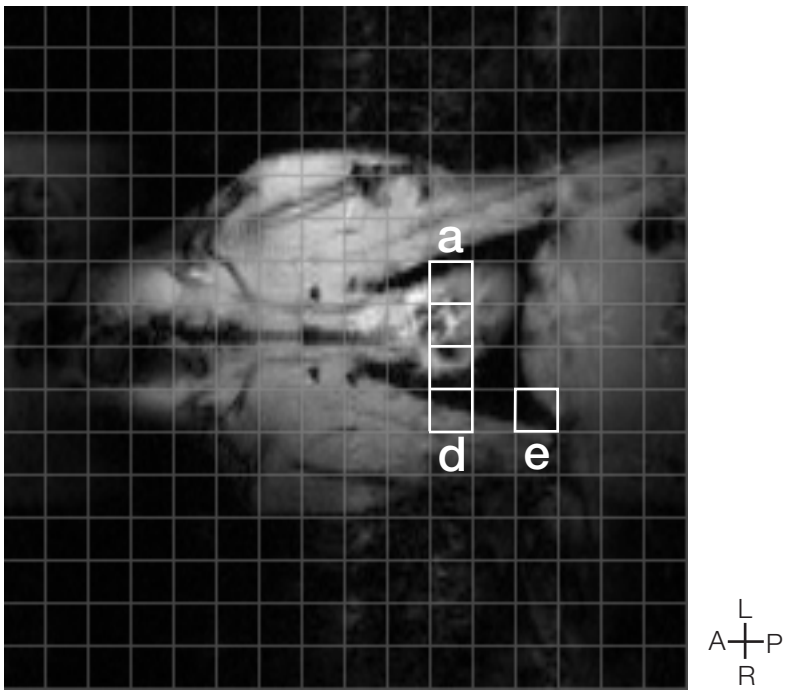

Figure 4.10: Regions from the coronal 2D CSI used to generate figure 4.11.

(**a**–**e**) are shown in figure 4.11.

The spectrum shown in figure 4.11**c** comes from a voxel nearly centered on the left ventricle and likely containing the pulmonary vein. Consequently, the spectra from this voxel is dominated by a single resonance at 209 ppm (*i.e.*, ^{129}Xe dissolved in blood), consistent with the large volume of freshly perfused blood in this region. The absence of a large ^{129}Xe-gas resonance in this voxel (*c.f.* figure 4.11 **d** and **e**) implies a small volume of the lung is contained in the voxel, even though this spectrum is a projection through the animal. A ^{129}Xe-tissue resonance is markedly absent from figure 4.11**c**, which is surprising as we would expect to see ^{129}Xe-tissue magnetization in the cardiac wall. There is an unusual broadening of the ^{129}Xe-blood resonance in the region of the ^{129}Xe-tissue resonance, and this may be due to exchange dynamics between rapidly flowing blood and the heart muscle.

As expected, spectra from voxels including significant lung volume (*e.g.*, figure 4.11 **d** and **e**) indicate ^{129}Xe magnetization in gas, blood, and tissue of the lungs. The ability to spatially resolve ^{129}Xe resonances in lung gas, and in lung tissue and pulmonary blood in the lungs may provide regional measure of lung function with higher specificity than

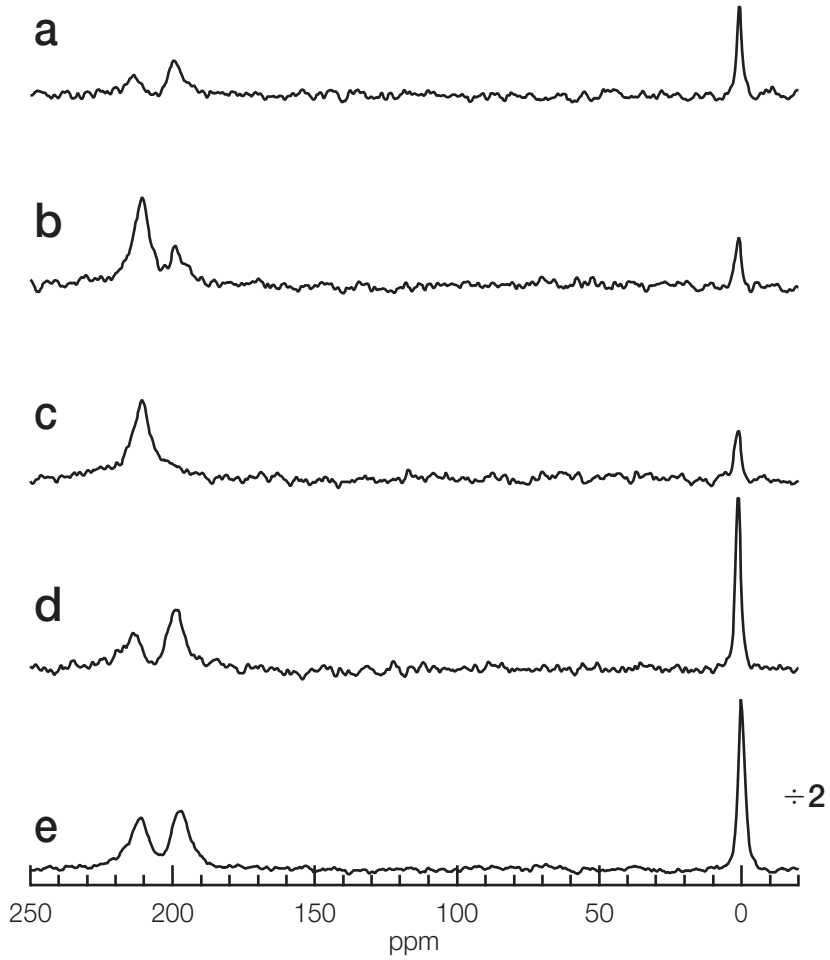

Figure 4.11: ^{129}Xe spectra obtained from individual voxels of the coronal 2D CSI dataset. The region from which each spectrum was taken is indicated in figure 4.10. The single resonance observed in blood in the heart at 209 ppm (**c**) is consistent with fast exchange of ^{129}Xe between red blood cells and plasma. The vertical scale for spectrum **e** is twice that of spectra **a**–**d**.

tomographic nuclear medicine techniques.

4.5 *In Vivo* ^{129}Xe Resonance Assignments

Throughout this chapter, we have demonstrated measurement of the tip-angle dependence

of *in vivo* ^{129}Xe spectroscopy, the dynamics of ^{129}Xe magnetization *in vivo*, and the spatial distribution of ^{129}Xe magnetization in the rat body that are all consistent with our assignment of the major ^{129}Xe spectral components observed in the rat at 2 T. This section gives additional analysis supporting our assignments of ^{129}Xe dissolved in blood (209 ppm), tissue (198 ppm), and fat (191 ppm).

4.5.1 ^{129}Xe blood resonance (209 ppm)

There is a discrepancy between our observation of a single ^{129}Xe-blood resonance in rats *in vivo*, and *in vitro* studies performed by other investigators in human blood. *In vitro* work has shown ^{129}Xe dissolved in whole human blood to have two well resolved resonances, assigned to ^{129}Xe in red blood cells and ^{129}Xe in plasma [112, 113]. These studies find that the position of the RBC resonance in human blood depends strongly on the blood oxygenation level, ranging from 216–222 ppm, but the plasma resonance is relatively independent of blood oxygenation level [112, 113]. However, two different values of the ^{129}Xe-plasma resonance in human blood have been reported: 197 ppm [112, 113] and 192 ppm [24].

The ^{129}Xe-RBC and ^{129}Xe-plasma resonances in human blood are known to be coupled by chemical exchange with a measured exchange time of 12 ms at 4.3 T and ambient laboratory temperature [24], and the NMR lineshape of chemically exchanging systems depends strongly on the time scale of the exchange process, τ. This effect is well known in NMR spectroscopy when a species is in exchange between two states with their associated spectral resonances separated by angular frequency $\delta\omega$.

When the time scale for exchange between nuclear moments is slow compared to the NMR time scale (determined by the non-exchanging peak separation $\delta\omega$), two resonances are observed. In the chemical exchange measurements in human blood [24], the NMR time scale of 130 μs (*i.e.*, 24 ppm at 4.3 T) is almost than two orders of magnitude shorter than the 12 ms xenon exchange time between blood components reported by Bifone *et al.* [24]. In this slow exchange regime, ^{129}Xe dissolved in human blood is expected to always have two resonances.

The results presented in this thesis find no evidence for two blood resonances in Sprague-Dawley rats *in vivo*. The spectrum of ^{129}Xe localized to a voxel apparently containing

predominately blood (figure 4.11c) shows a single resonance at 209 ppm. In fact, no resonance in the 216–222 range is observed anywhere in the rat body *in vivo*. We hypothesize several factors that may contribute to our observation of only one resonance in rat blood *in vivo*.

Fast exchange occurs when the exchange time τ obeys the condition $\tau\delta\omega \ll 1$, (*i.e.*, the spin diffusion time is short compared to the transverse spin relaxation time). When chemical exchange is fast compared to the NMR time scale, the individual resonances become completely averaged and a single resonance is observed [124-126]. The RBC-plasma exchange process where exchange was decoupled and measured to be "slow" at 23 °C and 9.4 T may move into the fast-exchange regime under the conditions of our *in vivo* studies: 37 °C and 2 T.

If we assume that the observed *in vivo* rat blood resonance of figure 4.11**c** is the result of fast-exchanging plasma and RBC resonances, the frequency of the observed blood resonance can be calculated [87, 124-126],

$$\nu_{blood} = p_{rbc}\nu_{rbc} + p_{plasma}\nu_{plasma}, \tag{4.2}$$

where p_{rbc} and p_{plasma} are the mole fractions of ^{129}Xe in red blood cells and plasma, respectively, and ν_{rbc} and ν_{plasma} are the pre-exchange frequencies. The coefficients p_{rbc} and p_{plasma} can be estimated from the xenon RBC:plasma partition coefficient, λ_{cp}, and the hematocrit, H. The concentration of xenon in whole blood (C_b) in terms of the concentration of xenon in red blood cells (C_{rbc}) and xenon in plasma (C_{plasma}) is

$$C_b = HC_{rbc} + (1 - H)C_{plasma}, \tag{4.3}$$

where H is the hematocrit (i.e. the RBC fraction of whole blood). The RBC:plasma partition coefficient, λ_{cp} is defined as

$$\lambda_{cp} = C_{rbc} / C_{plasma}. \tag{4.4}$$

Combining equation 4.3 and equation 4.4, the mole fractions can be written

$$p_{rbc} = \frac{\lambda_{cp} H}{1 + H(\lambda_{cp} - 1)} \;,\; p_{plasma} = \frac{1 - H}{1 + H(\lambda_{cp} - 1)}. \tag{4.5}$$

The ^{129}Xe blood resonance frequency under fast exchange conditions can be calculated with equation 4.2 and equation 4.5. Using the values obtained in human blood at 9.4 T and ambient temperature (ν_{rbc} = 216 ppm, ν_{plasma} = 192 ppm) [24], the Sprague-Dawley hematocrit of 0.43 [127], and the RBC-plasma partition coefficient (obtained in dog blood) λ_{cp} = 3.31 [90], the calculated ν_{blood} is 209 ppm, the same as chemical shift we measure *in vivo*.

This analysis shows that our *in vivo* observations are consistent with ^{129}Xe in fast exchange between RBC and plasma components. A variety of factors could contribute to the observation of fast-exchange at in rats *in vivo* at 2 T. The efficiency of exchange is strongly temperature dependent, and all *in vivo* experiments were performed at 37 °C. Also, the mean rat RBC diameter is approximately 6 μm [128], smaller than the human RBC diameter of 8 μm [129], potentially allowing for more efficient mixing of intra/extra cellular components (and shortening of the ^{129}Xe-RBC/^{129}Xe-plasma exchange time). Although this argument is compelling, a systematic study of the xenon in blood of different species and under different experimental conditions has yet to be performed.

Other studies performed in rats at 4.7 T by Sakai *et al.* [130] assign nonlocalized *in vivo* ^{129}Xe chemical shifts of ^{129}Xe-RBC and ^{129}Xe-plasma to 213 and 192 ppm, respectively. A resonance at 209 ppm is present in figure 4.5**a** near the beginning of ^{129}Xe delivery. This resonance could be assigned to "^{129}Xe-RBC", however the corresponding "plasma" resonance at 192 ppm is not observed. Additionally, a resonance at 191 ppm is present in figure 4.5**c**, but no "RBC" resonance is observed at 209 ppm. The data presented in this thesis requires a different assignment of the resonances, with the assignment of the resonance at 191 ppm described in section 4.5.3.

4.5.2 ^{129}Xe tissue resonance (198 ppm)

The ^{129}Xe resonance at 198 ppm first appears in the lung alveolar region promptly after ^{129}Xe magnetization is introduced into the lungs (figure 4.5**a**). This 198 ppm signal increases with time and becomes larger than the blood signal as ^{129}Xe perfuses into more distant organs such as brain and kidney (figure 4.1 and figure 4.5**b**). One-dimensional CSI

data acquired with a small tip-angle pulse show ^{129}Xe magnetization at 198 ppm present in the thorax, kidneys, and the brain (figure 4.6). Two-dimensional CSI data shows ^{129}Xe magnetization at this frequency in the thorax, in the lungs, and in the heart (figure 4.8**B** and figure 4.9**B**). We thus conclude that the ^{129}Xe resonance observed at 198 ppm is consistent with ^{129}Xe magnetization dissolved in tissue.

4.5.3 ^{129}Xe fat resonance (191 ppm)

The resonance observed at 191 ppm is assigned to ^{129}Xe in epicardial fat based on chemical shift, dynamics, and localization in the rat body, as discussed above. The chemical shift of this resonance is similar to the chemical shift of xenon dissolved in other fatty tissues, such as beef fat [130] and long-chain fatty acids [94]. Autoradiograpic studies [131] of ^{133}Xe uptake find ^{133}Xe activity is located primarily in myocardium during the first minutes of uptake, and afterwards in epicardial fat. This epicardial fat, with its low blood flow and high partition coefficient, leads to a very slow observed washout. In fact, xenon radioactivity has been shown by autoradiography to be present in epicardial fat in significant concentration for at least eight minutes after intracoronary injection of ^{133}Xe [131]. The inability of nuclear medicine techniques to separate fat and tissue compartments has hampered the use of ^{133}Xe washout as a method to measure myocardial blood flow, as the high solubility in cardiac fat limits the number of measurements obtainable in each study [21, 132, 133]. We have shown that ^{129}Xe magnetization in epicardial fat and in myocardial tissue are easily separable with NMR spectroscopy, and given increases in ^{129}Xe-fat SNR, images of each component may be made.

4.5.4 Summary

The results presented here show that ^{129}Xe magnetization is present in lungs, blood, brain, kidney, myocardium, and epicardial fat after inhalation of laser polarized ^{129}Xe. ^{129}Xe resonances are observed *in vivo* at 209, 198, and 191 ppm and are consistent with ^{129}Xe magnetization dissolved in blood, tissue, and epicardial fat, respectively. ^{129}Xe magnetization flows from gas in lungs, to lung epithelium, into the blood, through the heart, and finally into organ tissue (heart, brain, kidney). In the heart ventricle, a single blood resonance is observed, indicating that the red blood cell and plasma components are in fast exchange *in*

vivo at 37 °C and 2 T in rat blood. Many types of function-weighted images can be constructed with CSI data *in vivo*. This technique may provide significant diagnostic information. In Chapter 5, a ^{129}Xe NMR method for the quantitative measurement of perfusion based on tip-angle-dependent measurement of ^{129}Xe-tissue resonances is presented.

4.6 Brain ^{129}Xe NMR and MRI

This section presents localized ^{129}Xe spectroscopy and imaging studies constrained to the head of Sprague-Dawley rats. The feasibility of brain MRI with laser-polarized ^{129}Xe in a small animal model is demonstrated with NMR spectroscopy and imaging of the rat brain *in vivo*. We present spectroscopic studies that reveal a complex ^{129}Xe dissolved-phase spectrum in the rat head, and we hypothesize the origin of two of the five observed dissolved-phase resonances *in vivo*. Although these studies are among the earliest we performed, these results demonstrate some of the necessary experimental features essential for the use of laser-polarized ^{129}Xe as magnetic resonance tracer for studies of cerebral perfusion.

4.6.1 Brain spectroscopy and uptake

The potential for magnetic resonance studies with dissolved-phase ^{129}Xe was explored through *in vivo* ^{129}Xe spectroscopy experiments using the NMR "surface" probe described in detail in section 3.7.1. This three-turn, doubly-tuned ^{1}H-^{129}Xe surface coil with a 3.5 cm diameter was constructed and used for all of the following experiments. The detected ^{129}Xe signal in these experiments comes from the distribution of ^{129}Xe magnetization constrained to the sensitive region of the RF coil, which falls off rapidly outside of the region of the rat head.

Spectroscopy was performed using with an estimated 20° tip angle pulse (averaged over region of interest of the brain). The spectrometer spectral width was set to 2 kHz, centered about the tissue-dissolved ^{129}Xe spectral regions, since no ^{129}Xe gas resonance was detected in broadband experiments. FID signals consisting of 1024 points were acquired with repetition time TR = 0.5 s. Each FID in the final dataset is the sum of two phase-cycled acquisitions.

Two datasets consisting of 256 pulses each were obtained from a single animal over

two runs of 50 seconds of Xe/O_2 (60%/40%) inhalation with a ^{129}Xe polarization of approximately 4.5%. After acquisition, the time-domain data was multiplied by a 20 Hz exponential line-broadening function, and then Fourier transformed. Each set of 128 spectra were summed over time, and the two datasets averaged together. The *in vivo* NMR spectrum of laser-polarized ^{129}Xe in the rat head obtained from this procedure is shown in figure 4.12.

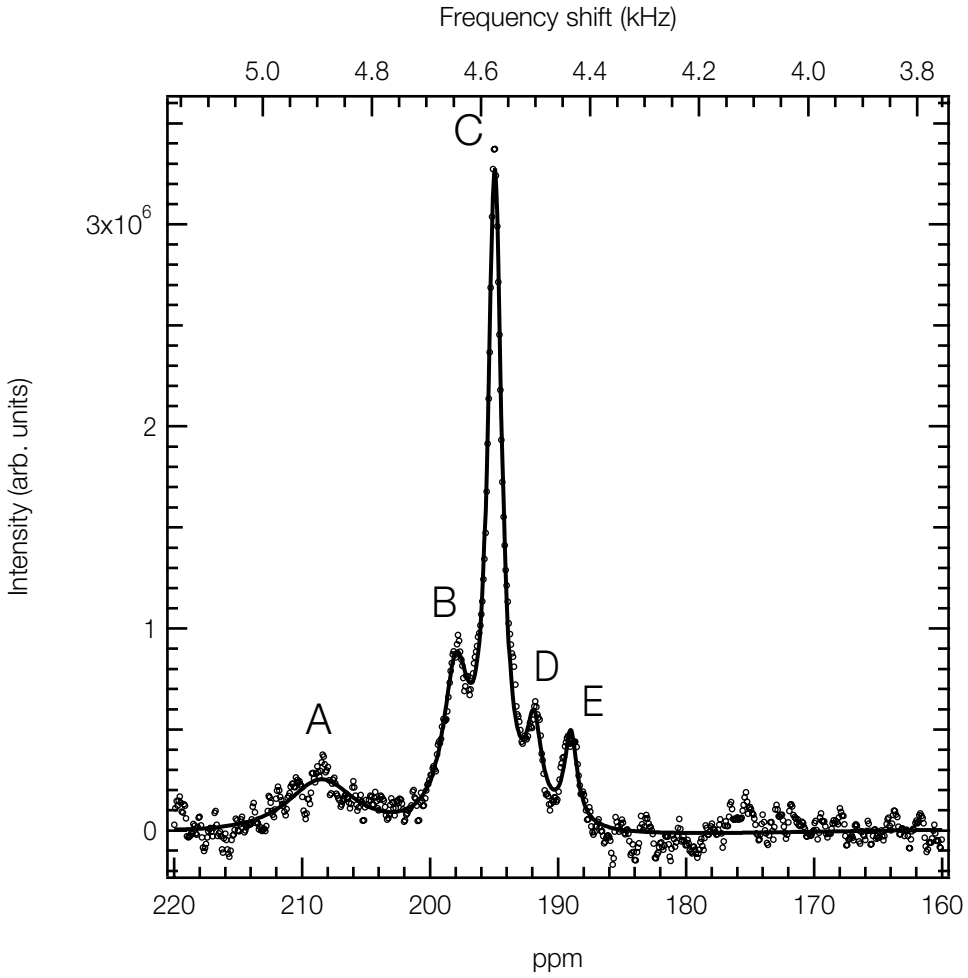

Figure 4.12: Spectrum of ^{129}Xe in the rat head at 2 T, acquired from 256 acquisitions over two runs of 50 seconds each. The solid curve is the result of a least-squares fit to a sum of five independent Lorentzians with a common baseline. Assignment of the resonances at 209 and 195 ppm to ^{129}Xe in blood and grey matter, respectively, is discussed in section 4.6.3.

As in section 4.2.1, the frequency and linewidth of each resonance in figure 4.12 was determined by a least-squares fit to five independent Lorentzians with a common baseline. The parameters obtained from this spectrum and hypothetical resonance assignments are given in table 4.3.

	A	B	C	D	E
Chemical shift (ppm)	208.5±0.1	197.97±0.03	194.94±0.01	191.87±0.04	189±0.04
Width (ppm)	6.7±0.6	2.4±0.1	1.31±0.02	1.4±0.1	1.2±0.1
Width (Hz)	161±14	57±3	31±0.5	33±3	28±3
T_2^* (ms)	2.0±0.2	5.6±0.3	10.3±0.2	9.6±0.9	11.4±1.2
Assignment	Blood	?	Grey matter	?	?

Table 4.3: NMR parameters extracted from the fit to the brain spectrum of figure 4.12. Assignments are discussed in the text.

The time dependence. of the dominant ^{129}Xe resonance seen in figure 4.12 (195 ppm) is plotted in figure 4.13 for each of the two datasets. The decrease in the amplitude of the 195 ppm resonance prior to the discontinuance of the Xe/O_2 mixture is likely due to many factors including the anesthetic effect of the xenon itself. Inhalation of 60% xenon is considered an anesthetic dose in humans [134], and cerebral perfusion is known to be reduced in anesthetic states. We have subsequently learned that animals should receive no more than 35% xenon to avoid significant alterations of blood flow by xenon inhalation. Additionally, the blood oxygen saturation of the rat measured by the pulse oximeter decreased substantially during the course of this experiment, beginning at typically 95% and dropping to as low as 45% before the breathing mixture was halted at t = 50 s. The changing oxygenation in the blood will decrease the ^{129}Xe-blood T_1 [112], and consequently reduce the ^{129}Xe magnetization reaching the brain. These issues are discussed in more detail in Chapter 5.

4.6.2 Brain imaging

Images of ^{129}Xe magnetization in the rat head were acquired using a 2D CSI pulse sequence. At the time that these imaging experiments were performed, the polarized ^{129}Xe

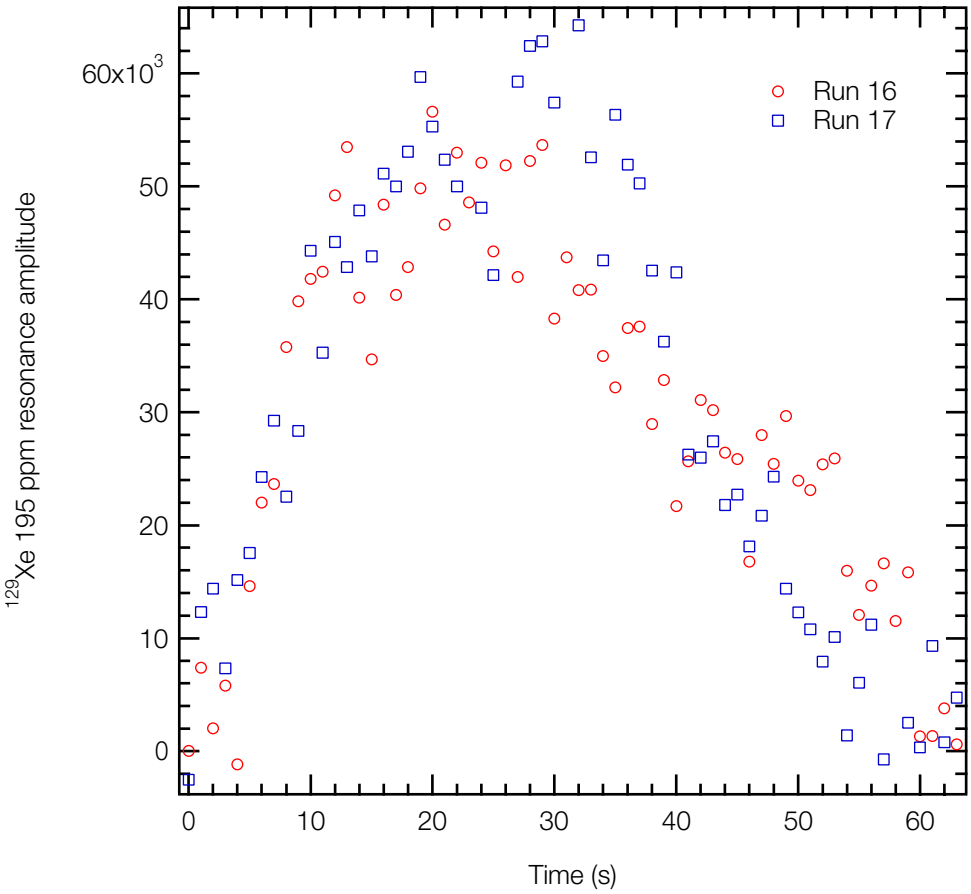

Figure 4.13: Uptake of 195 ppm "grey matter" peak, in two consecutive runs. In both runs, the delivery of polarized xenon was stopped at $t = 50$ s. The decrease of ^{129}Xe signal during the delivery is likely to have contributions from the changing blood oxygenation level in both the lung and the blood during the experiment, as well as from changes in CBF due to the large inhaled xenon fraction (60%) [115].

accumulation stage had not been incorporated into the polarizer apparatus and only single batches of polarized gas could be produced. In order to maximize the attainable SNR of the very limited amount of gas available in these early exploratory experiments, 100% xenon was delivered to the animal, at approximately 3.5% polarization.

A two-dimensional ^{129}Xe CSI image with a 50 mm $\times$ 50 mm FOV was collected in the horizontal plane in a single experiment of 40 s xenon delivery. The CSI sequence was started about 5 seconds prior to delivery of the ^{129}Xe gas, and continued for a total imaging duration of 73 s. A 1 ms single-cycle Sinc pulse with an average 20° tip angle (averaged

over the brain region) was used in acquisition. The dataset was acquired with 16 × 16 phase-encode values and two phase-cycled averages per phase-encoding step. For each phase-encode, FIDs were obtained (256 points) in 128 ms. The duration of the phase-encode gradient was 500 μs. The slice thickness was 10 mm. The frequency of the spectrometer was set to the 195 ppm dissolved-phase resonance, determined prior to the *in vivo* experiment by observing the ^{129}Xe gas resonance in a glass phantom, and the receiver bandwidth was 2 kHz.

The 256 × 16 × 16 CSI data set was zero-filled along both phase-encode dimensions to produce a final dataset of 256 × 32 × 32. The data were then Fourier transformed along each dimension. A Lorentzian was fit to the resonance at 195 ppm in each of the 1024 spectra, and the amplitude of the fit was used to generate the ^{129}Xe image. It should be noted that the individual spectra in the CSI data set had only one resolvable peak (195 ppm), compared to the 5 dissolved peaks of figure 4.12. This is ostensibly due to the low polarization and short running time of the CSI experiment, and potentially to the reduction of signal that accompanies the use of 100% xenon.

A proton image was acquired with a conventional spin-echo pulse sequence with a slice thickness of 10 mm, a field of view of 50 mm × 50 mm, 500 ms TR, 20 ms TE, and 40 kHz receiver bandwidth.

The horizontal ^{129}Xe CSI image of ^{129}Xe in the brain is shown as a greyscale image in in figure 4.14**A** alongside the ^{1}H image (figure 4.14**B**) and in a false-color image overlaid on the ^{1}H image in figure 4.14**C**.

The image of ^{129}Xe magnetization in the rat brain is not homogeneous, and in particular the ^{129}Xe signal in the cerebellum is less than the signal in the cerebrum. This signal difference may be due to lower blood flow in the cerebellum than in the cerebrum, as normal rodent cerebellar blood flow is somewhat lower than that of cerebral gray matter [135]. Additionally, the inhalation of 80% xenon for one minute is known to produce significant increases in rCBF (regional cerebral blood flow) in cerebral neocortex (a factor of nearly two) in rats, and smaller increases in most other gray and white matter forebrain structures [115]. In contrast, hindbrain cerebellum structures show very little change in rCBF as a function of xenon concentration [115].

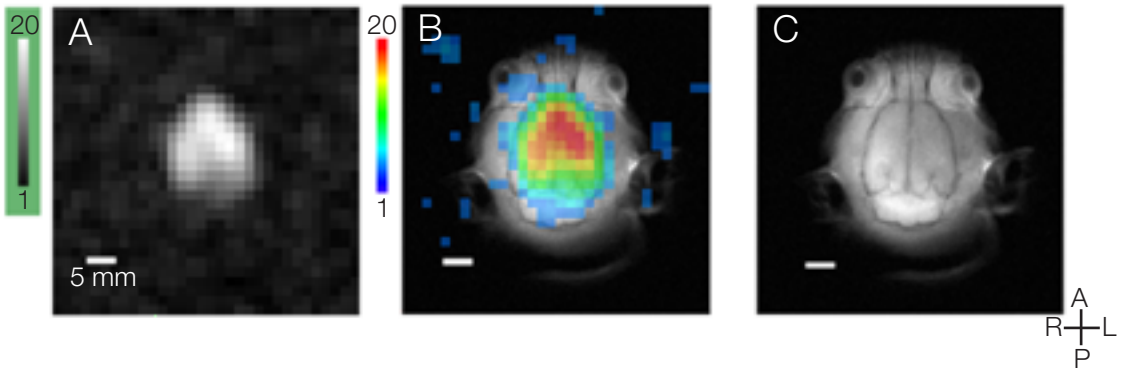

Figure 4.14: 2D CSI ^{129}Xe image of the rat brain (**A**), ^{1}H spin-echo image (**C**), and false-color ^{129}Xe image overlaid on the ^{1}H image (**B**). FOV is 50 $\times$ 50 mm, with a slice thickness of 10 mm. The gray scale and the false-color scale indicate SNR. The false color ^{129}Xe image has a SNR threshold of 3. The maximum ^{129}Xe voxel SNR is roughly 20. The in-plane resolution of the 10 mm thick ^{129}Xe image is 3.1 mm $\times$ 3.1 mm, yielding a voxel size of 98 μL.

4.6.3 Brain ^{129}Xe resonance assignment

To date, two groups have demonstrated *in vivo* ^{129}Xe spectroscopy in brain tissue: rodent results obtained at Michigan [25] and human results from the University of Virginia [136, 137]. In both of these studies, multiple dissolved-phase ^{129}Xe resonances are observed, with a prominent peak at 195 ppm. Although our results in the spectrum of figure 4.12 indicate five dissolved-phase ^{129}Xe NMR resonances, our imaging work had signal-to-noise sufficient to resolve only a single resonance at 195 ppm.

Assignment of the complex ^{129}Xe spectra seen in the brain is difficult. First, the dominant ^{129}Xe resonance at 195 ppm is assigned to ^{129}Xe dissolved in grey matter based on several factors. The cerebral blood volume in the rat is relatively low, roughly 5% [138]. Since xenon is lipophilic, with blood/brain partition coefficient close to unity [90], and since xenon freely diffuses into brain issue, the ^{129}Xe NMR signal observed is expected to be dominated by ^{129}Xe in brain tissue, not by ^{129}Xe in brain blood. Additionally, cerebral blood flow is very high (~1 mL g^{-1} min^{-1}) compared to the surrounding fat and muscle of the head, and this is supported by the image of ^{129}Xe in the rat head (figure 4.14), where

the ^{129}Xe signal is localized to the brain and is not seen in the surrounding fat or muscle. The circulation though the gray matter, with its densely packed cells, is greater than through the white matter, and so we conclude that ^{129}Xe magnetization would be expected to accumulate there more rapidly than in white matter. This leads us to assign the 195 ppm peak to gray matter.

The broad resonance at 209 ppm is assigned to ^{129}Xe in brain blood strictly on the basis of studies in the body indicating blood at the same spectral location. We cannot confidently carry our peak assignments further, since we have not yet accurately localized the spectral components. However, it should be noted that the richness of the brain spectra clearly implies that chemical exchange between the molecular environments of the different compartments is slow on the NMR time scale corresponding to 3-4 ppm intrinsic separation (70–90 Hz, 1.8–2.3 ms). These currently unassigned resonance may arise from different tissues and fluids in the brain (*e.g.* white matter, CSF, adipose tissue) and present new imaging opportunities. The *in vivo* chemical shift may also depend on the local blood oxygenation level [113].

Given the increases in ^{129}Xe polarization described in Chapter 6, and the increased imaging times that will follow from with lower xenon concentration, it is likely that images of these dissolved-phase ^{129}Xe resonances could be made and the grey and white matter resonances identifiable on the basis of their flow characteristics.

4.7 Prospects

This chapter concludes with a brief discussion of our attempts to improve the resolution of ^{129}Xe MRI using imaging sequences other than CSI, and present some preliminary results obtained from the thorax using projection reconstruction imaging.

Perhaps the most commonly used high-resolution MRI sequences are the class of sequences know as gradient-echo sequences (see Appendix A). These imaging sequences sample *k*-space one line (or more) at a time, allowing images to be acquired rapidly. We have been able to obtain gradient-echo images of ^{129}Xe gas in glass phantoms with both the volume and the surface probe, and with modest shimming we have been able to obtain upwards of 32 echoes per RF pulse. However, we have not been able to obtain an *in vivo*

^{129}Xe gradient-echo image in either the brain or the thorax.

We have estimated the typical ^{129}Xe *in vivo* T_2^* from the FWHM of the *in vivo* resonances to range from 2–20 ms (table 4.1 and table 4.3). These relatively short ^{129}Xe transverse relaxation times (T_2^*) require correspondingly shorter echo times in order that sufficient transverse ^{129}Xe magnetization exist to form a detectable echo. We have tried echo times on the order of 500 μs, we have not been able to observe *in vivo* ^{129}Xe echoes. This clearly requires further study.

An alternative imaging method we have successfully implemented *in vivo* is the method of projection reconstruction (PR) imaging (see Appendix A). PR is similar to CSI in that the recorded signal is the FID, and not a gradient-echo. Unlike CSI, however, PR samples *k*-space an entire line at a time, at the cost of lost spectroscopic information. Although our experience with *in vivo* PR imaging is limited, the comparison between CSI and PR is marked. Two coronal images acquired in the same animal and with the same field of view are shown in figure 4.15. The CSI image (figure 4.15**A**) is the gas image shown previously in figure 4.8**G**, and was obtained over two four-minute experiments. The PR image (figure 4.15**B**) was obtained in a single 48 s experiment. The polarization in both experiments is identical. It should be noted that, although at the cost of spectral information, the PR image was acquired an order of magnitude more rapidly.

Projection reconstruction images may be able to be used in combination with frequency-selective RF pulses in order to obtain images of each ^{129}Xe chemical shift are to be made [139]. This may become problematic if the pulse duration of a narrow-band excitation pulse approaches the resonance T_2^*. Again, this requires careful consideration.

All of the imaging sequences will see tremendous gains from increases in polarization,. and we will show in Chapter 6 that likely improvements to the system will result in 2D CSI images with resolution comparable to ^{1}H imaging (i.e., 10 μL voxels). These high-resolution CSI images will enable studies to be made of suitable organs such as the heart, kidney and brain, and measurement of the combined gas/tissue images in the lungs will facilitate. Although we have not focused on ^{129}Xe lung imaging extensively in this thesis, the ^{129}Xe-gas images of the CSI dataset of figure 4.8 add figure 4.9 clearly points to the complementary nature of ^{1}H and ^{129}Xe imaging, as dark air spaces in ^{1}H images are regions of ^{129}Xe-gas signal intensity. It may be of substantial clinical significance to extend the nuclear

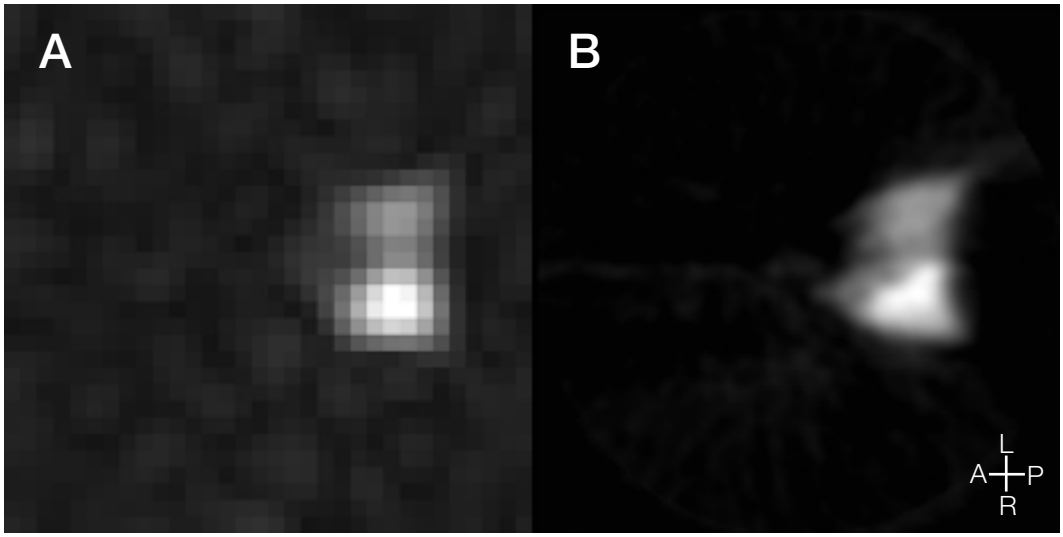

Figure 4.15: Coronal gas imaging: (**A**) CSI and (**B**) projection reconstruction (PR) ^{129}Xe gas imaging. FOV is 100 mm $\times$ 100 mm in both. CSI: zero-filled from 16 $\times$ 16 to 32 $\times$ 32, 8 minutes acquisition (*i.e.*, the sum of two 4-minute acquisitions.) PR: 64 views, 48 s total acquisition. Both images acquired with a 200 μs RF pulse width, 100 ms pre-delay, P_2 gated.

medicine ventilation/perfusion (V/Q) scan which is the current standard for functional lung imaging [140] to laser-polarized ^{129}Xe CSI. Given the large chemical shift separation for ^{129}Xe-gas and ^{129}Xe-tissue, we have demonstrated how one can easily acquire gas ventilation and tissue perfusion images in rats with a single procedure. With the anticipated increases in SNR outlined in Chapter 6 and corresponding improved spatial and temporal resolution, the extension to larger animals and humans should be actively pursued.

Chapter 5

Method for measurement of tissue perfusion with laser-polarized ^{129}Xe NMR

This chapter presents a framework whereby laser polarized ^{129}Xe NMR can directly measure tissue perfusion *in vivo*. In general, the time-dependent ^{129}Xe tissue NMR signal depends on the tissue perfusion rate (f_{BT}), the local ^{129}Xe longitudinal relaxation time (T_1), and the NMR sampling parameters. We present a model of the *in vivo* transport of laser polarized ^{129}Xe to tissue under realistic experimental NMR conditions, and demonstrate how control of the NMR parameters allow f_{BT} and T_1 to be independently extracted from the steady-state ^{129}Xe-tissue signal. *In vivo* rodent ^{129}Xe NMR results are then used to estimate the signal-to-noise ratio (SNR) attainable with this technique. We estimate that an inhaled 30% xenon/70% O_2 mixture polarized to 5% provides sufficient SNR in rodent grey matter to make this new ^{129}Xe magnetic tracer method a practical quantitative technique for measurement of perfusion and ^{129}Xe tissue T_1, enabling tomographic T_1 and perfusion maps. The laser-polarized ^{129}Xe magnetic resonance tracer method may also be applicable to the measurement of rCBF and functional neuronal activation.

The present chapter begins with a review of the kinetics of freely diffusible indicators, common to all tracer techniques for quantitative perfusion measurement. The features and limitations of current methods are then discussed. The ^{129}Xe magnetic resonance tracer theory and method are then presented, with the goal of quantitative non-invasive method for measurement of blood flow.

5.1 Diffusible Tracer Kinetics

In the body, blood passes from artery to vein through a capillary bed which provides the surface through which substances diffuse into tissue. Perfusion of tissue by blood provides cells the materials required for their function (*e.g.*, O_2 and nutrients). The availability of any substance to a tissue depends on the blood flow to the tissue. Measurement of the rate of blood flow into tissue (*i.e.*, perfusion) yields information about organ viability and function; this is extremely important in both biomedical research and clinical studies.

The first non-invasive technique for the quantitative measurement of tissue perfusion was outlined by Kety in 1951 [17], and is based on the study of the exchange of biologically inert diffusible tracers[1] between blood and tissue. When an inert gas tracer is introduced by respiration, blood flow carries it to the tissues of the body. The time rate of concentration of tracer within the tissue follows from the conservation of mass at the capillary level, known in circulatory physiology as the Fick principle [147]: the amount of diffusible tracer taken up by the tissue per unit time is equal to the quantity brought to the tissue by arterial blood minus the quantity carried away. If we assume tracer leaves perfused tissue only by venous outflow then,

$$\frac{dQ_i}{dt} = V\frac{dC_i}{dt} = F_i(C_a - C_v), \tag{5.1}$$

where Q_i is the mass of tracer in the tissue i, V is the volume of perfused tissue, C_i is the tracer concentration in tissue i (typically g/mL), F_i is the blood flow to the tissue (typically mL/min), and C_a, and C_v are the local tracer concentration in arterial and venous blood (g/mL). It is common to divide through by the volume of the perfused tissue and rewrite equation 5.1 as

$$\frac{dC_i}{dt} = f_i(C_a - C_v), \tag{5.2}$$

where f_i is the blood flow per unit volume of tissue (typically given as mL mL^{-1} min^{-1}).

1.Biologically inert diffusible tracers, *i.e.,* substances which are not metabolized by or produced in the tissue under study, include ^{131}I-trifluroiodomethane [141], ^{14}C-alcohols [142], ^{14}C-antipyrine [143], ^{14}C-iodoantipyrine [135], and the gases Xe [144], Kr [145], and H_2 [146].

If we assume free diffusion of the tracer across the capillary, and the equilibration of tracer partial pressure between tissue and venous blood, then the tissue and blood concentrations of tracer are related by the partition coefficient λ_i,

$$C_v = \frac{C_i}{\lambda_i}. \tag{5.3}$$

The essential result of the Kety tracer method is obtained by combining equation 5.2 and equation 5.3:

$$\frac{dC_i}{dt} = f_i\left(C_a - \frac{C_i}{\lambda_i}\right). \tag{5.4}$$

The blood flow to a given homogeneous region of perfused tissue (e.g., the brain) can be calculated from equation 5.4 if both λ and the time dependence of the tissue concentration of tracer, $C_i(t)$, are known. It should be noted that blood flow is often expressed in the literature per unit mass of tissue (including its blood), *i.e.*, mL g^{-1} min^{-1}.

The validity of all tracer methods derived from Kety's formulation depend upon the assumption inherent in equation 5.3: instantaneous tissue/venous blood tracer equilibrium at the level of the single capillary. It is assumed that equilibration of tracer in tissue with arterial blood is limited only by perfusion, not by the diffusion of tracer through the capillary walls and extravascular tissues. There is considerable evidence that inert gases such as xenon are sufficiently diffusible between blood and tissue to satisfy this requirement [17, 141, 148], and therefore the assumption of instantaneous diffusion equilibrium is a valid one. For many other tracer substances, however, this is not true (*e.g.*, ^{14}C-antipyrine) [142, 148].

The assumption of instantaneous diffusion implies that the concentration of tracer in venous blood is continuously in equilibrium with the tissue which it drains. This is possible only if the tissue is homogeneous with respect to blood flow and tracer solubility [149]. This requirement for homogeneous tissue perfusion in the brain is approached in the limit that the regions of interest are the small, anatomically discrete structures of the brain— the ultimate goal of our method is to measure and image blood flow at this distance scale. Additionally, the presence of arteriovenous shunts would tend to limit the equilibration of

the tissue with the blood perfusing it. However anatomical studies find that no such shunts exist in the brain [150, 151].

5.2 Tracer Methods

The the autoradiographic method of rCBF measurement was the first tomographic application of the principles of inert gas exchange between blood and tissue. Autoradiography was developed by Landau *et al.* [152], and Freygang and Sokoloff [141], using the inert gas ^{131}I-labeled trifluoroiodomethane, $CF_3{}^{131}I$, as a flow tracer. Following the administration of the tracer gas, the animal was decapitated, and the head was immediately frozen in LN_2. The frozen head was sawed into 5 mm thick slices, and the sections placed on x-ray film to produce images of the postmortem tissue density of radiotracer. Autoradiographs accurately represent anatomical structures, and given a tracer with a known tissue/blood partition coefficient, are simple to analyze. Freygang and Sokoloff observed varying degrees of rCBF alteration in response to hypo- and hypercapnia [141]. They also observed local increases in blood flow correlating with visual stimulation, concluding that the autoradiographical method for measuring rCBF was capable of responding to functional activation. There is one significant disadvantage to the autoradiography method: each measurement requires animal sacrifice and hence this method is not suited to multiple studies in the same animal, nor can it be applied to humans.

The tremendous advances in cerebrovascular physiology and metabolism that came from the autoradiographic method motivated the further development of less invasive tracer techniques. Radiotracer techniques such as positron emission tomography (PET) with ^{18}F and ^{15}O–H_2O and single photon emission tomography (SPECT) with ^{133}Xe [19], permit "*in vivo* autoradiographs" to be made and analyzed using simple extensions to the Kety model [153-155]. Additionally, transmission computed tomography (CT) techniques using nonradioactive xenon gas [23] analyze the dynamics of the radiographic enhancement produced by the inhaled high-Z Xe nucleus with sequential CT. These nuclear medicine techniques are limited for several reasons, including radioactive tracer dose limitations, tracer recirculation, and low signal-to-noise. Additionally, PET techniques have an inherent spatial resolution of 2–4 mm due to the finite lifetimes of

positrons in tissue [156] and require a complementary imaging technique such as MRI or CT for accurate anatomical mapping of the PET functional information.

Magnetic resonance imaging provides an anatomical specificity unmatched by other non-invasive imaging methods. The ability to map perfusion with MRI would allow non-invasive, high-resolution evaluation of both tissue viability and function. MRI based perfusion imaging methods are not subject to the intrinsic limitations of radiotracer or X-ray techniques and can provide functional information and anatomical registration with a single modality and apparatus. Two distinct MRI tracer techniques have been developed to measure perfusion: arterial spin labeling (ASL) of endogenous water, and injected exogenous MR contrast.

In the ASL method, moving spins in flowing blood (typically water proton nuclear spins flowing to the brain in the arterial blood) are continuously polarization-saturated in the neck with localized RF [157-159]. This perturbs their longitudinal magnetization, thus "labeling" them. The labeled spins flow into the brain and diffuse into brain tissue and exchange with brain tissue water, and the steady-state regional tissue magnetization thus depends on the rate of tissue perfusion. Analysis of perfusion with ASL is similar to steady-state PET and SPECT methods, in which a radiotracer with a moderately short half-life (e.g., ^{15}O-H_2O) is administered continuously, and a steady-state tracer accumulation within various tissue compartments is measured. The quantitative determination of perfusion with this method depends on a number of parameters (including relaxation rates), which are usually determined in separate experiments [160, 161]. Spin labeling techniques currently suffer from low SNR, which affects both the speed at which perfusion maps can be made and the lower limit of detectable perfusion. Additionally, ASL is limited by the *in vivo* ^{1}H T_1 (of order 1 s at 1.5 T) which restricts the distance between the labeling and measuring regions.

The second MRI method, the exogenous contrast technique, is moderately invasive, requiring injection of a paramagnetic contrast agent. Exogenous MR contrast agents are injected as a bolus into the body. They come in two varieties: relaxivity agents and magnetic susceptibility agents. Relaxivity contrast agents shorten the proton longitudinal relaxation time (T_1) through a dipolar interaction between the proton nuclear spin and the paramagnetic contrast agent. Magnetic susceptibility contrast agents shorten the proton

transverse relaxation time (T_2) because of the strong dephasing local magnetic field gradients induced by the high magnetic susceptibility of the agent [162, 163]. The transit time of the bolus of contrast agent through tissue is very short (a few seconds), and unlike the steady-state approach used in ASL, the wash-in and wash-out kinetics of the changes in proton signal intensity are measured. There is a nonlinear relationship between the MR signal and the contrast agent concentration [164]. This leads to difficulty in the determination of tissue perfusion from the need to convert changes in regional MR signal intensity to contrast agent concentration.

Both of these MR perfusion imaging methods rely on the measurement of a difference in signal intensity between a magnetic-labeled state and a control state. This is proportional to perfusion but is not necessarily quantitative. Thus in these methods, MRI does not directly measure the tracer concentration; it must be measured indirectly through its small effect on MR signal intensity. As a result of the considerable ^{1}H signal background in both cases, both techniques suffer from low SNR. ASL techniques can partially overcome this by signal averaging, but injected contrast methods are dose limited as to the amount of contrast that can given, and by the contamination of the measurement by tracer recirculation.

There is an increasing interest in the use of MR imaging in mapping flow and blood oxygenation changes for "activation" studies. Although quantitative perfusion measurements are not necessarily needed to map brain function for applications such as presurgical mapping, the additional information obtained by quantitative measure of perfusion changes could enhance the evaluation of complex diseases. Since the pioneering work of Roy and Sherrington [27], it is known that there exists a close spatial and temporal correspondence between local changes in brain neuronal activity and changes in regional cerebral blood flow (rCBF). Although the details of this flow regulation are not completely understood [165], it established that blood flow changes by 50% or more in grey matter within an area close to that of increased electrical activity [166], and within a few seconds after the onset of increased activity [167]. The PET technique [168] has been used for many years to measure rCBF during functional brain activation and is regarded by many as the "gold-standard" for quantitative rCBF measurement. The most widespread MRI technique for brain mapping is the functional MRI (fMRI) technique. The metabolic changes

associated with brain functional activation affect the concentration of paramagnetic deoxyhemoglobin content in tissue (the BOLD effect). However, functionally-induced changes in MR image intensity depend on several parameters, including blood flow, hematocrit, oxygen extraction, local vascular geometry, and baseline blood oxygen saturation [167]. Therefore, fMRI measures of regional metabolic brain activity, though tightly coupled to perfusion, cannot currently be used to measure perfusion quantitatively [169].

5.3 Laser-polarized ^{129}Xe MR Tracer Theory

This section presents a new magnetic resonance tracer method for *in vivo* quantitative perfusion measurement. The very high SNR per atom of laser-polarized ^{129}Xe, the zero biological background MR signal from the ^{129}Xe nuclei, and the desirable chemical and biological properties of xenon make it possible to combine the advantages of MR based perfusion methods with the strengths of freely diffusible tracer methods. I will show that this new technique differs from other MR-based perfusion techniques in that changes in the regional ^{129}Xe MR signal intensity correspond to changes in tracer concentration, and as a result the laser-polarized ^{129}Xe magnetic resonance tracer technique can be regarded as directly comparable with PET tracer techniques, but is not subject to many of the limitations of radiotracer techniques.

After introduction into the lungs by ventilation, laser-polarized ^{129}Xe is transported by blood flow and perfuses into tissue. A schematic of the flow of laser-polarized ^{129}Xe magnetization *in vivo* is shown in figure 5.1. The ^{129}Xe MR signal from perfused tissue is entirely due to in-flowing magnetization from the blood, and the ^{129}Xe NMR signal in a given volume of tissue is a measure of the total ^{129}Xe magnetic moment in that compartment. The transport of inert gases through the body is well described by the Kety-Schmidt equations (*e.g.*, equation 5.4) which are widely used in models of xenon uptake for cerebral blood flow studies [170]. These equations are formulated in terms of tracer concentration per unit mass of tissue, but can be modified to describe ^{129}Xe magnetization by the inclusion of NMR relaxation rates ($1/T_1$). Peled *et al.* [171] and Martin *et al.* [172] have published models which extend the Kety-Schmidt model in this way. In the region where ^{129}Xe magnetization is sampled by RF pulsing (*i.e.*, the dashed region of figure 5.1), the

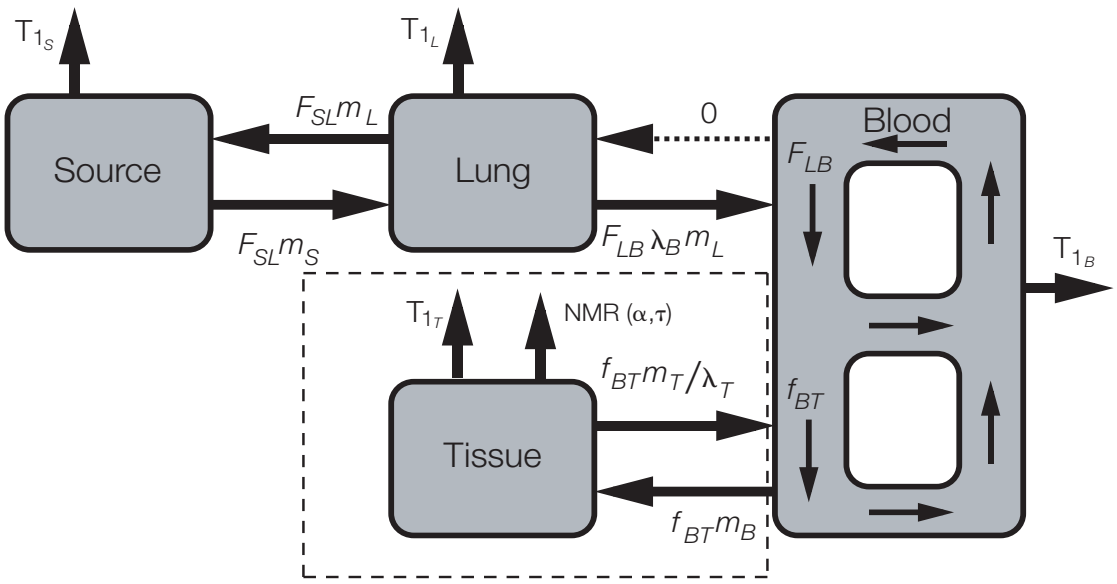

Figure 5.1: Schematic of the flow of inhaled laser-polarized ^{129}Xe magnetization *in vivo*. The long arrows indicate magnetization exchange between compartments, and the short arrows indicate ^{129}Xe magnetization destruction mechanisms. The dashed region represents the region of NMR pulsing. T_{1i}, λ_i, and m_i are the longitudinal relaxation time, xenon partition coefficient, and magnetization, respectively for i = (**S**ource, **L**ung, **B**lood, and **T**issue). F_{SL} is the rate of flow from the polarized ^{129}Xe source to the lungs, F_{LB} is the total flow of blood through the lungs, and f_{BT} is the fractional blood flow to the tissue. The ^{129}Xe tissue resonance RF tip angle, and the time between RF pulses are α and τ, respectively.

discrete losses of longitudinal magnetization must be accounted for; a model to describe the *in vivo* time evolution of laser-polarized ^{129}Xe magnetization in the dashed region of figure 5.1 is now presented.

Given that ^{129}Xe is a freely diffusible tracer *in vivo* [173], in the absence of NMR pulsing, the time evolution of the tissue magnetization is

$$\frac{d}{dt}M_T(t) \;=\; M_B^{tissue} f_{BT} - M_T(t)\left(\frac{f_{BT}}{\lambda} + \frac{1}{T_1}\right), \tag{5.5}$$

where $M_T(t)$ is the longitudinal ^{129}Xe magnetization in the tissue of interest (per unit volume of tissue), $M_B{}^{tissue}$ is the longitudinal ^{129}Xe blood magnetization at the tissue of inter-

est (per unit volume of blood), f_{BT} is the fractional blood flow (*i.e.*, perfusion) to the tissue, λ is the xenon blood/tissue partition coefficient, and T_1 is the longitudinal relaxation time of ^{129}Xe tissue magnetization. MR imaging experiment typically define perfusion as the volume of blood delivered to a unit volume of tissue per unit time. In this case, the units of f_{BT} in this case are milliliters of blood per milliliters of tissue per minute.

Longitudinal magnetization in conventional NMR arises *in situ* from the induced Boltzmann polarization, but in the description of laser-polarized ^{129}Xe magnetization of equation 5.5, T_1 appears only as a sink of laser-polarized ^{129}Xe magnetization. This is because the laser-polarized ^{129}Xe polarization *in vivo* is orders of magnitude greater than the Boltzmann polarization for any magnetic field used in NMR. The form of equation 5.5 is similar to equations used in nuclear medicine to describe the wash-in of radiotracers (e.g., ^{15}O-H_2O in PET). However, whereas the half-life of a radioisotope is independent of its environment, the ^{129}Xe T_1 can depend on both the tissue composition and the local blood oxygenation level.

The ^{129}Xe magnetization in arterial blood that perfuses the tissue of interest, M_B^{tissue}, is analogous to the "arterial input function" in the language of tracer kinetics. We assume that M_B^{tissue} can be made time-independent since ^{129}Xe magnetization can be delivered by inhalation for times long relative to the typical several-second heart-tissue transit time. We neglect in equation 5.5 any contribution from ^{129}Xe magnetization returning by recirculation, as it is expected to be very small given the short ^{129}Xe T_1 in venous blood (approximately 4 s) [112] and the long total circulation times (approximately 20 s in humans [174]). Subject to the initial condition that the tissue magnetization is fully relaxed $M_T(t=0)=0$, the solution to equation 5.5 for the case where M_B^{tissue} is time-independent, is given by

$$M_T(t) \;=\; M_{EQ}\left(1 - e^{-\left(\frac{f_{BT}}{\lambda} + \frac{1}{T_1}\right)t}\right), \tag{5.6}$$

where M_{EQ} is the steady-state value of $M_T(t)$,

$$M_{EQ} \;=\; \frac{f_{BT} M_B^{tissue}}{\frac{f_{BT}}{\lambda} + \frac{1}{T_1}}. \tag{5.7}$$

In order to realistically describe the NMR detectable ^{129}Xe tissue signal, the loss of magnetization due to discrete NMR pulsing is now included. Chemical shifts of ^{129}Xe allow spectral separation of gas, blood, and tissue resonances, and in the following discussion NMR tips are assumed to be applied only to the ^{129}Xe tissue resonance. Following the notation of Look and Locker [175], M_N^- and M_N^+ are the longitudinal tissue magnetizations just prior to, and immediately after the N^{th} pulse. The time between NMR tips is τ. The fraction of longitudinal magnetization remaining immediately after a tip of angle α is simply $cos\,\alpha$, so we can write

$$M_N^+ = M_N^- cos\alpha\,. \tag{5.8}$$

Between tips, the longitudinal tissue magnetization approaches M_{EQ}, as given by equation 5.6. The time-dependence of the longitudinal tissue magnetization, is plotted in figure 5.2. It is calculated with equation 5.6 for the time interval between pulses and with equation 5.8 for the loss after each pulse.

An exact solution for the tissue magnetization as a function of pulse number is desired. Rewriting $M_T(t)$ in terms of the discrete time interval τ, equation 5.6 becomes

$$M_{N+1}^- = M_N^+ + (M_{EQ} - M_N^+)\left(1 - e^{-\left(\frac{f_{BT}}{\lambda} + \frac{1}{T_1}\right)\tau}\right). \tag{5.9}$$

Combining equation 5.8 and equation 5.9 and writing in terms of M_N^-:

$$M_{N+1}^- = M_N^- cos\alpha + (M_{EQ} - M_N^- cos\alpha)\left(1 - e^{-\left(\frac{f_{BT}}{\lambda} + \frac{1}{T_1}\right)\tau}\right). \tag{5.10}$$

Making the substitution $u \equiv e^{-\left(\frac{f_{BT}}{\lambda} + \frac{1}{T_1}\right)\tau}$, $y \equiv cos\alpha$, and defining the initial tissue magnetization as M_0, M_N is related to M_0 by induction according to equation 5.10:

$$M_1 = uyM_0 + (1-u)M_{EQ} \tag{5.11}$$

$$M_2 = u^2y^2M_0 + (1-u)(1+uy)M_{EQ} \tag{5.12}$$

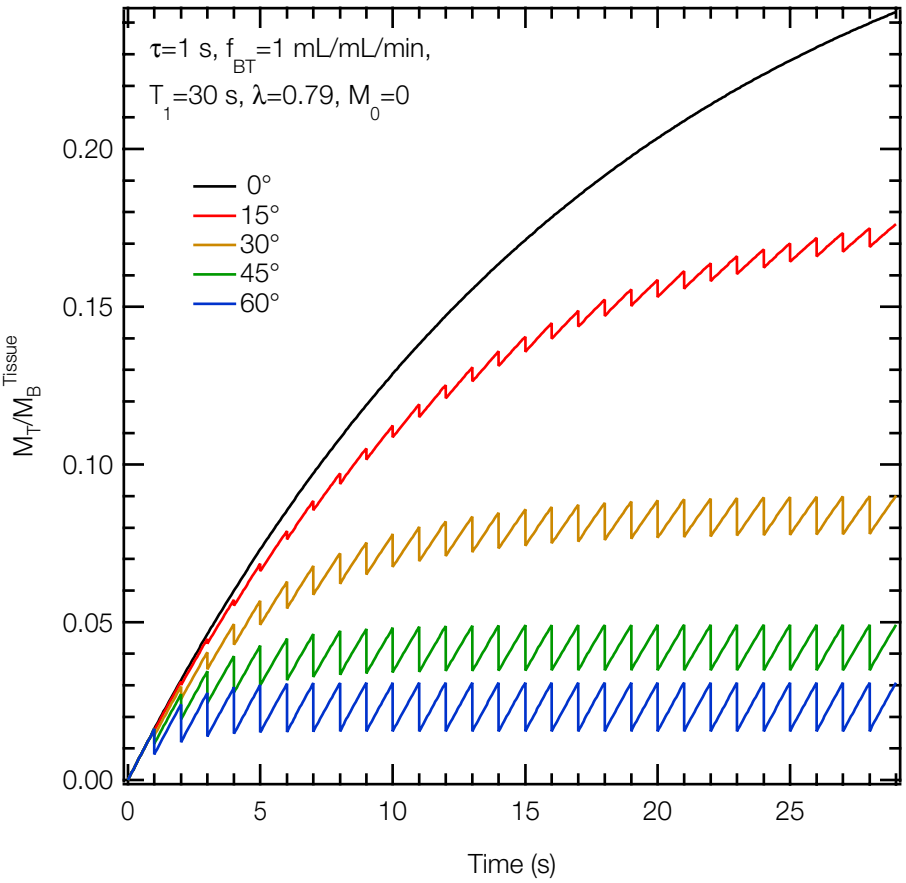

Figure 5.2: Time-dependence of the longitudinal ^{129}Xe tissue magnetization relative to the steady-state blood magnetization at the tissue, M_B^{tissue}, evaluated for several tip angles. Typical rat grey matter parameters are used for f_{BT}, T_1, and λ. The 0° curve is well described by the models of Martin *et al.*, and Peled *et al.* [171, 172].

$$M_3 = u^3 y^3 M_0 + (1-u)(1+uy+u^2y^2)M_{EQ} \tag{5.13}$$

.
.
.

$$M_N = u^N y^N M_0 + M_{EQ}(1-u)\sum_{q=0}^{N-1} u^q y^q, \tag{5.14}$$

where we now drop the superscripts. By the convergence of geometric sums, equation 5.14

is rewritten

$$M_N = M_0 u^N y^N + M_{EQ}(1-u)\left(\frac{1-u^N y^N}{1-uy}\right). \tag{5.15}$$

Explicitly, equation 5.15 is

$$M_N = M_0 cos\alpha^N \; e^{-N\left(\frac{f_{BT}}{\lambda}+\frac{1}{T_1}\right)\tau} + \frac{f_{BT}M_B^{tissue}}{\left(\frac{f_{BT}}{\lambda}+\frac{1}{T_1}\right)}\left(1-e^{-\left(\frac{f_{BT}}{\lambda}+\frac{1}{T_1}\right)\tau}\right)\frac{\left[1-cos\alpha^N \; e^{-N\left(\frac{f_{BT}}{\lambda}+\frac{1}{T_1}\right)\tau}\right]}{\left[1-cos\alpha e^{-\left(\frac{f_{BT}}{\lambda}+\frac{1}{T_1}\right)\tau}\right]} \tag{5.16}$$

The detected time-dependent tissue NMR signal is proportional to the transverse component of M_N after a tip,

$$S_N \propto M_N sin\alpha\,. \tag{5.17}$$

In steady-state ($N \to \infty$), the ^{129}Xe tissue signal is (from equation 5.17)

$$S_\infty \propto \frac{f_{BT}M_B^{tissue}}{\left(\frac{f_{BT}}{\lambda}+\frac{1}{T_1}\right)}\frac{\left(1-e^{-\left(\frac{f_{BT}}{\lambda}+\frac{1}{T_1}\right)\tau}\right)}{\left[1-cos\alpha e^{-\left(\frac{f_{BT}}{\lambda}+\frac{1}{T_1}\right)\tau}\right]} sin\alpha\,. \tag{5.18}$$

The calculated *in vivo* tissue uptake of polarized ^{129}Xe given by equation 5.17 is shown in figure 5.3. The tissue signal is plotted in terms of $M_B{}^{tissue}$, the steady-state blood magnetization at the tissue. Typical rodent grey matter parameters were used in generating this family of curves: f_{BT} = 1 mL/mL/min [115], T_1 = 30 s [25], and λ = 0.79 [90]. The rate at which the ^{129}Xe tissue signal approaches its steady-state value strongly depends on the NMR parameters: tip angle α and sampling rate $1/\tau$. The destruction of ^{129}Xe magnetization by RF pulsing is under experimental control and can be adjusted to isolate certain features of ^{129}Xe magnetization *in vivo*.

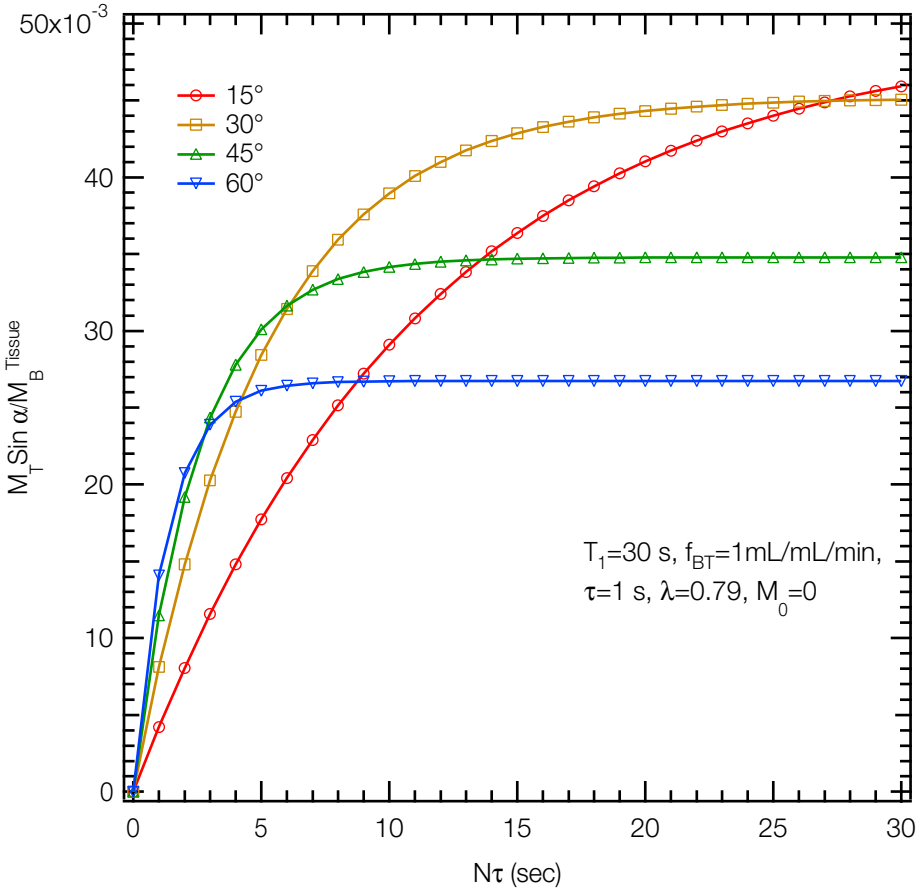

Figure 5.3: Time dependence of the laser-polarized ^{129}Xe tissue signal from equation 5.17, plotted relative to the steady-state blood magnetization at the tissue, M_B^{tissue}. The rate at which the ^{129}Xe tissue signal reaches steady-state strongly depends on the ^{129}Xe tissue resonance tip angle α, and the NMR pulse rate, τ. Typical rat grey matter parameters (f_{BT}, T_1, and λ) were used in generating this family of curves. For all these curves, $\tau = 1$ s.

The steady-state ^{129}Xe tissue signal of equation 5.18 is plotted as a function of f_{BT} in figure 5.4. At low tip angles the contribution of f_{BT} to the steady-state ^{129}Xe tissue signal cannot be determined without knowledge of T_1. However, at high tip angles relaxation due to NMR sampling dominates, and the steady-state ^{129}Xe tissue signal is relatively independent of T_1. This is clearly seen in figure 5.4, where at large tip angles the influence of local T_1 on the steady state ^{129}Xe magnetization is negligible. The steady-state ^{129}Xe tissue signal in this high tip-angle regime is simply proportional to blood flow, independent of T_1. The steady-state ^{129}Xe tissue signal of equation 5.18 is plotted as a function of α in fig-

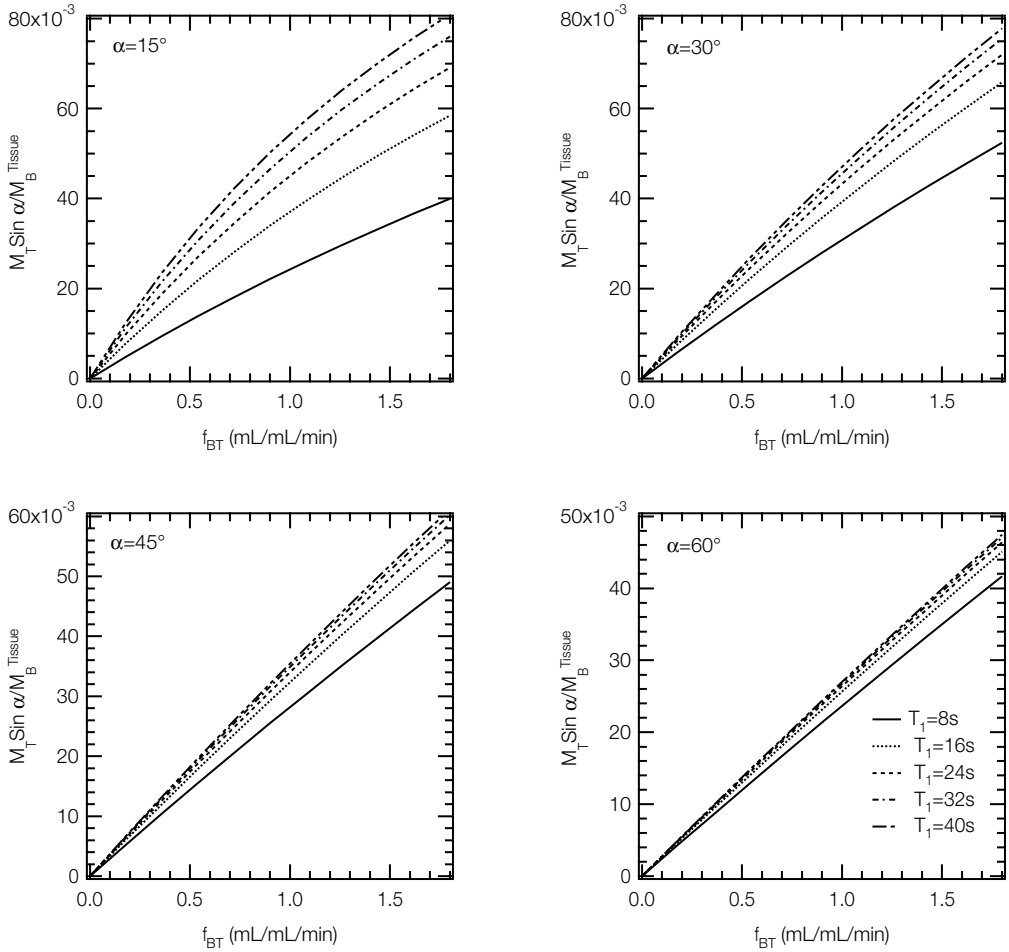

Figure 5.4: Steady-state ^{129}Xe tissue signal from equation 5.18 plotted as a function of f_{BT}, for a family of tissue T_1. For all these curves, $\lambda = 0.79$ and $\tau = 1$ s.

ure 5.5 and figure 5.6. These figures illustrate a method for independent extraction of T_1 and f_{BT}; the steady-state ^{129}Xe tissue signal measured as a function of α can be fit to equation 5.18 to extract both T_1 and f_{BT}. A simulation of this method is presented below.

5.4 Estimate of Steady-State Brain SNR

As demonstrated in Chapter 4, ^{129}Xe polarized to approximately 5% and delivered to rats by inhalation results in a ^{129}Xe magnetic moment density in brain tissue sufficiently large to image (figure 4.14). The ^{129}Xe *in vivo* brain spectrum (figure 4.12) reveals a rich ^{129}Xe dissolved-phase structure, dominated by the ^{129}Xe resonance at 195 ppm. Having

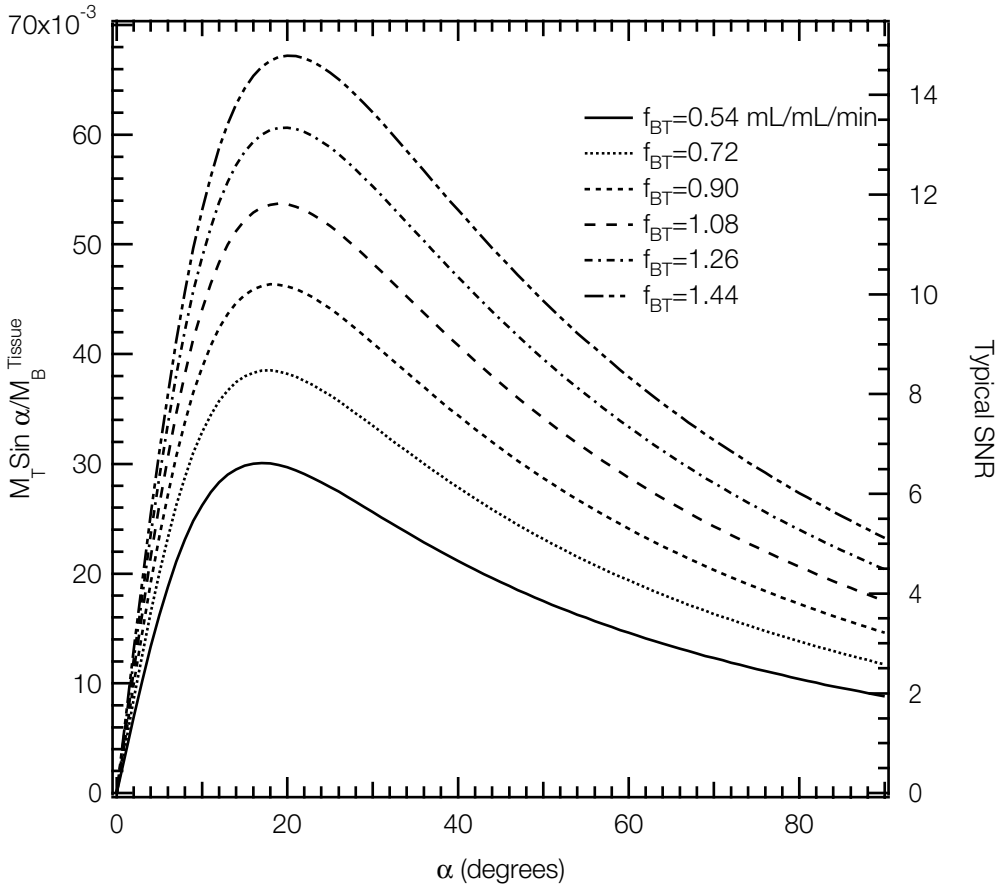

Figure 5.5: Steady state ^{129}Xe tissue signal (equation 5.18) plotted as a function of tissue tip angle α, for several values of f_{BT}. For all these curves, τ = 1 s and the typical rodent grey matter parameters of T_1 = 30 s and λ = 0.79 are used. Typical experimental SNR (per pulse) obtained with the scale factor ζ is shown on right-hand scale (see section 5.4 for details).

observed ^{129}Xe-tissue NMR resonances in the brain, the next step is a feasibility estimate of the ^{129}Xe magnetic resonance tracer method of perfusion measurement, described in section 5.3, using experimentally reasonable parameters for rat grey matter. The ability to make a measurement of tissue perfusion with laser-polarized ^{129}Xe NMR relies on the attainable signal-to-noise ratio (SNR) of the ^{129}Xe tissue and blood resonances. In this section, the measured steady-state ^{129}Xe-blood signal from the rat thorax is used to scale the model of equation 5.18 to obtain an estimate of the steady-state ^{129}Xe-tissue SNR in rat grey matter. This estimate is used in section 5.5 for statistical simulations of the ^{129}Xe

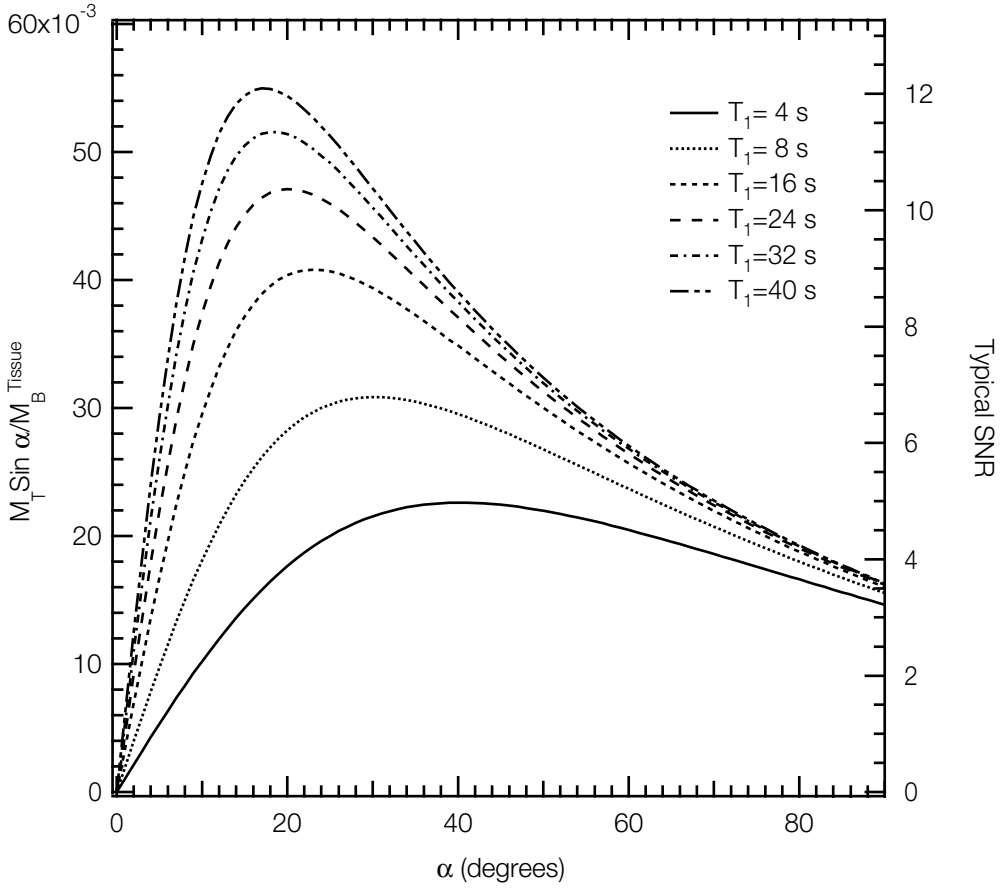

Figure 5.6: Steady state ^{129}Xe tissue signal (equation 5.18) plotted as a function of tissue tip angle α, for several values of tissue T_1. For all these curves, $\tau = 1$ s and the typical rodent grey matter parameters of $f_{BT} = 1$ mL/mL/min and $\lambda = 0.79$ are used. As in figure 5.4, the typical experimental SNR (per pulse) obtained with the scale factor ζ is shown on right-hand scale.

magnetic resonance tracer method. The tissue SNR estimate is then discussed in relationship to our *in vivo* rat brain spectroscopy results.

Estimates of the SNR of laser-polarized ^{129}Xe in perfused brain tissue relative to the SNR of proton MRI have been made previously [171, 172]. These estimates use compartmental models to transport inspired laser-polarized ^{129}Xe gas through the lungs, arterial blood, and finally into cerebral tissue, and the ratio of the cerebral polarized ^{129}Xe SNR to the ^{1}H SNR is given as the ratio of cerebral tissue ^{129}Xe magnetization to the typical *in vivo* ^{1}H magnetization. These models neglect the destruction of ^{129}Xe magnetization by NMR

pulsing and can not be used to estimate the ^{129}Xe cerebral magnetization except in the limit of small NMR tip angle. One way to calculate the ^{129}Xe tissue magnetization in the presence of NMR tipping would be to extend these compartmental models of [171, 172] with equation for the dashed region of figure 5.1. Instead, we now present an estimate of typical ^{129}Xe tissue SNR based on our *in vivo* ^{129}Xe measurements, obtained with the polarizer operating in its typical configuration. We avoid the complication of additional model-dependent assumptions by looking at the actual ^{129}Xe NMR signal acquired under specific experimental conditions, including the *in vivo* efficiency of ^{129}Xe gas polarization delivery and knowledge of pulmonary parameters such as the ^{129}Xe T_1 in the lung.

5.4.1 ^{129}Xe blood magnetization

It is difficult to estimate the typical steady-state cerebral ^{129}Xe-tissue SNR from the *in vivo* ^{129}Xe brain spectroscopy results of section 4.6 because the ^{129}Xe grey matter resonance at 195 ppm never reached steady-state during the experiment. Additionally, the *in vivo* dynamics of the grey matter resonance (figure 4.13) were not the result of a simple uptake/ washout experiment from which the ^{129}Xe grey matter tissue saturation rate constant could be measured and the steady-state value calculated. Analysis of the ^{129}Xe grey matter resonance dynamics of figure 4.13 is complicated by the fact that the changing ^{129}Xe signal was due to many non-quantifiable factors including the anesthetic effect of the xenon itself. In order to circumvent some of the difficulty in interpreting the *in vivo* brain results, a measured steady-state ^{129}Xe-blood signal obtained from an experiment in the thorax will now be used to estimate the steady-state ^{129}Xe-blood magnetization at the brain, and this result and equation 5.18 used to scale the results shown in figure 5.5 and figure 5.6 in units of steady-state grey matter tissue SNR for an typical measurement.

The relevant *in vivo* thoracic results have been described in detail in Chapter 4. In particular, whole body ^{129}Xe CSI in the rat with a 30° tip angle was shown to constrain ^{129}Xe magnetization to the thorax by sampling and destroying ^{129}Xe longitudinal magnetization before it reaches distant organs. A ^{129}Xe spectrum obtained from the rat thorax is shown in figure 5.7. This spectrum was obtained while the ^{129}Xe blood resonance was at steady state (*i.e.*, t = 25 s from the dataset of figure 4.3). The intensity of the ^{129}Xe blood resonance in the thorax is dominated by polarized ^{129}Xe in oxygenated thoracic blood.

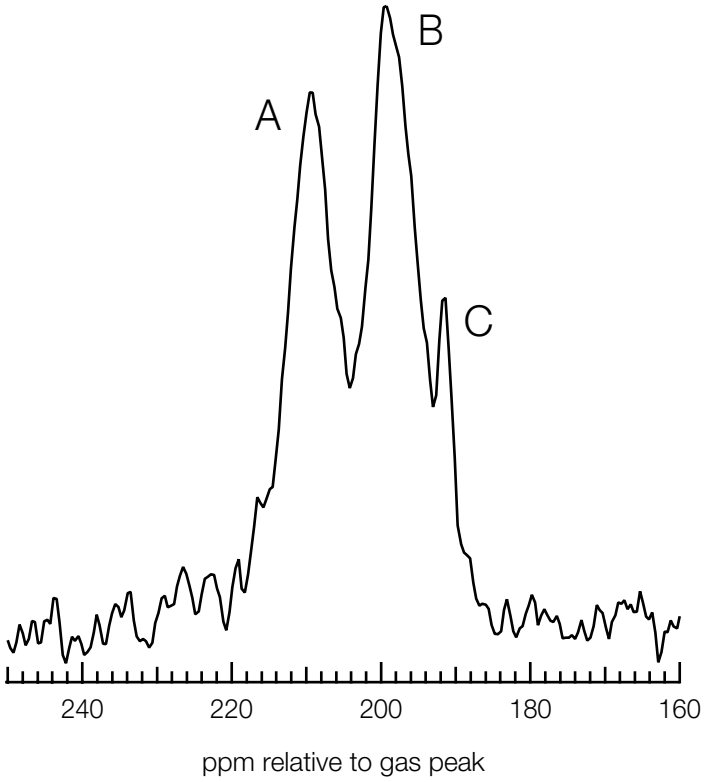

Figure 5.7: Individual NMR spectrum of laser-polarized ^{129}Xe in the rat thorax. This spectrum was obtained at t = 25 s, after the ^{129}Xe blood resonance had achieved steady state. This spectrum was obtained with two phase-cycled averages, with TR = 428 ms. The tip angle for the blood resonance is approximately 30°, and for the gas resonance is estimated at 1°.

Circulatory round-trip times are generally long with respect to the blood T_1, so we neglect the contribution from polarized ^{129}Xe in venous thoracic blood. We assume the volume of blood contributing to the thoracic ^{129}Xe blood signal, V_B^{thorax}, is equal to the left ventricle blood volume (*LVBV*) and the arterial fraction of the total pulmonary blood volume (*PBV*). Assuming that the pulmonary blood volume is split uniformly between the venous and arterial sides, the volume of blood contributing to the thoracic ^{129}Xe blood NMR signal is

$$V_B^{thorax} = LVBV + \frac{1}{2}PBV. \tag{5.19}$$

In steady-state, the total ^{129}Xe-blood magnetic moment in thoracic blood is

$$\mu_B^{thorax} = M_B^{thorax} V_B^{thorax}, \tag{5.20}$$

where $M_B{}^{thorax}$ is the steady-state ^{129}Xe thoracic blood magnetization (*i.e.*, the magnetic moment concentration). The NMR signal is the Fourier transform of the detected FID, and is characterized by a Lorentzian line. The area under this line (*i.e.*, the total signal energy) is proportional to the transverse magnetization. We define the thoracic ^{129}Xe-blood signal as

$$S_B^{thorax} \equiv \Gamma_B^{thorax} A_B^{thorax} = \kappa \mu_B^{thorax} sin\beta, \tag{5.21}$$

where $A_B{}^{thorax}$ and $\Gamma_B{}^{thorax}$ are the measured amplitude and width (FWHM) of the thoracic ^{129}Xe-blood resonance, κ is a factor which depends on the characteristics of the probe and receiver, and β is the ^{129}Xe-blood resonance tip angle. The SNR of the thoracic ^{129}Xe blood signal is defined in the frequency domain as

$$(SNR)_B^{thorax} \equiv \frac{A_B^{thorax}}{\sigma_N}, \tag{5.22}$$

where σ_N is the r.m.s. value of the noise signal [176]. Combining equation 5.20, 5.21, and 5.22, we write the steady-state thoracic ^{129}Xe-blood SNR as,

$$(SNR)_B^{thorax} = \frac{\kappa M_B^{thorax} V_B^{thorax} sin\beta}{\Gamma_B^{thorax} \sigma_N}. \tag{5.23}$$

In order to estimate ^{129}Xe tissue SNR, we need to estimate the blood magnetization at the tissue of interest, $M_B{}^{tissue}$. To do this, we again consider the case where NMR sampling is constrained to the tissue resonance and assume that ^{129}Xe-blood magnetization decays only due to T_1 in the blood. The steady-state value of the ^{129}Xe-blood thoracic magnetization $M_B{}^{thorax}$ is the source of magnetization which perfuses distant tissue, and so the arterial magnetization is simply

$$M_B^{tissue} = M_B^{thorax} e^{-t_{BT}/T_{1_B}}, \tag{5.24}$$

where $M_B{}^{tissue}$ is the steady-state ^{129}Xe blood magnetization at the tissue of interest, T_{1_B} is the ^{129}Xe relaxation time in arterial blood, and t_{BT} is the blood transit time from the left ventricle to the tissue of interest. Writing the thoracic blood SNR in terms of the blood magnetization at the tissue by combining equation 5.23 and equation 5.24,

$$(SNR)_B^{thorax} = \frac{\kappa M_B^{tissue} V_B^{thorax} sin\beta}{\Gamma_B^{thorax} \sigma_N e^{-t_{BT}/T_{1_B}}}. \tag{5.25}$$

5.4.2 ^{129}Xe tissue magnetization

We now estimate the steady-state ^{129}Xe brain SNR in the highly-perfused grey matter of the rat brain in order to evaluate the feasibility of measurement of cerebral perfusion with the ^{129}Xe magnetic resonance tracer method. As above, the total ^{129}Xe-tissue magnetic moment in the tissue of interest is

$$\mu_T = M_T V_T, \tag{5.26}$$

and the steady-state ^{129}Xe tissue SNR at the tissue of interest is

$$(SNR)_T = \frac{\kappa M_T V_T sin\alpha}{\Gamma_T \sigma_N}, \tag{5.27}$$

where M_T is the steady-state ^{129}Xe tissue magnetization, V_T is volume of tissue contributing to the ^{129}Xe tissue signal, α is the ^{129}Xe tissue resonance tip angle, and Γ_T is the FWHM of the ^{129}Xe-tissue resonance. We assume that the probe, receiver and noise characteristics (and thus κ) remain unchanged from equation 5.21.

5.4.3 Scaling factor ζ

The ratio of the steady-state transverse ^{129}Xe-tissue magnetization to the steady-state longitudinal ^{129}Xe-blood magnetization plotted in figure 5.5 and figure 5.6, can now be rewritten in terms of measurable quantities: the steady-state ^{129}Xe blood and tissue SNRs. Combining equation 5.25 and equation 5.27,

$$\frac{(SNR)_T}{(SNR)_B^{thorax}} = \frac{M_T sin\alpha}{M_B^{tissue}} \frac{V_T}{V_B^{thorax}} \frac{\Gamma_B^{thorax}}{\Gamma_T} \frac{e^{-t_{BT}/T_{1_B}}}{sin\beta}. \tag{5.28}$$

The steady-state ^{129}Xe-tissue SNR can now be expressed in terms of $(M_T sin\alpha) / M_B^{tissue}$,

$$(SNR)_T = \zeta \frac{M_T sin\alpha}{M_B^{tissue}} \tag{5.29}$$

where we have defined a dimensionless scale factor ζ,

$$\zeta \equiv \frac{(SNR)_B^{thorax}}{sin\beta} \frac{V_T}{V_B^{thorax}} \frac{\Gamma_B^{thorax}}{\Gamma_T} e^{-t_{BT}/T_{1_B}}. \tag{5.30}$$

Evaluating ζ for grey matter in a typical 250 g male Sprague-Dawley rat (with the parameter values specified in table 5.1), we obtain $\zeta = 220$. This value of ζ is used to scale $(M_T sin\alpha) / M_B^{tissue}$ in figure 5.5 and figure 5.6, with the estimated steady-state tissue SNR indicated along the right-hand axis of these figures. It is important to note both the limitations and assumptions of this *in vivo* ^{129}Xe-tissue SNR estimate. The measurement of the thoracic ^{129}Xe-blood SNR used to calculate ζ was made under typical polarizer operation conditions (approximately 4.5% ^{129}Xe polarization with a 60% xenon fraction) with typical NMR parameters (*i.e.*, probe quality factor *Q*, filling factor, and receiver bandwidth). These conditions are by no means assumed to be optimal, however the measurement of the ^{129}Xe-tissue resonance is assumed to be made with these parameters unchanged from the thoracic experiment. Additionally, the volume of thoracic blood contributing to the ^{129}Xe-blood signal and the volume of grey matter contributing to the ^{129}Xe-tissue resonance are estimates based on generic rat anatomy. All combined, these estimates represent perhaps order of magnitude certainty for the attainable ^{129}Xe-grey matter SNR with reasonable ^{129}Xe polarization levels.

5.4.4 Results from ^{129}Xe grey matter spectroscopy

As a check of the validity of the ^{129}Xe-grey matter SNR estimate, we now compare the calculated steady-state ^{129}Xe grey matter SNR for a 250 g male Sprague-Dawley rat with the measured *in vivo* experimental results. We assume typical rodent grey matter parameters of f_{BT} = 1 mL/mL/min, λ = 0.79, and T_1 = 32 s, and use the NMR parameters from figure

PBV (mL/100 g BW)	$LVBV$ (mL/100g BW)	V_B^{thorax} (mL, 250 g rat)	V_T (mL)	T_{1B} (sec)	t_{BT} (sec)	$(SNR)_B^{thorax}$	Γ_B^{thorax} (Hz)	Γ_T (Hz)	$sin\,\beta$
0.33[a]	0.1[a]	0.68[b]	1.2[c]	6[d]	2[e]	18[f]	150[g]	31[h]	0.5

Table 5.1: Parameters used to evaluate ζ for grey matter in a 250 g Sprague-Dawley rat.

a. from [118]
b. from equation 5.19.
c. Total brain volume is nominally 2 mL [177]. An 60% grey matter volume fraction is assumed here.
d. from [24].
e. estimated.
f. from figure 5.7.
g. from table 4.1.
h. from table 4.3.

4.12: $\alpha = 20°$ and $\tau = 500$ ms. Evaluating the model of equation 5.18 for grey matter we find $(M_T sin\alpha) / M_B^{tissue} = 0.033$. Scaling this number by the value of ζ calculated above and averaging over N pulses, we estimate a steady-state ^{129}Xe grey matter SNR of $7.3\sqrt{N}$. We now compare this to the ^{129}Xe brain spectrum acquired from a 250 g male Sprague-Dawley rat, shown in figure 4.12. This *in vivo* spectrum was acquired ($N = 256$ pulses) during xenon uptake, and the ^{129}Xe grey matter signal at 195 ppm never reached steady-state during the measurement; the dynamics of this resonance are shown in figure 4.13. The measured SNR of the 195 ppm resonance is 55. With $N = 256$, the estimated steady-state ^{129}Xe grey matter SNR is 116. It is not surprising that the predicted steady-state ^{129}Xe grey matter SNR is higher than the grey matter SNR obtained from a time-averaged spectrum acquired during uptake; however they agree within a factor of two.

In order to more carefully compare the steady-state ^{129}Xe-grey matter calculation to experiment, we examine an individual spectrum from the brain ^{129}Xe spectroscopy data set. The spectrum in figure 5.8 was acquired at $t = 32$ s after the start of xenon delivery, where the 195 ppm grey matter resonance was at its maximum value achieved during the run. Although ^{129}Xe-tissue steady-state was not achieved during this experiment, we expect the spectrum obtained at this time point to be closer to the steady-state value. The measured SNR of this spectrum is 6, and the calculated steady-state ^{129}Xe-grey matter SNR (with $N = 2$) is 10. Thus the scaling of figure 5.5 and figure 5.6 obtained with ζ can be considered representative of typical experimentally values within a factor of two.

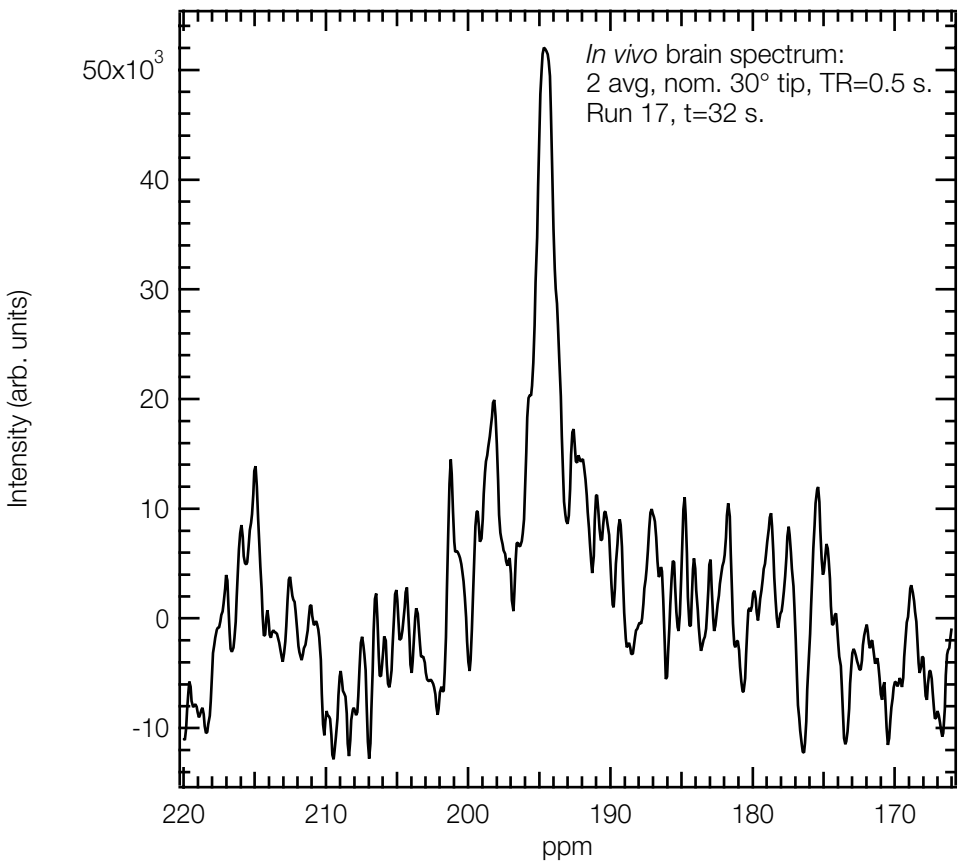

Figure 5.8: Individual ^{129}Xe spectrum acquired from the rat head. NMR pulsing was synchronous with the introduction of the Xe/O_2 mixture, and this spectrum was acquired at t = 32 s after the start of xenon delivery. The uptake dynamics are shown in figure 4.13. The spectrum shown here is the maximum tissue resonance achieved during this run, however ^{129}Xe-tissue steady-state was not achieved during this experiment. The SNR of the 195 ppm grey matter resonance ($N = 2$ pulses) is approximately 6.

5.5 Determination of f_{BT} and T_1

In order to determine the efficacy with which the tissue perfusion f_{BT} and the ^{129}Xe tissue depolarization time T_1 can be extracted from measurement of the tip angle dependence of the steady-state ^{129}Xe tissue NMR signal, we simulated realistic experimental datasets by evaluating equation 5.18 for a wide range of T_1 and f_{BT} values. For each value of T_1 and f_{BT}, we calculated $(M_T sin\alpha) / M_B^{tissue}$ for each of 9 values of the ^{129}Xe-tissue resonance tip angle $\alpha <$ spaced evenly from 10° to 90°. To these datasets, we added Gaussian-distributed

noise. We fixed the noise standard deviation and not the SNR as a function of T_1, f_{BT}, and α in these datasets to simulate experimental data realistically. Two noise levels were used, corresponding to a range of tissue SNR from 5 to 85 and from 1 to 17, over the ranges of α, f_{BT}, and T_1 used in the simulation. These noise levels were picked because the range of SNRs is typical of both our experimental results and our calculated ^{129}Xe brain tissue SNRs, for experiments of a reasonable number of pulses.

In order to extract f_{BT} and T_1 from the simulated data, it is convenient to rewrite equation 5.18 as:

$$\frac{M_T sin\alpha}{M_B^{tissue}} = A\frac{(1 - e^{-B\tau})}{[1 - cos\alpha e^{-B\tau}]} sin\alpha \tag{5.31}$$

where

$$A \equiv \frac{f_{BT}}{\left(\frac{f_{BT}}{\lambda} + \frac{1}{T_1}\right)}, \quad B \equiv \left(\frac{f_{BT}}{\lambda} + \frac{1}{T_1}\right). \tag{5.32}$$

The coefficients A and B are determined by a non-linear least-squares fit of equation 5.31 to the steady-state tissue signal measured as a function of α. T_1 and f_{BT} are then determined via the algebraic relationships

$$f_{BT} = AB, \quad T_1 = \frac{1}{B\left(1 - \frac{A}{\lambda}\right)}. \tag{5.33}$$

Note that the determination of f_{BT} from the steady-state tissue signal is independent of knowledge of the partition coefficient λ.

T_1 and f_{BT} were extracted from the best fit of equation 5.31 to the simulated datasets, with all parameters assumed to be known. This fitting procedure was run as a Monte Carlo, with the fit versus α for a given T_1 and f_{BT} repeated 10 times with random Gaussian noise added to each of the points. The result of this procedure is shown in figure 5.9 and figure 5.10, for two noise amplitudes. The best-fit parameter values of A and B were used in equation 5.33 to determine f_{BT} and T_1. These are plotted against the actual values, with the error bars indicating the standard deviation of the extracted parameter obtained from the Monte Carlo simulation. The solid lines are drawn to guide the eye along the line with

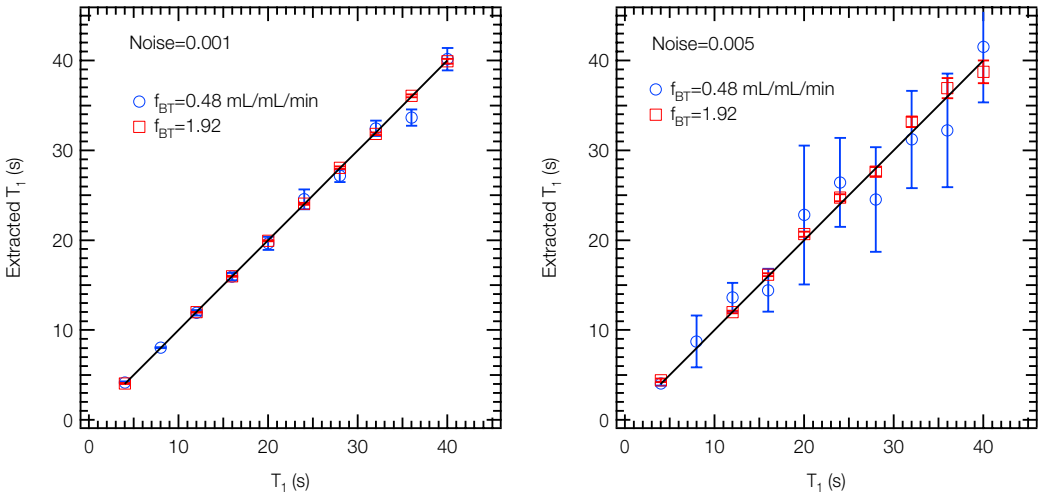

Figure 5.9: T_1 extracted from simulated data. The T_1 values obtained from a best fit of the simulated data to equation 5.31 are plotted against the actual T_1. The solid line is drawn to guide the eye along the line with unity slope. For all these curves, $\lambda = 0.79$ and $\tau = 1$ s.

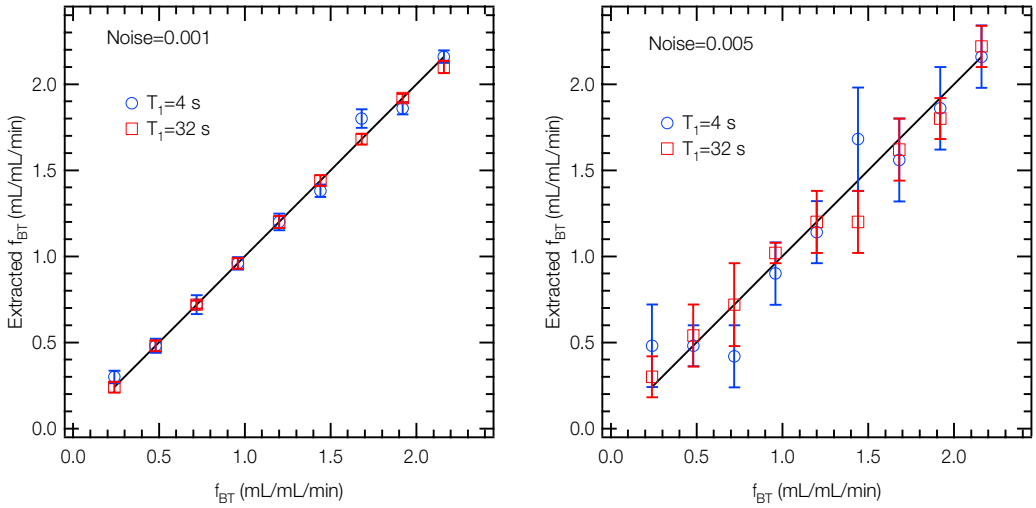

Figure 5.10: f_{BT} extracted from simulated data. The f_{BT} values obtained from a best fit of the simulated data to equation 5.31 are plotted against the actual f_{BT}. The solid line is drawn to guide the eye along the line with unity slope. For all these curves, $\lambda = 0.79$ and $\tau = 1$ s.

unity slope. It is clear from these results that this procedure provides accurate determinations of f_{BT} and T_1 and is feasible over the expected range of *in vivo* f_{BT} and T_1, for the SNR

range of ^{129}Xe-tissue NMR we have experimentally observed. These simulations demonstrate that straightforward control of NMR parameters will allow f_{BT} and T_1 to be extracted independently from the steady-state ^{129}Xe tissue signal.

5.6 Discussion

This section addresses the caveats and likely difficulties in the application of ^{129}Xe magnetic resonance tracer method for measurement of tissue perfusion. The possible applications of this new method are summarized in conclusion.

Absolute measurement of f_{BT} in the biologically relevant units of mL of blood/mL of tissue/min necessitates knowledge of the steady-state ^{129}Xe blood magnetization M_B^{tissue}, and quantitative perfusion maps can be calculated if this is known. Determination of M_B^{tissue} requires measurement of the ^{129}Xe NMR signal in a known volume of blood *in vivo*. In section 5.4, assumptions about the origin of the thoracic ^{129}Xe-blood signal under particular experimental conditions allowed M_B^{tissue} to be estimated. A general and more accurate approach is to use the ^{129}Xe blood signal from a single voxel of blood in the carotid artery (for rCBF measurement) or in the left heart chamber (for cardiac perfusion measurement) as a direct measure of M_B^{tissue}. Measurements of this type should be feasible since we have shown in Chapter 4 that it is possible to isolate the ^{129}Xe blood signal arising from a single voxel in the rodent heart using localized NMR spectroscopy. Depending on the voxel volume, many acquisitions may have to be averaged to get a reasonable blood signal from a voxel small enough to be homogeneously filled with blood in the carotid. If this is not possible, the blood signal in the heart may suffice as a measure of M_B^{tissue}. In particular, as the heart-brain transit time is reasonably short compared to the ^{129}Xe-blood T_1, NMR measurement of the ^{129}Xe blood magnetization in the left ventricle will be about 1.4 times larger than at the brain and may be more easily acquired given the large volume of blood in the left ventricle.

Image contrast in MRI comes from a variety of sources, and depending on the imaging sequence the resultant MR image depends on the physical parameters. Differences in the value of a physical parameter can be inferred from images acquired with sequences where the signal is most affected by variation in the desired parameter; these qualitative

images are known as "weighted" images, (e.g., T_1-weighted, T_2-weighted). Even if M_T is uncalibrated in units of M_B^{tissue}, a perfusion-weighted image can be generated by tomographic measurement of the steady-state ^{129}Xe-tissue signal at high tip angle. Cerebral functional studies can be made by the subtraction of two images acquired at high tip angle: one acquired during functional activation and one acquired during baseline activation. These perfusion-weighted images also have the advantage that they can be acquired relatively quickly, since the steady-state ^{129}Xe tissue signal needs to be measured at only a single tip angle.

An important caveat for the method we describe here follows from the relatively small spectroscopic separation of the ^{129}Xe blood and tissue NMR resonances, roughly 15 ppm. This corresponds to a 350 Hz blood-tissue separation at 2 T. The observed ^{129}Xe T_2^* varies from 2 ms in blood to 20 ms in brain tissue (see table 4.3), corresponding to NMR spectral linewidths of about 150 Hz and 15 Hz, respectively. Thus an RF pulse centered about the tissue resonance with duration short enough (*i.e.*, with a sufficient bandwidth) to tip the ^{129}Xe tissue magnetization will modestly perturb the ^{129}Xe-blood magnetization. If we assume that the ^{129}Xe-blood longitudinal magnetization is tipped by an angle β, and M_B^{tissue} is the steady-state value prior to the NMR pulse, then immediately following the tip the longitudinal ^{129}Xe-blood magnetization at the tissue of interest is simply $M_B^{tissue} cos\ \beta$. Repeated pulsing will result in M_B^{tissue} achieving a steady-state value that is less than the unperturbed value. Under certain experimental conditions, this perturbation may be entirely negligible. For example, the blood flow rate to tissue in typical regions of interest is high compared to the RF pulsing rate $1/\tau$, and the total blood volume in the rat brain is relatively low, roughly 5% of the total brain volume [138]. Thus it seems reasonable to assume that with typical NMR pulse rates on the order of $\tau \sim 1$ s, the blood magnetization at the tissue, M_B^{tissue}, will be completely replenished between pulses, minimizing the influence of RF pulsing on the steady-state value of M_B^{tissue}.

If the blood flow is insufficient to replenish M_B^{tissue}, it is possible that this perturbation can be minimized with proper design of the RF pulse shape and phase. A thorough treatment of amplitude-modulated RF pulses that will excite a specific band of frequencies within a complex NMR spectrum with uniform intensity and phase but with negligible excitation is given by Geen *et al.* [139].

Accurate quantification of perfusion with the ^{129}Xe magnetic tracer technique requires accurate measurement of the ^{129}Xe-tissue tip angle α. In general the geometry of the RF probe determines the degree of uniformity of the tip angle distribution in the sample. An aspect of coil design that can improve the tip angle uniformity in the sample is the use of a transmitter coil which provides a homogeneous B_1 field throughout the tissue. This can be achieved by using a volume coil (e.g., a quadrature birdcage coil [178, 179]) or a slotted tube resonator [81]. An essentially homogeneous B_1 field can also be obtained by using a surface coil transmitter which is much larger than the receiver coil [180].

Another approach to tip angle calibration and uniformity is the use of RF pulses which are based on adiabatic spin rotation and are part of a class of pulses known as BIR (**B**$_1$ **I**nsensitive **R**otation) [83-86]. These adiabatic pulses generate a uniform tip angle despite spatial variations in B_1 (even over several orders of magnitude), provided that the B_1 field is above a threshold value, thereby combining the high sensitivity of surface coil receivers with uniform sample excitation. These adiabatic pulses have the additional advantage that they eliminate the calibration of RF power between experiments. We have performed promising preliminary experiments with ^{129}Xe NMR using BIR-4 pulses. The tip angle uniformity over a large volume of ^{129}Xe gas using a surface coil was excellent, however the off-resonant behavior of these BIR-4 pulses is quite complicated, and ^{129}Xe magnetization outside the excitation profile was dephased and destroyed. The realization of a ^{129}Xe-tissue-selective BIR pulse with no spin-destruction outside the excitation bandwidth may be very difficult, but remains to be explored.

As shown above in equation 5.33, the determination of f_{BT} using the steady-state ^{129}Xe NMR tracer method does not depend on the xenon blood-tissue partition coefficient λ. In addition, ^{129}Xe-tissue T_1-weighted images can be made without knowledge of λ (*i.e.,* maps of T_1/λ). Nevertheless, quantitative determination of ^{129}Xe-tissue T_1 depends on knowledge of λ, which is currently determined from *ex vivo* studies. Therefore, accurate *in vivo* determination of λ remains an important challenge if ^{129}Xe T_1 measurements are to be fully exploited for their possible diagnostic value. In the simulations of section 5.5, we assumed λ was known exactly. However, the xenon-blood partition coefficient varies widely across tissue types (see table 4.2), and in the various brain tissues by almost a factor of two. Additionally, the partition coefficient may be a function of hematocrit level and tis-

sue pathology.

It is worth emphasizing that the ^{129}Xe magnetic tracer method for determination of f_{BT} is independent of both the local ^{129}Xe-tissue T_1 and the ^{129}Xe-blood T_1. Although the ^{129}Xe-blood T_1 will affect the magnitude of the ^{129}Xe-tissue magnetization, all measurements of M_T can be normalized to measurements of M_B^{tissue} arriving via blood flow at the tissue. The ratio, $(M_T sin\alpha) / M_B^{tissue}$, is fit in the procedure of section 5.5, and although M_B^{tissue} must be time-independent during a measurement, there is no requirement that it remain constant from run to run. Independence of the ^{129}Xe-blood T_1 is critical, as the blood T_1 may depend on many factors including oxygenation, hematocrit, and vessel size.

An assumption central to the ^{129}Xe magnetic tracer technique presented in this chapter is that the ^{129}Xe-tissue magnetization achieves steady-state during laser-polarized ^{129}Xe inhalation. Although we have observed saturation of the ^{129}Xe-blood signal in the rat thorax, saturation has not been observed in experiments of ^{129}Xe uptake into rat grey matter (typically during inhalation of a 60% xenon/40% O_2 mixture). It is known that in humans the inhalation of high concentrations of xenon produces marked effects: 60–70% xenon produces general anesthesia, 40–50% xenon results in light-headedness, euphoria, and changes in the electroencephalogram [134, 181-183], and in all of these cases cerebral blood flow is affected. A similar pharmacological effect is likely the dominant cause of the time-dependent decrease in the ^{129}Xe grey matter resonance shown in figure 4.13.

Non-anesthetic doses of 35% inhaled xenon are frequently employed in clinical human brain studies with xenon CT using a steady-state method [22, 184-192]. At these sub-anesthetic levels of 35% xenon, little or no effect on rCBF during inhalation has been observed in PET studies [193], nor have significant increases in intercranial pressure been observed at these levels [194]. Therefore, it is reasonable to expect that inhalation of such lower concentrations of laser-polarized xenon will lead to grey matter steady-state ^{129}Xe NMR signal without significant changes in rCBF.

We have demonstrated a highly promising method for the use of laser polarized ^{129}Xe NMR to measure tissue perfusion directly. This method is particularly suited to measurement of rCBF, as well as cardiac and kidney perfusion – all organs from which we have measured significant ^{129}Xe-tissue MR signal. Based on our studies in rodents, and previous data on the pharmacological effects of xenon inhalation, an inhaled 35% Xe/65% O_2 mix-

ture with a nominal 5% ^{129}Xe polarization will provide sufficient SNR in grey matter to make this new method feasible. At high tip angles, images of the steady-state ^{129}Xe tissue magnetic moment density are maps of local tissue perfusion, f_{BT}. As images of the ^{129}Xe tissue NMR signal in the rodent brain have already been achieved, brain activation studies should be possible by watching correlations of the high tip angle ^{129}Xe steady-state tissue signal (*i.e.*, f_{BT}) with an applied stimulus. In addition, quantitative determination of f_{BT} and T_1 can be provided by measurement of the steady-state ^{129}Xe tissue signal as a function of ^{129}Xe-tissue tip angle α. The determination of f_{BT} with this method is independent of both the ^{129}Xe-tissue T_1 and partition coefficient λ. Given sufficient ^{129}Xe tissue SNR, tomographic T_1 and perfusion maps also follow from this technique.

Chapter 6

Conclusion

We have demonstrated that ^{129}Xe polarized to approximately 5% and delivered to rats by inhalation results in a ^{129}Xe magnetic moment density in perfused tissues sufficiently large to image with chemical-shift MRI. Additionally, we have shown that careful control of the NMR parameters will allow laser-polarized ^{129}Xe to be used as a magnetic resonance tracer *in vivo*. The next major advances in the use of these methods will accompany increases in ^{129}Xe polarization. This chapter outlines some of the places where there is the potential to make significant gains in ^{129}Xe polarization and production rates. A summary of future prospects for the ^{129}Xe magnetic resonance tracer method, and some suggestions of additional applications for large quantities of polarized ^{129}Xe, conclude this dissertation.

6.1 SNR and Spatial Resolution

The spatial resolution of *in vivo* dissolved-phase ^{129}Xe MRI is limited by the attainable ^{129}Xe SNR. For a given imaging sequence, there is a simple relationship between voxel size and SNR [195, 196]; for an imaging experiment of a fixed number of RF pulses, the amount of signal in a voxel is proportional to the size of the voxel, *i.e.*,

$$SNR \propto \Delta V, \tag{6.1}$$

where the spatial resolution is characterized by the voxel dimensions, $\Delta V = \Delta x \Delta y \Delta z$. In practice, the voxel size in an MR image is typically chosen to give an acceptable SNR for the region of interest. A factor of ten increase in ^{129}Xe polarization from the approximately

3.5% polarization used to acquire the 2D CSI brain image of figure 4.14 will allow images (with the same SNR per voxel) to be obtained with 10 μL voxels. This increase in ^{129}Xe polarization from the modest 3–7% used in the *in vivo* experiments of this thesis to 35% will allow the spatial resolution of ^{129}Xe images to approach that of standard ^{1}H MR images (*i.e.*, 1–2 μL) over reasonable acquisition times. The following sections address several directions where significant increases in ^{129}Xe polarization should be attainable on near- and moderate- time scales.

6.1.1 Wall coatings

Improvements in wall coatings that reduce wall-induced ^{129}Xe relaxation in the optical pumping cell can lead to significant increases in the ^{129}Xe polarization until such point as $\Gamma_{wall} \ll \gamma_{SE}$. As shown in figure 3.8, even a factor of two increase in T_{wall}, from 300 seconds to 600 seconds, will result in an calculated 30% increase in ^{129}Xe polarization. In particular, the surface-induced relaxation of ^{129}Xe is assumed to be due to the dipolar cross-relaxation between the proton spins on the surface and the nuclear spin of the ^{129}Xe [57, 65, 197]. The probability of a ^{129}Xe spin flip at the surface can be reduced in several ways. One is to lower the total magnetic moment of the coating nuclei by replacing them with deuterons. The deuterium magnetic moment is 6.5 times smaller than the proton, and deuterated paraffin was first investigated for wall coatings in Rb vapor cells [198]. The use of deuterated or partially deuterated silanes as wall coatings for ^{129}Xe may prove to be quite fruitful.

A second way to reduce the probability of a ^{129}Xe-surface spin-flip is to reduce the interaction time between the ^{129}Xe and the surface by decreasing the permeability of the coating. Fluorinated coatings have been suggested in this regard [65, 199]. One potential problem with this class of coatings for OPSE cells may be the strong affinity of Rb for fluorinated surfaces (such as Teflon) which results in rapid carbon formation at the surface.

6.1.2 Laser diode spectral narrowing

High power broadband LDAs have been the workhorses that enable spin-exchange optical pumping of ^{129}Xe *in situ* at the MRI laboratory. However, the 500–1000 GHz FWHM bandwidth of a typical high power LDA is a poor match to the 50 GHz pressure broadened

Rb absorption line. Additionally, the high-intensity off resonant light produces heating in the OPSE cell which may be detrimental to both wall coatings and makes control of the optimum Rb density in the cell difficult. These problems have motivated the development of frequency narrowed external cavity high power diode lasers which are more suited for production of laser-polarized ^{129}Xe. Work at Michigan and Wisconsin has successfully produced 1–2 W of narrowed diode light in a 20–80 GHz bandwidth [71, 72]. This work is currently being extended to higher power devices, including the very promising results of 15 W in a 50 GHz FWHM line [73] and 18 W in an 80 GHz FWHM line [74].

Calculations of the ^{129}Xe polarization as a function of laser linewidth are shown in

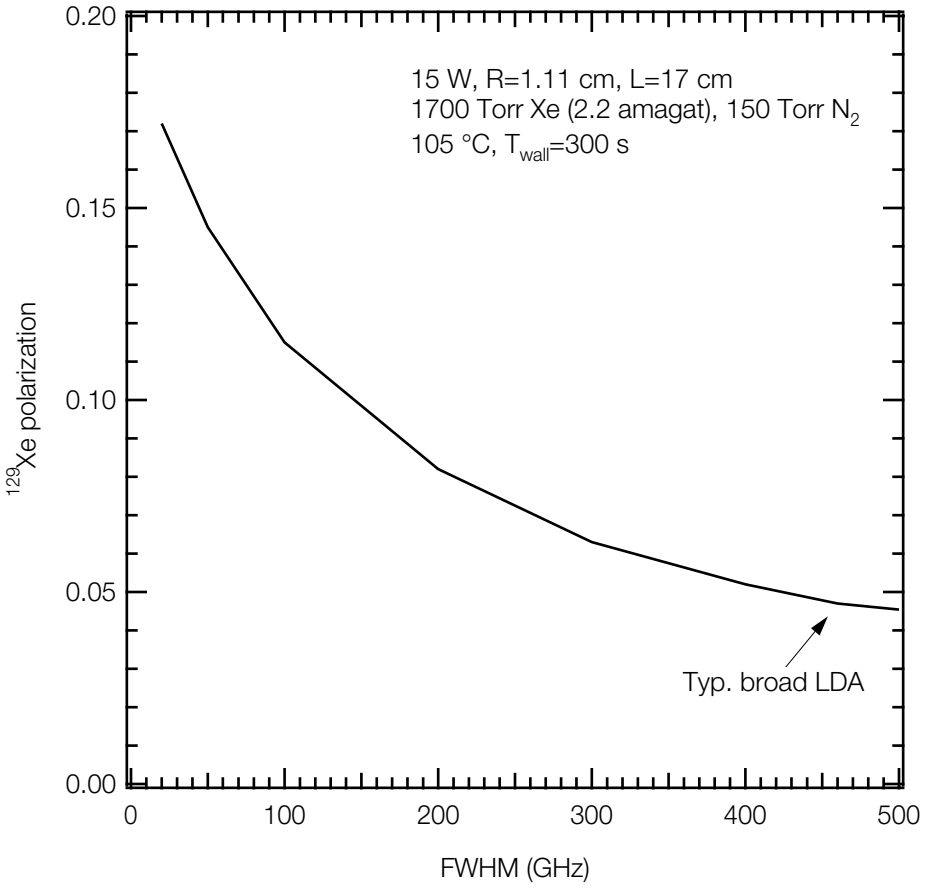

Figure 6.1: Calculated steady-state ^{129}Xe polarization as a function of LDA linewidth for 15 W of laser power. The operating pressure, T_{wall}, and geometry are typical for the cells used in this experiment. A Lorentzian laser lineshape was assumed. The width parameter of a typical Optopower LDA is noted above for comparison.

figure 6.1. The operating pressure, T_{wall}, and geometry of the simulation cell are typical for the cells used in experiments in this thesis, and we assume 15 W of laser power penetrates into the cell. The simulations suggest that narrowing the spectral profile of high power diode lasers to roughly 50 GHz will provide an increase in ^{129}Xe polarization of roughly a factor of 3 over the broadband case, with no change in polarizer cell operation.

6.1.3 Polarizer automation

One of the most tedious aspects of running the polarizer is the manual operation of the many valves involved in the polarization and accumulation process. Currently, the operation of these valves and metering of gases adds about 50 seconds of dead time to the polarization cycle, and precludes unattended operation. The ability to automatically cycle the polarizer will allow exploration of a much broader OPSE parameter space. Operation at low xenon pressure and rapid spin-exchange rates (*i.e.,* high cell temperature) can be explored since automated accumulation will make rapid cycling for large number of accumulation cycles feasible.

One of the most dramatic gains in ^{129}Xe polarization attainable with an automated system comes from the use of liquid helium to cool the cryotrap. At LHe temperatures, ^{129}Xe ice relaxation times of order $T_{ice} \sim 500$ hours have been measured [76], and permitting very long ^{129}Xe-ice accumulation times. This would allow the polarization stage to be operated at very low cell pressure (e.g., 150 Torr Xe) and resultant high polarization. Calculations of the ^{129}Xe polarization as a function of laser linewidth are shown in figure 6.2. The xenon pressure has been reduced to 100 Torr (0.13 amagat per batch) and the temperature increased to 125 °C. The high operating temperatures mean shorter spin-up times, and operation at these low xenon pressures is only practical if the system can be cycled rapidly, in an automated fashion. Although only 0.13 amagat of xenon is produced per batch in this configuration, the automated system could accumulate polarized ^{129}Xe for an entire week before relaxation in the ice became significant at these temperatures. Again, the use of a narrowed diode light source in this low pressure configuration suggests significant gains. The simulations suggest that operation of the polarizer in the low xenon pressure regime with an LDA narrowed to roughly 50 GHz will result in a ^{129}Xe polarization of nearly 70% . Even with our existing laser system, ^{129}Xe polarizations of approximately

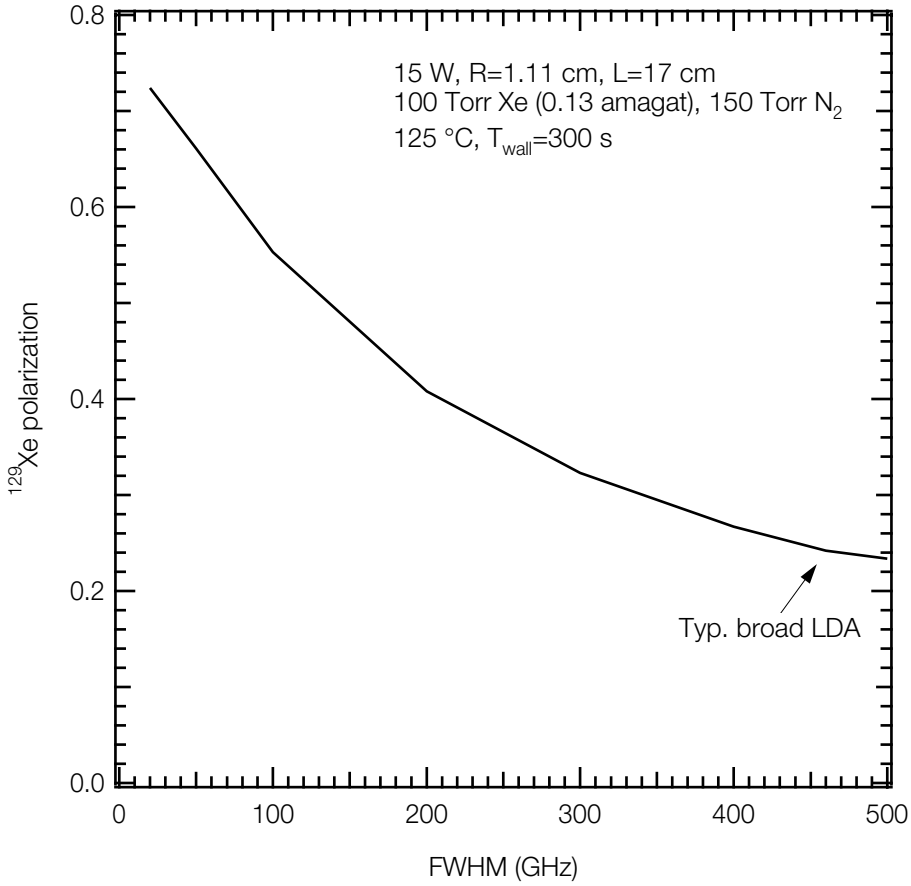

Figure 6.2: Calculated ^{129}Xe polarization as a function of LDA linewidth for 15 W of laser power. The xenon pressure has been reduced to 100 Torr. Cell geometry is the same as in figure 6.1. As above, a Lorentzian laser lineshape is assumed.

20% are attainable with 100 Torr of xenon.

Pneumatic rack-and-pinion actuators have already been adapted in our lab to operate the glass valves of the polarizer. Full automation should be relatively simple to implement, requiring computer operation and the addition of several pressure gauges as process monitors to ensure fail-safe unattended operation.

6.1.4 Recovery of xenon

The breathing mixture exhaust from the animal contains Xe, O_2, CO_2, N_2, anesthesia gases and H_2O vapor. Currently, the anesthesia gases are scavenged by an activated charcoal filter, and the remainder of the gas vented to atmosphere because the current cost of natural

xenon is relatively inexpensive at roughly $12 per liter. Although the cost of isotopically enriched xenon (85% ^{129}Xe) is several hundred dollars per liter, the nearly four-fold increase in delivered magnetization attainable becomes economically feasible if the xenon can be recovered after use The same increase in resolution to 10 μL can be obtained with use of 85% enriched xenon polarized to 9.5%. A brief outline of a method for reclaiming the xenon from exhausted breathing gases is now described. Volatile substances such as Halothane can easily be removed with a cold trap. The critical pressure and temperature of xenon is 55 atm and 16 °C. The critical temperatures for N_2 and O_2 at this pressure are -147 and -117 °C, respectively. If the gas mixture is compressed to 55 atm and cooled below 16 °C , only xenon will liquefy and thus easily reclaimed.

6.2 Conclusion

The ^{129}Xe magnetic resonance tracer method described in this thesis may prove to be a robust and broadly applicable method for non-invasive, high-resolution tomographic measurement of tissue perfusion. Increases in ^{129}Xe polarization via the schemes described above will allow some key questions to be addressed by way of increased NMR signal. Of particular importance for rCBF measurement in various brain tissues are the identification of the ^{129}Xe resonances observed in the brain. It may be possible to assign these multiple resonances based on both their *in vivo* dynamics and by high resolution chemical-shift imaging. Similar chemical shift structure has been observed in ^{129}Xe spectra obtained from the human head [137], implying that the ^{129}Xe magnetic resonance tracer method may be directly applicable to studies in humans, thus emphasizing the importance of our method. Automation of the polarization and accumulation stage as described above will allow the accumulation of the large volumes (*i.e.*, tens of Liters) of polarized ^{129}Xe needed for detailed human study.

The possibility of low field imaging with laser-polarized noble gases should not be overlooked. Results obtained at low field (*i.e.,* 0.003–0.1 T) [200, 201] suggest many new MRI applications including low-cost tabletop MRI instruments. As discussed in Chapter 3, the polarizer system as described in this thesis is easily adaptable for stand-alone operation in a low magnetic field environment.

The large quantities of highly polarized ^{129}Xe produced by the apparatus of this thesis have additional applications beyond the realm of *in vivo* MRI. The study of xenon-protein interactions by NMR is greatly enhanced by the use of laser-polarized ^{129}Xe [202]. We have performed preliminary work to study the cross-polarization between ^{129}Xe and protein protons by developing a system for the study of laser-polarized ^{129}Xe in cross linked bovine serum albumin [203]. Polarized ^{129}Xe targets for neutron scattering [204], and the production of polarized ^{129}Xe ice for sensitive searches of macroscopic spin-dependent forces [205-207] are applications for which an automated ^{129}Xe polarizer as described in this dissertation may make significant impact.

Appendix A

NMR Imaging

This section is a brief overview of the basic physics of NMR and its application to the imaging techniques known as MRI. The details presented here are limited to the techniques used in this thesis, and a more complete discussion is found in the literature [10, 208-211].

A.1 Fundamentals

NMR is a technique for manipulating the magnetic moment of a nuclear system that possesses a non-zero spin angular momentum. A free induction decay (FID) can be evoked from a spin system in response to an applied radio-frequency pulse, and the precessing magnetization detected [212-214]. The goal of NMR imaging is the reconstruction of an image of the nuclear spin density from the detected NMR signal. In order to more easily discuss the fundamentals of the relationship between the detected NMR signal and the formation of an image, nuclear spin relaxation is ignored in the following discussion. The equation of motion for an ensemble of magnetic moments in a static magnetic field neglecting relaxation is simply

$$\frac{d\boldsymbol{M}}{dt} = \gamma \boldsymbol{M} \times \boldsymbol{B}, \tag{A.1}$$

where $\boldsymbol{M}$ is the magnetic moment per unit volume (i.e., the magnetization), and γ is the gyromagnetic ratio [197]. With no loss of generality, the orientation of $\boldsymbol{B}$ is specified to lie along the z-direction, $\boldsymbol{B} = B_0\mathbf{z}$. The solution to equation A.1 in this case corresponds to $\boldsymbol{M}$

precessing about $\boldsymbol{B}$ at the Larmor frequency,

$$\omega_0 \;=\; \gamma B_0 \,. \tag{A.2}$$

In all of the imaging methods described here, a complex signal $S(t)$ results from a spin system in response to an applied resonant rf pulse. In the presence of an additional magnetic field gradient applied along $\boldsymbol{z}$, $\boldsymbol{G} \equiv \nabla B_z$, the Larmor frequency becomes a function of position,

$$\omega(\boldsymbol{r}) \;=\; \gamma(B_0 + \boldsymbol{G}\cdot\boldsymbol{r}) \tag{A.3}$$

where $\boldsymbol{G}\cdot\boldsymbol{r}$ is simply the additional magnetic field at position $\boldsymbol{r}$. This linear relationship between the Larmor frequency and the nuclear spin position, $\boldsymbol{r}$, was first exploited by Lautebur in 1973 [215]. All NMR imaging methods use magnetic field gradients in addition to B_0 to "encode" the spatial coordinates of the sample.

A.2 The detected signal and the Fourier relationship

For a pickup coil placed with its symmetry axis transverse to $\boldsymbol{B_0}$, the induced signal voltage in the receiver coil is proportional to the precessing transverse magnetization. The signal arising from volume element dV containing a local spin-density $\rho(\boldsymbol{r})$ precessing in a magnetic gradient is from equation A.3

$$dS(\boldsymbol{G}, t) \propto dV\rho(\boldsymbol{r})e^{i\gamma B_0 t}e^{i\gamma(\boldsymbol{G}\cdot\boldsymbol{r})t}. \tag{A.4}$$

The detection of transverse magnetization is accomplished with a heterodyne technique in which the signal from the coil is mixed with a reference oscillator. In general, the reference oscillator can be set so that signal from the γB_0 term in equation A.4 can be neglected. The total signal in the pickup coil is obtained from integrating equation A.4 across the object,

$$S(\boldsymbol{G}, t) \;=\; \iiint \rho(\boldsymbol{r})e^{i\gamma(\boldsymbol{G}\cdot\boldsymbol{r})t}d\boldsymbol{r}\,. \tag{A.5}$$

In general, the amplitude of the spatial encoding gradients $\boldsymbol{G}$ is time-dependent, and the product $\boldsymbol{G} \cdot \boldsymbol{r}$ is an integral over time. Following Mansfield [216] the wave vector is defined

$$\boldsymbol{k} \equiv \frac{\gamma}{2\pi} \int_0^t \boldsymbol{G}(t')dt' , \tag{A.6}$$

where $\boldsymbol{G}(t')$ is the time-dependent spatial encoding gradient. Rewriting equation A.5 in terms of $\boldsymbol{k}$,

$$S(\boldsymbol{k}) \;=\; \iiint \rho(\boldsymbol{r}) e^{2\pi i \boldsymbol{k}(t) \cdot \boldsymbol{r}} d\boldsymbol{r}, \tag{A.7}$$

which is related to the spatial spin density by the inverse Fourier transform

$$\rho(\boldsymbol{r}) \;=\; \iiint S(\boldsymbol{k}) e^{-2\pi i \boldsymbol{k}(t) \cdot \boldsymbol{r}} d\boldsymbol{k}. \tag{A.8}$$

The spatial spin density at any location can be obtained as the inverse Fourier transform of the signal S($\boldsymbol{k}$). This is the fundamental relationship of all Fourier-based NMR imaging methods. It should be noted that the voltage induced in the receiver coil is typically acquired via computer, and is digitized and represented in a finite number of data points. All the Fourier transforms applied to the sampled data are thus computed as discrete Fourier transforms (DFTs).

The space spanned by $\boldsymbol{k}$ is known in MRI literature as "*k*-space" [217, 218]. Since the acquired time-domain signal is discretely sampled, *k*-space is spanned by discrete points. The choice of the time-dependence and amplitude of the imaging gradients determine the path through *k*-space, since $\boldsymbol{k}$ (from equation A.6) is determined by the time integrals of the applied gradients. The difficulty and art of forming an image is to sample a sufficient part of *k*-space to allow $\rho(\mathbf{r})$ to be reconstructed, with the greatest signal-to-noise, and in the least time. Many ways of sampling *k*-space are used, and the imaging methods used in this thesis are now briefly outlined.

A.3 Two-dimensional projection reconstruction imaging

The projection-reconstruction (PR) technique is the first form of NMR imaging, and was introduced by Lauterbur in 1973 [215]. This imaging method is similar to X-ray CT in which a tomographic image is reconstructed from a series of 1D projections.

The NMR spectrum of an object measured in the presence of a linear magnetic-field gradient is a one-dimensional projection of an object onto the direction of the applied gradient. If the FID is acquired with the imaging gradient $\boldsymbol{G}$ applied in an arbitrary direction, a single radial line in k-space is sampled. In the 2D PR method, the imaging gradient $\boldsymbol{G}$ is varied such that k-space is sampled in a polar raster, i.e., the planar angle and magnitude are given according to

$$\phi = atan\left(\frac{G_y}{G_x}\right), |\boldsymbol{G}| = \sqrt{G_x^2 + G_y^2}. \tag{A.9}$$

As the polar angle varies, a k-space is sampled along radial lines from the origin at an angle ϕ [215]. A set of FIDs is acquired with different values of ϕ which span polar space from 0 to 2π (figure A.1). Assuming a two-dimensional spin-distribution, $\rho(x,y)$, the detected signal (from equation A.7) is

$$S(k, \phi) = \int_{-a/2}^{a/2}\int_{-\infty}^{\infty}\int_{-\infty}^{\infty}\rho(x, y)e^{2\pi i\boldsymbol{k}\cdot\boldsymbol{r}}dxdydz, \tag{A.10}$$

where the outer integral is just the process of averaging across a slice of sample (of thickness a). In order to reconstruct $\rho(x,y)$ from $S(k, \phi)$, the inverse 2D Fourier transform (equation A.8) is rewritten in polar coordinates,

$$\int_{-a/2}^{a/2}\rho(x, y)dz = \int_0^{\pi}\int_0^{k_{max}} S(k, \phi)e^{-2\pi i\boldsymbol{k}\cdot\boldsymbol{r}}|k|\,dk d\phi\,. \tag{A.11}$$

The dk integral of equation A.11 is the one-dimensional radial projections $\rho\phi(r)$,

$$\int_{-a/2}^{a/2}\rho_{\phi}(r)dz = \int_{-k_{max}}^{k_{max}} S(k, \phi)e^{-2\pi ikr}|k|\,dk, \tag{A.12}$$

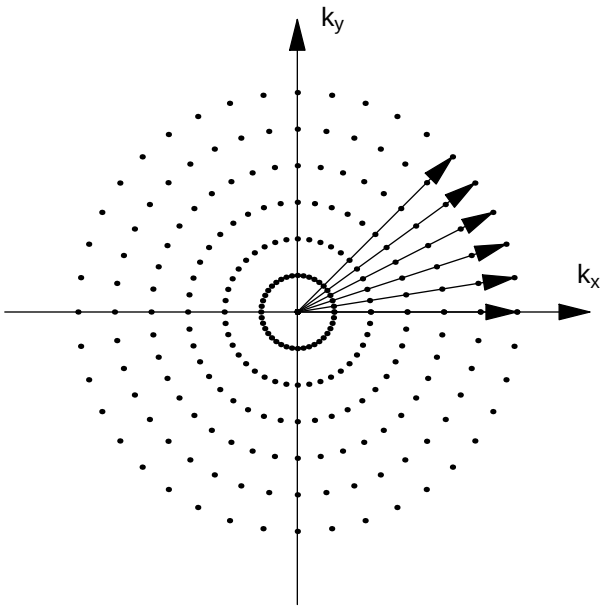

Figure A.1: Sampling of *k*-space by 2D projection reconstruction. G_x and G_y are applied simultaneously as read gradient and the data acquired on a polar raster. Each acquisition samples a radial line in *k*-space from $k = 0$ to k_{max} on a polar raster. The discrete sampled points in *k*-space are indicated here by dots.

where *r* is the component of radial displacement along the gradient direction. In practice, the gradient is swept to vary ϕ, and for each value of ϕ the projection $\rho_\phi(r)$ is calculated from the time-domain data by 1D FT. The 2D image is reconstructed from the set of $\rho_\phi(r)$ using one of the several techniques for reconstructing images from one-dimensional projections developed for x-ray tomography [219-221]. The PR images in this thesis were processed using the iterative convolution back-projection method [220].

A.4 Spin-warp/gradient echo imaging

Fourier imaging [222] is the most widespread class of NMR imaging methods. Fourier imaging and PR imaging differ primarily in the way *k*-space is sampled; Fourier imaging methods sample *k*-space uniformly on a cartesian grid, while sampling in the PR method is concentrated near $\boldsymbol{k} = 0$. Spin-warp imaging [223] is the most common variant of Fourier imaging. As in section A.3, when a FID is recorded in the presence of a gradient (the "read" gradient), a single line in *k*-space is acquired. In two-dimensional spin warp imag-

ing an additional gradient is applied perpendicular to the frequency-encode gradient, prior to the signal readout. This results in a phase modulation (or "warp") to the signal dependent on the position of the spin-density in this perpendicular direction. This gradient is known as the phase-encode gradient. For each measurement, the phase-encode gradient takes a different value, allowing a different line in *k*-space to be acquired From equation A.7, the detected signal is

$$S(k_x, k_y) = \int_{-a/2}^{a/2}\int_{-\infty}^{\infty}\int_{-\infty}^{\infty}\rho(x, y)e^{2\pi i(k_x x + k_y y)}dxdydz, \tag{A.13}$$

and the image is reconstructed by inverse Fourier transformation of the *k*-space data,

$$\int_{-a/2}^{a/2}\rho(x, y)dz = \int_{-k^y_{max}}^{k^y_{max}}\int_{-k^x_{max}}^{k^x_{max}} S(k_x, k_y)e^{-2\pi i(k_x x + k_y y)}dk_x dk_y. \tag{A.14}$$

Typically, the detected signal in spin-warp imaging is not the FID but is a gradient echo. In the gradient echo method, a negative prephase in the readout direction shifts the origin of *k*-space away from $\boldsymbol{k} = 0$ (see figure A.2)., allowing more complete sampling of the *k*-space plane. After phase encoding, a "gradient echo" is produced during readout by allowing the spins to precess in a read gradient of opposite sign to that applied during the prephase, and the signal is detected as the spins regain coherence [223]. The spin warp imaging technique is the standard imaging technique used today for ^{1}H imaging, however echo imaging methods require that transverse magnetization relaxation time, T_2, be sufficiently long so that the spins rephase before the signal decays and an echo is physically obtainable.

A.5 Chemical shift imaging

Spectroscopic imaging is a combination of spatial and spectral imaging. Combining spatial localization with spectroscopy, an NMR spectrum is obtained at each spatial position, and an image of each chemical-shift component may be produced. This imaging technique is known as chemical shift imaging (CSI) [224-228], and is typically performed by spatially encoding the NMR signal prior to reading in the absence of a magnetic field gradient. If the local 2D spin-density now includes a spatially varying frequency distribution,

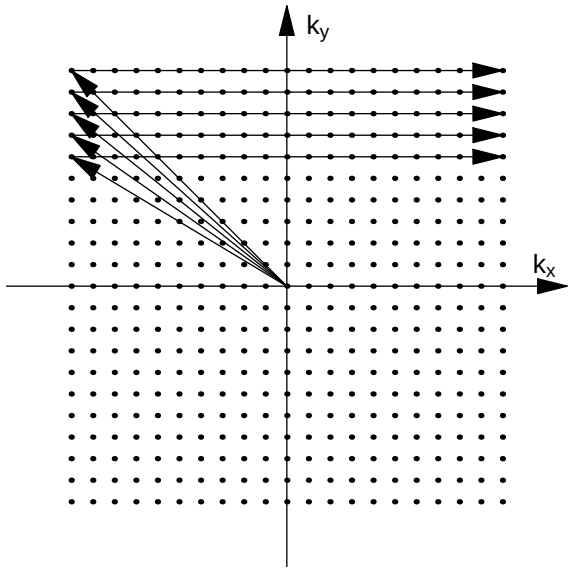

Figure A.2: Sampling of *k*-space by 2D gradient echo. The *x*- and *y*- gradients are responsible for frequency and phase encoding, respectively. The signal is acquired during the presence of the frequency encode gradient, and is called the readout gradient. In this example, a negative "prephasing" read gradient shifts the origin of *k*-space away from $k_x = 0$ prior to the frequency encode. An entire line in the readout direction is sampled in a single acquisition.

$\rho(x,y,\omega)$, the detected signal (from equation A.5) is

$$S(t) = \iiint \rho(x, y, \omega) e^{i\gamma(G_x x + G_y y)t} e^{i\omega t} dx dy dz d\omega , \tag{A.15}$$

where ω is the chemical shift offset frequency with respect to the demodulation frequency ω_0. As above, rewriting equation A.15 in *k*-space,

$$S(k_x, k_y, k_\omega) = \iiint \rho(x, y, \omega) e^{2\pi i(k_x x + k_y y + k_\omega \omega)} dx dy dz d\omega , \tag{A.16}$$

where $\boldsymbol{k}$ is as in equation A.6, and k_ω is defined as

$$k_\omega(t) \equiv \frac{t}{2\pi} . \tag{A.17}$$

The signal spans three-dimensional *k*-space; the position in (k_x, k_y) is determined by the time integral of the phase-encode gradients G_x and G_y applied prior to readout, and k_ω is sampled as a function of time during readout with no applied gradients. By sampling the FID after a phase-encoding and in the absence of any applied gradients, information about spatial distribution can be separated from information about chemical shift. This is possible because a pulsed gradient encodes positional information in the initial phases of FID but does not affect the frequency distribution in space after the gradient has been turned off and spins precess freely. The net effect is to measure the Fourier transform of the spatial and frequency distribution of the spins, which is then inverted to obtain the spatial distribution of chemical shifts over the sample. The 2D spectroscopic image is obtained by 3D Fourier transform,

$$\int_{-a/2}^{a/2} \rho(x, y, \omega) dz = \iiint S(k_x, k_y, k_\omega) e^{-2\pi i(k_x x + k_y y + k_\omega \omega)} dk_x dk_y dk_\omega . \qquad \text{(A.18)}$$

Unlike imaging sequences where the presence of a read gradient allows an entire *k*-space line to be acquired each experiment, in CSI the FID is acquired in the absence of a read gradient (the presence of which would disperse frequency information). Each point in *k*-space is acquired with a separate phase encode step, so that a two-dimensional $N \times N$ pixel CSI image requires N^2 phase encode steps, increasing the total imaging time by a factor of N compared to gradient echo sequences. In practice, this increase in acquisition time limits CSI imaging to two spatial dimensions.

BIBLIOGRAPHY

[1] T E Chupp, M Wagshul, K P Coulter et al., "Polarized, high-density, gaseous ^{3}He targets," Phys. Rev. C **36**, 2241-2244 (1987).

[2] J R Johnson, A K Thompson, T E Chupp et al., "The Slac High-Density Gaseous Polarized He-3 Target," Nucl. Instrum. Methods Phys. Res. Sect. A-Accel. Spectrom. Dect. Assoc. Equip. **356** (1), 148-152 (1995).

[3] K P Coulter, A B McDonald, W Happer et al., "Neutron Polarization With Polarized He-3," Nucl. Instrum. Methods Phys. Res. Sect. A-Accel. Spectrom. Detect. Assoc. Equip. **270** (1), 90-94 (1988).

[4] R J Hoare, "Precision measurement techniques and fundamental tests with polarized noble gases," Harvard University, 1993.

[5] E R Oteiza, "Search for a permanent electric dipole moment in ^{129}Xe using simultaneous ^{3}He magnetometry," Harvard University, 1992.

[6] D Bear, T E Chupp, K Cooper et al., "Improved frequency stability of the dual-noble-gas maser," Phys. Rev. A **57** (6), 5006-5008 (1998).

[7] D Bear, R E Stoner, R L Walsworth et al., "Limit on Lorentz and CPT violation of the neutron using a two-species noble-gas maser," Phys. Rev. Lett. **85** (24), 5038-5041 (2000).

[8] M A Rosenberry, "A precision measurement of the ^{129}Xe electric dipole moment using dual noble gas masers," The University of Michigan, 2000.

[9] M A Rosenberry and T E Chupp, "Atomic electric dipole measurement using spin exchange pumped masers of ^{129}Xe and ^{3}He," Phys. Rev. Lett. **86** (1), 22-25 (2001).

[10] F W Wehrli, "From NMR diffraction and zeugmatography to modern imaging and

beyond," Progress in Nuclear Magnetic Resonance Spectroscopy **28**, 87-135 (1995).

[11] T G Walker and W Happer, "Spin-exchange optical pumping of noble-gas nuclei," Rev. Mod. Phys. **69** (2), 629-642 (1997).

[12] R R Ernst, G Bodenhausen, and A Wokaun, *Principles of nuclear magnetic resonance in one and two dimentions* (Oxford University Press, New York, 1997).

[13] M S Albert, G D Cates, B Driehuys et al., "Biological magnetic resonance imaging using laser-polarized ^{129}Xe," Nature **370**, 199-201 (1994).

[14] S S Kety and C F Schmidt, "The nitrous oxide method for the quantative determination of cerebral blood flow in man: theory, procedure, and normal values.," J. Clin. Invest. **27**, 476-483 (1948).

[15] S S Kety and C F Schmidt, "The determination of cerebral blood flow in man by the use of nitrous oxide in low concentrations," Am. J. Physiol. **143**, 53-66 (1945).

[16] S S Kety, "Measurement of local blood flow by the exchange of an inert, diffusible substance," in *Methods in Medial Research*, edited by H D Bruner (Chicago, 1960), pp. 228-236.

[17] S S Kety, "The theory and applications of the exchange of inert gas at the lungs and tissues," Pharmacol. Rev. **3**, 1-41 (1951).

[18] S-Y Yeh and R E Peterson, "Solubility of krypton and xenon in blood, protein solutions, and tissue homogenates," J. Appl. Physiol. **20**, 1041-1047 (1965).

[19] N A Lassen, "Cerebral blood flow determined by radioactive diffusible tracers with special regard to the use of xenon-133," in *Cerebral metabolism and neural function*, edited by J V Passonneau, R A Hawkins, W D Lust et al. (Williams and Wilkins, Baltimore, 1980), pp. 144-150.

[20] M D Cosgrove and P Mowat, "Evaluation of the xenon-133 renal blood flow method," Br. J. Urol. **46**, 134-147 (1974).

[21] M L Marcus, "Methods of measurement of myocardial blood flow in patients: a critical review," Circulation **76**, 245-253 (1987).

[22] D Gur, S K Wolfson, H Yonas et al., "Progress in cerebrovascular disease: local cerebral blood flow by xenon enhanced CT," Stroke **13** (6), 750-758 (1982).

[23] K Nambu, R Suzuki, and K Hirakawa, "Measurement with Xenon-enhanced dynamic helical CT," Radiology **195**, 53-57 (1995).

[24] A Bifone, Y Q Song, R Seydoux et al., "NMR of laser-polarized xenon in human blood," Proc. Natl. Acad. Sci. **93**, 12932-12936 (1996).

[25] S D Swanson, M S Rosen, K P Coulter et al., "Brain MRI with laser-polarized ^{129}Xe," Magn. Reson. Med. **38**, 695-698 (1997).

[26] J G Wilson, G E Santyr, M E Anderson et al., "Longitudinal relaxation times of ^{129}Xe in rat tissue homogenates at 9.4 T," Magn. Reson. Med. **41**, 933-938 (1999).

[27] C S Roy and C S Sherrington, "On the regulation of the blood-supply of the brain," J. Physiol. **11**, 85-108 (1890).

[28] M S Rosen, T E Chupp, K P Coulter et al., "Polarized ^{129}Xe optical pumping/spin exchange and delivery system for magnetic resonance spectroscopy and imaging studies," Rev. Sci. Instrum. **70**, 1546-1552 (1999).

[29] B Driehuys, G D Cates, E Miron et al., "High-volume production of laser-polarized ^{129}Xe," Appl. Phys. Lett. **69**, 1668-1670 (1996).

[30] A Kastler, "Quelques suggestions concernant la production optique et la detection optique d'une inegalite de population des niveaux de quantification spatiale des atomes. Application a l'experience de Stern et Gerlach et a la resonance magnetique," J. Phys. Radium **11**, 225-265 (1950).

[31] W Happer, "Optical pumping," Rev. Mod. Phys. **44** (2), 169-249 (1972).

[32] M E Wagshul and T E Chupp, "Laser optical pumping of high-density Rb in polarized ^{3}He targets," Phys. Rev. A **49** (5), 3854-3869 (1994).

[33] S Appelt, A B Baranga, C J Erickson et al., "Theory of spin-exchange optical pumping of He-3 and Xe-129," Phys. Rev. A **58** (2), 1412-1439 (1998).

[34] E S Hrycyshyn and L Krause, "Inelastic collisions between excited alkali atoms and

molecules. VII. Sensitized fluorescence and quenching in mixturesof rubidium with H_2, HD, D_2, N_2, CH_4, CD_4, C_2H_4, and C_2H_6," Can. J. Phys. **48**, 2761-2768 (1970).

[35] A Corney, *Atomic and Laser Spectroscopy* (Clarendon Press, Oxford, 1977).

[36] L W Anderson, F M Pipkin, and J C Baird, "Hyperfine structure of hydrogen, deuterium, and tritium," Phys. Rev. **120** (4), 1279-1289 (1960).

[37] R A Bernheim, "Spin relaxation in optical pumping," J. Chem. Phys. **36** (1), 135-140 (1962).

[38] M A Bouchiat, J Brossel, and L C Pottier, "Evidence for Rb-rare-gas molecules from the relaxation of polarized Rb atoms in a rare gas. Experimental Results.," J. Chem. Phys. **56**, 3703-3714 (1972).

[39] W Farr and E W Otten, "Rb-magnetometer for a wide-range and high sensitivity," Appl. Phys. **3** (5), 367-378 (1974).

[40] G D Cates, R J Fitzgerald, A S Barton et al., "Rb-^{129}Xe spin-exchange rates due to binary and three-body collisions at high Xe pressures," Phys. Rev. A **45**, 4631-4639 (1992).

[41] K P Coulter, "Measurements of parity violation in a search for candidate resonances for a test of time reversal invariance in neutron absorption," Princeton University, 1989.

[42] R Gupta, W Happer, G Moe et al., "Nuclear magnetic-resonance of diatomic alkali molecules in optically pumped alkali vapors," Phys. Rev. Lett **32** (11), 574-577 (1974).

[43] C J Erickson, D Levron, W Happer et al., "Spin relaxation resonances due to the spin-axis interaction in dense rubidium and cesium vapor," Phys. Rev. Lett. **85** (20), 4237-4240 (2000).

[44] S Kadlecek, L W Anderson, and T G Walker, "Field dependence of spin relaxation in dense Rb vapor," Phys. Rev. Lett. **80** (25), 5512-5515 (1998).

[45] N D Bhaskar, J Pietras, J Camparo et al., "Spin destruction in collisions between cesium atoms," Phys. Rev. Lett. **44** (14), 930-933 (1980).

[46] Z Wu, T G Walker, and W Happer, "Spin-rotation interaction of noble-gas alkali-

metal atom pairs," Phys. Rev. Lett. **54** (17), 1921-1924 (1985).

[47] M E Wagshul, "Polarization of ^{3}He by spin exchange with high density laser optically pumped Rb vapor," Harvard University, 1991.

[48] H M Goldenberg, D Kleppner, and N F Ramsey, "Atomic beam resonance experiments with stored beams," Phys. Rev. **123** (2), 530-537 (1961).

[49] J A Fedchak, P Cabauy, W J Cummings et al., "Silane coatings for laser-driven polarized hydrogen sources and targets," Nucl. Instr. Meth. Phys. A **391** (405-416) (1997).

[50] M Stephens, R Rhodes, and C Wieman, "Study of wall coatings for vapor-cell laser traps," J. Appl. Phys. **76** (6), 3479-3488 (1994).

[51] P Minguzzi, F Strumia, and P Violino, "Temperature effects in the relaxation of optically oriented alkali vapors," Nuovo Cimento **46B** (2), 145-162 (1966).

[52] R M Herman, "Theory of spin exchange between optically pumped Rb and foreign gas nuclei," Phys. Rev. Lett. **40**, 391 (1965).

[53] T G Walker, K Bonin, and W Happer, "Electron-noble-gas spin-flip scattering at low energy," Phys. Rev. A **35** (9), 3749-3752 (1987).

[54] L D Schearer and G K Walters, "Nuclear spin-relaxation in the presence of magnetic-field gradients," Phys. Rev. **139** (5A), 1398-1402 (1965).

[55] G D Cates, S R Schaefer, and W Happer, "Relaxation of spins due to field inhomogeneities in gaseous samples at low magnetic fields and low pressures," Phys. Rev. A **37** (8), 2877-2885 (1988).

[56] J Kestin, K Knierim, E A Mason et al., "Equillibrium and transport properties of the noble gases and their mixtures at low density," J. Phys. Chem. Ref. Data **13** (1), 229-303 (1984).

[57] X Zeng, E Miron, W A Vanwijngaarden et al., "Wall Relaxation of Spin Polarized Xe-129 Nuclei," Phys. Let. A **96** (4), 191-194 (1983).

[58] M E Wagshul and T E Chupp, "Optical pumping of high-density Rb with a broadband dye laser and GaAlAs diode laser arrays: application to ^{3}He polarization," Phys.

Rev. A **40**, 4447-4454 (1989).

[59] M S Rosen, S D Swanson, K P Coulter et al., "Polarized gas delivery system/ method," United States Patent 6,085,743 (July 11, 2000).

[60] J Sagiv, "Organized Monolayers by Adsorption. I. Formation and Structure of Oleophobic Mixed monolayers on Solid Surfaces," J. Amer. Chem. Soc. **102** (1), 92-98 (1980).

[61] J Sagiv, "Organized Monolayers by Adsorption. II. Molecular Orientation in Mixed Dye Monolayers Built on Anisotropic Polymeric Surfaces," Israel J. Chem. **18**, 339-345 (1979).

[62] J Sagiv, "Organized Monolayers by Adsorption. III. Irreversible Adsorption and Memory Effects in Skeletonized Silane Monolayers," Israel J. Chem. **18**, 346-353 (1979).

[63] L-H Lee, "Wettability and Conformation of Reactive Polysiloxanes," J. Colloid Interface Sci. **27** (4), 751-760 (1968).

[64] T Killian, "Thermionic phenomena caused by vapors of rubidium and potassium," Phys. Rev. **27**, 578-587 (1926).

[65] B Driehuys, G D Cates, and W Happer, "Surface relaxation mechanisms of laser-polarized ^{129}Xe," Phys. Rev. Lett. **74** (24), 4943-4946 (1995).

[66] T E Chupp, R J Hoare, R L Walsworth et al., "Spin-exchange-pumped ^{3}He and ^{129}Xe Zeeman masers," Phys. Rev. Lett. **72** (15), 2363-2366 (1994).

[67] M V Romalis, "Laser polarized ^{3}He target used for a precision measurement of the neutron spin structure," Princeton University, 1997.

[68] T B Smith, "A precision measurement of the neutron spin structure functions using a polarized ^{3}He target," The University of Michigan, 1998.

[69] C J Jameson, A K Jameson, and J K Hwang, "Nuclear-spin relaxation by intermolecular magnetic dipole coupling in the gas phase. ^{129}Xe in oxygen," J. Chem. Phys. **89** (7), 4074-4081 (1988).

[70] R W Mair, D G Cory, S Peled et al., "Pulsed-field-gradient measurements of time-

dependent gas diffusion," J. Mag. Reson. **135**, 478-486 (1998).

[71] I A Nelson, B Chann, and T G Walker, "Spin-exchange optical pumping using a frequency-narrowed high power diode array," Appl. Phys. Lett. **76** (11), 1356-1358 (2000).

[72] J N Zerger, M J Lim, K P Coulter et al., "Polarization of ^{129}Xe with high power external-cavity laser diode arrays," Appl. Phys. Lett. **76** (14), 1798-1800 (2000).

[73] B Chann, I Nelson, and T G Walker, "Frequency-narrowed external-cavity diode-laser-array bar," Opt. Lett. **25** (18), 1352-1354 (2000).

[74] T G Walker (private communication).

[75] S Dushman, *Scientific Foundations of Vacuum Technique*, 2nd ed. (John Wiley & Sons, Inc., New York, 1962).

[76] M Gatzke, G D Cates, B Driehuys et al., "Extraordinarily Slow Nuclear-Spin Relaxation in Frozen Laser- Polarized Xe-129," Phys. Rev. Lett. **70** (5), 690-693 (1993).

[77] G D Cates, D R Benton, M Gatzke et al., "Laser production of large nuclear-spin polarization in frozen xenon," Phys. Rev. Lett. **65**, 2591-2594 (1990).

[78] R J Fitzgerald, M Gatzke, D C Fox et al., "^{129}Xe spin relaxation in frozen xenon," Phys. Rev. B **59** (13), 8795-8811 (1999).

[79] P A Redhead, J P Hobson, and E V Kornelsen, *The physical basis of ultrahigh vacuum* (Chapman and Hall, London,, 1968).

[80] R A Haefer, *Cryopumping: theory and practice* (Oxford University Press, New York, 1989).

[81] D W Alderman and D E Grant, "An efficient decoupler coil design which reduces heating in conductive samples in superconducting spectrometers," J. Magn. Reson. **36**, 447-451 (1979).

[82] V R Cross, R K Hester, and J S Waugh, "Single coil probe with transmission-line tuning for nuclear magnetic double resonance," Rev. Sci. Instrum. **47** (12), 1486-1488 (1976).

[83] R A de Graaf, "Adibatic RF pulses in in vivo NMR spectroscopy," Utrecht

University, 1998.

[84] R A de Graaf and K Nicolay, "Adiabatic rf pulses: applications to in vivo NMR," Concepts Magn. Reson. **9**, 247-268 (1997).

[85] M Garwood and Y Ke, "Symmetric pulses to induce arbitrary flip angles with compensation for RF inhomogeneity and resonance offsets," J. Magn. Reson. **94**, 511-525 (1991).

[86] M Garwood and K Ugurbil, "B_1 insensitive adiabatic RF pulses," in *NMR Basic Principles and Progress*, edited by P Diehl, E Fluck, H Günther et al. (Springer-Verlag, New York, 1992), Vol. 26, pp. 109-147.

[87] S D Swanson, M S Rosen, K P Coulter et al., "Distribution and dynamics of laser-polarized ^{129}Xe magnetization in vivo," Magn. Reson. Med. **42**, 1137-1145 (1999).

[88] R C Welsh, T E Chupp, K P Coulter et al., "Magnetic resonance imging with laser-polarized ^{129}Xe," Nucl. Instr. Meth. Phys. Res. **402**, 461-463 (1998).

[89] W G Proctor and F C Yu, "On the nuclear magnetic moments of several stable isotopes," Phys. Rev. **81** (1), 20-30 (1951).

[90] R Y Z Chen, F C Fan, S Kim et al., "Tissue-blood partition coefficient for xenon: temperature and hematocrit dependence," J. Appl. Physiol. **49**, 178-183 (1980).

[91] P K Weathersby and L D Homer, "Solubility of inert gases in biological fluids and tissues: a review," Undersea Biomed. Res. **7**, 277-296 (1980).

[92] S-Y Yeh and R E Peterson, "Solubility of carbon dioxide, krypton, and xenon in lipids," J. Pharm. Sci. **52** (5), 453-458 (1963).

[93] S-Y Yeh and R E Petterson, "Solubility of carbon dioxide, krypton, and xenon in aqueous solution," J. Pharm. Sci. **53** (7), 822-824 (1964).

[94] K W Miller, N V Reo, A J Schoot Uiterkamp et al., "Xenon NMR: Chemical shifts of a general anesthetic in common solvents, proteins, and membranes," Proc. Natl. Acad. Sci. USA **78** (8), 4946-4949 (1981).

[95] G J Schrobilgen, "The noble gases," in *NMR and the periodic table*, edited by R K

Harris and B E Mann (Academic Press, New York, 1978), pp. 439-454.

[96] D Raftery, H Long, T Meersmann et al., "High-field NMR of adsorbed xenon polarized by laser pumping," Phys. Rev. Lett. **66** (5), 584-587 (1991).

[97] D Raftery, H Long, L Reven et al., "NMR of optically pumped xenon thin films," Chem. Phys. Lett. **191** (5), 385-390 (1992).

[98] J-L Bonardet, T Domeniconi, P N'Gokoli-Kékélé et al., "Hydrocarbon diffusion measurements and coke distribution in zeolite pellets: a study by ^{1}H NMR imaging and ^{129}Xe spectroscopy," Langmuir **15**, 5836-5840 (1999).

[99] F D Magalhaes, R L Laurence, W C Conner et al., "Study of molecular tansport in beds of zeolite crystallites: semiquantitative modeling of ^{129}Xe NMR experiments," J. Phys. Chem. B **101**, 2277-2284 (1997).

[100] M-A Springuel-Huet, A Nosov, J Kärger et al., "^{129}Xe NMR study of the bed resistance to molecular transport in assemblages of zeolite crystallites," J. Phys. Chem. **100**, 7200-7203 (1996).

[101] T Room, S Appelt, R Seydoux et al., "Enhancement of surface NMR by laser-polarized noble gases," Phys. Rev. B **55** (17), 11604-11610 (1997).

[102] A Bifone, T Pietrass, J Kritzenberger et al., "Surface study of supported metal particles by ^{129}Xe NMR," Phys. Rev. Lett. **74** (16), 3277-3280 (1995).

[103] E Brunner, R Seydoux, M Haake et al., "Surface NMR using laser-polarized ^{129}Xe under magic angle spinning conditions," J. Mag. Reson. **130**, 145-148 (1998).

[104] E Brunner, "Applications of laser-polarized ^{129}Xe under continuous flow," Magn. Reson. Chem. **37**, S14-S22 (1999).

[105] R Seydoux, A Pines, M Haake et al., "NMR with a continuously circulating flow of laser-polarized ^{129}Xe," J. Phys. Chem. **103**, 4629-4637 (1999).

[106] R F Jr. Tilton, "Nuclear magnetic resonance studies of ^{129}Xe with myoglobin and hemoglobin," Biochemisty **21**, 6850-6857 (1982).

[107] T R Stengle, S M Hoesseini, H G Basiri et al., "NMR chemical shifts of xenon in

acqueous solutions of amphiphiles: a new probe of the hydrophobic environment," J. Solution Chem. **13** (11), 779-787 (1984).

[108] T R Stengle, S M Hoesseini, and K L Williamson, "NMR chemical shifts of xenon in mixed aprotic solvents: a probe of liquid structure," J. Sol. Chem. **15** (9), 777-790 (1986).

[109] T R Stengle and K L Williamson, "Nuclear magnetic resonance of xenon adsorbed in solid polymers: a probe of the amorphous state," Macromolecules **20**, 1428-1430 (1987).

[110] M Albert, V D Schepkin, and T F Budinger, "Measurement of ^{129}Xe T_1 in blood to explore the feasibility of hyperpolarized ^{129}Xe MRI," J. Comput. Assist. Tomogr. **19**, 975-978 (1995).

[111] C H Tseng, S Peled, L Nascimben et al., "NMR of laser-polarized ^{129}Xe in blood foam," J. Magn. Reson. **126** (1), 79-86 (1997).

[112] J Wolber, A Cherubini, A S K Dzik-Jurasz et al., "Spin-lattice relaxation of laser-polarized xenon in human blood," Proc. Natl. Acad. Sci. USA **96**, 3664-3669 (1999).

[113] J Wolber, A Cherubini, M O Leach et al., "Hyperpolarized ^{129}Xe as a sensitive NMR probe for blood oxygenation," Eur. Radiol. **9**, B42 (1999).

[114] J Jokisaari, "NMR of noble gases disolved in isotropic and anisotropic liquids," Prog. NMR Spect. **26**, 1-26 (1994).

[115] L Junck, V Dhawan, H T Thaler et al., "Effects of xenon and krypton on regional cerebral blood flow in the rat," J. Cereb. Blood Flow Metab. **5**, 126-132 (1985).

[116] R Kawai, M Lemaire, J-L Steimer et al., "Physiologically based pharmacokinetic study on a cyclosporin derivative, SDZ IMM 125," J. Pharmacokin. Biopharm. **22** (5), 327-365 (1994).

[117] A M Andersen and Ladefoged J, "Partition coefficient of ^{133}Xe between various tissues and blood in vivo," Scand. J. Clin. Lab. Invest. **19**, 72-78 (1967).

[118] L C Ou, G L Sardella, N S Hill et al., "Possible role of pulmonary blood volume in chronic hypoxic pulmonary hypertension," J. Appl. Physiol. **74**, 3020-3026 (1993).

[119] P Anversa, C Beghi, Y Kikkawa et al., "Myocardial infarction in rats: infarct size,

myocyte hypertrophy and capillary growth," Circ. Res. **10**, 26-27 (1986).

[120] K Rakusan, "Vascular capacity and hematocrit in experimental cardiomegaly due to aortic constriction in rats," Can. J. Physiol. Pharmacol. **49**, 819-824 (1971).

[121] J R MacFall, H C Charles, R D Black et al., "Human lung air spaces: Potential for MR imaging with hyperpolarized ^{3}He," Radiology **200** (2), 553-558 (1996).

[122] M Viallon, G P Cofer, S A Suddarth et al., "Functional MR microscopy of the lung using hyperpolarized He-3," Mag. Reson. Med. **41** (4), 787-792 (1999).

[123] J B West and P D Wagner, "Ventilation-perfusion relationships," in *The lung: scientific foundations*, edited by R G Crystal (Raven Press, Ltd., New York, 1991), pp. 1289-1305.

[124] H S Gutowsky, D W McCall, and C P Slichter, "Nuclear magnetic resonance multiplets in liquids," J. Chem. Phys. **21** (2), 279-292 (1953).

[125] L M Jackman and F A Cotton, "Dynamic nuclear magnetic resonance spectroscopy," (Academic Press, Inc., New York, 1975), pp. 660.

[126] J I Kaplan and G Fraenkel, *NMR of chemically exchanging systems* (Academic Press, Inc., New York, 1980).

[127] W Lin, R P Paczynski, K Kuppusamy et al., "Quanitative measurements of regional cerebral blood volume using MRI in rats: effects of arterial carbon dioxide tension and mannitol," Magn. Reson. Med. **38**, 420-428 (1997).

[128] K Zaleska-Freljan and L Cywinska, "The effect of different krill meals fed to laboratory rats on their blood indices," Comp. Biochem. Physiol. **98A** (1), 133-136 (1991).

[129] G J Stanisz, J G Li, G A Wright et al., "Water dynamics in human blood via combined measurements of T_2 relaxation and diffusion in the presence of gadolinium," Magn. Reson. Med. **39**, 223-233 (1998).

[130] K Sakai, A M Bilek, E Oteiza et al., "Temporal dynamics of hyperpolarized ^{129}Xe resonances in living rats," J. Magn. Reson. Series B **111**, 300-304 (1996).

[131] D J Shaw, A Pitt, and G C Friesinger, "Autoradiographic study of ^{133}Xe

disappearance method for measurement of myocardial blood flow," Cardiovasc. Res. **6**, 268-276 (1971).

[132] A Maseri, A L'Abbate, C Michelassi et al., "Possibilities, limitations, and technique for the study of regional myocardial perfusion in man by Xenon-133," Cardio. Res. **11**, 277-290 (1977).

[133] A Maseri, A Pesola, A L'Abbate et al., "Contributions of recirculation and fat diffusion to myocardial washout curves obtained by external counting in man," Circ. Res. **35**, 826-835 (1974).

[134] J H Lawrence, W F Loomis, C A Tobaias et al., "Preliminary observations on the narcotic effect of xenon with a review of values for solubilities of gases in water and oils," J. Physiol. **105**, 197-204 (1946).

[135] O Sakurada, C Kennedy, J Jehle et al., "Measurement of local cerebral blood flow with iodo[^{14}C]-antipyrine," Am. J. Physiol. **234**, H59-H66 (1978).

[136] J R Brookeman, J P Mugler, B Driehuys et al., "MR spectroscopy of the dissolved phase of hyperpolarized Xe-129 in the human brain," Radiology **202** (2), KH03-KH03 (1997).

[137] J P Mugler, B Driehuys, J R Brookeman et al., "MR imaging and spectroscopy using hyperpolarized ^{129}Xe gas: preliminary human results," Magn. Reson. Med. **37**, 809-815 (1997).

[138] P Sandor, J Cox-van Put, W de Jong et al., "Continuous measurements of cerebral blood volume in rats with the photoelectric technique: effect of morphine and naloxone," Life Sciences **39** (18), 1657-1665 (1986).

[139] H Geen and R Freeman, "Band-selective radiofrequency pulses," J. Magn. Reson. **93** (1), 93-141 (1991).

[140] A Alavi, "Perfusion-ventillation lung scans in the diagnosis of pulmonary thromboembolism," Appl. Radiol. **6**, 182-188 (1977).

[141] W H Freygang and L Sokoloff, "Quantitative measurements of regional circulation in the central nervous system by the use of radioactive inert gas," Adv. Biol. Med. Phys. **6**,

263-279 (1958).

[142] B Eklof, N A Lassen, L Nilsson et al., "Regional cerebral blood flow in the rate measured by the tissue sampling technique; a critical evaluation using four indicators ^{14}C-antipyrine, ^{14}C-ethanol, ^{3}H-water and ^{133}xenon," Acta Physiol. Scand. **91**, 1-10 (1974).

[143] M Reivich, J Jehlie, L Sokoloff et al., "Measurement of regional cerebral blood flow with antipyrine-^{14}C in awake cats," J. App. Physiol. **27** (2), 296-300 (1969).

[144] N A Lassen, L Hendricksen, and O Paulson, "Regional cerebral blood flow in stroke by ^{133}Xe inhalation and emisson tomography," Stroke **12**, 284-288 (1981).

[145] N A Lassen and O Munck, "The cerebral blood flow in man determined by the use of radioactive krypton," Acta Physiol. Scand. **33**, 30-49 (1955).

[146] C Fieschi, L Bozzao, and A Agnolli, "Regional clearance of hydrogen as a measure of cerebral blood flow," Acta Neurol. Scand. Suppl. 14 **41**, 46-52 (1965).

[147] A Fick, "Über die messung des blutquantums in den herzventrikeln," Verhandl. d. Phys.-Med. Ges. zu Wüzburg **2**, 16-28 (1870).

[148] M Tomita and F Gotoh, "Local cerebral blood flow values as with diffusible tracers: validity of assumptions in normal and ischemic tissue," J. Cereb. Blood Flow Metab. **1**, 403-411 (1981).

[149] C Fieschi, G Issacs, and S S Kety, "On the question of heterogeneity of local blood flow in grey matter of the brain," in *Blood flow through organs and tissues*, edited by W H Bain and A M Harper (E. & S. Livingstone, Ltd., London, 1968), Vol. 20, pp. 226-231.

[150] A C P Campbell, "The vascular architecture of the cat's brain - A study by vital injection," in *The circulation of the brain and spinal cord: a symposium on blood supply*, edited by S Cobb, A M Frantz, W Penfield et al. (Williams and Wilkins, Baltimore, 1938), Vol. 18.

[151] E Scharrer, "Arteries and veins in the mammalian brain," Anat. Record **78**, 173-196 (1940).

[152] W M Landau, W H Freygang, L P Roland et al., "The local circulation of the living brain; values in the unasthetized and anesthetized cat," Trans. Am. Neurol. Assoc. **80**, 125-

129 (1955).

[153] I Kanno and N A Lassen, "Two methods for calculating regional cerebral blood flow from emission computed tomography of inert gas concentrations," J. Comput. Assist. Tomogr. **3** (1), 71-76 (1979).

[154] K L Zierler, "Equations for measuring blood flow by external monitoring of radioisotopes," Circ. Res. **16**, 309-321 (1965).

[155] K Hoedt-Rasmussen, E Sveinsdottir, and N A Lassen, "Regional cerebral blood flow determined by intra-arterial injection of radioactive inert gas," Circulation Res. **18** (3), 237-247 (1966).

[156] L Sokoloff, "Localization of functional activity in the central nervous system by measurement of glucose utilization with radioactive deoxyglucose," J. Cereb. Blood Flow **1**, 7-36 (1981).

[157] J A Detre, J S Leigh, D S Williams et al., "Perfusion imaging," Magn. Reson. Med. **23**, 37-45 (1992).

[158] V M Mai and S S Berr, "MR perfusion imaging of pulmonary parenchyma using pulsed arterial spin labeling techniques: FAIRER and FAIR," J. Magn. Reson. Imaging **9**, 483-487 (1999).

[159] D S Williams, J A Detre, J S Leigh et al., "Magnetic resonance imaging of perfusion using spin inversion of arterial water," Proc. Natl. Acad. Sci. USA **89**, 212-216 (1992).

[160] W Zhang, D S Williams, J A Detre et al., "Measurement of brain perfusion by volume-localized NMR spectroscopy using inversion of arterial water spins: accounting for transit time and cross-relaxation," Magn. Reson. Med. **25**, 362-371 (1992).

[161] A C McLaughlin, F Q Ye, J J Pekar et al., "Effect of magnetization transfer on the measurement of cerebral blood flow using steady-state arterial spin tagging approaches: a theoretical investigation," Magn. Reson. Med. **37**, 501-510 (1997).

[162] B R Rosen, J W Belliveau, J M Vevea et al., "Perfusion imaging with NMR contrast agents," Magn. Reson. Med. **14**, 249-265 (1990).

[163] A Villringer, B R Rosen, J W Belliveau et al., "Dynamic imaging with lanthanide

chelates in normal brain: contrast due to magnetic susceptibility effects," Magn. Reson. Med. **6**, 166-174 (1988).

[164] T Roberts, "Physiologic measurements by contrast-enhanced MR imaging: expectations and limitations," J. Magn. Reson. **7**, 82-90 (1997).

[165] A Villringer and U Dirnagl, "Coupling of brain activity and cerebral blood flow: basis of functional neuroimaging," Cerebrovasc. Brain. Metab. Rev. **7**, 240-276 (1995).

[166] A Puce, "Comparative assessment of sensorimotor function using functional magnetic resonance imaging and electrophysiological methods," Clin. Neurophysiol. **12**, 450-459 (1995).

[167] F Calamante, D L Thomas, G S Pell et al., "Measuring cerebral blood flow using magnetic resonance imaging techniques," J. Cereb. Blood. Flow. Metab. **19**, 701-735 (1999).

[168] R S J Frackowiak, in *Human Brain Function*, edited by R S J Frackowiak, K J Friston, C D Frith et al. (Academic Press, San Diego, 1997).

[169] P C M van Zijl, S M Eleff, J A Ulatowski et al., "Quantitative assessment of blood flow, blood volume and blood oxygenation effects in functional magnetic resonance imaging," Nature Med. **4**, 159-167 (1998).

[170] S S Kety, "Measurement and visualization of tissue perfusion by means of freely diffusible tracers," in *Diffusion and perfusion magnetic resonance imaging: applications to functional MRI*, edited by D Le Bihan (Raven Press, New York, 1995), pp. 201-204.

[171] S Peled, F A Jolesz, C H Tseng et al., "Determinants of tissue delivery for ^{129}Xe magnetic resonance in humans," Magn. Reson. Med. **36**, 340-344 (1996).

[172] C C Martin, R F Williams, J H Gao et al., "The pharmacokinetics of hyperpolarized xenon: Implications for cerebral MRI," J. Magn. Reson. Img. **7**, 848-854 (1997).

[173] N A Lassen, "Regional cerebral blood flow measurements in stroke: the necessity of a tomographic approach," J. Cereb. Blood Flow Metabol. **1** (2), 141-142 (1981).

[174] N R Davis and W W Mapleson, "Structure and quantification of a physiological model of the distribution of injected agents and inhaled anaesthetics," Br. J. Anaesth. **53**,

399-405 (1981).

[175] D C Look and D R Locker, "Nuclear spin-lattice relaxation measurements by tone-burst modulation," Phys. Rev. Lett. **20**, 987-989 (1986).

[176] R R Ernst, "Sensitivity enhancement in magnetic resonance: I. Analysis of the method of time averaging," Rev. Sci. Inst. **36** (12), 1689-1695 (1965).

[177] H H Donaldson, *The rat; reference tables and data for the albino rat (Mus norvegicus albinus) and the Norway rat (Mus norvegicus)* (Wistar Institute of Anatomy and Biography, Philadelphia, 1915).

[178] P A Bottomley and C J Hardy, "Rapid, reliable in vivo assays of human phosphate metabolites by nuclear magnetic resonance," Clin. Chem. **35** (3), 392-395 (1989).

[179] P A Bottomley, H C Charles, P B Roemer et al., "Human in vivo phosphate metabolite imaging with ^{31}P NMR," Magn. Reson. Med. **7** (3), 319-336 (1988).

[180] P A Bottomley, C J Hardy, and P B Roemer, "Phosphate metabolite imaging and concentration measurement in human heart by nuclear magnetic resonance," Magn. Reson. Med. **14**, 425-434 (1990).

[181] L E Morris, J R Knott, and C B Puttinger, "Electroencephalographic and blood gas observation in human surgical patients during xenon anesthesia," Anesthesiology **16**, 312-319 (1955).

[182] S C Cullen and E G Gross, "The anesthetic properties of xenon in animals and human beings with additional observations on krypton," Nature **113**, 580-582 (1951).

[183] H Yonas, B Grundy, D Gur et al., "Side effects of xenon inhalation," J. Comput. Assist. Tomogr. **5**, 591-592 (1981).

[184] V Dhawan, V M Haughton, H T Thaler et al., "Accuracy of stable xenon/CT measurements of cerebral blood flow: Effects of extrapolated estimates of brain-blood partition coefficients," J. Comput. Assist. Tomogr. **8**, 208-212 (1984).

[185] B P Drayer, S K Wolfson, O M Reinmuth et al., "Xenon enhanced CT for analysis of cerebral integrity, pefusion and blood flow," Stroke **9**, 123-130 (1978).

[186] D B Drayer, D Gur, H Yonas et al., "Abnormality of the xenon brain-blood partition coefficient and blood flow in cerebral infarction," Radiology **135**, 349-354 (1980).

[187] D Gur, H Yonas, D Hervert et al., "Xenon enhanced dynamic computed tomography: Multilevel cerebral blood flow studies," J. Comput. Assist. Tomogr. **5**, 334-340 (1981).

[188] D Gur, H Yonas, and W F Good, "Local cerebral blood flow by xenon-enhanced CT: Current status, potential improvements, and future directions," Cerebrovasc. Brain. Metab. Rev. **1** (1), 68-86 (1989).

[189] J S Meyer, L A Hayman, S Nakajima et al., "Local cerebral blood flow and tissue solubility measured by stable xenon-enhanced computerized tomography," Adv. Neurol. **30**, 73-84 (1981).

[190] J S Meyer, L A Hayman, T Amano et al., "Mapping of local blood flow of human brain by CT scanning during stable xenon inhalation," Stroke **12**, 426-436 (1981).

[191] V Haughton, J Donegan, P Walsh et al., "Clinical cerebral blood flow measurement with inhaled xenon and CT," Am. J. Radiol. **134** (281-283) (1980).

[192] F Kelcz, S K Hilal, P Hartwell et al., "Computed tomographic measurement of the xenon brain blood partition coefficient and implication of regional cerebral blood flow: A preliminary report," Radiology **127**, 385-392 (1978).

[193] M Liotti, C C Martin, J-H Gao et al., "Xenon effects on regional cerebral blood flow assesed by ^{15}O-H_2O positron emmision tomography: Implications for hyperpolarized xenon MRI," J. Magn. Reson. Imag. **7**, 761-764 (1997).

[194] D W Marion and K Crosby, "The effect of stable xenon on ICP," J. Cereb. Blood Flow Metab. **11**, 347-350 (1991).

[195] W A Edelstein, G H Glover, C J Hardy et al., "The intrinsic signal-to-noise ratio in NMR imaging," Magn. Reson. Med. **3**, 604-618 (1986).

[196] A Macovski, "Noise in MRI," Magn. Reson. Med. **36**, 494-497 (1996).

[197] A Abragam, *Principles of nuclear magnetism* (Oxford University Press, New York, 1961).

[198] M A Bouchiat and J Brossel, "Relaxation of optically pumped Rb atoms on paraffin-coated walls," Phys. Rev. **147** (1), 41 (1966).

[199] J D Leroux, V V Teplyakov, and D R Paul, "Gas-transport properties of surface fluorinated poly(vinyltrimethylsilane) films and composite membranes," J. Membr. Sci. **90** (1-2), 55-68 (1994).

[200] C H Tseng, G P Wong, V R Pomeroy et al., "Low-field MRI of laser polarized noble gas," Phys. Rev. Let. **81** (17), 3785-3788 (1998).

[201] L Darrasse, G Guillot, P J Nacher et al., "Low-field He-3 nuclear magnetic resonance in human lungs," Comptes Rendus Acad. Sci. Ser. II-B **324** (11), 691-700 (1997).

[202] G Navon, Y Q Song, T Room et al., "Enhancement of solution NMR and MRI with laser-polarized xenon," Science **271** (5257), 1848-1851 (1996).

[203] S D Swanson, M S Rosen, and T E Chupp, "A system for study of laser-polarized ^{129}Xe in proteins," submitted to The International Society for Magnetic Resonance in Medicine (2001).

[204] N R Roberson, C R Gould, and J D Bowman, "Tests of Time Reversal Invariance in Neutron Physics," (World Scientific, Teaneck, NJ, 1987).

[205] B J Venema, P K Majumder, S K Lamoreaux et al., "Search for a coupling of the earths gravitational-field to nuclear spins in atomic mercury," Phys. Rev. Lett. **68** (2), 135-138 (1992).

[206] D J Wineland, J J Bollinger, D J Heinzen et al., "Search for Anomalous Spin-Dependent Forces Using Stored-Ion Spectroscopy," Phys. Rev. Lett. **67** (13), 1735-1738 (1991).

[207] J E Moody and F Wilczek, "New Macroscopic Forces," Phys. Rev. D **30** (1), 130-138 (1984).

[208] P A Bottomley, "NMR imaging techniques and applications: a review," Rev. Sci. Instrum. **53** (9), 1319-1337 (1982).

[209] P T Callaghan, *Principles of nuclear magnetic resonance microscopy* (Oxford University Press, New York, 1993).

[210] R R Ernst, "Methodology of magnetic resonance imaging," Q. Rev. Biophysics **19** (3/4), 183-220 (1987).

[211] D G Nishimura, *Principles of magnetic resonance imaging* (Stanford, 1996).

[212] F Bloch, "Nuclear induction," Phys. Rev. **70**, 460-474 (1946).

[213] F Bloch, W W Hansen, and M Packard, "The nuclear induction experiment," Phys. Rev., 474-485 (1946).

[214] R R Ernst and W A Anderson, "Application of Fourier transform spectroscopy to magnetic resonance," Rev. Sci. Inst. **37** (1), 93-102 (1966).

[215] P C Lauterbur, "Image formation by induced local interactions - examples employing nuclear magnetic resonance," Nature **242**, 190-191 (1973).

[216] P Mansfield and P K Grannell, "'Diffraction' and microscopy in solids and liquids by NMR," Phys. Rev. B **12** (9), 3618-3634 (1975).

[217] S Ljunggren, "A simple graphical representation of fourier-based imaging methods," J. Magn. Reson. **54**, 338-343 (1983).

[218] D B Twieg, "The k-space formulation of the NMR imaging process with applications in analysis and synthesis of imaging methods," Med. Phys. **10** (5), 610-621 (1983).

[219] R A Brooks and G Di Chiro, "Principles of computer assisted tomography (CAT) in radiographic and radioisotopic imaging," Phys. Med. Biol. **21**, 689-732 (1976).

[220] T F Budinger and G T Gullberg, "Three-dimentional reconstruction of isotope distributions," Phys. Med. Biol. **19**, 387-389 (1974).

[221] L A Shepp, "Computerized tomography and nuclear magnetic resonance," J. Comput. Assist. Tomogr. **4**, 94-107 (1980).

[222] A Kumar, D Welti, and R R Ernst, "NMR Fourier zeugmatography," J. Magn. Reson. **18**, 69-83 (1975).

[223] W A Edelstein, J M S Hutchinson, G Johnson et al., "Spin warp NMR imaging and application to human whole-body imaging," Phys. Med. Biol. **25**, 751-756 (1980).

[224] P C Lauterbur, D N Levin, and R B Marr, "Theory and simulation of NMR spectroscopic imaging and field plotting by projection reconstruction involving an intrinsic frequency dimension," J. Magn. Reson. **59**, 536-541 (1984).

[225] A A Maudsley, S K Hilal, W H Perman et al., "Spatially resolved high resolution spectroscopy by "four-dimensional" NMR," J. Magn. Reson. **51**, 147-152 (1983).

[226] T R Brown, B M Kincaid, and K Ugurbil, "NMR chemical shift imaging in three dimentions," Proc. Natl. Acad. Sci. USA **79**, 3523-3526 (1982).

[227] S J Cox and P Styles, "Towards biochemical imaging," J. Magn. Reson. **40**, 209-212 (1980).

[228] J C Haselgrove, V H Subramanian, J. S. Leigh Jr. et al., "In vivo one dimentional imaging of phosphorus metabolites by phosphorus-31 nuclear magnetic resonance," Science **220**, 1170-1173 (1983).

COLOPHON

This thesis was typeset in Adobe Framemaker 5.5.6 on a Macintosh 8500-132 with 112 MB of RAM. The text face is Minion, a neohumanist face designed by Robert Slimbach and issued in digital form by Adobe Systems, Mountain View California in 1989. It is supplemented here with Mathematical Pi, designed at Linotype-Hell AG and issued in digital form by Adobe Systems in 1990, and by Symbol, designed and issued by Design Science, Inc. in 1992. Figures are set in Helvetica Neue, issued in digital form by Linotype-Hell AG in 1988.